Acousto-optic imaging : challenges of in vivo imaging

Jean-Baptiste Laudereau

THÈSE DE DOCTORAT
DE L'UNIVERSITÉ PIERRE ET MARIE CURIE

Spécialité

Imagerie

(EDPIF- Physique en Île-de-France)

Préparée à l'Institut Langevin - Ondes et Images

Présentée par

Jean-Baptiste LAUDEREAU

Pour obtenir le grade de

DOCTEUR de l'UNIVERSITÉ PIERRE ET MARIE CURIE

Sujet de la thèse :

ACOUSTO-OPTIC IMAGING: CHALLENGES OF *IN VIVO* IMAGING

Soutenue le 21 octobre 2016

devant le jury composé de :

M.	**LEUNG**	**Terence S.**	**Rapporteur**
M.	**DUJARDIN**	**Christophe**	**Rapporteur**
M.	**FABRE**	**Claude**	**Examinateur**
M.	**DOLFI**	**Daniel**	**Examinateur**
M.	**BERCOFF**	**Jérémy**	**Examinateur**
M.	**RAMAZ**	**François**	**Directeur de thèse**
M.	**GENNISSON**	**Jean-Luc**	**Co-Directeur de thèse**
Mme.	**CHAUVET**	**Anne**	**Membre invitée**

Remerciements

Before I switch to french for less official acknowledgements, I would like to thank my two referees Terence S. Leung and Christophe Dujardin for having accepted to review my PhD thesis and who made very relevant comments after both reading the manuscript and hearing the defence. In particular, I would like to thank again Terence S. Leung who accepted to attend a defence in french. I finally would like to thank all members of the jury for having evaluated my work and their very positive comments.

Je voudrais ensuite remercier toute l'équipe d'imagerie acousto-optique dans son ensemble pour les nombreuses discussions que nous avons eues. Plus particulièrement, un grand merci à mes deux directeurs de thèse, François Ramaz et Jean-Luc Gennisson, pour avoir su me faire confiance pour mener ce projet tout en étant toujours présents pour répondre à mes interrogations. Je souhaiterais ensuite remercier Jean-Pierre Huignard pour son expertise scientifique qui m'a été d'une grande aide tout au long de ces trois années. Car ce sujet ne serait certainement pas ce qu'il est sans les autres thésards de l'équipe, je vais poursuivre en remerciant Émilie Benoit qui a planté des bases solides pour ce sujet sur lesquelles j'ai pu m'appuyer tout au long de cette thèse. Merci ensuite à Clément Dupuy pour ses gels de grande qualité, ses talents de codeur ou les manips en musique, et qui a contribué à la réussite de bon nombre d'entre elles. Merci enfin à Baptiste Jayet avec qui, bien que sur des sujets différents, j'ai beaucoup échangé durant toute la période où nous avons partagé la salle de manip. Après les thésards, je tiens à remercier les membres de passage avec qui j'ai eu l'occasion de travailler, Kevin Contreras pendant son post-doc et Baptiste Blochet pendant son projet de recherche. Je tiens enfin à remercier un ancien membre de l'équipe, Max Lesaffre, qui par ses conseils y est pour beaucoup dans mon choix de me lancer dans cette thèse. Je vais clôturer ce paragraphe sur l'imagerie acousto-optique en adressant tous mes encouragements et vœux de réussite à Caroline Venet et Maïmouna Bocoum, qui prendront la suite de mes travaux: il reste encore tant de chose à faire, je leur fais pleinement confiance pour faire aboutir ce projet.

Toujours dans l'Institut Langevin, je voudrais remercier toute l'équipe Physique des Ondes pour la Médecine dirigée par Mickael Tanter pour son expertise dans le domaine des ultrasons et grâce à qui le couplage imagerie acousto-optique/échographie a pu prendre corps. En particulier, je souhaiterais adresser un grand merci à ce dernier pour ses encouragements tout au long de ces trois dernières années, à Jean Provost pour les nombreuses discussions sur les ondes planes que nous avons eues en début de première année, Marc Gesnik et Mafalda Correia pour les séquences ultrasonores dont je me suis inspiré.

D'une manière plus générale, je souhaiterais remercier tout le reste de l'Institut Langevin pour

la qualité, tant scientifique qu'humaine, de l'environnement dans lequel j'ai pu travailler ces trois dernières années. En particulier, je tiens à remercier le bureau R31 et tous ses membres passés que j'ai pu croiser au cours de ma thèse: Olivier, Vincent, Clément, Marion, Peng, Aurélien; Émilie, Baptiste, Amir, Fabien; Camille, Sylvain et Nicolas que je n'ai croisés que rapidement; le ficus (qui tient bon), sans oublier Yann ! Nos discussions plus ou moins scientifiques, notre arbre à badge de conférence et toutes les autres petites traditions me manqueront. A quick word to Slava and Sander who made this office an English speaking office, I guess Peng is feeling less lonely now.

Je voudrais ensuite remercier tous les autres collaborateurs extérieurs à l'Institut Langevin avec qui j'ai eu la chance de travailler. Je souhaite commencer par un grand merci à Anne Chauvet et Thierry Chanelière qui m'ont accueilli au Laboratoire Aimé Cotton pour toutes les expériences de holeburning spectral appliqué à l'imagerie acousto-optique. Je remercie plus particulièrement Anne qui a passé beaucoup de temps à brainstormer avec moi afin de résoudre les problèmes expérimentaux qui se sont présentés et qui a toujours répondu à toutes mes questions de physique. J'ai beaucoup appris au cours de cette retraite sur le plateau d'Orsay et j'en garderai un très bon souvenir malgré les trois heures de transports quotidiennes. Toujours dans le holeburning spectral, je souhaite remercier Philippe Goldner et Alban Ferrier qui m'ont accueilli à l'Institut de Recherche de Chimie Paris pour une bonne partie des caractérisations préliminaires et grâce à qui j'ai pu faire mes armes en matière de cryogénie. Je vais poursuivre en remerciant tous ceux sans qui les preuves de concept de l'imagerie multi-modale n'auraient certainement pas vu le jour: Vincent Servois et Pascale Mariani de l'Institut Curie pour l'application au mélanome uvéal et Ivan Cohen de l'Institut de Biologie de Paris pour les expériences (très) préliminaires sur le cerveau de rat. Je vais terminer en remerciant aussi Jean-Michel Tualle du Laboratoire de Physique du Laser grâce à qui j'ai pu me familiariser avec la détection par capteurs CMOS intelligents.

Je vais quitter le domaine scientifique en remerciant toute ma famille qui m'a toujours soutenu, et en particulier mes parents qui ont su me guider avec clairvoyance dans mes choix aux moments importants et sans qui je ne serais probablement pas là où j'en suis aujourd'hui. Je remercie aussi toute la famille de Laura au grand complet qui m'a toujours accueilli avec chaleur depuis que nous sommes ensembles. Je vais ensuite remercier tous mes amis que je ne nommerai pas individuellement au risque d'en oublier certains. Un grand merci à tous mes amis PC1 pour tout ce que nous avons vécu d'événements heureux, de soirées mémorables et de repas du mercredi ! Dans la même veine, je voudrais remercier les Bichons (le lecteur non-averti me pardonnera le sobriquet, je ne l'ai pas choisi) dont je fréquente certains depuis beaucoup trop longtemps mais que j'ai pourtant toujours autant de plaisir à revoir.

Comme je garde le meilleur pour la fin, je vais ouvrir une parenthèse ici pour remercier tous ceux que j'ai oubliés dans les paragraphes précédents. Il y a encore beaucoup de gens que je souhaiterais ajouter, mais je ne veux pas risquer d'avoir des remerciements aussi longs que le manuscrit !

Je vais donc conclure en remerciant Laura avec qui je partage le quotidien depuis six ans maintenant et qui a vécu cette expérience de la thèse en même temps que moi. Je te remercie de ne pas (trop) t'être moquée de moi malgré le fait que tu aies été docteure en physique avant moi. Merci pour ton soutien au cours de ces trois dernières années, nous avons vécu beaucoup de belles choses, j'espère en vivre encore beaucoup avec toi.

Bref, merci à tous !

Résumé

Imagerie acousto-optique : les défis de l'imagerie *in vivo*

Les tissus biologiques sont des milieux fortement diffusant pour la lumière. En conséquence, les techniques d'imagerie actuelles ne permettent pas d'obtenir un contraste optique en profondeur à moins d'user d'approches invasives. L'imagerie acousto-optique (AO) est une approche couplant lumière et ultrasons (US) qui utilise les US afin de localiser l'information optique en profondeur avec une résolution millimétrique. Couplée à un échographe commercial, cette technique pourrait apporter une information complémentaire permettant d'augmenter la spécificité des US. Grâce à une détection basée sur l'holographie photoréfractive, une plateforme multi-modale AO/US a pu être développée. Dans ce manuscrit, les premiers tests de faisabilité ex vivo sont détaillés en tant que premier jalon de l'imagerie clinique. Des métastases de mélanomes dans le foie ont par exemple été détectées alors que le contraste acoustique n'était pas significatif. En revanche, ces premiers résultats ont souligné deux obstacles majeurs à la mise en place d'applications cliniques.

Le premier concerne la cadence d'imagerie de l'imagerie AO très limitée à cause des séquences US prenant jusqu'à plusieurs dizaines de secondes. Le second concerne le speckle qui se décorrèle en milieu vivant sur des temps inférieurs à 1 ms, trop rapide pour les cristaux photorefractif actuellement en palce. Dans ce manuscrit, je propose une nouvelle séquence US permettant d'augmenter la cadence d'imagerie d'un ordre de grandeur au moins ainsi qu'une détection alternative basée sur le creusement de trous spectraux dans des cristaux dopés avec des terres rares qui permet de s'affranchir de la décorrélation du speckle.

Mots-clés : imagerie acousto-optique; ultrasons; milieux diffusant; holographie photoréfractive; holeburning spectral; imagerie médicale

Abstract

Acousto-optic imaging: challenges of *in vivo* imaging

Biological tissues are very strong light-scattering media. As a consequence, current medical imaging devices do not allow deep optical imaging unless invasive techniques are used. Acousto-optic (AO) imaging is a light-ultrasound coupling technique that takes advantage of the ballistic propagation of ultrasound in biological tissues to access optical contrast with a millimeter resolution. Coupled to commercial ultrasound (US) scanners, it could add useful information to increase US specificity. Thanks to photorefractive crystals, a bimodal AO/US imaging setup based on wavefront adaptive holography was developed and recently showed promising ex vivo results. In this thesis, the very first ones of them are described such as melanoma metastases in liver samples that were detected through AO imaging despite acoustical contrast was not significant. These results highlighted two major difficulties regarding in vivo imaging that have to be addressed before any clinical applications can be thought of.

The first one concerns current AO sequences that take several tens of seconds to form an image, far too slow for clinical imaging. The second issue concerns in vivo speckle decorrelation that occurs over less than 1 ms, too fast for photorefractive crystals. In this thesis, I present a new US sequence that allows increasing the framerate of at least one order of magnitude and an alternative light detection scheme based on spectral holeburning in rare-earth doped crystals that allows overcoming speckle decorrelation as first steps toward in vivo imaging.

Keywords: acousto-optic imaging; ultrasound; scattering media; photorefractive holography; spectral holeburning; medical imaging

Contents

List of abbreviations

- **AM**: Amplitude Modulation
- **AOCT**: Acousto-Optical Coherent Tomography
- **AOI**: Acousto-Optic Imaging
- **AOM**: Acousto-Optic Modulator
- **APD**: Avalanche Photodiode
- **ASE**: Amplified Spontaneous Emission
- **AWG**: Arbitrary Waveform Generator
- **BGO**: Bismuth Germanate, $Bi_{12}GeO_{20}$
- **BSO**: Bismuth Silicon Oxide, $Bi_{12}SiO_{20}$
- **BTO**: Bismuth Titanate, $Bi_{12}TiO_{20}$
- **CL**: Cylindrical Lens
- **CNR**: Contrast-to-Noise Ratio
- **CT**: Computerized Tomography (XRays)
- **DORT**: French acronym for Decomposition of the Time-Reversal Operator
- **DOT**: Diffuse Optical Tomography
- **DPAOM**: Double-Pass Acousto-Optic Modulator
- **FDA**: US Food and Drug Administration
- **FFT**: Fast Fourier Transform
- **FTAOI**: Fourier-Transform Acousto-Optic Imaging
- **FWHM**: Full Width at Half Maximum
- **GPU**: Graphic Processing Units
- **HIFU**: High Intensity Focused Ultrasound
- **LCOF**: Liquid Core Optical Fibre
- **LCOS**: Liquid Crystals on Silicon
- **LCLV**: Liquid Crystal Light Valve
- **LD**: Laser Diode
- **MI**: Mechanical Index
- **MMOF**: Multi-Mode Optical Fibre
- **MOPA**: Master Oscillator Power Amplifier
- **MRI**: Magnetic Resonance Imaging
- **NA**: Numerical Aperture
- **NIR**: Near-Infrared Light
- **OCT**: Optical Coherence Tomography
- **OPT**: Optical Projection Tomography
- **PBS**: Polarization Beam Splitter
- **PD**: Photodiode
- **PDH**: Pound-Drever-Hall locking method

- **PET**: Positron Emission Tomography
- **PNP**: Peak Negative Pressure
- **PRC**: Photorefractive Crystal
- **PSF**: Point Spread Function
- **SHB**: Spectral Holeburning
- **SLM**: Spatial Light Modulator
- **SMOF**: Single-Mode Optical Fibre
- **SNR**: Signal-to-Noise Ratio
- **SPS**: $Sn_2P_2S_6$, tin thiohypodiphosphate
- **TA**: Tapered Amplifier
- **TL**: Thick Lens
- **TRUE**: Time-Reversed Ultrasonically Encoded focusing
- **TWM**: Two-Wave Mixing
- **US**: Ultrasound
- **YAG**: Yttrium Aluminium Garnet

List of symbols

General notations

- $\mathcal{E}$: light electric field ($\mathrm{V \cdot m^{-1}}$)
- E: light electric field amplitude ($\mathrm{V \cdot m^{-1}}$)
- $\mathcal{E}_R$ (E_R): reference electric field in interferometry
- $\mathcal{E}_S$ (E_S): scattered electric field and signal in interferometry
- λ: light wavelength (m)
- Λ: ultrasound wavelength (m)
- c: speed of light ($\mathrm{m \cdot s^{-1}}$)
- V_{US}: speed of ultrasound ($\mathrm{m \cdot s^{-1}}$)

- t: time (s)
- τ: alternative time variable (s)
- ν: frequency (conjugated to t) (Hz)
- ν_0: light frequency (Hz)
- ν_{US}: ultrasound frequency (Hz)
- ω: pulsation ($\mathrm{rad \cdot s^{-1}}$)
- ω_0: light pulsation ($\mathrm{rad \cdot s^{-1}}$)
- ω_{US}: ultrasound pulsation ($\mathrm{rad \cdot s^{-1}}$)
- $\mathbf{k}_0$: light wave-vector ($\mathrm{rad \cdot m^{-1}}$)
- k_0: modulus of light wave-vector ($\mathrm{rad \cdot m^{-1}}$)
- $\mathbf{K}_{US}$: wave-vector of the acoustic wave ($\mathrm{rad \cdot m^{-1}}$)
- K_{US}: modulus of the acoustic wave-vector ($\mathrm{rad \cdot m^{-1}}$)
- $\mathbf{k}_S$: signal beam wave-vector in interferometry ($\mathrm{rad \cdot m^{-1}}$)
- $\mathbf{k}_R$: reference beam wave-vector in interferometry ($\mathrm{rad \cdot m^{-1}}$)
- ψ: phase terms (rad)

- ρ: density of a material ($\mathrm{kg \cdot m^{-3}}$)
- S: area of an object ($\mathrm{m^2}$)

- P_{US}: acoustic pressure wave (Pa)
- P_0: amplitude of acoustic pressure wave (Pa)
- $\mathbf{u}$ (u): acoustic displacement vector (modulus) (m)
- $\mathbf{u_0}$ (u_0): amplitude vector (modulus) of displacement field (m)
- Z: acoustic impedance ($\mathrm{Pa \cdot s \cdot m^{-1}}$)

- T: temperature (K)

- k_B: Boltzmann constant ($\mathrm{m}^2 \cdot \mathrm{kg} \cdot \mathrm{s}^{-2} \cdot \mathrm{K}^{-1}$)

- e: elementary charge (C)
- μ: charge mobility ($\mathrm{m}^2 \cdot \mathrm{V}^{-1} \cdot \mathrm{s}^{-1}$)
- $\mathbf{j}$: current density ($\mathrm{A} \cdot \mathrm{m}^{-2}$)

- n: refractive index of a material
- n_0: 0^{th} order refractive index
- ϵ: permittivity of a material ($\mathrm{m}^{-3} \cdot \mathrm{kg}^{-1} \cdot \mathrm{s}^4 \cdot \mathrm{A}^2$)
- ϵ_0: permittivity of vacuum ($\mathrm{m}^{-3} \cdot \mathrm{kg}^{-1} \cdot \mathrm{s}^4 \cdot \mathrm{A}^2$)

- ε: depth of a modulation process (units depend on the process)

- ϕ: photons number per unit of time and surface ($\mathrm{m}^{-2} \cdot \mathrm{s}^{-1}$)
- Ψ: light power *flux* (W)
- Φ: light irradiance ($\mathrm{W} \cdot \mathrm{m}^{-2}$)
- s_{PD}: electric signal on a photodiode (V)
- G: autocorrelation of the electric field

- σ: cross-section of a phenomenon (m^2)
- α: absorption of an object (m^{-1})
- $\mathcal{T}$: transmission of an object

- x: ultrasound propagation direction (m)
- $\mathbf{u}_x$: unit vector along x-axis
- y: ultrasound probe axis (m)
- $\mathbf{u}_y$: unit vector along y-axis
- z: light propagation direction (m)
- $\mathbf{u}_z$: unit vector along z-axis
- r: radial coordinate inside an object (m)
- φ: angular coordinate inside an object (rad)
- η: spatial frequency (m^{-1})
- s: curved length of a path (m)

- J_n: n^{th} order Bessel function of the first kind
- δ: Dirac distribution

- $\mathcal{R}(a)$: real part of a
- $\widetilde{a}$: 1D Fourier transform of a
- $\widehat{a}$: 2D Fourier transform of a
- A: Radon transform of a
- $\mathcal{B}[a]$: backprojection operator of a
- **grad** a: gradient of a
- $\underline{\underline{a}}$: notation for tensor a

Scattering media

- l_a: absorption mean-free-path (m)
- μ_{a}: absorption coefficient (m^{-1})
- l_s: scattering mean-free-path (m)
- μ_{s}: scattering coefficient (m^{-1})
- g: anisotropy coefficient
- l^*: transport mean-free-path (m)
- μ'_{s}: reduced scattering coefficient (m^{-1})
- μ_{ext}: extinction coefficient (m^{-1})
- μ_{eff}: effective scattering coefficient (m^{-1})

- c_i: concentration of Intralipid-10% ($\mathrm{g} \cdot \mathrm{L}^{-1}$)

- $\mathbf{r}$: radial position vector inside the medium (m)
- $\mathbf{r}'$: radial position vector outside the medium (m)

- l_j: length of the j^{th} scattering event (m)
- s_p: length of optical path number p (m)
- a_p: weight of path p

- $\mathcal{S}$: speckle pattern (no dimension)
- Ψ_S: overall scattered power *flux* (W)
- Φ_S: scattered irradiance ($\mathrm{W} \cdot \mathrm{m}^{-2}$)
- Σ: Gaussian fit of scattered light irradiance

Acousto-optic imaging

- ξ: piezooptical coefficient (no dimension)

- Ψ_T: tagged photons power *flux* (W)
- Ψ_{UT}: untagged photons power *flux* (W)

- I: acousto-optic image to be recovered ($\mathrm{W} \cdot \mathrm{m}^{-2}$)

- $\Delta\psi_s$: light phase variation due to scatterers position modulation
- $\Delta\psi_s^j$: light phase variation due to scatterers position modulation over the j^{th} scattering event
- $\Delta\psi_n$: light phase variation due to refractive index modulation
- $\Delta\psi_n^j$: light phase variation due to refractive index modulation over the j^{th} scattering event
- $\Delta\psi_0^j$: light phase variation over the static j^{th} scattering event
- $\Delta\psi_p$: light phase variation over the p^{th} optical path with both contributions

- α_s^j, α_n^j, ψ_s^j, ψ_n^j: random coefficients of the ultrasound modulation over the j^{th} scattering event
- α_u^p, ψ_u^p, α_p, ψ_p: resp. coefficients of the ultrasound modulation of the optical path number p for displacement (subscript u) and pressure
- δ_s, δ_n: overall amplitude of the ultrasound modulation on resp. the scatterers position and refractive index

- $\mathcal{S}_j$: speckle pattern of the j^{th} harmonic (no dimension)

- $\Omega(\mathbf{r}, \mathbf{r}')$: probability of tagging a photons at r and detecting it at $\mathbf{r}'$

Photorefractive effect

- $\underline{\underline{\eta}}$ (η_{ij}): impermeability tensor ($\mathrm{m}^3 \cdot \mathrm{kg}^1 \cdot \mathrm{s}^{-4} \cdot \mathrm{A}^{-2}$)
- $\underline{\underline{r}}$ (r_{ijk}): electrooptic tensor ($\mathrm{m} \cdot \mathrm{V}^{-1}$)
- r_{eff}: effective electrooptic coefficient ($\mathrm{m} \cdot \mathrm{V}^{-1}$)

- Φ_D: light irradiance after the photorefractive crystal ($\mathrm{W} \cdot \mathrm{m}^{-2}$)

- $\Delta\mathbf{k}$ (Δk): interference pattern wave-vector (modulus) ($\mathrm{rad} \cdot \mathrm{m}^{-1}$)
- k_D: Debye wave-vector ($\mathrm{rad} \cdot \mathrm{m}^{-1}$)

- $\mathbf{E}^{\text{sc}}$ (E^{sc}): space-charge field (modulus) ($\mathrm{V} \cdot \mathrm{m}^{-1}$)

- τ_{PR}: photorefractive response time (s)
- γ: photorefractive gain in amplitude (m^{-1})
- γ_{PR}: photorefractive gain in intensity (m^{-1})

- N^0: number of neutral centres per unit volume (m^{-3})
- N^+: number of ionized centres per unit volume (m^{-3})
- N_A: number of acceptor traps per unit volume (m^{-3})
- N_D: number of donor traps per unit volume (m^{-3})
- N_{eff}: effective number of centres per unit volume (m^{-3})
- n: number of electrons per unit volume (m^{-3})
- p: number of holes per unit volume (m^{-3})

- σ_n, σ_p: photoexcitation cross-section of electrons, holes (m^2)
- β_n, β_p: thermal excitation rate of electrons, holes (s^{-1})
- α_n, α_p: absorption coefficient of photoexcitation of electrons, holes (m^{-1})
- μ_n, μ_p: electrons, holes mobility ($\mathrm{m}^2 \cdot \mathrm{V}^{-1} \cdot \mathrm{s}^{-1}$)
- $\mathbf{j}_n$, $\mathbf{j}_p$: current density of electrons, holes ($\mathrm{A} \cdot \mathrm{m}^{-2}$)
- γ_n, γ_p: recombination rate for electrons, holes (s^{-1})
- τ_n, τ_p: characteristic time before recombination for electrons, holes (s)
- r_n, r_p: characteristic travelled distance before recombination (m)

- ξ_0: hole/electron competition factor
- $\mathcal{A}_n$, $\mathcal{A}_p$: correcting factor with thermal energy contribution

- $\mathbf{E}_{loc}$: photoinduced electric field ($\mathrm{V}{\cdot}\mathrm{m}^{-1}$)
- $\mathbf{E}_{loc,1}$ ($E_{loc,1}$): modulated part of the photoinduced electric field ($\mathrm{V} \cdot \mathrm{m}^{-1}$)
- n_1: modulated part of the refractive index

- H: transfer function of the photorefractive crystal
- $\varphi(t)$: phase modulation

Plane waves imaging

- θ: angle of propagation of the plane wave
- θ_m: maximum angle of propagation

- $\widetilde{R}$: temporal response shape of the optical detection (in Fourier space)
- BW: bandwidth of the optical detection (Hz)

- $\mathcal{I}$: reconstructed acousto-optic imaging with plane waves
- PSF: point-spread function of the plane waves technique

- $\mathscr{A}$: Airy disk
- $\mathscr{B}$: first correcting term of the plane waves image
- $\mathscr{C}$: second correcting term of the plane waves image

- c_p: inductive part of the second correcting term
- $f(\nu)$: filter used in the filtered backprojection
- rect: rectangle function

Spectral holeburning

- T_1: lifetime of a level (s)
- T_2: lifetime of the coherences (s)
- T^*: correcting lifetime of the lifetime a state (s)
- $T_{2,max}$: maximum lifetime a state (s)
- T_{PE}: decay time of the photon echo (s)

- Γ_h: homogeneous linewidth (Hz)
- Γ_{inh}: inhomogeneous linewidth (Hz)
- Γ_{HB}: linewidth of a hole (Hz)
- Γ_l: laser linewidth (Hz)

- f: oscillator strength of the transition
- g_i: degeneracy factor of level i
- σ_h: maximum of the homogeneous cross-section (m^2)
- ν_c: center frequency of the inhomogeneous spectral line (Hz)
- $A_{i\to j}$: Einstein coefficient A for the transition i to j (s^{-1})
- $B_{i\to j}$: Einstein coefficient B for the transition i to j ($\mathrm{J}^{-1}\cdot\mathrm{m}^3\cdot\mathrm{s}^{-2}$)

- α_m: maximum absorption of the crystal (m^{-1})
- $\Delta\alpha$: absorption variation due to holeburning process (m^{-1})
- ϕ_s: saturation number of photons per unit of time and surface ($\mathrm{m}^{-2}\cdot\mathrm{s}^{-1}$)
- Φ_s: saturation irradiance ($\mathrm{W}\cdot\mathrm{s}^{-1}$)

- $\mathcal{L}$: Lorentzian laser spectral line

- ν_b: burning frequency (Hz)
- T_b: burning duration (s)
- ϕ_b: burning photons number per unit of time and surface ($\mathrm{m}^{-2}\cdot\mathrm{s}^{-1}$)
- Ψ_b: burning power *flux* (W)
- Φ_b: burning irradiance ($\mathrm{W}\cdot\mathrm{m}^{-2}$)

- ν_p: probing frequency (Hz)
- T_p: probing duration (s)
- ϕ_p: probing photons number per unit of time and surface ($\mathrm{m}^{-2}\cdot\mathrm{s}^{-1}$)
- Ψ_p: probing power *flux* (W)
- Φ_p: probing irradiance ($\mathrm{W}\cdot\mathrm{m}^{-2}$)

- w: spontaneous emission rate (s^{-1})
- β: decay rate from excited state (s^{-1})
- γ: decay rate from metastable state (s^{-1})
- κ: transition rate between the two split ground states (s)
- ζ, ζ_B: effective lifetime in holeburning without and with magnetic field (s)

- $\mathbf{B}_0$ (B_0): magnetic field (G)
- δ_g, δ_e: ground and excited states splitting ($\mathrm{Hz}\cdot\mathrm{G}^{-1}$)
- Δ_g, Δ_e: ground and excited states splitting (Hz)

Introduction

Efficient treatment of diseases needs an accurate diagnosis and understanding of the mechanisms that are involved. In such dynamics, medical imaging is of prime relevance for it is used at several stages in medical processes from detection, to surgery and therapy monitoring. Recent developments in medical imaging reduced treatments invasiveness by allowing physicians to better adapt their procedures. Classical medical imaging techniques such as Magnetic Resonance Imaging (MRI), X-rays computerized tomography (CT) or ultrasound scans benefited from a lot of improvements during the end of last century and are now minimally invasive with high sensitivity. Among these techniques, ultrasound is of prime interest for it is cheaper, more compact and wide-spread than the others. Nowadays, several ultrasound scanners can be found in all hospitals and are part of a lot of medical procedures, such as cancer diagnosis and therapy or intraoperative surgical imaging.

It appeared these last few years that, if they now have a good sensitivity (*i.e.* the ability of detecting a pathology or not), conventional medical imaging techniques often suffer from a lack of specificity (*i.e.* the ability of distinguishing different pathologies). Current trends in medical imaging are then focused on increasing patient's specificity. Two approaches are being explored. The first one is molecular imaging and uses biomarkers that specifically interact with a given kind of biological species and increase the associated contrast. The second one is multi-modality that couples different medical imaging techniques in order to overcome detection failures or remove uncertainties. Among these recent developments, multi-waves imaging techniques offer promising outcomes. Such techniques usually couple a specific and poorly resolved modality with a low specificity but highly resolved one in such a way that it is possible to get the best out from the two techniques.

Regarding such challenges, optical contrast has promising potential for it contains both structural (detection of interfaces for instance) and spectral (the chemical nature) information about the biological species it interacts with. The two main current medical optical techniques that can be found in hospitals are microscopy and pulse oximetry. The first one is widely used during surgical procedures for instance by anatomopathologists. In anatomopathology, thin histological sections are used in order to assess the limits of objects to be resected. The second one is used in order to monitor blood oxygenation inside a finger or an ear.

These two biomedical optics techniques give an example of the different kind of information light can bring about tissues: microscopy provides optical-resolution images of cellular structures whereas pulse oximetry provides spectral information about blood in order to measure its oxy-

genation. On the other hand, these techniques highlight the major issue of optical imaging in biological samples. Microscopy only works on thin and transparent histological sections, pulsed oximetry works on thicker samples but only provides a spatially unresolved measurement of a biological parameter.

These limitations come from multiple light scattering and explain why optical imaging was missing from the list of medical imaging modalities up to now. When propagating inside biological samples, light is scattered by the structures it encounters so that the information it carries is not interpretable for conventional imaging techniques based on geometrical optics. As a consequence, conventional approaches are subject to a compromise between resolution and imaging depth. Optical-resolution techniques must work on ballistic photons that do not experience any scattering events and are limited to shallow depths. On the other hand, techniques working with multiply scattered photons are limited to a resolution equal to one fifth of the sample thickness.

A way of overcoming this difficulty is to couple light and ultrasound. Beside the fact that it is widely used and easy to find, ultrasound is not scattered by biological tissues. The goal of such multi-waves techniques is then to super-resolve optical information coming from deep areas. Acousto-optics is one of these techniques. When propagating through an illuminated area, ultrasound locally modulates light through acousto-optic effect and generates *tagged photons*. The measurement of those photons power gives information about the light irradiance inside the scattering medium with an ultrasonic resolution.

The detection of tagged photons is very challenging and is studied since mid-90s. Several techniques were developed such as camera techniques, self-adaptive interferometry or ultra-narrowband filters. Recent works at the Institut Langevin led to the development of a multi-modal platform coupling conventional ultrasound and acousto-optic imaging that allows adding optical contrast to structural information provided by ultrasound. Such a platform may increase diagnosis accuracy and constitutes the very first step toward clinical imaging. As a consequence, current works are focused on the improvement of the platform in order to address challenges of *in vivo* imaging.

This manuscript is composed of four distinct parts. The first part aims at introducing the principle of acousto-optic imaging. I will first give the physical properties of light propagation inside biological media and list a few examples of current optical imaging techniques. The idea is to show the main limitations induced by scattering inside biological tissues and how it is usually overcome. I will show that in order to perform proper deep optical imaging, it is necessary to work in the near-infrared (NIR) region and deal with speckle patterns – a random interference pattern. I will then introduce the principle of acousto-optic imaging and the corresponding theoretical background. The idea is to show that the measurement of tagged photons *flux* gives a signal proportional to the local light irradiance inside the scattering medium integrated over the ultrasound volume. I will also show that the amount of acousto-optic signal is proportional to the pressure squared. After these quick derivations, I will list several possible ways of filtering tagged photons.

In the second part, I will describe the principle of the multi-modal platform. I will first describe how acousto-optic imaging can be coupled to conventional ultrasound by describing with more details a particular detection scheme based on photorefractive holography. I will show that this kind of detection allows performing interferometry while adapting scattered and reference wavefronts. I will show that such a method allows overcoming most of the issues induced by speckle patterns. Once this detection scheme is described, I will give more details about our multi-modal platform and first examples of promising proofs of concept. These results will allow to highlight

the main limitations of the technique that prevent from switching to clinical imaging for now. I will show that current acousto-optic sequences lead to low imaging framerates and that the photorefractive detection is limited by speckle decorrelation *in vivo*. These two points will be addressed separately in two parts.

In a third part, I will address the problem of low acousto-optic imaging framerate. I will suggest a novel ultrasound sequence based on plane waves and a tomographic reconstruction approach. I will first derive a theoretical framework for the technique in order to assess a few properties and a proper reconstruction method. Among others, I will show that, because of the limited emission angle of linear arrays, the lateral resolution of plane waves images is degraded. On the other hand, I will show that such a sequence leads to increased signal-to-noise ratio (SNR) and allows to decrease the imaging rate up to a factor of about fifty.

In the fourth and last part, I will study the use of spectral holeburning as an ultra-narrowband filter in order to directly measure the *flux* of tagged photons. Such a technique is not sensitive to speckle decorrelation and makes an interesting candidate for *in vivo* imaging but was left aside because it works at cryogenic temperatures. The technique as it was suggested is limited by the short lifetime of the hole. I will show that the presence of an external magnetic field increases this lifetime by two orders of magnitude.

Part I

Optical imaging of thick biological tissues

CHAPTER 1

Optical properties of biological tissues

Table of contents

Light can interact with its surroundings in two ways: it can be either absorbed or scattered. Light absorption is related to the chemical nature of the species it encounters and generally carries information about metabolism. Typical absorbing biological species are melanin, blood, proteins or even water [1]. On the other hand, light scattering will occur in the presence of interfaces associated with discontinuities of refraction index and will be influenced by anisotropy. Light scattering will generally give information about the structure of tissues. For comparison purpose, PET (Positron Emission Tomography) scans have very specific contrast that gives accurate functional information, but need isotopes and usually gives poor information about biological structures [2]. Conventional use of CT scans (X-rays) and ultrasound on the other hand only gives information about biological structures – tissues density for CT, acoustic impedance losses for ultrasound [3, Chapters 2 and 5]. MRI is the only technique that can give both structures [4] and functional imaging [5] but suffers from very high costs and low imaging rates. Recent advances in ultrasound led to efficient Doppler imaging which is able to image blood flows [6] and gave first promising results in functional imaging [7]. Because optical imaging naturally contains both type of contrast, it generally makes a powerful imaging tool. However, it is very important to keep in mind that a medical imaging modality is expected to image entire organs and have to reach depth of several centimetres. This requirement is the major obstacle to the development of optical medical imaging modalities: light is multiply scattered by biological structures beyond 1 mm so that the information it carries is completely lost. In this first chapter, I will describe the properties of light-tissues interaction and show few existing techniques that meet medical imaging requirements, among which is acousto-optic imaging.

1.1 Optical contrast in medical imaging

Over years, optical imaging was thought of as alternative methods to invasive procedures such as surgery. The most straightforward way of performing optical medical imaging is to place a powerful light source behind patient's organs to image and look at what comes through. Based on this idea, the first optical techniques were optical imaging in transmission. Diaphanography [8], based on the idea of Cutler in 1931 [9], was the first technique of this kind that was developed in clinical applications. It consisted in a transillumination technique with visible or near-infrared (NIR) light used for imaging breast lesions. The concept is based on the fact that blood and tumours absorb NIR light whereas normal breast mostly transmit it as shown on figure 1.1. The main advantage of such a technique was that it was non invasive, non ionizing and easy to set up. Few years later, B. Monsees [10] demonstrated the inefficiency of such transillumination techniques as a diagnosis tool for breast tumours and optical imaging was abandoned in favour of mammography.

The major issue of transillumination techniques such as diaphanography is that the resolution in a multiple-scattering regime is limited to one fifth of the imaging depth [11]. It then rapidly appears that optical techniques fail at imaging early stage tumours of few millimetres sizes. Because of this issue, most of optical clinical techniques are now endoscopic or spectroscopic techniques. The latter techniques are generally used for patients monitoring and take advantage of all bio-

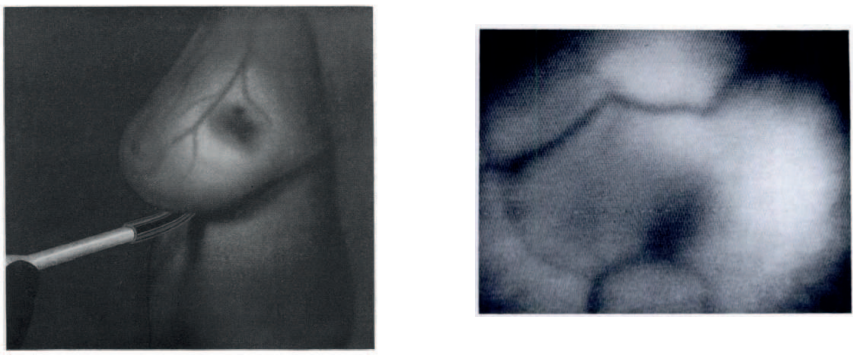

(a) Cutler's experiment (b) Marshall *et al.* experiment

Figure 1.1 – Breast imaging through transillumination showing the high absorption of blood and suspicious area compared to normal breast. (a) Figure extracted from [9]. The blood vessels are visible, the black area is an haematoma. (b) Figure extracted from [8]. Clinical application of transillumination imaging for detection of breast tumours. The blood vessels are also appearing, the dark area is a carcinoma.

logical chromophores having very different absorption spectra. These techniques usually measure a physiological parameter integrated over the diffused light volume. One of the main techniques in this field is the pulse oximetre in which the oxygen saturation of blood is measured through global light absorption through a finger or an ear [12]. As an other example, light is also widely used in brain studies, as shown in the review of E. M. C. Hillman [13], in order to perform surface functional imaging or *in vivo* microscopy of exposed cortex.

Human body is mostly composed of water that strongly absorbs non visible light as can be seen on the spectrum extracted from [14] presented on figure 1.2(a). On the other hand, most of the other chromophores (coloured species) that constitute biological tissues strongly absorb in the visible domain. For instance, blood is very absorbing under 600 nm as shown on figure 1.2(b) also extracted from [14]. It comes that biological samples are very absorbing in general, except within a particular region between 600 nm and 1.3 µm. This spectral domain is called the optical therapeutic window and explains why transilluminated biological samples appear red. For medical imaging applications, in which high depths are to be reached, it is thus preferable to work around this wavelength range. People work usually between 700 nm and 900 nm. Recent work of Hong *et al.* [15] revealed the existence of a second narrow optical window between 1.3 and 1.4 µm in which scattering is a bit lower. Exploiting the photoluminescence of single-walled carbon nanotubes, they performed through-scalp and through-skull optical fluorescence brain imaging on living mice. With this approach, they obtained unprecedented dynamic images of brain blood perfusion with a resolution of 10 µm at a depth over 2 mm.

It was recently shown that techniques such as X-rays or conventional ultrasound that image structural alterations in tissues often lack of specificity. In the field of breast cancer imaging for instance, it was shown that mammography has a severe issue of false-positive [16] – breast lesions that are diagnosed as cancerous as they are not – and, more significant for patients, of false-negative [17] – breast lesions that are not detected or diagnosed as not cancerous as they actually are. Some works showed that coupling mammography to Diffuse Optical Tomography (DOT) – that consists in solving an inverse light scattering problem in order to recover images, see section 1.4.2 – allows imaging the haemoglobin concentration in the surroundings of breast lesions [18]. On the other hand, it was shown that optical imaging using fluorescent markers of tumorous tissues provides very specific information similar to what is usually obtained with

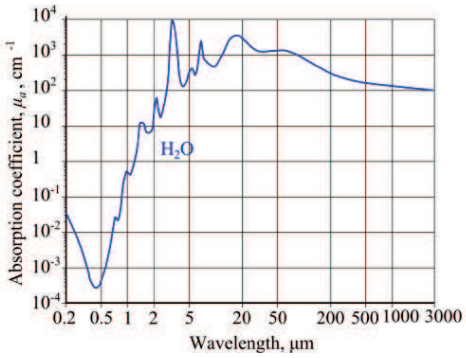

(a) Absorption spectrum of water [14]

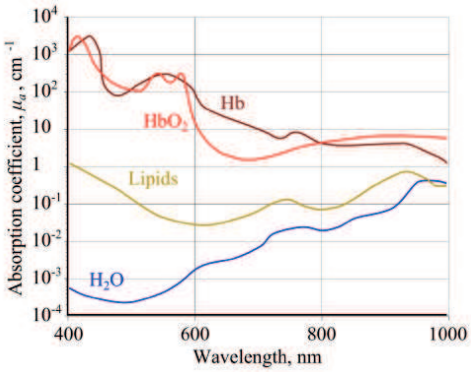

(b) Absorption spectra of several chromophores [14]

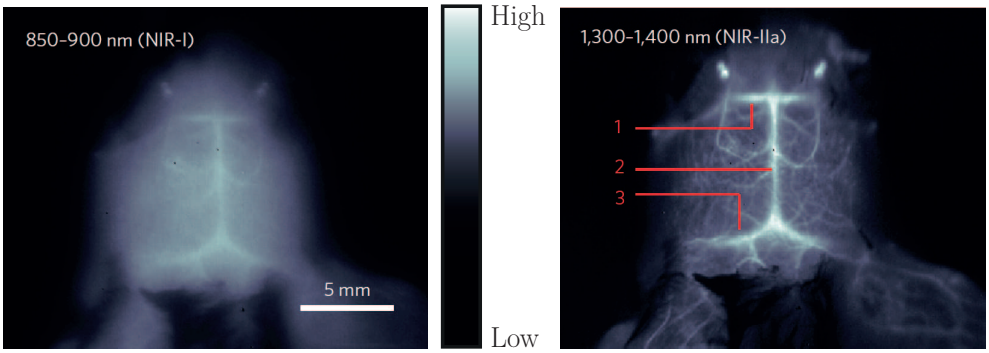

1: Inferior cerebral vein 2: Superior sagittal sinus 3: Transverse sinus

(c) The optical window around 1.3 and 1.4 µm [15]

Figure 1.2 – (a) and (b) Spectra extracted from [14] showing the optical window between 650 nm and 1.3 µm. (c) Figure extracted from [15] that shows through-scalp and through-skull fluorescence images of the brain vasculature within the NIR regions between 850 nm and 900 nm (left) and 1.3 and 1.4 µm (right)

PET scans, but without the need of radioactive markers. For instance, Koenig *et al.* developed a whole-body fluorescence optical tomography device based on a principle very close to DOT that allowed imaging lung tumours in mice [19].

If transillumination optical imaging alone turned not to be an efficient technique, these recent works showed that optical imaging brings very interesting new information when coupled to structural imaging techniques.

1.2 Light-tissues interactions

Light can interact in two ways with its surroundings. It can be either absorbed or scattered and these two phenomena have a very important influence of how light is measured from the outside. As explained in the previous section, the first optical medical imaging methods were left aside partly because of light scattering that strongly degrades the obtainable resolution. However, a lot of medical applications are still based on light and in particular on light absorption. In this section I suggest to further explore how light can interact with biological tissues in order to introduce the general formalism that will be used in the subsequent manuscript.

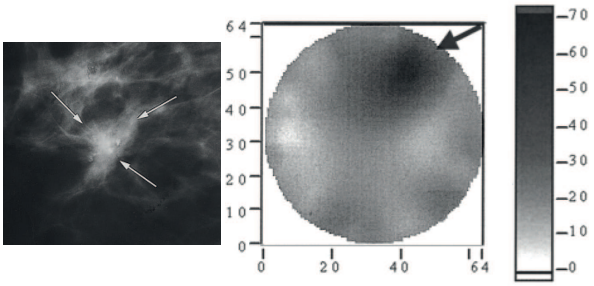

Mammogram showing invasive ductal carcinoma | DOT image of hemoglobine concentration (colorbar in μM)

(a) Mammogram and DOT image [18]

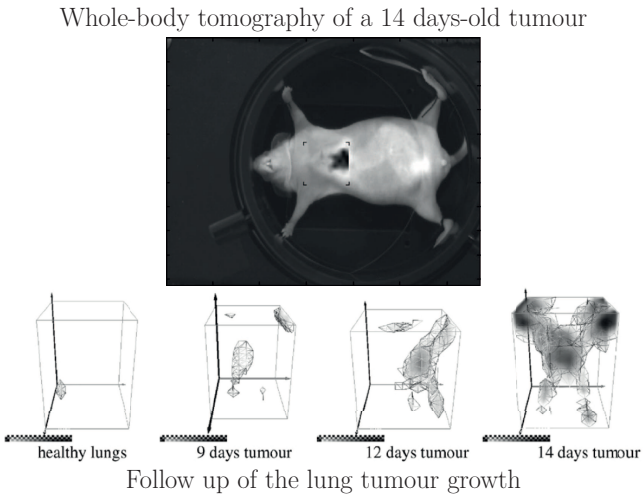

(b) Fluorescence image of lung tumours in a mouse [19]

Figure 1.3 – Two examples of recent optical imaging techniques. (a) Figure extracted from [18]. Mammography coupled with DOT for haemoglobin concentration. The arrows point the tumour out. (b) Figure extracted from [19]. Whole-body fluorescence optical tomography of lung tumours in a mouse.

1.2.1 Absorption

Inside a homogeneous medium, light propagates along a straight line and the loss of energy is given by the Beer-Lambert law. In such a case, light interacts with the different chemical species that absorb photons. Light energy is then dissipated through heat or light emission (fluorescence, phosphorescence). All these phenomena can be characterized through a global absorption coefficient μ_{a}, usually given in cm^{-1}, that quantifies the amount of energy lost along with light propagation. This coefficient is defined so that, after propagating over a distance z, the light power *flux* is given by:

$$\Psi(z) = \Psi_0 \exp(-\mu_{\mathrm{a}} z) \tag{1.1}$$

where Ψ_0 stands for the input light power *flux*. This coefficient defines the absorption mean free path which is the average distance a photon can propagate through before experiencing an absorption event. The absorption mean free path is noted l_a and is defined such as:

$$l_a = \frac{1}{\mu_{\mathrm{a}}} \tag{1.2}$$

As explained above, absorption is strongly wavelength dependent. In the case of biological tissues, typical absorption coefficients are of the order of 0.5 cm^{-1} within the optical therapeutic window [20].

1.2.2 Scattering

When propagating inside a homogeneous sample, light energy is dissipated through absorption. In practice, a lot of objects are not homogeneous and constituted of interfaces associated with refractive index changes. These inhomogeneities are responsible for scattering and physics of light attenuation can not be reduced to the Beer-Lambert law. Scattering was studied in a lot of books such as the two volumes of A. Ishimaru [21, 22] or the book of Bohren and Huffman [23], I will

only remind a few properties that will be needed later on. In the whole manuscript, I will only consider elastic scattering in which scattered light has the same frequency as incident light.

Rayleigh scattering

When interacting with a particle, an incident electromagnetic wave induces charges oscillations and local oscillating dipoles. These dipoles radiate and light is re-emitted in an other direction as shown on figure 1.4. When scattering particles are very small compared to the wavelength, the electromagnetic field is homogeneous at the scale of the scatterer. All local dipoles oscillate in-phase and the particle acts as a unique dipole. In far field, the scattering is isotropic in first approximation meaning that each possible emission direction is as likely as the others. This is known as Rayleigh scattering and it can be shown in such a case that the scattered power is strongly wavelength dependent – it decreases as $1/\lambda^4$ [21, Chapter 2].

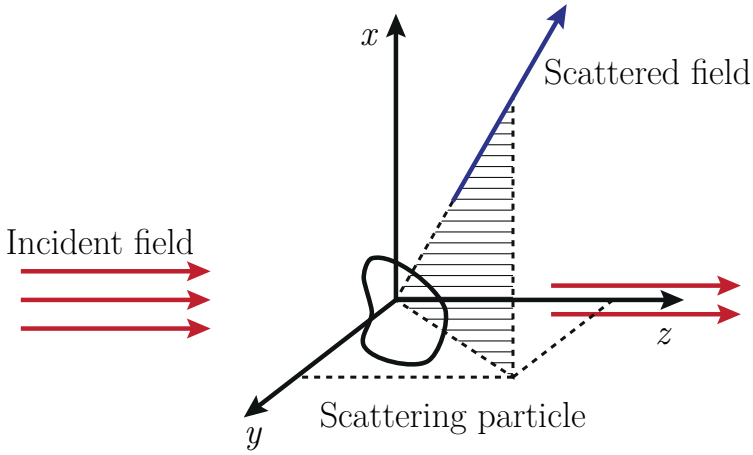

Figure 1.4 – Schematic of the interaction between an incident electromagnetic wave and a single particle.

In case of multiple scattering particles, the phenomenon can be characterized by the typical distance a photon can walk through before being scattered. This distance is called the scattering mean free path and noted l_s. From this parameter, it is possible to define a macroscopic coefficient that quantifies scattering inside the medium light propagates through. This coefficient is noted μ_s, usually given in cm^{-1}, and is related to the statistical distribution of scattering events:

$$\mu_\mathrm{s} = \frac{1}{l_s} \tag{1.3}$$

In Rayleigh scattering, each scattering event induces the loss of light previous history (polarization, phase and direction). The scattering mean free path is generally function of the kind of scatterers and their concentration in the medium.

Mie scattering

When particles size becomes bigger compared to the wavelength, the electromagnetic field can not be considered as homogeneous over the particle volume anymore. This case is described by the Mie theory [21, Chapter 2] of which Rayleigh scattering is just a particular case. In this case, the scattering is not isotropic anymore and mostly occurs in the forward direction, *i.e.* directions close to the incident wave one.

The anisotropy of the scattering is defined by an anisotropy coefficient g such as:

$$g = \langle \cos\theta \rangle \tag{1.4}$$

where θ is the angle of scattering as drawn on figure 1.5. This anisotropic scattering preserves light information over several scattering events so one defines a new mean free path called transport mean free path l^* that corresponds to the characteristic distance light can propagate through before losing the memory of its past history. From this characteristic distance, it is possible to define a corresponding macroscopic coefficient called the reduced scattering coefficient noted μ_s' given in cm^{-1}.

$$\mu_s' = \frac{1}{l^*} \tag{1.5}$$

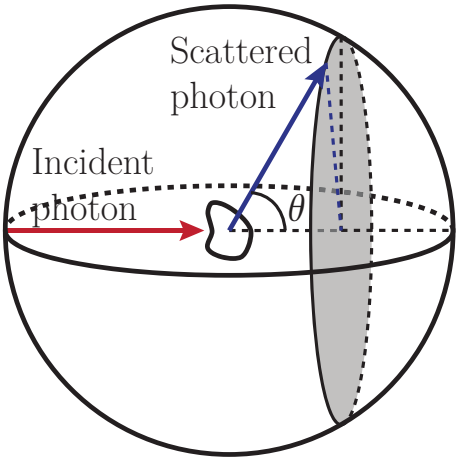

Figure 1.5 – Schematic of the scattering anisotropy.

These new coefficients that quantify the ability of scattering to scramble light information (see figure 1.6) are related to the scattering coefficient through the two relationships:

$$\begin{cases} \mu_s' &= \mu_s\,(1-g) \\ l^* &= \dfrac{l_s}{1-g} \end{cases} \tag{1.6}$$

The anisotropy coefficient g varies between 0 and 1. The case $g = 0$ corresponds to identical contributions of all angles and isotropic scattering. This is what happens in Rayleigh scattering. When $g = 1$, all photons are scattered in their incident direction and there is no more scattering – as expressed by the reduced scattering coefficient $\mu_s' = 0$. In such a case, light information is never lost and the transport mean free path is infinite. A physical interpretation of the transport mean free path is displayed on figure 1.6.

1.2.3 The case of biological samples

Biological samples are very inhomogeneous media in which all characteristic sizes are found from few nanometres for proteins up to over 10 microns for cells. It leads to very different orders of magnitude in terms of optical properties. A lot of reviews [1, 14, 24] or handbooks [20] can be found that gather a lot of measurements of optical properties of biological samples. Table 1.1 gives the orders of magnitude of optical properties gathered in [1] for human tissues.

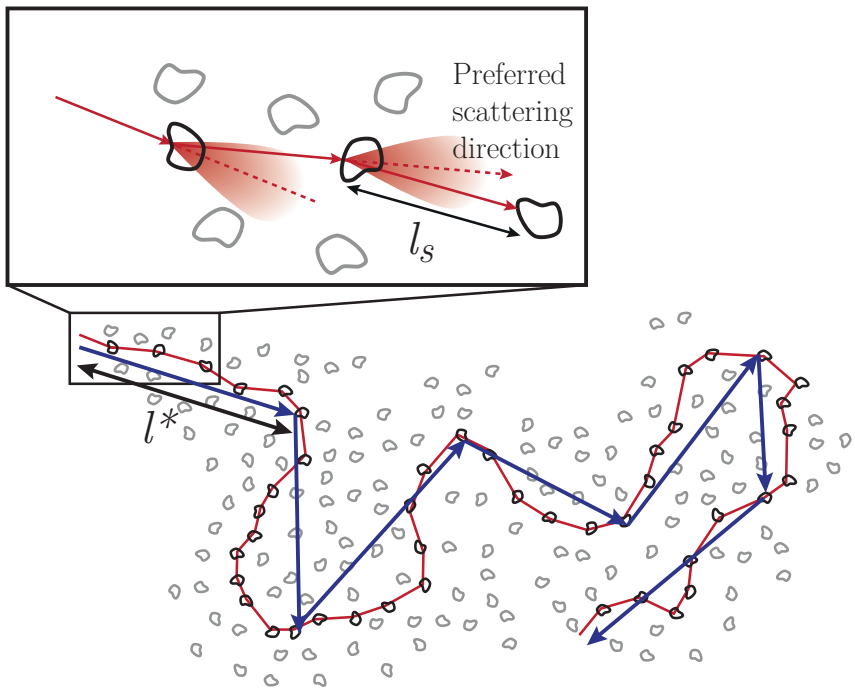

Figure 1.6 – Schematic of the transport mean free path. It corresponds to the typical distance beyond which the light loses the memory of its initial direction.

n	Refractive index	1.35 – 1.45
μ_a	Absorption coefficient	1 cm^{-1} – 10 cm^{-1} at 630 nm
μ_s	Scattering coefficient	100 cm^{-1} – 500 cm^{-1} in the visible range
g	Anisotropy coefficient	~ 0.9
μ'_s	Reduced scattering coefficient	2 cm^{-1} – 70 cm^{-1} in the visible range

Table 1.1 – Table of the typical optical properties of human tissues taken from [1]

These orders of magnitude concern biological tissues as various as blood, brain or bladder. For instance, typical absorption coefficient of biological tissues are of the order of 1 cm^{-1} or lower around 800 nm, except for epidermis – of the order of several tens of cm^{-1} – and blood – few cm^{-1} [20, Chapter 2]. Red blood cells are very anisotropic scatterers in the near-infrared range for which the anisotropy coefficient is over 0.99 [20, Chapter 2]. Scattering usually decreases as the wavelength is increased [20, Chapter 2], thus explaining the advantage of working further in the infrared [15].

1.3 Light propagation in scattering samples

Multiple-scattering makes deep optical imaging in biological samples challenging. Transmitted photons experience random trajectories that are impossible to deduce from the output direction of these photons. In this section, I will study the propagation of photons inside scattering media and will come out with several propagation regimes: the ballistic regime in which all photons propagate in straight lines, the diffusive regime, in which all photons have random trajectories, and two intermediate regimes, the single-scattered regime and the snake-like regime, also called quasi-ballistic.

1.3.1 The propagation regimes

As explained above, Beer-Lambert law does not completely quantifies light attenuation in the presence of scattering. When light propagates through a scattering sample, it is possible to define two kinds of photons: the ballistic photons that did not experience any scattering events, and the scattered photons that experienced at least one. Three propagation regimes can then be considered depending on the medium thickness L compared to the scattering mean free path. The case $L \ll l_s$ is called ballistic regime. If $L \sim l_s$, light propagation is in a single-scattering regime. Finally, the case $L \gg l_s$ is called the multiple-scattering regime. Figure 1.7 shows the different propagation regime one can experience in a multiply scattering medium.

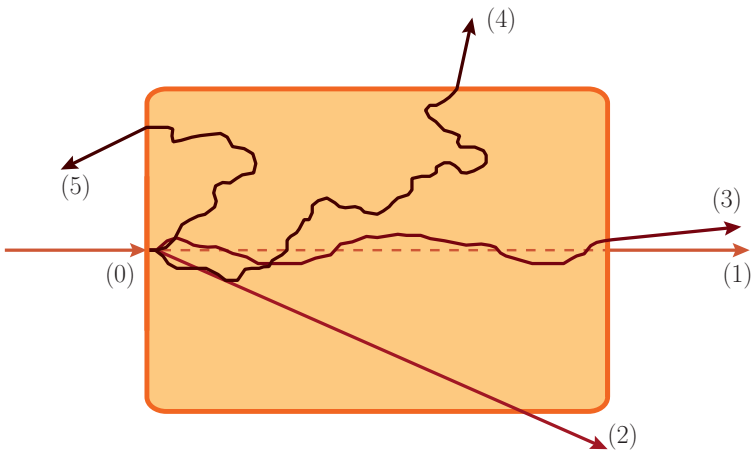

Figure 1.7 – Schematic of the different possible propagation regimes in a multiply scattering sample. (0) stands for incident photons. (1) stands for ballistic photons that are transmitted without experiencing any scattering event and propagate in straight line. (2) stands for single-scattered photons that experienced only one scattering event. In the multiple scattering regime, two particular cases are represented here: the snake-like photons (3) that appear in anisotropically scattering media and are multiply scattered photons that keep memory of their incident path, and diffused photons (4) and (5) that appear far from the transport mean free path and that correspond to a quasi-isotropic irradiance. (5) represents an example of backscattered photons that are photons scattered back in the direction of the light source, either through single or multiple scattering.

Ballistic photons

The ballistic photons are photons that do not experience any scattering events and propagate in straight lines. The ballistic power *flux* Ψ_b decreases exponentially as ballistic photons are absorbed or scattered. It thus verifies:

$$\Psi_b(L) = \Psi_0 \exp\left[-(\mu_a + \mu_s) L\right] \tag{1.7}$$

The ballistic power *flux* obeys a generalized Beer-Lambert law that takes scattering into account. The coefficient $\mu_a + \mu_s$ is called the extinction coefficient and is noted μ_{ext}. Here, it is to be noted that a photon that went through a scattering event but was re-emitted in the ballistic light direction is not considered as a ballistic photon anymore.

If $L \ll l_s$, photons do not have time to scatter and only ballistic photons are collected at the output. The medium is not turbid and attenuation is only due to light absorption: optical information is interpretable in terms of geometrical optics. However, in biological samples within the optical

therapeutic window, $\mu_s \gg \mu_a$ so that the number of ballistic photons decreases as $\exp(-\mu_s z)$, where z is the depth inside the medium. It means that ballistic light vanishes over few scattering mean free path, *i.e.* few hundreds of microns.

Single-scattering

When the size of the scattering medium increases, an intermediate regime appears in which photons only experience a unique scattering event. This particular regime occurs for samples in which $L \sim l_s$. In this regime, ballistic and scattered photons coexist and multiple scattering events are neglected.

In the single-scattering regime, all particles are assumed illuminated by the incident field only. Because ballistic light vanishes very fast along with the medium thickness the same happens for single scattered photons. In general, interpretable information for conventional imaging devices is carried by ballistic and single-scattered photons. Reflection-mode imaging devices provide images with single-scattered photons as transmission configurations work with ballistic light.

Multiple scattering

When the scattering medium becomes thick compared to the scattering mean free path $L \gg l_s$, multiple scattering events can not be neglected anymore. This is the multiple-scattering regime in which photons have experienced more than one scattering event. In general, scattering is not isotropic so that optical information is preserved over several scattering events. As explained above, this defines the transport mean free path l^* beyond which optical information is scrambled. For a thickness contained within $l_s < L < l^*$, it is usually considered that single-scattered and multiply scattered photons coexist. In the multiple-scattering regime, images quality is then driven by the ratio between multiply scattered and ballistic or single-scattered light. The fast decrease of this ratio along with the thickness of the scattering sample is the major imaging depth limitation of optical methods.

Far from the transport mean free path, the luminance is quasi isotropic and there are no ballistic nor single-scattered photons anymore. This regime is called the diffusive regime in which the scattered light power *flux* obeys a diffusion equation. At a distance r far from l^*, the scattered light irradiance $\Phi_s(r)$ obeys the following equation [21]:

$$\Phi_s(r) \propto \Psi_0 \frac{\exp\left[-\sqrt{3\mu_a(\mu_a+\mu_s')}r\right]}{r} \tag{1.8}$$

where the proportionality factor is function of the absorption and the reduced scattering coefficients [25]. Far from the transport mean free path, this expression defines the effective extinction coefficient:

$$\mu_{\text{eff}} = \sqrt{3\mu_a(\mu_a+\mu_s')} \sim \sqrt{3\mu_a\mu_s'} \text{ in case of strong scattering} \tag{1.9}$$

In strongly anisotropic media, some photons, so-called snake-like or quasi-ballistic photons, are multiply scattered but propagate almost in straight lines. In this intermediary regime, those photons are not strictly speaking ballistic photons for they are multiply scattered, but are not diffused photons for they partially retained their initial direction. The power *flux* of these photons decreases as:

$$\Psi_{qb}(r) = \Psi_0 \exp\left[-(\mu_a+\mu_s')L\right] \tag{1.10}$$

Photons time of flight

All regimes described earlier can be dissociated thanks to the length of their corresponding optical paths through the scattering medium. Intuitively, ballistic photons travel over L as snake-like photons travel over a bit longer paths. Diffused photons, on the other hand, travel over optical paths of very various lengths but always longer than L. It results in a distribution of times-of-flight at the output of the sample, as represented on figure 1.8.

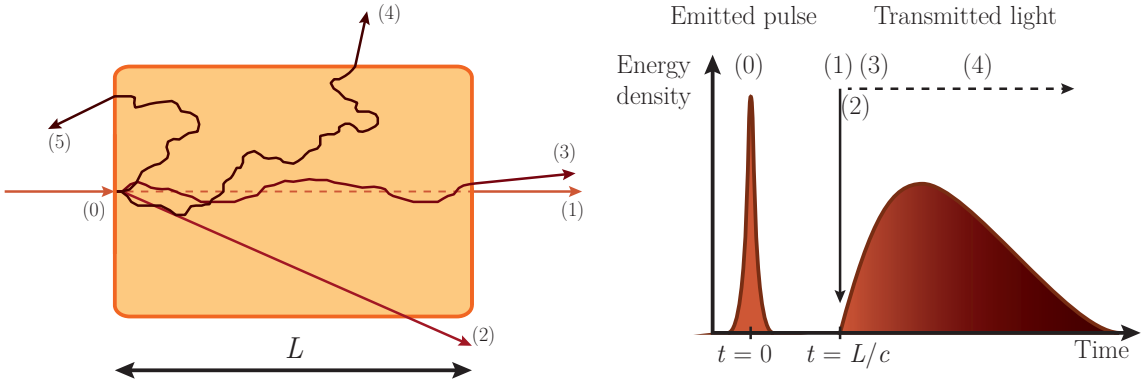

Figure 1.8 – Schematic of the times-of-flight distribution for scattered photons.

1.3.2 Of multiply scattered electric field

Expression of the multiply scattered electric field

Let us consider a static highly scattering medium. As shown above, ballistic and single-scattered photons – that contains the information interpretable by conventional imaging devices – exponentially vanish with the thickness of the sample. As explained in section 1.1, optical medical imaging aims at imaging entire organs so that light must propagate through several centimetres of biological tissues. At such depths, the light is in the diffusive regime so that only multiply scattered photons remain and the light irradiance spatial repartition obeys equation 1.8.

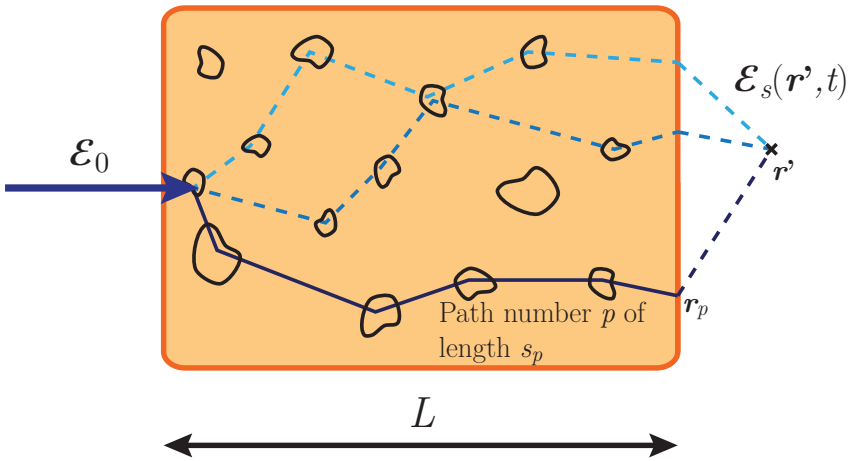

Figure 1.9 – The scattering sample is illuminated by an electromagnetic plane wave. When propagating along a given optical path, the electric field accumulates a phase shift defined by the length of this path.

Let us consider that the sample is illuminated by a plane wave propagating along the z-direction,

of pulsation ω_0 and wave vector $\mathbf{k}_0 = \frac{2\pi}{\lambda}\mathbf{u}_z$, where $\mathbf{u}_z$ is the unit vector of the z-axis. In the subsequent manuscript, I will not consider the effects of scattering on light polarization. I will just use the scalar approximation for the multiply scattered electric field and assume that polarization of transmitted – or backscattered – light is random. The incident field is:

$$\mathcal{E}_0 = E_0 \exp\left[i\left(\omega_0 t - \mathbf{k}_0 \cdot z\mathbf{u}_z\right)\right] \tag{1.11}$$

In the following, absorption in the scattering medium will be neglected. In absence of absorption, the scattered field outside the sample can be expressed through the contribution of each possible optical path followed by the photons:

$$\mathcal{E}_S\left(\mathbf{r}', t\right) = E_0 e^{i\omega_0 t} \cdot \sum_p a_p \exp\left(\frac{i2\pi n_0 s_p}{\lambda}\right) \exp\left(i\mathbf{k}_0 \cdot \left(\mathbf{r}' - \mathbf{r}_p\right)\right) \tag{1.12}$$

where a_p is the amplitude, s_p is the length and $\mathbf{r}_p$ the exit position of path number p. Here the scattered field outside the sample is the coherent sum of different optical path p of length s_p, see figure 1.9. In case the light source is a sufficiently coherent source, this sum over random paths leads to an random interference pattern so-called speckle pattern.

Speckle pattern

A speckle pattern is composed of bright – where interferences are constructive – and dark spots – where interferences are destructive – called speckle grains and shown on figure 1.10. The spatial repartition of light irradiance is random: the spatial auto-correlation of a speckle pattern is non zero only over a characteristic coherence area equal to the size of a speckle grain. From a speckle grain to another, the phase of the electric field is also random.

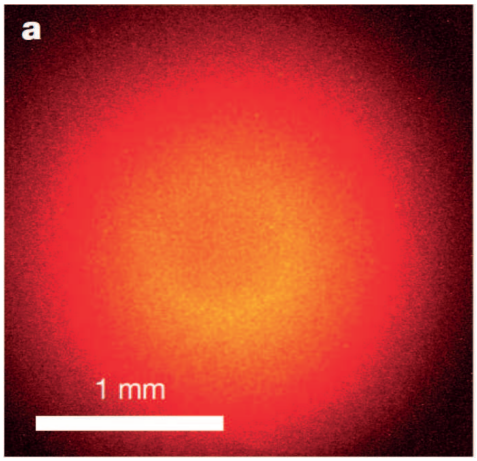

Figure 1.10 – Picture of a speckle pattern, figure extracted from [26].

A given shape of a speckle pattern corresponds to a given occurrence of the medium disorder. Because this disorder can not be completely known, speckle patterns are impossible to describe accurately. However, it contains a lot of very useful information about the statistics of the scattering medium. Speckle statistics was widely studied by Joseph W. Goodman [27, 28]. The aim of this manuscript is not at fully describing speckle properties, but few essential ones that are involved in acousto-optic imaging will be given below.

Among the important properties that are to be kept in mind, the first is that speckle is unpolarized light, basically meaning that all kind of light polarizations exist. The second property that

is used in several optical techniques and sometimes in acousto-optic imaging is that the statistical distribution of light intensity in a speckle pattern is always the same. The probability $p(\Phi)$ of finding the irradiance Φ in a speckle pattern is [28]:

$$p(\Phi) = \frac{1}{\Phi} \exp\left(-\frac{\Phi}{\langle\Phi\rangle}\right) \tag{1.13}$$

where $\langle\Phi\rangle$ stands for the mean value of the irradiance. The direct consequence of this distribution is that the standard deviation of the irradiance is equal to the mean value. It comes that the speckle contrast, defined as the ratio between the standard deviation and the mean irradiance, is equal to 1 for a polarized pattern. When adding N uncorrelated speckle patterns on an intensity basis, this contrast decreases by a factor of $1/\sqrt{N}$ whereas adding the complex amplitudes does not reduce the contrast at all.

The third important property comes from the random phase from a grain to another. When integrating the ultrasound modulation over several speckle grains, it sums with random phases and the measured modulation depth does not increase with the number of speckle grains. This issue in acousto-optics imaging will be detailed a bit more in chapter 2.

The final property of speckle that will draw our attention to is a direct consequence of the fact that the speckle pattern directly depends on the occurrence of the scattering medium disorder. When the scattering medium is not static, the disorder changes along time and speckle patterns decorrelate. M. Gross experimentally showed that speckle decorrelates over a characteristic time of the order of 1 ms in *in vivo* breast [29]. This decorrelation time is shorter as the number of scattering events is high – *i.e.* with imaging depth – and scatterers move fast.

1.4 Optical imaging of scattering samples

Optical imaging techniques can be divided into two main categories. The first kind of techniques works with ballistic or single-scattered photons and were referred to as "conventional" imaging techniques earlier, though I will show that some of them are not that straightforward. This regime can be understood as a generalized case of geometrical optics. The second kind of techniques use multiply scattered photons. Because they followed random optical paths, the information they carry is not interpretable in terms of geometrical optics. This section aims at giving a quick overview of the different optical imaging techniques and their corresponding depth of view. A review of these techniques can be found in [30].

1.4.1 Ballistic and single-scattered light

The main advantage of techniques working with ballistic light is that they benefit from optical resolution. On the other hand, their depth of imaging is limited as information is lost in the presence of a parasitic scattered light background .

Microscopy

The most classical optical imaging technique one can think of is the optical microscope. Conventional transmission microscopes map the absorption of the sample through ballistic light as reflection microscopes work with single-scattered photons and map the scattering structures. As a consequence, they are limited to depths lower than the scattering mean free path beyond which multiply scattered photons add parasitic background and induce a loss of resolution.

A way of overcoming this difficulty is to spatially reject photons that did not scatter along the incident direction. This is the confocal microscope [31] in which one or two pinholes are used to limit the illuminated area and the field of view, see figure 1.11(a) extracted from the previous reference. This configuration allows removing out-of-focus photons that typically experienced multiple scattering and participate to image blurring. Such an approach allows increasing the imaging depth up to the transport mean free path. Two-photons microscopy [32] is a similar technique that makes use of second harmonic generation or two-photons excitation of fluorophores in the biological sample. By focusing ballistic energy both in space and time – through the use of pulsed lasers – the frequency-doubled photons are only generated at the focal point, see figure 1.11(b) extracted from [33]. In this case, no pinholes are used and collected photons are usually multiply scattered the origin of which is precisely known. The major drawback of such techniques is that, because of their reduced field of view, they require mechanical scanning of the sample.

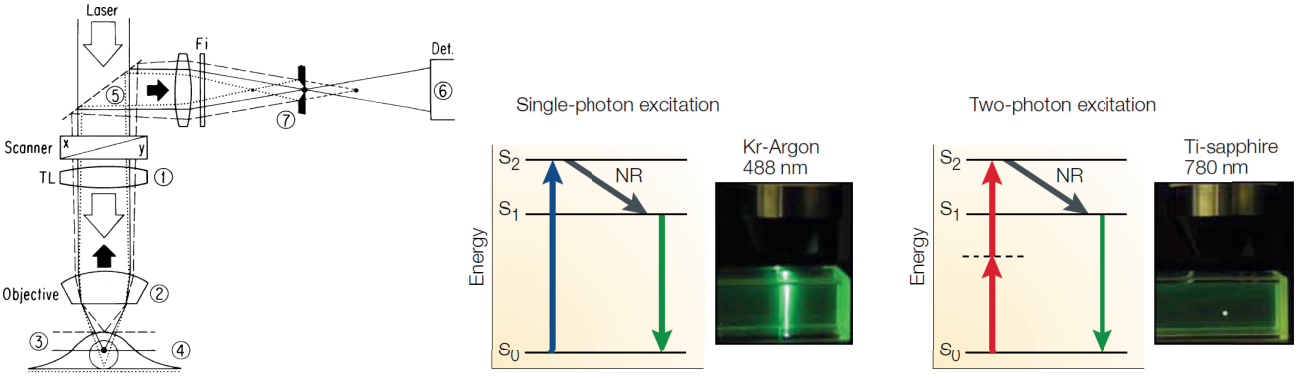

(a) Confocal microscopy [31]

(b) Two-photons microscopy [33]

Figure 1.11 – (a) Schematic of the confocal microscope extracted from [31]. The pinhole (7) is used to reject out-of-focus light. (b) Principle of two-photons microscopy extracted from [33] showing two-photons excitation of fluorophores.

Optical coherence tomography

In order to increase the imaging depth of conventional microscopy, people developed the previous techniques using spatial gating methods in order to discriminate ballistic and single-scattered from multiply scattered photons. Optical coherence tomography (OCT) is a different approach that uses the fact that single-scattered photons usually follow shorter paths that multiply scattered photons. Such techniques use a temporal coherence gating in order to reject multiply scattered photons that followed too long paths. The idea is to make scattered light interfere with a reference beam using a low coherence optical source so that only single-scattered photons interfere. By demodulating the resulting interference pattern, it is possible to map the reflectivity of the sample.

Two different OCT approaches exist. The first one is in-line OCT [34] (figure 1.12(a) extracted from the previous reference) that performs longitudinal optical sectioning of samples – along the light propagation direction – and needs lateral scanning of the optical beam in order to recover a section one line after another. The second one is full-field OCT [35] (figure 1.12(b) extracted from the previous reference) that performs *en-face* images very similar to what is obtained in microscopy. As such techniques work with single-scattered light they are also limited to about one transport mean free path.

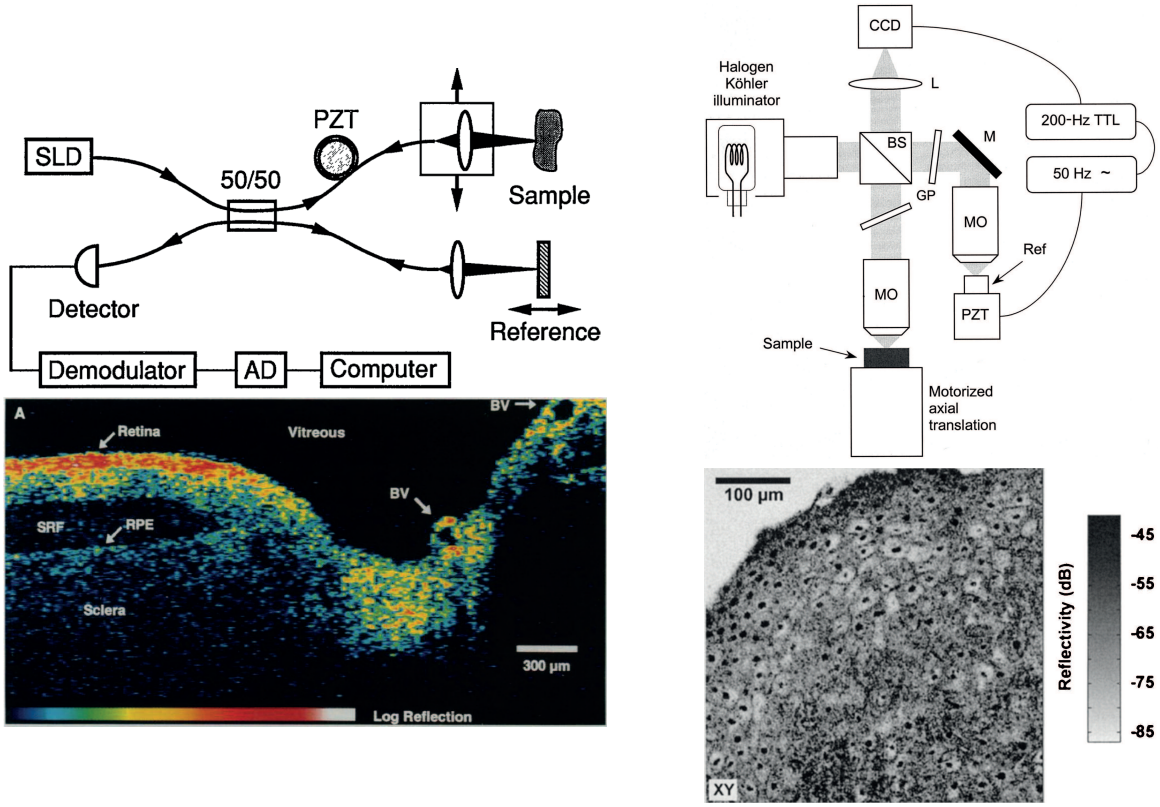

(a) Schematic of in-line OCT [34]

(b) Schematic of full-field OCT [35]

Figure 1.12 – Schematic of in-line OCT with a typical image (longitudinal section of a human retina and optic disk *in vitro*) extracted from [34] (a) and full-field OCT with a typical image (*en-face* image of fixed human oesophagus epithelium at 100 µm below the surface) extracted from [35] (b).

Temporal windowing

OCT techniques use a temporal coherence gating in order to discriminate single- from multiple-scattering. They benefit from the fact that single-scattered photons follow shorter optical paths than multiply scattered ones. Other techniques use the same property but work with photons times-of-flight instead of optical length. Such approaches use temporal windowing to reject multiply scattered photons. These techniques are subject to a compromise between resolution and level of signal: longer windows increase the measured light power and the number of multiply scattered photons as well, thus reducing the resolution.

In practice, ballistic photons reach the output of the sample after few hundreds of picoseconds whereas first multiply scattered photons arrive after few nanoseconds. It is thus necessary to use very short temporal windowing. Several techniques exist, but almost always rely on pulsed light sources and a powerful pump beam that activate non-linear effects. For instance, such techniques can be based on the optical Kerr effect [36]. The setup used in this previous reference is displayed on figure 1.13. A non-linear crystal is placed between two crossed polarizers. The light source is a picosecond pulsed laser source at 1060 nm. A portion of the light beam is frequency-doubled in order to illuminate the sample, the other is sent through a delay line and pumps the non-linear crystal. When the pump pulse reaches the non-linear crystal, it changes its birefringence and the filter lets light through, otherwise light is absorbed by the polarizers. Such a filter is called Duguay filter. By changing the delay between the arrival of the pumping pulse and the scattered light, it is possible to select the imaging plane from which the ballistic photons will be measured. The major drawback of this approach is that the transmission of the filter is weak.

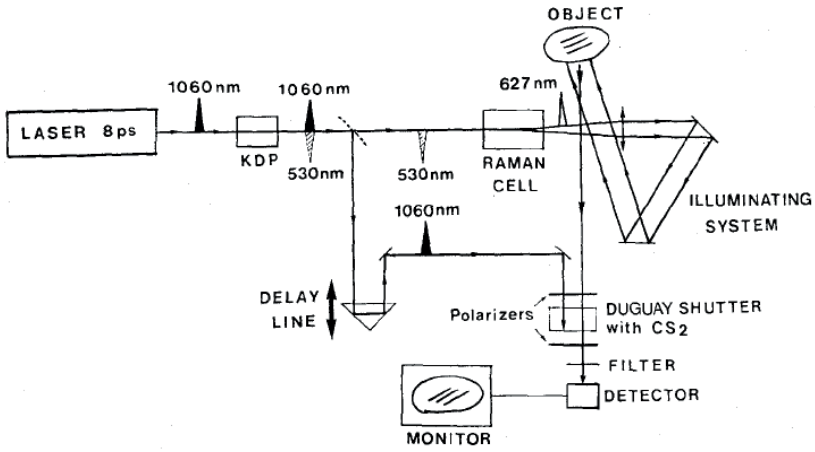

Figure 1.13 – Schematic of a temporal windowing based on the Kerr effect. The figure is extracted from [36]

Imaging from the reflection matrix

Recent advances in spatial light modulators (SLM) and computing science allowed a lot of new approaches that are able to retrieve single-scattering contribution from multiple scattering by recording a reflection matrix from various input fields.

Kang *et al.* [37] developed a technique combining temporal coherence gating in order to remove as many multiply scattered photons as possible and multiple illumination incidences tilted thanks to a SLM (see figure 1.14(a) extracted from the same reference). The approach is based on the fact that, outside the sample, the angle of propagation of single-scattered photons is correlated to the angle of incident photons whereas multiple-scattering leads to completely random directions. The idea is then to record the reflection matrix of the medium for a set of wave-vectors and perform synthetic focusing with the different incidences so that single-scattering adds coherently whereas multiple-scattering does not. The authors thus claim an increase of the ratio between single- and multiply scattered photons of the order of the number of different incidences used.

On a similar basis, very recent work of A. Badon *et al.* [38] records a time-gated reflection matrix of a scattering sample by electronically scanning the focal point of a microscope objective thanks to a SLM (see figure 1.14(b) extracted from the same reference). The *en-face* reflectivity image of the selected plane is extracted from the reflection matrix through mathematical treatment similar to the DORT method – french acronym for the Decomposition of the Time-Reversal Operator – developed by C. Prada and M. Fink [39] for ultrasound. The authors claim that such a technique so-called smart-OCT is able to reach depth twice as high as conventional OCT.

1.4.2 Working with multiply scattered light

The techniques presented in section 1.4.1 have all the major advantage of benefiting from optical resolution. Though the most recent of them can reach imaging depth of a few transport mean free paths, they are all limited by the weak ratio between single- and multiply scattered photons. Given that the latter are highly predominant for depths beyond the transport mean free path, it can be interesting to work with multiply scattered light instead. Obviously, as optical information is not interpretable in terms of geometrical optics in this regime, optical resolution can not necessarily be reached. With multiply scattered photons, imaging depth is almost always obtained at the cost of the resolution.

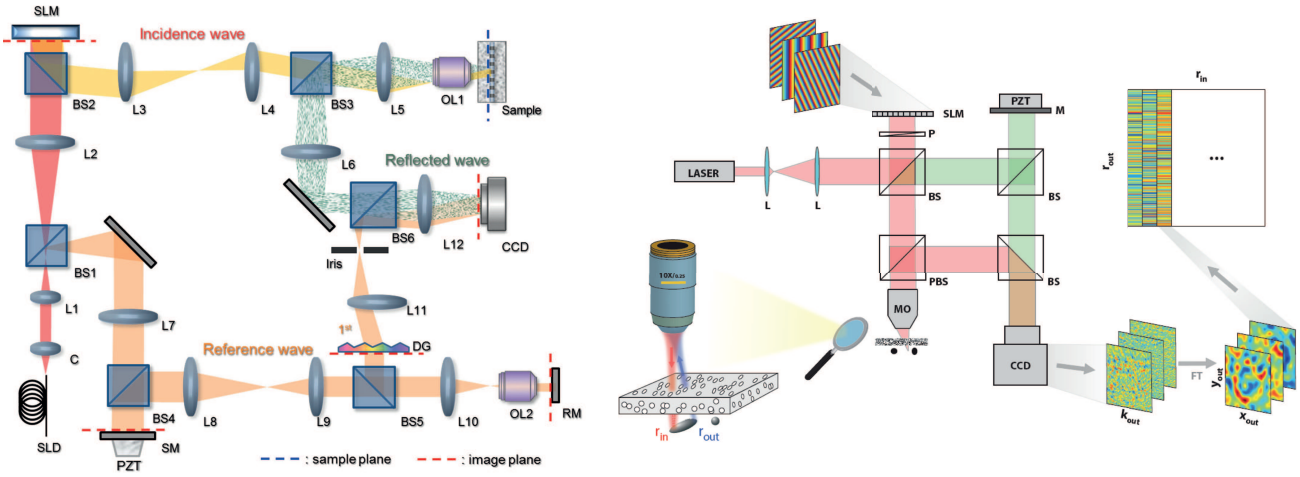

(a) Collective accumulation of single-scattered waves [37]

(b) Smart-OCT [38]

Figure 1.14 – Schematic of the collective accumulation of single-scattered waves extracted from the supplementary infos of [37] (a) and smart-OCT extracted from [38] (b).

Snake-like photons

The first means of imaging with multiply scattered photons consists in extending the concept of temporal windowing presented above to snake-like photons. Such an approach, though working with multiply scattered photons, could have been mentioned as a ballistic imaging technique because snake-like light keeps a quasi-linear trajectory. In such a case, higher times-of-flight correspond to photons that went further from the ballistic direction. As a consequence, the resolution decreases as the temporal windowing increases [40].

Diffuse optical tomography

Recent advances in the knowledge of light propagation in scattering media led to the development of Diffuse Optical Tomography (DOT) [41]. The basic principle of DOT consists in placing the scattering sample inside a matrix of NIR light sources and detectors (see figure 1.15 extracted from [13]). For each light source, the diffused light is measured at the position of each detector. All these data are then used in an attempt to solve the inverse light scattering problem in the medium in order to recover parameters of interest [42]. Typical resolution of DOT is higher on the edges of the sample than in the center.

As stated in section 1.1, DOT is often used for breast imaging [18] and fluorescence imaging [19]. Because NIR light is not very absorbed by the skull, another major field of use is haemodynamics mapping for functional brain imaging [13].

The main difficulty of DOT comes from the inverse problem which is intrinsically non-linear and ill-posed. Beside the fact that computing the inverse solution is very time-consuming, efficient reconstruction needs precise modelling of the scattering sample geometry, the noise and the measurement itself.

Imaging with speckle

When working with coherent multiply scattered light, it is possible to use the properties of speckle patterns to extract information from inside the scattering medium. These techniques are based on

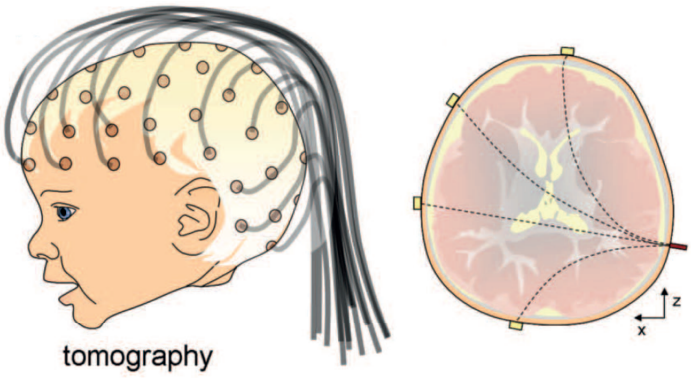

Figure 1.15 – Schematic of a DOT setup for brain imaging. Figure extracted from [13].

the fact that the presence of structures or objects will alter speckle patterns statistical properties. Though these techniques are usually not depth-resolved because speckle pattern in the imaging plane integrates information about the whole volume, they allows extracting useful information from the multiply scattered light with very simple setups.

The first example that can be discussed here is laser speckle contrast imaging [43] which provides a simple way of imaging blood perfusion. The idea of this technique consists in illuminating a biological sample with a laser and filming the backscattered light with a CCD camera. Blood flows decorrelate the speckle proportionally to their velocity (through Doppler effect). By quantifying this amount of decorrelation, it is possible to map blood perfusion of tissues. This amount of decorrelation can be quantified either spatially by mapping the contrast of the time-integrated speckle or temporally by mapping the correlation time of speckle grains. Though images of blood vessels may be obtained close to the surface through thin static scattering layers such as the skull [43], this technique is not strictly speaking an imaging technique of strongly scattering media for it images integrated perfusion from the surface (see typical images of [44]). However, it demonstrates that multiply scattered photons still contain information that can be recovered.

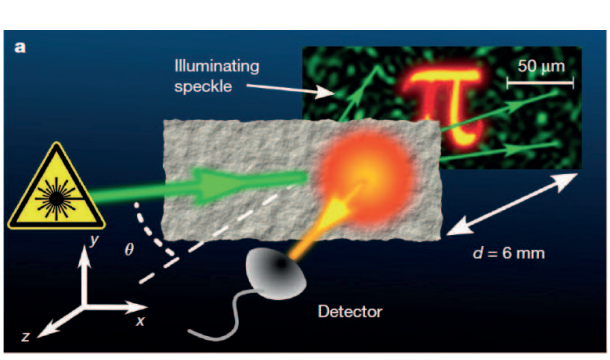

(a) Imaging setup of J. Bertolotti *et al.* [26]

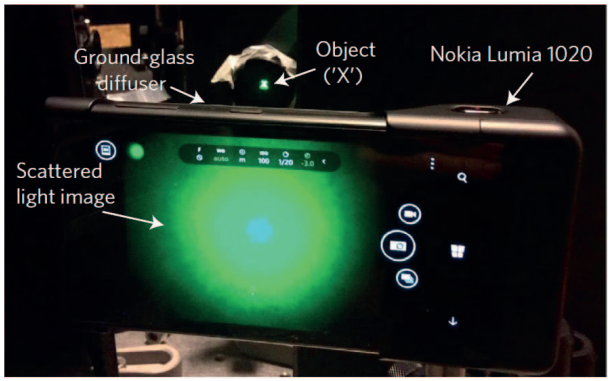

(b) Imaging setup of O. Katz *et al.* [45]

Figure 1.16 – Imaging techniques using the memory effect as used by J. Bertolotti *et al.* [26] and O. Katz *et al.* [45]

On the other hand, it appears that tilting the angle of the illumination direction just translates the speckle pattern if the tilt is of a sufficiently small amount. This effect is known as the memory effect and was recently used by J. Bertolotti *et al.* [26] to image a fluorescent object hidden behind a strongly scattering medium. The idea consisted in illuminating the scattering medium with various (small) angles of incidence and measuring the total fluorescence signal that scattered

through in return. The authors show that it is thus possible to recover the autocorrelation function of the fluorescent object from mapping the fluorescence intensity as a function of the angle of illumination. The object is finally recovered from its autocorrelation function through an iterative phase-retrieval algorithm. A similar approach was used by O. Katz *et al.* [45] to image an object illuminated by a spatially incoherent but narrowband source from the other side of a scattering medium with a simple smartphone. They show that such an approach works also for imaging an object after reflection on a scattering medium or between two of them. The basic issue here is that it works for object of small optical *etendue* – the field-of-view scales as the inverse of the optical thickness of the obstacle – and is not depth resolved – it is impossible to make a difference between a small object close to the scattering obstacle and a big one very far. It is however to be noticed here that these techniques are not strictly speaking techniques to image inside scattering media but rather through them.

Multi-waves imaging

The previous examples showed that, except for DOT, purely optical techniques still have difficulties in working in the diffused light regime. As I showed previously, the major drawback of DOT lies in solving the light scattering inverse problem, which is very time-consuming. A way of overcoming this difficulty is to use multi-waves imaging techniques [46] that couple light and ultrasound. The basic principle of these techniques relies on the fact that scattering coefficients of tissues are significantly lower for ultrasound than for light [47]. Ultrasound multiple scattering is negligible for frequencies generally up to a few tens of MHz for depths up to a few tens of centimetres. The idea of such light-ultrasound-coupling techniques is to use ballistic ultrasound to locate optical information that is normally lost through multiple scattering. Two different of these exist: photoacoustic, also called optoacoustic, and acousto-optic imaging, also called ultrasound modulated optical tomography.

Photoacoustic imaging Photoacoustic imaging was described in a lot of reviews such as [48]. The technique is based on the photoacoustic effect discovered by Alexander Graham Bell who noticed at the end of the 19^{th} century that absorbed light was able to produce a sound wave. The theoretical framework of photoacoustic imaging is not the point of this manuscript and can be found in many works such as [49] but I will give a quick description in order to highlight the difference with acousto-optic imaging.

In photoacoustic imaging, the sample is illuminated with nanoseconds light pulses that scatter inside. Light absorption by biological chromophores such as haemoglobin or melanin is rapidly converted into heat and produces a small local temperature rise. This temperature increase induces thermal expansion that relaxes at the end of the light pulse, thus generating a broadband ultrasound wave. It is to be noted that when the electromagnetic wave is in the microwave range, the technique is called thermoacoustic, though its principle is the same. This ultrasound wave is detected from the surface, either with a transducer array [50] or all-optical detection, through a Fabry-Perot cavity [51] or non contact holography setups [52, 53] for instance. The detected ultrasound echoes are then backpropagated the same way as for conventional ultrasound scans to give an image of the absorbing properties of the biological sample with an acoustical resolution. One property of photoacoustic signals is that the frequency of the generated ultrasonic wave is inversely proportional to the size of the absorbing target so that the resolution of the technique is limited by the reception bandwidth of the detection scheme. On the other hand, high frequencies are strongly absorbed by biological tissues so that small objects are usually detected close to

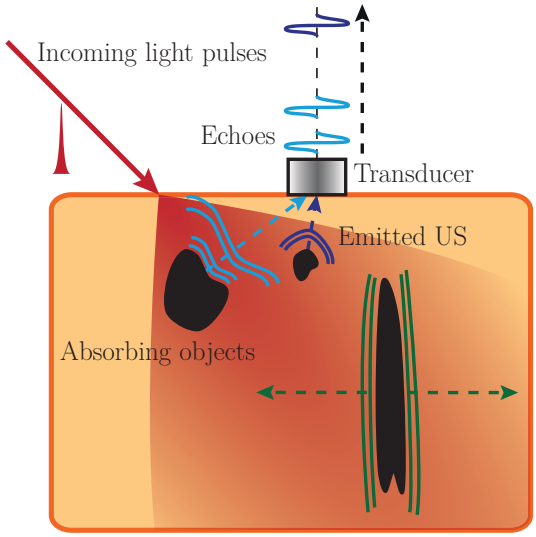

Figure 1.17 – Schematic of the principle of photoacoustic imaging.

the surface. Though transducer arrays allow deep imaging and easy coupling with commercial ultrasound scanners [54], their limited bandwidth act as a band-pass filter on the final image: small objects are not resolved as big ones are seen only through their contour [55]. On the other hand, all-optical systems benefit from a much higher bandwidth and possible non-contact mode but are not as easy to implement, partially because of the speckle pattern of reflected probing beam [52, 53].

The techniques described above are mainly single-side access techniques, more practical for clinical approaches. However, similarly to conventional ultrasound, they suffer from the fact that vertical interfaces or elongated objects perpendicular to the array direction do not emit ultrasound toward the probe and remain undetected. In order to overcome this difficulty people developed tomographic approaches for small animal imaging with ring-shaped [56] or hemispheric [57] transducer arrays. I give other examples of such approaches in chapter 4. Moreover, recent works led to the development of photoacoustic microscopy [58] that uses a microscope objective to achieve optical resolution photoacoustic imaging. Such a technique provides images very similar to conventional microscopy – with same kind of limitations – but maps tissues absorption instead of scattering structures.

Photoacoustic has generated a real enthusiasm for the past 20 years so that a lot of different techniques appeared that started showing first clinical applications such as breast cancer [59]. A review by S. Mallidi *et al.* [60] gives a quick overview of several clinical applications of photoacoustic imaging, mainly in the field of cancer detection.

Acousto-optic imaging Contrary to photoacoustic imaging, acousto-optic imaging uses emitted ultrasonic waves instead of received ones. The technique will be studied deeply in next chapter, I will only give a quick overview of the principle here in order to highlight the difference with photoacoustic imaging. Acousto-optic imaging is based on the acousto-optic effect, well-known in the optical community. The scattering sample is illuminated by a continuous NIR light beam – or at least long pulses – and ultrasound is sent at the same time. When propagating through an illuminated area, the ultrasound pulse modulates the refractive index and the scatterers position, resulting in the generation of side-bands in scattered light, shifted from light carrier frequency by the ultrasound one. The number of photons contained within these side-bands, so-called *tagged photons*, is proportional to the integrated local light irradiance over the ultrasound volume. These

photons come from a limited area of the scattering sample so the volume of the ultrasound pulse acts as a localized tagged photons source. By scanning ultrasound in the scattering sample, it is possible to map the spatial distribution of light irradiance with a resolution which is the volume of the ultrasound pulse. Contrary to photoacoustics that only maps absorption, acousto-optic imaging directly maps the light irradiance so that it is also sensitive to scattering properties of tissues.

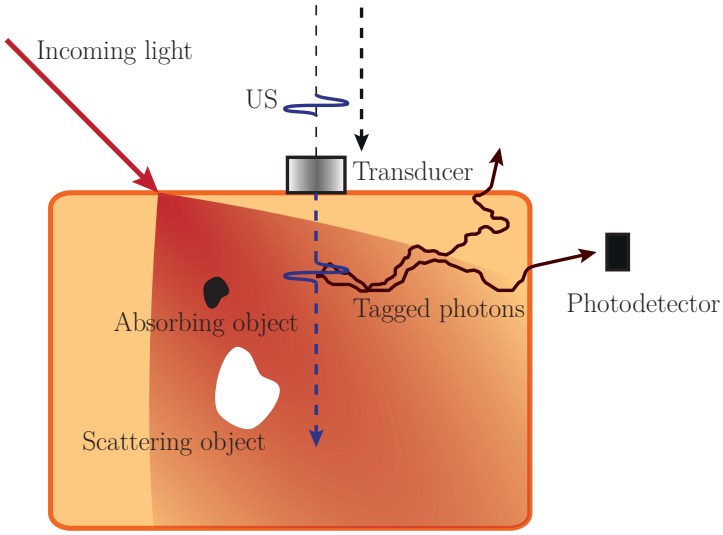

Figure 1.18 – Schematic of the principle of acousto-optic imaging.

As can be deduced from the previous overview, the technique entirely lies on the ability to filter and count tagged photons. However, frequency shifts here are of the order of few MHz – in comparison with 10^{14} or 10^{15} Hz for light frequency – on very few photons: there is no classical optical filters that reach this kind of finesse with sufficiently high untagged photons rejection rate. This major difficulty – plus other ones that I will describe in more details in next chapters – strongly delayed the development of acousto-optic imaging compared to photoacoustics. It explains why acousto-optic imaging is still at the state of proofs of concepts though it was suggested practically at the same time as photoacoustic imaging by W. Leutz and G. Maret in the 90s [61].

1.5 Summary on optical imaging of scattering media

Optical contrast is very useful for biomedical imaging because light can bring both structural and functional/chemical information about the medium it propagates through. I showed in this chapter that the different biological species interact with light of various manners so that the latter was successfully used as a monitoring technique. However, it appears that optical techniques are not compatible with medical imaging requirements. First attempts to use optical contrast in medical imaging were transillumination techniques through breast in order to detect the presence of tumours. However, such an approach turned to be inefficient and was abandoned.

The difficulty to set optical medical imaging techniques comes from the fact that biological samples are highly scattering media. I showed in this chapter that light interacts with biological structures such as cells or fibres so that it is scattered in random directions. In biological tissues though, this scattering is highly anisotropic and it is possible to define a macroscopic parameter called the transport mean free path that quantifies the typical distance light can propagate through before the information it contains is completely scrambled by scattering. In biological tissues, this

distance is of the order of 1 mm, as typical imaging depth of medical imaging is several centimetres. One thus understands the difficulty of optical medical imaging techniques.

For small depths compared to the transport mean free path, light is weakly scattered and its information can be recovered in terms of geometrical optics. These weakly scattered photons are called ballistic photons when they did not experience any scattering events and single-scattered photons when they experienced only a single one. This range of depth is the imaging region of microscopy. Several techniques were invented in order to reject multiply scattered photons that carry uninterpretable information for conventional imaging and allowed greater imaging depth – about one order of magnitude higher. However, all these techniques are limited by the exponential decay of ballistic and single-scattered photons along with depth compared to the growing number of multiply scattered photons.

A lot of efforts were then made these last few decades in order to find techniques able to work with these abundant multiply scattered photons. I presented several techniques working with scattered light in this chapter. It appeared that the only one compatible with medical imaging requirements up to now is Diffuse Optical Tomography (DOT) that consists in solving an inverse scattering problem from a set of carefully acquired data. However, this technique requires a lot of time-consuming calculations to solve this ill-posed problem. A means of overcoming this difficulty is to use light-ultrasound coupling techniques.

These techniques benefit from the ballistic propagation of ultrasound up to few tens of MHz in biological tissues. The idea is to use ultrasound to localize optical information otherwise lost through scattering. Two main approaches exist of which I gave a quick overview here. The first one is photoacoustic imaging that uses light pulses to generate ultrasonic waves through light absorption and thermal expansion. The other technique is acousto-optic imaging in which light is locally modulated by an ultrasound pulse and the quantification of this modulation leads to a measurement of the local scattered light irradiance.

I will not further describe photoacoustic imaging though I will say a few more words in chapter 4. The next chapter will be devoted to the theoretical framework of acousto-optic imaging in order to fully enhance the major difficulties of the technique and the corresponding solutions that were brought out.

CHAPTER 2

Acousto-optic imaging

Table of contents

In the previous chapter, I brought the interest of optical biomedical imaging into light. I showed that due to multiple light scattering, most of optical techniques are limited to depths under a transport mean free path l^*. DOT, that consists in solving an inverse light scattering problem from carefully acquired data, is perhaps the only purely optical technique that meets the requirements of medical imaging for now. However, it involves heavy calculations to solve this problem which is intrinsically ill-posed and non-linear. I showed that a way of overcoming this difficulty is to use multi-waves imaging techniques that couple ultrasound and light. In this section, I will focus on acousto-optic imaging that uses emitted ultrasound to map the light irradiance inside the scattering medium. Acousto-optic imaging principle relies on two major points: modulation of light through ultrasound and detection of modulated light. In this chapter, I will first sum up the principle of acousto-optic imaging before detailing the theoretical framework. The idea is to highlight the benefits and the main difficulties of acousto-optic imaging. The last point of this chapter will focus on the detection of modulated light and gives an overview of the different possible detection schemes.

2.1 Introduction to acousto-optics

I briefly introduced the principle of acousto-optic imaging in chapter 1. In this section, I will give a more detailed qualitative overview of the technique.

2.1.1 From acousto-optic effect to imaging

The acousto-optic effect in transparent crystals is long known and was first demonstrated independently by P. Debye and F. W. Sears [62] and R. Lucas and P. Biquard [63] in 1932. When propagating inside the illuminated crystal, a continuous ultrasonic wave modulates the density – and consequently the refractive index – at ultrasound frequency ν_{US}. As a consequence, light propagates through a phase grating of period Λ, where Λ is the ultrasound wavelength. In case the crystal is considered as infinitely thin, light is diffracted in directions θ_p such as:

$$\sin\theta_p = p\frac{\lambda}{\Lambda}, \quad p = 0, \pm1, \pm2, ... \tag{2.1}$$

where λ stands for the light wavelength (see figure 2.1) and p is an integer. Such a case is called the Raman-Nath diffraction regime. It appears that, in addition to light diffraction, the frequency of each diffracted beam is shifted from light frequency by multiples of ultrasound frequency:

$$\nu_p = \nu + p\nu_{US} \tag{2.2}$$

This is the effect used in acousto-optic imaging. In a scattering medium, the origin of light modulation is a bit different and will be further studied later on, but the consequence is the same. When interacting with light, ultrasound generates side-bands in scattered light shifted by a multiple of ν_{US} as shown on figure 2.2. In practice, only the first two side-bands simply shifted by ν_{US} contain a significant number of photons. In this case, these so-called tagged photons – in

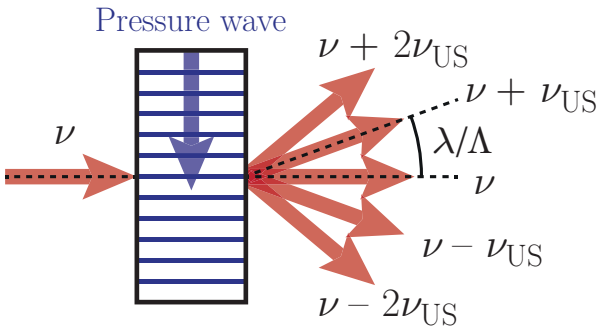

Figure 2.1 – Schematic of the acousto-optic effect in a crystal in the Raman-Nath regime. The ultrasound modulates the refractive index of the medium, resulting in a phase grating on which light diffracts. The different directions of diffraction are given by multiples of the ratio between light and ultrasound wavelengths. The frequency of all orders is also shifted by a multiple of ultrasound frequency.

opposition to untagged photons that did not interact with ultrasound – have two straightforward but fundamental properties.

- Tagged photons can only come from a region where there are both light and ultrasound. It means that the ultrasound volume acts as a localized virtual tagged photons source. Even if information tagged photons carry is lost during the multiple scattering process, knowing the position of ultrasound gives their origin.
- The number of tagged photons is proportional to the local light irradiance at the position of ultrasound. It means that counting the number of tagged photons gives an information about the light irradiance inside the scattering medium with an accuracy of the order of the ultrasound volume.

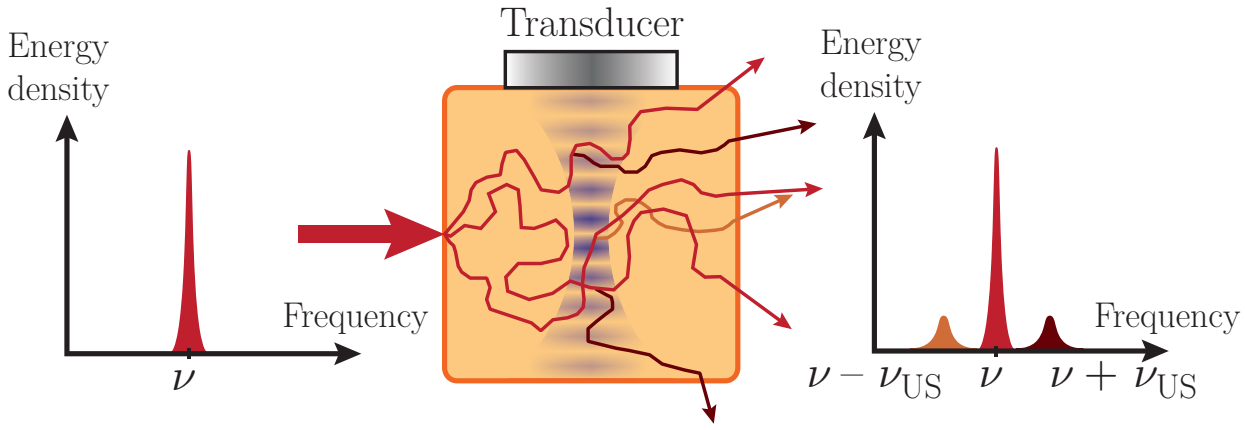

Figure 2.2 – Schematic of the acousto-optic effect in a scattering medium. The presence of the acoustic beam generates two side-bands in the scattered light shifted from light frequency by the ultrasound frequency.

Because it directly maps light intensity, acousto-optic imaging is also sensitive to scattering properties. As shown on figure 2.3, a decrease of the number of tagged photons can be induced for instance by photons being absorbed or scattered in another direction. In practice in the

diffusive regime, acousto-optic imaging contains information about the effective extinction coefficient $\mu_{\text{eff}} = \sqrt{3\mu_{\text{a}}\left(\mu_{\text{a}} + \mu'_{\text{s}}\right)}$ so that it is not easy to extract the contribution of absorption from the one of scattering.

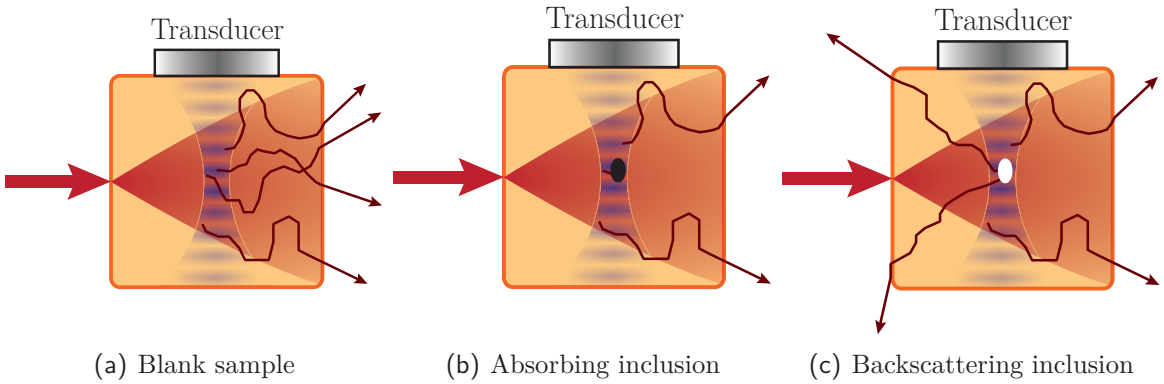

(a) Blank sample (b) Absorbing inclusion (c) Backscattering inclusion

Figure 2.3 – Typical contrast in acousto-optic imaging. (a) Blank sample. (b) Absorbing inclusion. Compared to the blank sample, the number of tagged photons decreases because light is absorbed. (c) Scattering inclusion. Compared to the blank sample, the number of tagged photons decreases because light is not scattered toward the detection (backscattered for instance).

It can easily be deduced from these previous points that if one is able to filter and count the number of tagged photons[1] – which amounts to quantify the scattered light modulation depth – it is possible to map the light irradiance inside the scattering medium by scanning the ultrasound as shown on figure 2.4. The filtering step constitutes the major difficulty of acousto-optic imaging.

- Because acousto-optic tagging is not a 100% efficient process and the ultrasound volume is generally small compared to the scattered light one, the number of tagged photons is very low compared to the untagged photons background. It is thus necessary to use very efficient filtering techniques in order to remove as many untagged photons as possible – or a very sensitive technique to detect a very small modulation.

- The frequency shift to be discriminated is very small – of the order of few MHz, $\sim 10^{-6}$ nm at 800 nm. There are no conventional filters that can reach this level of finesse and one has to find other techniques.

- Given the two previous points, natural filtering approaches are interferometric techniques. The major issue these techniques encountered was that, because of the speckled wave-front of scattered light, interferences with a plane wave reference can not exceed the signal-to-noise ratio (SNR) of a single speckle grain. All speckle grains have random phases so that averaging the ultrasound modulation over several of them generally leads to an incoherent summation of the acousto-optic signal.

- In order to overcome this difficulty, one developed holographic techniques able to adapt reference and scattered light wave-fronts in order to have ultrasound modulation adding coherently from a speckle grain to another. These techniques have a characteristic response time that works as a low-pass filter so that they are not able to follow changes in scattered light that occur faster than this response time. I showed in section 1.3.2 of chapter 1 that

[1] Interestingly, it is to be noticed that, through energy conservation, counting either tagged or untagged photons is equivalent.

speckle decorrelates over a characteristic time of the order of 1 ms or less which is too fast for most of holographic techniques.

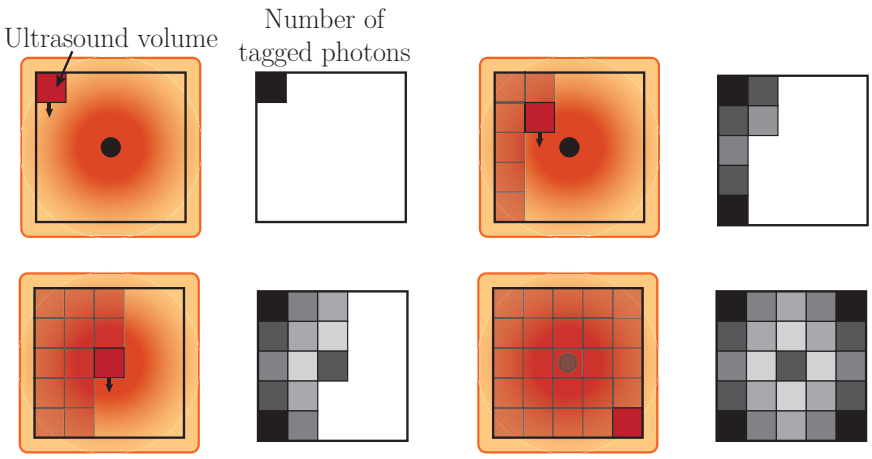

Figure 2.4 – Schematic of an imaging scan. The ultrasound volume acts as a tagged photons virtual source. By moving this source inside the scattering medium and counting the number of tagged photons for each position, it is possible to map the local light intensity.

Before giving the theoretical framework of acousto-optic imaging, it can be interesting to say a few words about typical applications of the technique.

2.1.2 Applications of the technique

Acousto-optic imaging was initially thought of as a breast cancer diagnosis tool [64] so that most of its following developments trended toward biomedical imaging. Though still at the state of proofs of concept, recent works on acousto-optic imaging started to highlight promising possibilities.

Pursuing in the field of cancer diagnosis, acousto-optic imaging turned out to be an interesting tool for melanomas detection. Because of melanin deposits in tumours, melanomas appear very dark so that they are easy to detect optically [65]. This application will be further studied in Part II. In the same vein, independent works at the ESPCI Paris [66] and at the Boston University [67] showed that acousto-optic imaging could be considered as a therapy monitoring tool for High Intensity Focused Ultrasound (HIFU) treatments [68]. The emission of focused long and powerful ultrasound bursts leads to an increase of tissues temperature that instantly necroses and kills tumorous cells inside a very small volume the size of the ultrasound focus. It appears that burnt tissues undergo a color change, thus suggesting that optical imaging techniques are of prime interest in order to follow the evolution of the lesion.

Leaving cancer applications aside, recent work of J. Honeysett *et al.* [69] showed that dual-wavelengths acousto-optic imaging using ultrasound contrast agents could potentially be used to quantify blood oxygenation in deep vessels whereas conventional NIR techniques fail at measuring quantitative values if superficial saturation varies. On the other hand, M. Kobayashi *et al.* showed that acousto-optic tagging could be used to precisely locate fluorescent [70] or chemiluminescent [71] objects embedded within highly scattering samples. Because photoacoustics developed faster than acousto-optics, it was eventually shown that the latter could be used as a scattered light fluence correcting tool for the first one in order to allow quantitative absorption measurement [72].

The principle of acousto-optic imaging is very similar to laser vibrometry that has a lot of applications in non-destructive testing for instance. I will not describe this kind of applications

here though the respective developments of the two techniques are very close. As a non-biomedical application however, it is interesting to cite the work of A. Lev and B. Sfez [73] that suggested acousto-optic imaging as a non-contact security imaging tool in order to detect objects hidden under opaque layers such as clothes. In this kind of applications, because ultrasound have to propagate in air, frequencies are significantly lower (50 kHz).

Except from using acousto-optic imaging as a correcting tool for photoacoustics, all these previous approaches are purely imaging modalities. Several works focused on another approach that consists in refocusing light inside a multiply scattering medium. Though it is not strictly speaking an imaging technique yet, it is worth mentionning it here. Such an approach is called Time-Reversed Ultrasonically Encoded focusing (TRUE focusing)[1] and consists in time-reversing the tagged photons wave-front – through phase conjugation [74] or SLM iterative optimization [75] for instance – in order to make light focusing back to the ultrasound focus volume. By moving the ultrasound focus – and thus light refocusing point – inside the scattering medium, it is possible to detect embedded optical absorbers.

2.2 Light/ultrasound mixing in multiply scattering media

In the previous section, I gave a quick overview of acousto-optic imaging technique. The goal of the next two sections is to set the theoretical framework of the technique. In this section I will focus on the interaction between light and ultrasound. In transparent media, only the refractive index variations are responsible for light modulation. However, mechanisms are a bit more complex in scattering media. In 1998, Mahan *et al.* [76] suggested an interpretation of the light modulation as an incoherent modulation of the scattering medium transmission through the modulation of its physical properties such as its absorption and scattering coefficients. Though Kobayashi *et al.* use such an incoherent modulation for their fluorescence [70] and chemiluminescence [71] experiments, this effect is usually very small and is not the main effect in conventional acousto-optic imaging with coherent sources. I will thus neglect such phenomena in the following. The light modulation in acousto-optic imaging with coherent light can be interpreted as a modulation of the optical paths by the ultrasound wave that has two origins: the modulation of the refractive index of the medium and the modulation of the scatterers position.

In the following, I will consider a scattering sample as represented on figure 2.5, illuminated by an electromagnetic plane wave as defined in chapter 1:

$$\mathcal{E}_0 = E_0 \exp\left[i\left(\omega_0 t - \mathbf{k}_0 \cdot z\mathbf{u}_z\right)\right] \tag{2.3}$$

where $\mathbf{k}_0 = k_0\mathbf{u}_z = \frac{2\pi}{\lambda}\mathbf{u}_z$. While the scattering medium is illuminated, an acoustic wave is sent inside the medium. For simplification purpose, the acoustic wave will be assumed to be a continuous plane pressure wave insonating the entire medium.

$$P_{US}\left(\mathbf{r}, t\right) = P_0 \sin(\mathbf{K}_{US} \cdot \mathbf{r} - \omega_{US} t + \psi_{\mathrm{US}}) \tag{2.4}$$

where $\mathbf{K}_{US} = K_{US}\mathbf{u}_x = \frac{2\pi}{\Lambda}\mathbf{u}_x$ and ψ_{US} is a phase term.

[1] The technique has a lot of other names depending on the physical principle that leads to refocusing

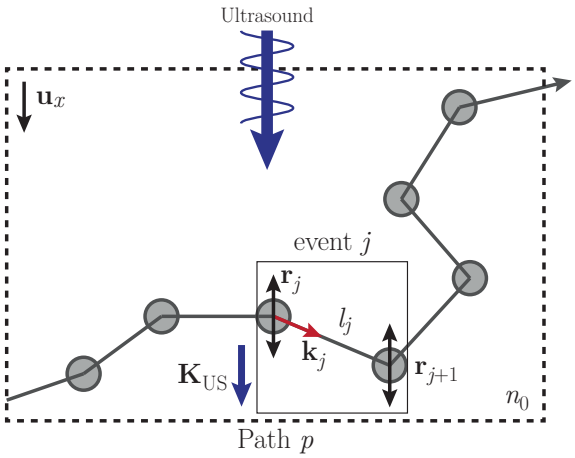

Figure 2.5 – Schematic of the parameters used in the acousto-optic effect model.

2.2.1 Modulation of the scatterers position

First theoretical studies of acousto-optic modulation only considered the scatterers position modulation. W. Leutz and G. Maret [61] first modelled the light modulation considering Brownian motion and a collective motion due to ultrasound in a homogeneously insonated volume. Further studies considering a spatially inhomogeneous pressure field were performed by Kempe *et al.* [77].

In the following, I will consider a scattering medium of scattering mean free path l_s – *i.e.* the average distance between two scattering events – and refractive index n_0. Let us consider the j^{th} scattering event of the optical path number p between the scatterers number j and $j+1$. For simplification purposes, it will be considered that scattering is isotropic and that the scattering mean free path is very long compared to the light wavelength. In such a case, the light phase variation over this scattering event $\Delta\psi_s^j$ is given by [61]

$$\Delta\psi_s^j(t) = n_0\mathbf{k}_j \cdot \left(\mathbf{r}_{j+1}(t) - \mathbf{r}_j(t)\right) \tag{2.5}$$

where $\mathbf{k}_j$ is the photon wave vector after the j^{th} scattering event, $\mathbf{r}_j$ and $\mathbf{r}_{j+1}$ are respectively the positions of the scatterers number j and $j+1$. The acoustic wave creates a displacement field $\mathbf{u}\left(\mathbf{r}_0^j, t\right) = \mathbf{u_0}\sin\left(\mathbf{K}_{US}\cdot\mathbf{r}_0^j - \omega_{US}t\right)$ that I will first assume homogeneous over the whole volume. $\mathbf{r}_0^j$ stands for the static position of the scatterer number j. The amplitude vector $\mathbf{u_0}$ is oriented along the x-axis. This acoustic wave modulates the position of the particles:

$$\begin{aligned}\Delta\psi_s^j(t) &= n_0\mathbf{k}_j\cdot\left(\mathbf{r}_0^{j+1} - \mathbf{r}_0^j + \mathbf{u}\left(\mathbf{r}_0^{j+1}, t\right) - \mathbf{u}\left(\mathbf{r}_0^j, t\right)\right)\\ &= \Delta\psi_0^j + \alpha_s^j n_0 k_0 u_0 \sin\left(\omega_{US}t + \psi_s^j\right)\end{aligned} \tag{2.6}$$

where $\Delta\psi_0^j = n_0\mathbf{k}_j\cdot\left(\mathbf{r}_0^{j+1} - \mathbf{r}_0^j\right) = n_0 k_0 l_j$ is the static phase variation due to the j^{th} scattering event without ultrasound, α_s^j is a proportionality factor that quantifies the strength of the ultrasound modulation on the scattering event depending on the orientation of the two scatterers and ψ_s^j is a phase term that depends on the position of the scattering event. α_s^j and ψ_s^j are given by:

$$\alpha_s^j = 2\frac{\mathbf{k}_j\cdot\mathbf{u_0}}{k_0 u_0}\sin\left(\frac{\mathbf{K}_{US}\cdot\left(\mathbf{r}_0^{j+1} - \mathbf{r}_0^j\right)}{2}\right) \text{ and } \psi_s^j = \frac{\pi}{2} - \frac{\mathbf{K}_{US}\cdot\left(\mathbf{r}_0^j + \mathbf{r}_0^{j+1}\right)}{2} \tag{2.7}$$

2.2.2 Modulation of the refractive index

Further work from L. V. Wang [78] included a refractive index modulation to previous work from W. Leutz and G. Maret [61] and Kempe *et al.* [77]. Similarly to what happens in transparent crystals, the acoustic pressure field induces a time-varying strain that creates a refractive index modulation through photoelasticity.

Considering the same scattering medium as previously, the refractive index contribution accumulated over the j^{th} scattering event can be expressed as [78]:

$$\Delta\psi_n^j(t) = \int_0^{l_j} k_0 n\left(\mathbf{r}_0^j, \mathbf{K}_{US}\cdot\mathbf{k}_j, s, t\right) \mathrm{d}s \tag{2.8}$$

where l_j is the length between the two scatterers number j and $j+1$. This expression can be developed as:

$$\Delta\psi_n^j(t) = \Delta\psi_0^j + \int_0^{l_j} k_0 \Delta n\left(\mathbf{r}_0^j, \mathbf{K}_{US}\cdot\mathbf{k}_j, s, t\right) \mathrm{d}s \tag{2.9}$$

where $\Delta\psi_0^j$ was already derived and taken into account in the previous section.

The term $\Delta n\left(\mathbf{r}_0^j, \mathbf{K}_{US}\cdot\mathbf{k}_j, s, t\right)$ can be expressed as [78]

$$\Delta n\left(\mathbf{r}_0^j, \mathbf{K}_{US}\cdot\mathbf{k}_j, s, t\right) = n_0 \xi K_{US} u_0 \sin\left(\mathbf{K}_{US}\cdot\mathbf{r}_0^j - \omega_{US}t + \mathbf{K}_{US}\cdot s\frac{\mathbf{k}_j}{k_0}\right) \tag{2.10}$$

where ξ is a coefficient that depends on the adiabatic piezooptical coefficient $\frac{\partial n}{\partial P}$, the density of the scattering sample ρ_0 and the sound velocity in the sample V_{US}:

$$\xi = \rho_0 V_{\text{US}}^2 \frac{\partial n}{\partial P} \tag{2.11}$$

The integral of equation 2.8 is equal to:

$$\Delta\psi_n^j(t) = \Delta\psi_0^j + \alpha_n^j n_0 k_0 \xi u_0 \sin\left(\omega_{US}t + \psi_n^j\right) \tag{2.12}$$

where the terms α_n^j and ψ_n^j were explicited by L. V. Wang:

$$\begin{aligned} \alpha_n^j &= 2\frac{K_{US}k_0}{\mathbf{K}_{US}\cdot\mathbf{k}_j}\sin\left(\frac{\mathbf{K}_{US}\cdot\left(\mathbf{r}_0^{j+1}-\mathbf{r}_0^j\right)}{2}\right) \\ \psi_n^j &= \frac{\mathbf{K}_{US}\cdot\left(\mathbf{r}_0^{j+1}+\mathbf{r}_0^j\right)}{2} \end{aligned} \tag{2.13}$$

2.2.3 Modulation of the optical path

The previous two sections gave the expressions of the coherent modulation of the refractive index and scatterers position. In first approximation, the contribution of these two terms can be interpreted as a global modulation of the optical paths.

The global phase variation $\Delta\psi_p(t)$ due to the optical path number p can be expressed as:

$$\Delta\psi_p(t) = \sum_j \Delta\psi_n^j(t) + \Delta\psi_s^j(t) \tag{2.14}$$

As the static contribution is to be taken into account only once, the global phase variation can

be expressed as:

$$\Delta\psi_p(t) = n_0 k_0 \sum_j l_j + n_0 k_0 \xi u_0 \sum_j \alpha_n^j \sin\left(\omega_{US} t + \psi_n^j\right) + n_0 u_0 k_0 \sum_j \alpha_s^j \sin\left(\omega_{US} t + \psi_s^j\right) \tag{2.15}$$

By developing the sine terms, it comes:

$$\begin{aligned} \Delta\psi_p(t) = \; & n_0 k_0 s_0^p + n_0 k_0 u_0 \left[\xi \sum_j \alpha_n^j \cos\psi_n^j + \sum_j \alpha_s^j \cos\psi_s^j\right] \sin\omega_{US} t + \\ & n_0 k_0 u_0 \left[\xi \sum_j \alpha_n^j \sin\psi_n^j + \sum_j \alpha_s^j \sin\psi_s^j\right] \cos\omega_{US} t \end{aligned} \tag{2.16}$$

that can be written under the form:

$$\Delta\psi_p(t) = n_0 k_0 s_0^p + n_0 k_0 u_0 \alpha_u^p \sin\left(\omega_{US} t + \psi_u^p\right) \tag{2.17}$$

where it was set:

$$\begin{aligned} \alpha_u^p &= \sqrt{\left(\xi \sum_j \alpha_n^j \cos\psi_n^j + \sum_j \alpha_s^j \cos\psi_s^j\right)^2 + \left(\xi \sum_j \alpha_n^j \sin\psi_n^j + \sum_j \alpha_s^j \sin\psi_s^j\right)^2} \\ \cos\psi_u^p &= \frac{\xi \sum_j \alpha_n^j \cos\psi_n^j + \sum_j \alpha_s^j \cos\psi_s^j}{\alpha_u^p} \\ \sin\psi_u^p &= \frac{\xi \sum_j \alpha_n^j \sin\psi_n^j + \sum_j \alpha_s^j \sin\psi_s^j}{\alpha_u^p} \end{aligned} \tag{2.18}$$

It then appears that the ultrasound modulation can be expressed as a modulation of the optical path:

$$\Delta\psi_p(t) = n_0 k_0 s_p(t) \tag{2.19}$$

where it was set $s_p(t) = s_0^p + \alpha_u^p u_0 \sin\left(\omega_{US} t + \psi_u^p\right)$. Because the position of scatterers are random, the different terms α_n^j, α_s^j, ψ_n^j and ψ_s^j are *a priori* random. The subscript u denotes the fact that the formula was derived for the ultrasound displacement.

The ultrasonic modulation of the optical path is then proportional to the particles displacement induced by the wave. Introducing the acoustic impedance of the medium Z, that I will assume to be constant for simplification purposes, it is possible to express the amplitude of the particles displacement as a function of the acoustical pressure:

$$u_0 = \frac{P_0}{Z\omega_{US}} \tag{2.20}$$

Interestingly, L. V. Wang quantified the ratio between the scatterers position and the refractive index modulations in his paper [78]. The two contributions mainly depend on the acoustic wave vector and the scattering mean free path through $K_{US} l_s$. It appears that the scatterers displacement contribution is constant whereas the refractive index modulation increases with $K_{US} l_s$ because its influence is integrated over the scattering mean free path. For values of the acoustic wave vector such as $K_{US} l_s < 0.56$ – that can be expressed otherwise as $\Lambda / l_s > \pi$ – the two contributions are basically equal and this remains almost true up to $K_{US} l_s \sim 1$. For instance, in

biological samples in which the scattering mean free path is of the order of 50 µm, the two contributions are equivalent for ultrasound frequencies up to about 10 MHz. Moreover, L. V. Wang estimated the modulation depth order of magnitude that typically varies between 10^{-2} and 10^{-6} so that it will be assumed in the following that ultrasound modulation is small.

2.3 The modulated light

Previous section highlighted that the ultrasonic wave modulates the scatterers position and the refraction index of the medium. I showed that it can be understood in first approximation as a modulation of the optical path proportional to the acoustic pressure. There are basically two approaches that can be used to derive the expression of modulated light. The first approach is a very simple one that consists in deriving the expression of the modulated speckle through the modulation of the optical path. The second approach consists in deriving the power spectral density of modulated light through the auto-correlation of the scattered electromagnetic field.

2.3.1 Expression of the modulated electromagnetic field

Assuming that the acoustic field is a propagating plane wave insonating the entire volume, it is possible to extract a first expression of the modulated field. In practice, most of what will be deduced from this simple approach can be extended to more complex acoustic field through plane waves decomposition and other values of the coefficients α_n^j, α_s^j, ψ_n^j or ψ_s^j. Let us consider the expression of the scattered field given in equation 1.12 in Chapter 1:

$$\mathcal{E}_S(\mathbf{r}', t) = E_0 e^{i\omega_0 t} \sum_p a_p \exp\left[i n_0 k_0 s_p(t)\right] \exp\left(i\mathbf{k}_0 \cdot (\mathbf{r}' - \mathbf{r}_p)\right) \tag{2.21}$$

Replacing the expression of the optical path derived in the previous section, it comes:

$$\mathcal{E}_S(\mathbf{r}', t) = E_0 e^{i\omega_0 t} \sum_p a_p e^{i n_0 k_0 s_0^p} \exp\left[i n_0 k_0 \alpha_p P_0 \sin(\omega_{US} t + \psi_p)\right] \exp\left(i\mathbf{k}_0 \cdot (\mathbf{r}' - \mathbf{r}_p)\right) \tag{2.22}$$

where α_p and ψ_p are two new coefficients related to α_u^p and ψ_u^p through the particle velocity expression and that allows expressing the optical path modulation in terms of acoustic pressure instead of displacement. The modulated term of the optical phase variation can be developed in terms of Bessel functions of the first kind J_m.

$$\mathcal{E}_S(\mathbf{r}', t) = E_0 e^{i\omega_0 t} \sum_p a_p e^{i n_0 k_0 s_0^p} \exp\left(i\mathbf{k}_0 \cdot (\mathbf{r}' - \mathbf{r}_p)\right) \sum_m J_m\left(n_0 k_0 \alpha_p P_0\right) e^{im\psi_p} \exp\left(im\omega_{US} t\right) \tag{2.23}$$

The scattered light then consists in several side-bands shifted by harmonics of ultrasound frequency:

$$\mathcal{E}_S(\mathbf{r}', t) = E_0 e^{i\omega_0 t} \sum_m \mathcal{S}_m(\mathbf{r}') \exp\left(im\omega_{US} t\right) \tag{2.24}$$

where $\mathcal{S}_m(\mathbf{r}')$ is a speckle pattern: $\mathcal{S}_m(\mathbf{r}') = \sum_p a_p J_m\left(n_0 k_0 \alpha_p P_0\right) e^{i\left(n_0 k_0 s_0^p + m\psi_p\right)} \exp\left[i\mathbf{k}_0 \cdot (\mathbf{r}' - \mathbf{r}_p)\right]$

Around zero, the Bessel functions of the first kind decrease fast with the index m – as power functions x^m – so that one usually considers that the speckle is only modulated at $\pm\omega_{US}$. In such

a case, there are three bands in the scattered light spectrum:

$$\begin{cases} \text{The untagged photons at } \omega_0 : & \mathcal{E}_{\mathrm{UT}}(\mathbf{r}', t) = E_0 \mathcal{S}_0(\mathbf{r}') e^{i\omega_0 t} \\ \\ \text{The tagged photons at } \pm\omega_{\mathrm{US}} : & \mathcal{E}_{\mathrm{T}}(\mathbf{r}', t) = E_0 \mathcal{S}_{\pm 1}(\mathbf{r}') e^{i(\omega_0 \pm \omega_{US})t} \end{cases} \tag{2.25}$$

Because the modulation depth is small, the Bessel functions can be approximated at first order to:

$$\begin{cases} J_0(n_0 k_0 \alpha_p P_0) & \sim 1 \\ \\ J_{\pm 1}(n_0 k_0 \alpha_p P_0) & \sim \dfrac{n_0 k_0 \alpha_p}{2} P_0 \end{cases} \tag{2.26}$$

that allows to deduce that the electric field modulation is basically proportional to the acoustic pressure in the case of a propagating plane wave. Interestingly, the amplitude and phase terms α_p and ψ_p are *a priori* random so that the tagged and untagged components are spatially uncorrelated [79].

2.3.2 Coherent acousto-optic modulation

The previous simple approach showed that the presence of ultrasound results in a modulation of the speckle pattern at the ultrasound frequency. In practice, it is difficult to deduce further properties from these results, in particular regarding the behaviour of tagged photons with ultrasonic parameters, because of the random walk approach. The classical way of describing the ultrasound modulation consists in deducing the tagged photons power from the autocorrelation of the scattered field and the Wiener-Khinchin theorem. This approach was used by Kempe *et al.* in [77] to calculate the modulation by an ultrasonic pulse. In his paper, the authors only consider the scatterers displacement. L. V. Wang [78] used the same formalism and added the contribution of the refractive index modulation.

The Wiener-Khinchin theorem states that the power spectral density is related to the Fourier transform of the auto-correlation of the electric field. The tagged photons power Ψ_T in a given sideband at $m\omega_{US}$ is thus derived from the corresponding Fourier component of the autocorrelation spectrum. The Fourier component at $m\omega_{US}$ is by definition:

$$\Psi_T = \frac{\omega_{US}}{2} \int_0^{2/\omega_{US}} G(\tau) \cos(m\omega_{US}\tau)\, \mathrm{d}\tau \tag{2.27}$$

The autocorrelation of the electric field is the summation of the autocorrelation function of the field $\mathcal{E}_p(t)$ along each path number p weighted by the probability to find such a path $\Omega(p)$:

$$G(\tau) = \int_0^{\infty} \Omega(p) \left\langle \mathcal{E}_p(t)\, \mathcal{E}_p^*(t+\tau) \right\rangle \mathrm{d}s_p \tag{2.28}$$

where "$*$" denotes complex conjugation and "$\langle\rangle$" stands for the average value. Taking both particles displacement and refractive index modulation, it comes out that:

$$\left\langle \mathcal{E}_p(t)\, \mathcal{E}_p^*(t+\tau) \right\rangle = E_0^2 \left\langle \exp\left[-i \left(\sum_j \Delta\psi_n^j(t) - \Delta\psi_n^j(t+\tau) + \sum_j \Delta\psi_s^j(t) - \Delta\psi_s^j(t+\tau) \right) \right] \right\rangle \tag{2.29}$$

The autocorrelation of the electric field has been derived by L. V. Wang [78] for a propagating plane wave and is:

$$G(\tau) = E_0^2 \int_0^\infty \Omega(p) \exp\left\{-\frac{2s_p}{l_s} n_0^2 k_0^2 (\delta_s + \delta_n) u_0^2 [1 - \cos(\omega_{US}\tau)]\right\} \mathrm{d}s_p \tag{2.30}$$

where δ_s and δ_n respectively stand for the contribution of scatterers displacement and refractive index modulation. The power spectral density of scattered light can thus be obtained by developing the exponential assuming small modulation depths. It appears that scattered light power contains a static component corresponding to unmodulated light and oscillating parts at multiples of ω_{US} that correspond to ultrasound tagging. Keeping only the first three, it comes:

$$\begin{cases} \text{Untagged photons power :} & \Psi_{UT} = \Psi_0 \left[1 - n_0^2 k_0^2 (\delta_s + \delta_n) u_0^2 \dfrac{2}{l_s} \displaystyle\int_0^\infty \Omega(p)\, s_p \mathrm{d}s_p\right] \\ \text{Tagged photons power :} & \Psi_T = \Psi_0 n_0^2 k_0^2 (\delta_s + \delta_n) u_0^2 \dfrac{2}{l_s} \displaystyle\int_0^\infty \Omega(p)\, s_p \mathrm{d}s_p \end{cases} \tag{2.31}$$

where Ψ_0 stands for the light power without ultrasound. For ultrasonic pulses, the same kind of calculations hold and was done by Kempe *et al.* in [77] and Sakadžić and Wang in [80]. It is possible to express the tagged photons power at the position $\mathbf{r}'$ outside the sample as:

$$\Psi_T(\mathbf{r}') \propto \Psi_0 \int \Omega(\mathbf{r}, \mathbf{r}') \Phi(\mathbf{r}) u_0(\mathbf{r})^2 \mathrm{d}\mathbf{r} \tag{2.32}$$

or in terms of acoustic pressure under the assumption that the particles velocity is given by $P_0(\mathbf{r})/Z$ with Z assumed to be constant:

$$\Psi_T(\mathbf{r}') = \beta \Psi_0 \int \Omega(\mathbf{r}, \mathbf{r}') \Phi(\mathbf{r}) P_0(\mathbf{r})^2 \mathrm{d}\mathbf{r} \tag{2.33}$$

In these expressions $\Omega(\mathbf{r}, \mathbf{r}')$ stands for the probability that a photon tagged in $\mathbf{r}$ reaches the area at $\mathbf{r}'$ outside the sample, $\Phi(\mathbf{r})$ stands for the light irradiance repartition inside the scattering sample and β a proportionality coefficient that ensures homogeneity.

This approach shows several interesting points. Beside the different side-bands that are also predicted here, it is interesting to notice that the tagged photons power is proportional to the pressure squared. Typical acousto-optic signals are then expected to quadratically vary with ultrasound pressure. Furthermore, the acousto-optic signal depends on the scattered light irradiance integrated over the ultrasound volume as it was qualitatively explained in section 2.1. It expresses the fact that photons are tagged over the entire ultrasound volume and indistinguishably counted by the detection for their origin was lost through scattering. Eventually, it appears here that tagged photons do not simply probe the scattered light irradiance, but $\Omega(\mathbf{r}, \mathbf{r}')\Phi(\mathbf{r})$ that depends also on the detector position.

2.4 Tagged photons filtering

As I showed in the previous sections, the ultrasound modulation carries information about the light irradiance inside the scattering medium. Because the technique works with multiply scattered light, it is *a priori* possible to obtain optical information at depths far beyond the transport mean free path. The challenge then consists in quantifying the amount of modulated light in order to extract this information. The two approaches previously derived give two points of view about

the same phenomenon. The random walk approach interpret the ultrasound modulation in terms of tagged photons generation whereas the coherent acousto-optic modulation interpret it as a temporal modulation of the scattered light power. As the two interpretations are physically equivalent, I will indifferently switch from one to the other. In this section, I will discuss several detection schemes that were used in order to measure the ultrasonic modulation whereas the next one will be devoted to the ultrasound sequence and the corresponding resolution.

2.4.1 Challenges of filtering modulated light

Because the goal of acousto-optic imaging is to measure a light modulation due to ultrasound, the technique is very similar to conventional laser vibrometry, the main difference being that laser vibrometry measures vibrations at the surface of samples whereas acousto-optic imaging aims at detecting vibrations deep inside. It is then not surprising that a lot of filtering techniques developed for acousto-optic imaging were also developed for laser vibrometry.

The first approaches used to measure the ultrasound modulation through the AC-component of a photomultiplier voltage placed after the scattering medium [64]. However, the tagging volume is usually very small compared to the total scattered light volume so that the modulation depth is intrinsically small - *i.e.* only very few photons are tagged compared to the amount of untagged photons. The main challenge of acousto-optic imaging is then to accumulate as many tagged photons while rejecting as many untagged photons as possible. Based on this observation, the most natural techniques were based on interferometric approaches that tried to measure the modulation through the beating between scattered light and a reference beam on a single detector of large aperture [77]. The basic issue of such approaches is that the speckle pattern of scattered light drastically decreases the SNR of the techniques.

Indeed, as I explained in chapter 1, the phase of the electric field from a speckle grain to another is random. If the single detector integrates N speckle grains of characteristic surface S_g, the measured signal s_{PD} is proportional to the interference pattern integrated over the detector area S:

$$s_{\mathrm{PD}} \propto \int_S |\mathcal{E}_S(\mathbf{r}',t) + \mathcal{E}_R(\mathbf{r}',t)|^2 = NS_gE_0^2 + NS_gE_R^2 + \int_S [\mathcal{E}_S(\mathbf{r}',t)\,\mathcal{E}_R^*(\mathbf{r}',t) + \mathcal{E}_S^*(\mathbf{r}',t)\,\mathcal{E}_R(\mathbf{r}',t)] \tag{2.34}$$

where $\mathcal{E}_S(\mathbf{r}',t)$ and $\mathcal{E}_R(\mathbf{r}',t) = E_R \exp[i(\omega_0 t - \mathbf{k}_0 \cdot z\mathbf{u}_z)]$ respectively stand for the scattered modulated light and the reference plane wave beam. In practice, the DC level $NS_gE_0^2 + NS_gE_R^2$ is much stronger than the cross terms that contain the modulation so that it is responsible for the noise in the acousto-optic signals. In case the reference power is high compared to scattered light – which is typically the case – and assuming that the technique is shot-noise limited, the noise $\mathcal{N}$ is given by:

$$\mathcal{N} = \sqrt{NS_g}E_R \tag{2.35}$$

By simply writing the scattered field in the single speckle grain number j under the form:

$$\mathcal{E}_S(j,t) = [(1-\varepsilon)E_0 + \varepsilon E_0 \cos(\omega_{US}t + \psi_j)]\, e^{i\omega_0 t} \tag{2.36}$$

and expressing the integral over the detector surface through the average value of the cross terms,

it comes:

$$\int_S \left[\mathcal{E}_S\left(\mathbf{r}',t\right)\mathcal{E}_R^*\left(\mathbf{r}',t\right) + \mathcal{E}_S^*\left(\mathbf{r}',t\right)\mathcal{E}_R\left(\mathbf{r}',t\right)\right] = NS_g\left[2E_0E_R\varepsilon\left\langle\cos\left(\omega_{US}t+\psi_j\right)\right\rangle_N + 2E_0E_R\left(1-\varepsilon\right)\right] \tag{2.37}$$

where ε is the modulation depth, ψ_j is the phase of the speckle grain number j, "$\langle\rangle_N$" stands for the averaging over the N speckle grains and the modulation depth was assumed constant in each one. Here I assumed that the reference beam frequency was tuned on the untagged photons but the same approach holds if the reference is tuned on one of the side-bands. If looking at the component at the ultrasound frequency, it appears that, if the phase ψ_j is uncorrelated and random from a grain to another, the averaging over N speckle grains can be expressed as:

$$\left\langle\cos\left(\omega_{US}t+\psi_j\right)\right\rangle_N = \frac{\cos\left(\omega_{US}t+\psi\right)}{\sqrt{N}} \tag{2.38}$$

The measured modulation depth thus increases proportionally to the square root of the number of speckle grains and the SNR is the same as if only one grain was taken into account, which is weak for the optical *etendue* of a single speckle grain is small. This shows that the random wave-front of speckle patterns is the major hindrance to the use of conventional interferometric techniques with a plane wave reference.

Obviously, in case all speckle grains have the same phase – or if the modulation can be measured in each speckle grain individually – the modulation depth thus increases as the number of the speckle grains so that SNR increases as the square root of the latter.

Efficient techniques must then either be:

- techniques able of sampling the speckle pattern in order to measure the modulation depth in each speckle grain individually.
- wave-front adaptive interferometry techniques in which wave-fronts are corrected in order to match reference and scattered light phase over the entire detector surface.
- purely light *flux* measurement, insensitive to the random wave-front, but narrow-band enough to discriminate tagged from untagged photons.

The main difficulty of interferometry-like techniques lies in the fact that, as explained in section 2.1, the scattered wave-front decorrelates along time in moving tissues. Efficient coherent detection techniques thus need to have response times faster than this decorrelation time.

2.4.2 Parallel speckle processing

As I showed in the previous section, the amount of light modulation due to ultrasound is small. In order to increase the SNR of the detection, it is necessary to accumulate the measured modulation over a high number of speckle grains. Because of the random wave-front of scattered light, the phase of this modulation is random from one grain to another so that it incoherently adds over large area single detectors. In order to overcome this difficulty, the first techniques that were used were camera-based techniques able to sample speckle patterns in order to parallel process each grain one by one.

The first use of a camera for detecting tagged photons in acousto-optic imaging was reported by S. Lévêque *et al.* in [81]. In this paper, the authors suggest to use parallel speckle detection thanks to a 10^5 pixels CCD camera in order to process as many speckle grains through a lock-in approach.

Because the camera exposure time is very long compared to the period of the ultrasonic modulation, they suggested to use a synchronous light excitation instead of a conventional synchronous detection. This technique was later used in other papers such as [82]. Progresses in CMOS technologies allowed recent development of smart-sensors arrays with a lock-in detection associated with each pixel in order to real-time demodulate all speckle grains in parallel [83, 84]. The ultrasound modulation is extracted from the interference between scattered light and a reference tuned on the untagged photons frequency. The beating component is analogically demodulated pixel by pixel and only the AC-component is encoded thus reducing the amount of transferred data. It allows single-shot acousto-optic signal recording whereas synchronous excitation needed at least four images. Until recently, the main limitation of such an approach was the limited number of pixels (24×24 pixels in [83], 64×64 in [84]). In 2016, Liu *et al.* used a commercial lock-in camera with a lot more pixels (300×300) and showed promising results inside decorrelating objects [85].

These previous approaches aim at directly measuring the modulation depth in each speckle grain. In case an analog lock-in detection in each pixel is not available, previous examples showed that the exposure time of cameras is often too long to properly measure the ultrasound modulation so that it is necessary to perform synchronous excitation. Because such approaches are not convenient, other techniques were developed that take advantage of this "drawback" in order to deduce the amount of modulated light. The principle of these techniques is the same as speckle contrast imaging techniques described in chapter 1. Because exposure times of cameras are often longer than the ultrasonic period, the presence of ultrasound induces a blurring of the speckle image. By quantifying this amount of blurring through the measurement of the speckle contrast (see section 1.3.2), it is possible to recover the modulation depth. The first proof of concept was performed by J. Li *et al.* [86] and a theoretical framework can be found in [87]. The major issue of this approach is that the exposure time of the camera must be shorter than the speckle decorrelation time so that the measured decorrelation is only due to ultrasound. Recently, S. Resink *et al.* showed that such a detection scheme may be coupled with nanosecond pulses in order to couple acousto-optic and photoacoustic imaging or solve this speckle decorrelation issue [88]. Because nanosecond pulses are used, there is no speckle decorrelation due to tissue moving at this time-scale. The measured speckle decorrelation is then only due to ultrasound. S. Resink and W. Steenbergen showed that acquiring two frames corresponding to two nanosecond pulses emitted at two different ultrasound phases allows recovering the modulation [89–91].

A third approach is digital holography suggested by M. Gross *et al.* in 2003 for acousto-optic imaging [92]. The technique consists in directly recording the electro-magnetic field corresponding to tagged photons on a camera. Contrary to lock-in detection that tunes the reference on untagged photons frequency and performs a temporal demodulation, digital holography tunes the reference beam on tagged photons frequency and spatially demodulates the interference pattern in order to recover the tagged photons component. In general, digital holography is performed in an heterodyne and off-axis configuration [93] meaning that the reference is slightly frequency shifted (few Hz) and tilted, so that it is possible to extract the tagged photons component in the camera plane. Providing that the scattering sample is far enough from the camera, a simple 2D Fourier transform gives the amplitude of the tagged photons field in the scattering sample output plane. It can be shown that such an approach is shot noise limited [94].

All these techniques have the similarity that generally one to four frames are used in order to recover one value of the acousto-optic signal at a given position of ultrasound. If it can be shown that parallel processing of speckle patterns can be made robust to speckle decorrelation *in vivo*, the major issue of the techniques is that framerates of usual cameras are currently too slow to time-resolve ultrasound propagation. As a consequence, one ultrasound pulse must be used for

each required pixel in the final image, thus drastically limiting the imaging speed.

2.4.3 Wave-front adaptive holography

A way of overcoming the imaging speed issue of cameras is to use detection schemes based on high surface single-detectors. Because the bandwidth of such detectors is typically of several MHz, it is possible to time-resolve ultrasound propagation with a temporal resolution under 1 µs – corresponding to a spatial sampling under 1.5 mm. However, as I explained above, speckle patterns lead to the measured AC-modulation increasing as the square root of the number of integrated speckle grains whereas the DC-level increases as the number of speckle grains. It thus results in SNR that is limited to the SNR of a single speckle grain. In order to increase this ratio, people developed holographic techniques that allow adapting the scattered and reference wave-fronts. The principle is as follows. The interference pattern between the scattered and reference light is recorded in a holographic medium. The interference is given by:

$$|\mathcal{E}_S(\mathbf{r}',t) + \mathcal{E}_R(\mathbf{r}',t)|^2 = E_0^2 + E_R^2 + \mathcal{E}_S(\mathbf{r}',t)\,\mathcal{E}_R^*(\mathbf{r}',t) + \mathcal{E}_S^*(\mathbf{r}',t)\,\mathcal{E}_R(\mathbf{r}',t) \tag{2.39}$$

"Recording" means that the light irradiance slightly modifies one of the physical properties of the material so that the transmission $\mathcal{T}(x,y)$ becomes spatially inhomogeneous and proportional to the interference pattern. This inhomogeneous transmission thus creates a grating on which light can diffract.

Two-waves mixing

The first interaction that was explored is Two-Waves Mixing (TWM). The idea is that the grating previously created is self-read by the very same beams that induced this interference pattern. The reference beam that diffracts on this grating can be expressed as:

$$\begin{aligned}\mathcal{T}(x,y)\,\mathcal{E}_R(\mathbf{r}',t) &\propto |\mathcal{E}_S(\mathbf{r}',t) + \mathcal{E}_R(\mathbf{r}',t)|^2 \mathcal{E}_R(\mathbf{r}',t) \\ &= (E_0^2 + E_R^2)\,\mathcal{E}_R(\mathbf{r}',t) + \mathcal{E}_S(\mathbf{r}',t)\,\mathcal{E}_R^*(\mathbf{r}',t)\,\mathcal{E}_R(\mathbf{r}',t) + \mathcal{E}_S^*(\mathbf{r}',t)\,\mathcal{E}_R(\mathbf{r}',t)^2\end{aligned} \tag{2.40}$$

Here, it was considered that the interference pattern immediately generates the grating. In practice, this is a dynamic process that usually refreshes over a characteristic time defined by the phenomenon underlying the hologram engraving, hence the term "self-adaptive" holography that often refers to these techniques. The transmission $\mathcal{T}(x,y)$ is in fact the average value of the interference pattern over this characteristic time, as it will be further explained in the next chapter. After the holographic medium, the diffracted reference contains a term proportional to $E_R^2\mathcal{E}_S(\mathbf{r}',t)$ that propagates in the same direction as the transmitted scattered light whereas the other terms propagate in the incident reference direction. This portion of the reference coherently interferes with scattered light everywhere. This basically means that, through its propagation in the holographic medium, the reference beam is partially distorted until it has the same wave-front as scattered light. The inhomogeneous transmission spatially adapts reference and scattered wave-fronts in order to have the ultrasound modulation coherently add over the whole detector surface.

The first materials that were studied in order to perform TWM were photorefractive crystals. First developed for imaging vibrations on rough surfaces [95, 96], it was independently applied to acousto-optic imaging by T. W. Murray *et al.* [97] and F. Ramaz *et al.* [98]. TWM in photorefractive crystals will be further studied in the next chapter, I will only recall quickly the principle

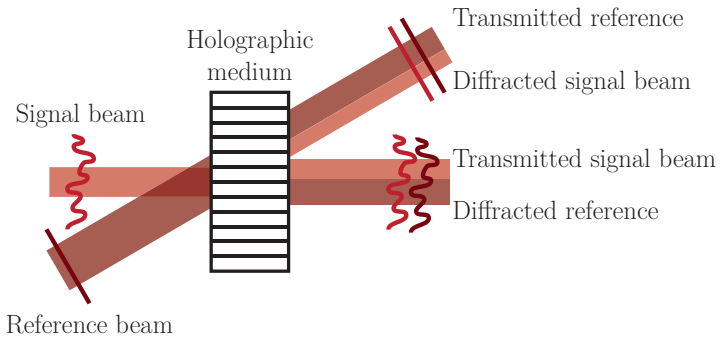

Figure 2.6 – Schematic of TWM process. The interference between reference and signal beams generates a hologram on which the two beams diffract. The reference that diffracts in the direction of the transmitted signal beam has the same wave-front as scattered light so that interferences are spatially coherent. The scattered light that diffracts in the direction of the transmitted reference has a plane wave-front. The detector is usually placed in the direction of the transmitted signal beam.

here. Photorefractive crystals are both photoconductive and electrooptic materials so that a spatially inhomogeneous irradiance induces an inhomogeneous charge distribution and local electric fields. These local electric fields induce a spatial modulation of the refractive index on which light can diffract. One usually characterizes such TWM processes through a photorefractive gain γ_{PR} such as $\exp(\gamma_{\mathrm{PR}} L)$ is the ratio between the signal beam power with and without reference beam. Here L stands for the interaction length of the two beams. The detection SNR is given, among others, by the number of speckle grains that can be sampled on the crystal surface: the higher the surface, the higher the SNR. Typical crystals in our experiments have a surface of about 1 cm^2 and can process up to 10^8 speckle grains, about two orders of magnitude higher than for cameras – usually having up to 10^6 pixels. Photorefractive crystals are widely used in acousto-optic imaging because of their relatively high gains (a few cm^{-1}) and low response time (a few milliseconds), though the latter is still a bit higher to properly follow speckle decorrelation *in vivo*.

Y. Suzuki *et al.* recently suggested the use of photorefractive polymers [99] the optical *etendue* of which can be up to one order of magnitude higher than for photorefractive crystals, but the very long response time (several seconds) prevents from using them in clinical applications. Liquid crystals were also investigated through the use of Liquid Crystals Light Valves (LCLV) because of their very high birefringence. The principle consists in a nematic liquid crystal phase sandwiched between a photoconductive crystal and a glass plate. An electrode is place on each face and a voltage is applied so that liquid crystals are oriented along the electric field. The presence of light induces the displacement of charges inside the photoconductive crystal that partially screen the electric field and induce a local reorientation of liquid crystals. Because the birefringence is high, it leads to a photorefractive effect [100]. The advantage of such an approach is that the photoconductive material is not coupled to the electrooptic one so that each one can be optimized independently from the other. Such an approach was suggested by U. Bortolozzo *et al.* for the detection of small displacements of vibrating surfaces [101]. Recently, U. Bortolozzo *et al.* showed that a coupled CMOS/phase-only LCOS SLM (Liquid Crystal on Silicon spatial light modulator) device could be used for detection of phase modulation through long multimode optical fibres [102]. The idea is to record the hologram on a CMOS camera and numerically print it on a liquid crystal-based spatial light modulator, thus allowing to fully control the gain and phase of the hologram or removing the DC-component.

Recently, gain media were explored in order to overcome the long response time of photore-

fractive crystals [103]. The idea is to use a pump beam to induce population inversion in a gain medium. The presence of an inhomogeneous irradiance due to an interference pattern between two other beams induces local stimulated emission. It results a spatial modulation of the gain and refractive index on which light can diffract. The main advantage of this approach is that the response time is given by the lifetime of the storing level, potentially much shorter than speckle decorrelation *in vivo* (measured to about 44 ± 6 µs by B. Jayet [103] for the transition at 1064 nm in Nd:YVO_4 crystals).

Phase conjugation

Another approach that was explored is phase conjugation also called four-waves mixing. The idea is to read the hologram with the conjugate of the reference beam, often obtained by reflecting the transmitted reference back to the holographic medium. As a consequence, the reflected reference diffracts onto the hologram and generates the conjugate of the scattered electric field that propagates backward to the scattering sample. It appears that such a backward propagation corrects the aberrations due to scattering. Because the backward scattered field is absorbed twice by the scattering medium, it was not used a lot for acousto-optic signal detection. The main example was given by B. Jayet *et al.* [104] with a Nd:YVO_4 gain medium. The hologram of untagged photons is engraved so that it is phase conjugated and measured after the scattering medium on a photodiode. The presence of ultrasound generates tagged photons that are not phase-conjugated and do not travel back to the detector, resulting in a decrease of the measured phase-conjugated power.

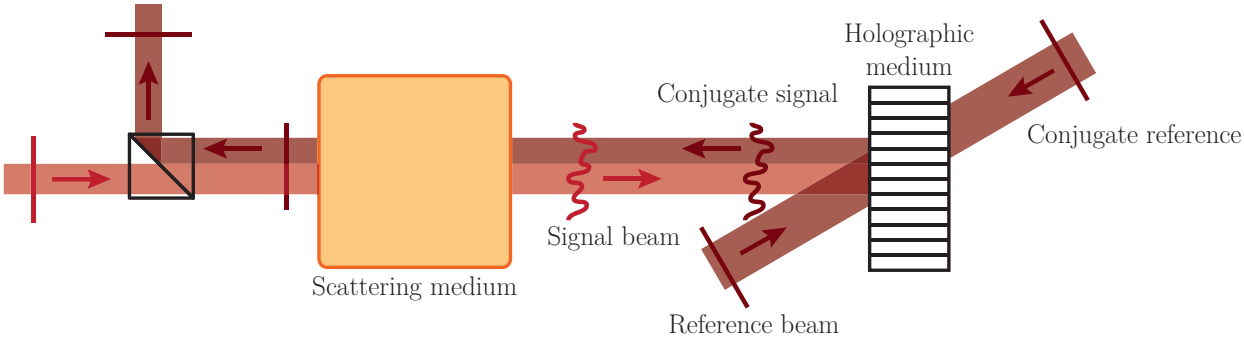

Figure 2.7 – Schematic of phase conjugation process for acousto-optic detection. Here the hologram is read by the reference conjugate so that the reference that diffracts has the same wave-front as the scattered light conjugate. It propagates backward to the sample where the different aberrations acquired through scattering are corrected. The emerging light is a plane wave that can be measured on a photodiode. The presence of ultrasound generates tagged photons that are not phase conjugated and the signal on the photodiode decreases.

Phase conjugation was mostly used in TRUE focusing in order to focus tagged photons back to the ultrasound focal point. By engraving the hologram of tagged photons, it is possible to generate the corresponding phase conjugated field that travel back to the ultrasonic focus. In this field, holographic media are mostly BSO photorefractive crystals [74, 105].

2.4.4 Spectral filtering

Ultra-narrowband spectral filtering techniques were developed in order to overcome the response time limitation of holographic media while keeping the advantage of using large area single-

detectors in terms of detection bandwidth. Because they directly measure the *flux* of tagged photons, such approaches are intrinsically insensitive to speckle decorrelation.

There are basically two main approaches that were suggested. The first one is based on the use of confocal Fabry-Perot interferometers and was first suggested by J.-P. Monchalin [106] in order to image vibrating rough surfaces. The transmission spectrum of a confocal Fabry-Perot interferometer is constituted of Lorentzian peaks separated by the free spectral range – inversely proportional to the length of the cavity. The width of these peaks is defined by the ratio between the free spectral range and a coefficient called the finesse, the value of which is defined by the reflectivity and surface quality of the mirrors. In his paper, J.-P. Monchalin suggests to tune the cavity length so the laser frequency is on one edge of this transimission peak – where the behaviour can be assumed to be linear. A vibration of the surface is then converted into a variation of the transmitted *flux* so that such an interferometer measures the velocity of the surface through Doppler shift. Confocal Fabry-Perot cavities were suggested for acousto-optic imaging by S. Sakadžić and L. V. Wang in 2004 [107]. The idea is to have a sufficiently long and high finesse cavity in order to have narrow transmission lines. The transmission is tuned on one of the side-bands of scattered light so that untagged photons are reflected by the cavity whereas tagged photons are transmitted.

However, because of their weak optical *etendue*, such detection schemes are inconvenient for speckle filtering. Recently, Li *et al.* suggested to use spectral holeburning [108] that will be further explained in the last two chapters. The idea is to use a powerful laser beam to burn a narrow transparent spectral band inside an inhomogeneously broadened line of a rare-earth doped crystal. By matching this transparent spectral region with one of the scattered light side-band, it is possible to have tagged photons mostly transmitted by the crystal whereas untagged photons are absorbed. They performed first proofs of concept in a Tm^{3+}:YAG crystal with a 2 at.% substitution rate. However, such techniques only work at cryogenic temperatures (< 4 K) and were left aside since.

2.4.5 Summary on filtering techniques

In this section, I showed that because the ultrasonic modulation is very small – *i.e.* there are very few tagged photons compared to the number of untagged photons – it is usually necessary to increase this amount. Because the frequency shift due to ultrasound is very small, it is very difficult to spectrally filter the two kinds of photons. A classical way of increasing the modulation depth – *i.e.* the ratio between tagged and untagged photons – is to use interferometric techniques on large area detectors. However, I showed that because of the random wave-front of scattered light, the SNR does not increase with the detector surface and is equal to the SNR of a single speckle grain.

In order to increase the SNR of the detection, several techniques were developed that can be sorted into three types. The first kind of techniques involves cameras able to parallel process each speckle grain one by one. The second type involves wave-front adaptive interferometry – or holography – in order to spatially adapt reference and scattered light wave-fronts. The third kind of techniques appeared in order to overcome bandwidth limitations in the first two types of detection schemes. These latter approaches involve ultra-narrowband filtering of tagged photons that is not sensitive to speckle patterns. In a more general way, camera-based and holographic techniques are often referred to as coherent techniques whereas spectral holeburning is often referred to as an incoherent technique.

2.5 Of acousto-optic imaging and resolution

I previously presented several possible techniques that were used to filter and count tagged photons. In section 2.3.2, it appeared that photons are tagged over the entire volume occupied by ultrasound, the shape of which will then naturally define the resolution of the technique. One thus explored a lot of different ultrasound sequences in order to obtain different resolutions and levels of acousto-optic signal. In this section I suggest to study a few examples of typical acousto-optic sequences and their corresponding resolution.

First proofs of concepts were performed using single-element focused transducers and continuous wave [64, 82] and suffered from very poor longitudinal resolution (in the ultrasound propagation direction $\mathbf{u}_x$). If the lateral and elevational resolution (along $\mathbf{u}_y$ and $\mathbf{u}_z$) of such an approach is approximately the lateral size of the focus (a few Λ), the longitudinal resolution is the entire scattering medium depth. A means of recovering the resolution consists in using a tomographic approach by rotating the emitting transducer around the sample [109].

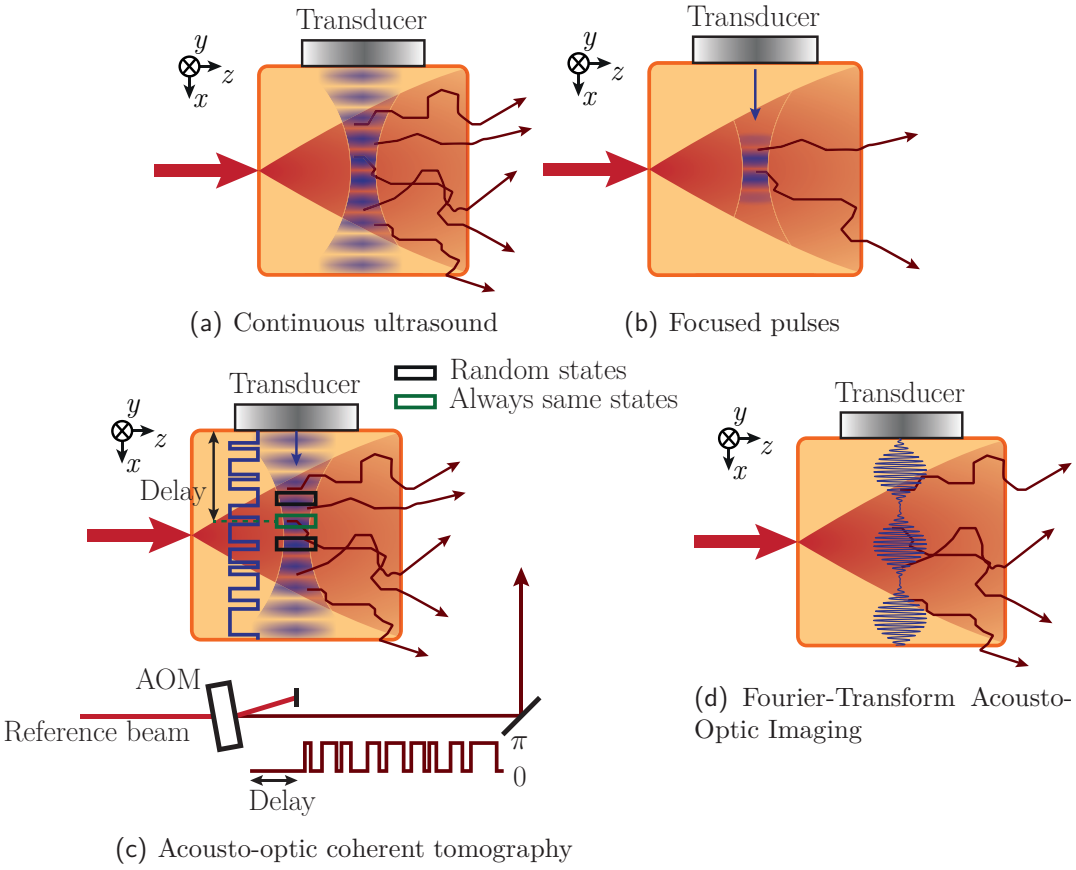

(a) Continuous ultrasound

(b) Focused pulses

(c) Acousto-optic coherent tomography

(d) Fourier-Transform Acousto-Optic Imaging

Figure 2.8 – Representation of four different ways of sending ultrasound in acousto-optic imaging and their corresponding resolution.

The most immediate way of recovering the longitudinal resolution is to use few-cycles-long focused pulses. In such a case, the lateral and elevational resolutions are still given by diffraction (a few Λ), but the longitudinal resolution is now the length of the pulse (also a few Λ). Such approaches took time to appear because, compared to continuous waves, the number of tagged photons is drastically lower as the ultrasound volume was decreased. As a consequence, they must be combined with more sensitive detection. The use of ultrasound pulses was reported together with photorefractive-based detection – that I will describe later – and broadband single detectors able to acquire time-resolved acousto-optic signals over the pulse propagation [110].

The major drawback of pulses is the low amount of acousto-optic signal. Other approaches appeared that aimed at increasing the number of tagged photons by increasing the length of the ultrasound pulses while keeping the longitudinal resolution intact. The first approach was developed at the Institut Langevin during M. Lesaffre's PhD and is called Acousto-Optical Coherent Tomography (AOCT). The technique was reported in [111] and [112–114]. It uses long exposure times of detectors in order to accumulate tagged photons signal over time. This is an interferometric approach that consists in sending long ultrasound pulses modulated by a pattern of short random phase jumps. A reference beam modulated with the same pattern is used to recover the resolution: only photons coming from the desired area always have the same phase state as the reference whereas other photons will have a random one. The principle of the technique is represented on figure 2.8(c). Over the pulse duration, only photons coming from the temporal coherence volume interfere constructively with the reference whereas the rest will interfere randomly. The coherence volume vertical position is selected by adjusting the delay between the reference beam and the ultrasound pulse and its size is given by the characteristic time between two phase jumps – *i.e.* the temporal autocorrelation of the modulation pattern. Such an approach allows increasing the number of measured tagged photons by increasing the integration time of the detection while keeping a decent spatial resolution.

In more recent works, K. Barjean *et al.* [83,115] developed a Fourier-based approach that benefits from long ultrasound pulses while allowing depth-resolved imaging by reconstructing the image from its Fourier components. The principle of the technique called Fourier-Transform Acousto-Optic imaging (FTAOI) is presented on figure 2.8(d). This technique was developed together with the lock-in approach described in 2.4. In this case the ultrasonic beam is amplitude-modulated (AM) and tagged photons signal is measured through demodulation at ultrasound frequency. It can be shown [115] that this tagged photons signal carries information about the Fourier coefficient at the AM-frequency of the acousto-optic line under the transducer. This information is recovered by demodulating the tagged photons signal a second time at the AM-frequency, and a line of the acousto-optic image is obtained by inverting the Fourier transform reconstructed by changing the modulation frequency. The resolution is then defined by the maximum AM-frequency that can be measured.

2.6 Conclusion on acousto-optic imaging

In this chapter, I showed that local acoustic modulation of scattered light could be used to recover the light irradiance inside a multiply scattering medium. I gave a quick theoretical framework that highlighted the main properties of acousto-optic signal. The main properties of the coherent modulated light are:

- Tagged light is modulated at the ultrasound frequency meaning that tagged photons are shifted from light frequency by this amount.
- The number of tagged photons – *i.e.* the modulation depth – is proportional to the local light irradiance integrated over the ultrasound volume.
- The tagged photons power is sensitive to the pressure squared.
- Tagged light has a speckle wave-front and is *a priori* spatially uncorrelated to untagged light.

It then appears that a detection scheme able to filter and count these tagged photons – *i.e.* able to measure the amount of modulation – allows recovering the local light irradiance deep inside the scattering medium with a resolution defined by the shape of ultrasound. I showed that this filtering step is not straightforward for four main reasons:

- The ratio between tagged and untagged light is weak (typically 1 over 1000).
- The frequency shift is small compared to light frequency($\sim$ MHz).
- The wave-front is random so that ultrasound modulation spatially adds incoherently on large-area single detectors.
- The random wave-front decorrelates with the motion of the scattering medium.

I gave a quick description of several methods that were developed in order to measure acousto-optic signal. These techniques can be sorted into two categories: coherent techniques that measure the amount of speckle modulation and incoherent techniques that directly measure the *flux* of tagged photons.

Because they work directly on speckles, coherent detection schemes (camera-based or holography), are intrinsically sensitive to speckle decorrelation. It is then important to distinguish robustness to speckle decorrelation from imaging rate. There are two characteristic times that must be accounted for. Speckle decorrelation involves response time – or bandwidth – of the filtering process. It quantifies the ability of the detection to measure decent acousto-optic signal in moving objects. The imaging speed on the other hand depends on the number of ultrasound pulses that are required to obtain a full image. It quantifies the ability of the technique to perform real-time imaging or not. A decent clinical imaging thus needs both low response time in order to measure high SNR acousto-optic signals and low imaging times in order to decently image moving objects. For instance, parallel processing of speckle patterns is robust to speckle decorrelation because exposure time can be made shorter than decorrelation of speckle or tandem pulses can be used. However, because the framerates of current accessible cameras are usually too low to time-resolve the propagation of ultrasound, one needs as many ultrasonic pulses as the required number of points in the final acousto-optic image, thus drastically decreasing the imaging rate. On the other hand, because they use single-detectors, photorefractive-based techniques are able to time-resolve the propagation of ultrasound thus allowing higher imaging speed. However, the long response time of photorefractive crystals makes them sensitive to speckle decorrelation so that the amount of acousto-optic signal decreases if the scattering medium moves too fast.

In the following of the manuscript, I will focus on two particular detection schemes: self-adaptive photorefractive holography and spectral holeburning. In Part II, I will give a few very promising results obtained during my PhD with photorefractive crystals and a recently developed multi-modal device. Such results give a very first insight of potential clinical application of acousto-optic imaging and experimentally highlight the advantages and limitations of the current technique in terms of clinical imaging requirements. I will show that, if using ultrasound pulses ensures a high resolution, the very small tagging volume leads to poor SNR and limited imaging speed. Part III will be dedicated to the description of a potential way of overcoming this difficulty through ultrasonic plane waves and a tomographic approach. Multi-modal imaging results will also highlight the interest of exploring detection schemes that are insensitive to speckle decorrelation. Part IV will be dedicated to further investigations about spectral holeburning as a potential measurement tool for acousto-optic imaging.

Part II

Acousto-optic imaging with photorefractive holography: toward clinical imaging?

CHAPTER 3

Bimodal acousto-optic/ultrasound imaging

Table of contents

Acousto-optic imaging allows recovering optical contrast deep inside multiply scattering samples. In the previous two chapters, I presented the potential benefits of optical contrast in medical imaging and the basic principle of acousto-optic imaging. I showed that the tagged photons filtering step is the most critical part of the technique. Several methods exist in order to deal with the challenges of acousto-optic imaging. These detection schemes can be sorted into three main categories: techniques involving cameras and parallel processing of speckle grains, wave-front adaptive interferometric approaches and ultra-narrowband spectral filtering. The first kind of techniques are mainly limited by the framerate of current cameras that do not yet allow to time-resolve the ultrasound propagation. The third kind of techniques often involves complex instrumentation such as cryostats or long and stabilized confocal Fabry-Perot cavities. Because they allow using large area single detectors, adaptive wave-front interferometric techniques can time-resolve the propagation of ultrasound so that they were naturally associated with ultrasonic pulses. This feature makes them good candidates for multi-modal platforms that couple acousto-optic imaging and commercial ultrasound scanners. In 2005, E. Bossy *et al.* [116] developed the first device coupling a conventional ultrasound scanner and a BSO (Bismuth Silicon Oxide, $Bi_{12}SiO_{20}$) photorefractive-based acousto-optic imaging platform. The major drawback of such a device lied in the BSO crystal working around 532 nm, region in which biological tissues start being very absorbing. More recently, S. Farahi *et al.* [117] developed a similar multi-modal platform using SPS ($Sn_2P_2S_6$, tin thiohypodiphosphate) photorefractive crystals working around 790 nm. Because it works at a more appropriate wavelength range, such a bimodal platform gave first very interesting results on biological samples and real pathologies. In this section, I suggest to first detail the principle of the imaging platform and how acousto-optic imaging can be combined with conventional ultrasound. I will detail the principle of a photorefractive-based acousto-optic detection and present first interesting results obtained with such a device.

3.1 Fusion of conventional ultrasound and acousto-optics

In order to properly understand how acousto-optic imaging and conventional ultrasound can be coupled, I will first give a quick overview of how conventional ultrasound works.

Conventional ultrasound scans are based on multi-element transducer arrays of several tens or hundreds of small piezoelectric transducers (64, 192, 256 or 512 elements for instance). Transducer arrays can have different shapes (1D or 2D, linear or curved...) depending on the application. In this manuscript, I use linear arrays with rectangular 0.2×0.4 mm^2 elements with a pitch of 0.2 mm[1], see figure 3.1(a). Each transducer can be electronically driven independently from the others with a variable delay. Because of Huygens-Fresnel principle, these delay lines define the shape of the ultrasound wave under the probe. For instance, pulsing all elements at the same time generates a plane wave propagating vertically under the probe, whereas applying a linear delay generates a plane wave propagating with a tilted angle.

[1]The first dimension denotes the lateral direction (along the probe) whereas the second denotes the elevation direction (out of plane)

In the case of conventional ultrasound scans, finite apertures are used to generate focused pulses of few cycles by applying a parabolic line such as the delay of the j^{th} element is equal to:

$$\Delta t\,(j) = \frac{\sqrt{(y_c - y_N)^2 + x_f^2} - \sqrt{(y_c - y_j)^2 + x_f^2}}{V_{\mathrm{US}}} \tag{3.1}$$

where y_c, y_j and y_N respectively stand for the position on the probe of the central element, the j^{th} element and the last element of the aperture whereas x_f stands for the vertical position of the focus, see figure 3.1(a). Elements on the edge of the aperture, further from the focal point, are pulsed first whereas elements around the center, closer to the focus, are pulsed last. This delay line only means that all pulses must arrive at the same time at the focus. It is thus possible to electronically control the focusing depth by adjusting the delays. When propagating inside the biological sample, the ultrasonic pulse encounters interfaces and scatterers that generate backscattered echoes. These echoes are recorded by the aperture elements and numerically refocused to their rightful place in order to reconstruct a line of the ultrasound scan as represented on figure 3.1(b). The focal point is then electronically scanned in order to recover the entire image, as shown on figure 3.1(c).

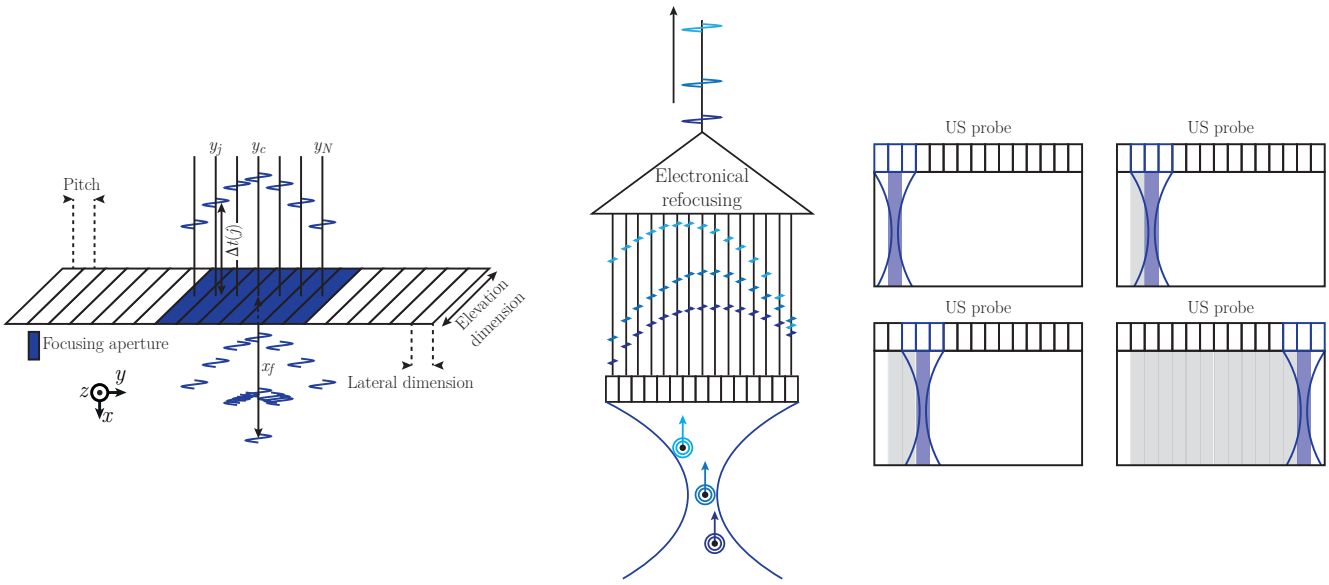

(a) Schematic of a multi-element array and focal law

(b) Receiving mode of ultrasound scans

(c) Scanning in ultrasound imaging

Figure 3.1 – Principle of conventional ultrasound. (a) Schematic of a linear probe for ultrasound imaging and a parabolic delay line in order to focus pulses. (b) Receiving mode of an ultrasound scan. All backscattered echoes are recorded by the different transducers and numerically refocused at their rightful origin in order to recover a line of the scan. (c) The focus is linearly scanned in order to recover the ultrasound scan.

In the case of acousto-optic imaging, only the emitting mode is used and the optical detection is completely dissociated from the receiving mode of the scanner. Considering the principle of conventional ultrasound, it then appears that the easiest way of coupling ultrasound scanners and acousto-optic imaging is to use linear scans and focused pulses. Because they use large-area single detectors of high bandwidths, photorefractive-based detection schemes are able to time-resolve the propagation of an ultrasound pulse. It means that a single pulse gives a full line of the final acousto-optic image with a resolution defined by the most limiting factor between the ultrasound pulse size and the photodetector bandwidth. Such acousto-optic sequences are thus very similar to conventional ultrasound sequences.

Figure 3.2 represents a typical acousto-optic line acquisition. The temporal variation of the number of tagged photons is recorded along with the pulse propagation. At short times, there is no acousto-optic signal for the pulse did not enter the diffuse light area. Then, the number of tagged photons starts changing proportionally to the light irradiance as the pulse propagates through the illuminated area. At long times, the acousto-optic signal is equal to zero as the pulse exits the illuminated area. Interestingly, since such a sequence does not need receiving mode, the imaging speed can theoretically be twice as high as conventional ultrasound sequences. In practice, given the very low amount of tagged light, it is necessary to average each line a lot of times so that the imaging speed is reduced.

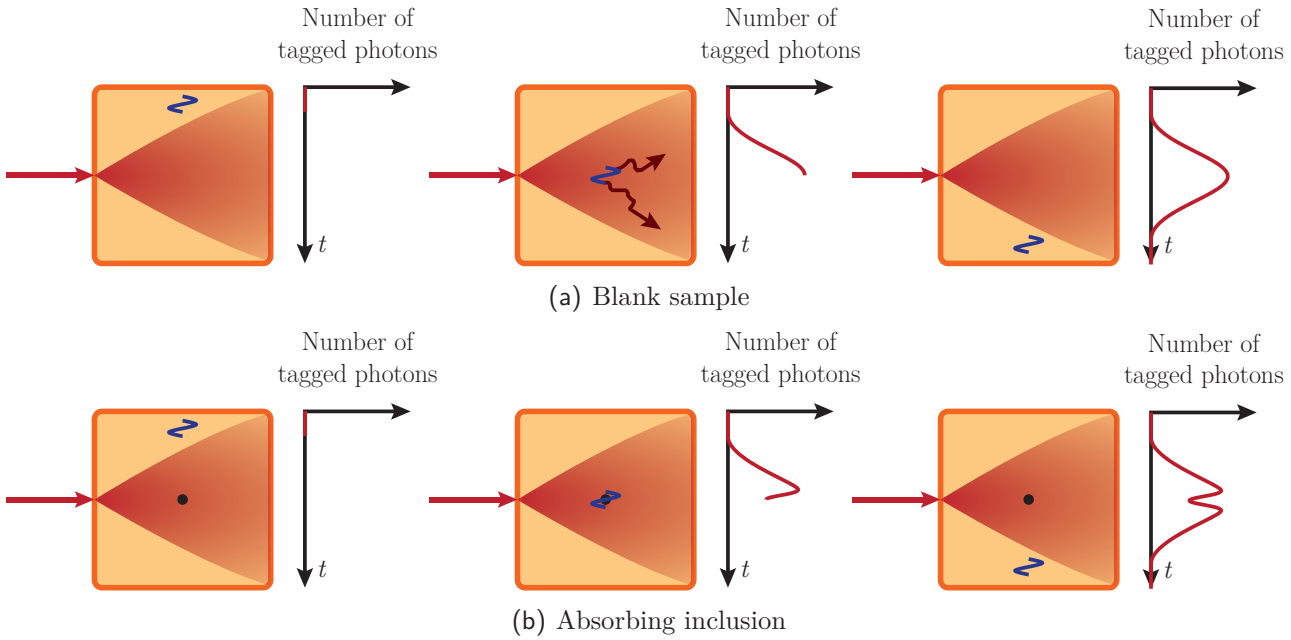

Figure 3.2 – Schematic of a time-resolved acousto-optic line thanks to ultrasound pulses. (a) Schematic of a typical acousto-optic line in a blank sample. (a) Schematic of a typical acousto-optic line with an absorbing inclusion.

The fusion of conventional ultrasound and acousto-optic imaging can be of prime interest. Beside the benefit of acquiring 2D acousto-optic images without mechanical translation of the probe, it then becomes possible to perform both ultrasound scans and acousto-optic images with the same device. The overlay of the different images can bring redundancy of the information that can either overcome detection failures of one of the techniques or resolve uncertainties. Moreover, the information contained in conventional ultrasound scans can potentially be used as *a priori* information in inverse problems in order to extract quantitative information from acousto-optic image.

In the following of the manuscript, the imbrication of acousto-optic sequences within conventional ultrasound sequences is not considered so that, though the same commercial scanner is used to perform both kind of imaging, the two sequences are still dissociated. E. Benoit obtained the first promising results using such a platform during her PhD [66]. Among others, she showed that it can be used for HIFU therapy monitoring. In this chapter, I will give a few other results, the main ones concerning *ex vivo* detection of melanoma metastases in liver. Before detailing these preliminary results that constitute very first steps toward clinical imaging, I will first give further details about the physical principle of a photorefractive detection. The idea is to grasp the main advantages and limitations of the technique.

3.2 Photorefractive detection of tagged photons

In this section I will further detail the detection of tagged photons through photorefractive holography. Because it was already studied in several previous PhDs [66, 111, 118] and articles [79, 97, 98, 110], a lot of calculations will not be detailed here and were moved in appendix A. I will only recall the main results here.

The main goal of the photorefractive detection is to have the scattered and reference beams coherently interfere all over the surface of a single detector. The interest of such crystals is that they can adapt the two wave-fronts through a phenomenon so-called Two-Wave Mixing (TWM). In order to introduce TWM, it is important to first explain the photorefractive effect. Once TWM is detailed, I will show how it can be used for tagged photons detection.

3.2.1 The photorefractive effect

The photorefractive effect is known since the mid 60's and was first considered as an unwanted effect. Its use as a tool for imaging vibrations was suggested at the end of the 90's. For instance, P. Delaye *et al.* [119] used photorefractive Fe:InP crystals under a DC-electric field around 1.06 µm in order to measure vibrations of rough surfaces. Acousto-optic imaging then widely benefited from these works so that a lot of theoretical derivations were inspired by the developments of this field.

Principle of photorefractive effect

The photorefrective effect occurs in materials that are both photoconductive and electrooptic. Several materials present a photorefractive effect such as polymers [99] or light valves [100][1]. In the following, I will focus on photorefractive crystals.

Typical photorefractive materials are crystals or oxides with a forbidden band, for instance:

- ferroelectric crystals such as lithium niobate ($LiNbO_3$), barium titanate ($BaTiO_3$) or SPS ($Sn_2P_2S_6$, tin thiohypodiphosphate),
- sillenites such as BSO (Bismuth Silicon Oxide, $Bi_{12}SiO_{20}$), BTO (Bismuth Titanate, $Bi_{12}TiO_{20}$) or BGO (Bismuth Germanate, $Bi_{12}GeO_{20}$),
- semi-conductors such as gallium arsenide (GaAs), cadmium telluride (CdTe) or indium phosphide (InP).

Such crystals are often doped or present intrinsic defects so that some energy levels can be found inside the forbidden band. These centres must be found under both neutral and ionized states. In the following, the concentration in cm^{-3} of these two states will be noted respectively N^0 and N^+. The presence of a photon of adapted energy can induce photoionization of these centres so that charge carriers, electrons (subscript n in the following) or holes (p), can reach the conductive band. It is possible to define the absorption coefficient in cm^{-1} associated with the photoexcitation of each type of carrier and noted respectively α_n and α_p. Photorefractive crystals also have traps that ensure electrical neutrality. Once inside one of the two bands – conduction band for electrons, valence band for holes[2] – such carrier can move inside the crystal through thermal energy or the

[1] In the case of light valves, the photoconductive part is decoupled from the electrooptic one.

[2] The excitation of a hole is equivalent to the excitation of an electron from the valence band to an ionized centre, leading to a lack of electron in the valence band. Holes are then "excited" to the valence band.

presence of an external electric field. In the presence of a spatially inhomogeneous illumination – an interference pattern for instance – carriers will be mostly excited in regions of high light energy and decay into centres elsewhere. Eventually, a steady-state occurs in which charge carriers are accumulated in regions of low light energy. This simple model is called the band transport model.

This inhomogeneous charge repartition generates a local electric field. Through Pockels effect, this photoinduced electric field generates a modulation of the refractive index of the material. The characteristic time needed for steady-state to establish is called the photorefractive response time, noted τ_{PR}, and represents the main difficulty concerning photorefractive detection *in vivo*. The principle of the photorefractive effect is represented on figure 3.3.

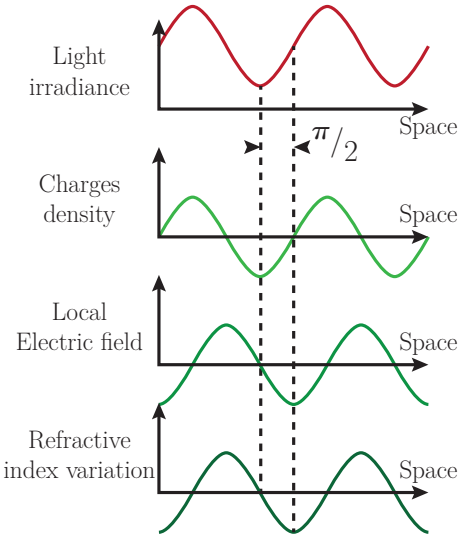

Figure 3.3 – Representation of the photorefractive effect. The presence of a spatially inhomogeneous light irradiance induces the displacement of charges that eventually accumulate in regions of low irradiance. The resulting inhomogeneous charge repartition generates local photoinduced electric field that modulates the refractive index through Pockels effect.

The band transport model

The band transport model that was qualitatively described above is represented on figure 3.4. The model is detailed in appendix A, I will only recall the main results. Let us assume that the crystal is illuminated by an interference pattern between two plane waves:

$$\begin{aligned} \mathcal{E}_S(\mathbf{r},t) &= E_S \exp\left[i\left(\omega_0 t - \mathbf{k}_S\cdot\mathbf{r}\right)\right] \\ \mathcal{E}_R(\mathbf{r},t) &= E_R \exp\left[i\left(\omega_0 t - \mathbf{k}_R\cdot\mathbf{r}\right)\right] \end{aligned} \tag{3.2}$$

The resulting irradiance is given by:

$$\Phi = \Phi_0\left[1 + \mathcal{R}\left(\varepsilon \exp\left(i\Delta\mathbf{k}\cdot\mathbf{r}\right)\right)\right] \tag{3.3}$$

where $\mathcal{R}$ denotes the real part, $\Delta\mathbf{k} = \mathbf{k}_R - \mathbf{k}_S$ is the difference of wave-vectors, Φ_0 is the average value of the irradiance and ε the modulation depth of the fringes:

$$\begin{aligned} \Phi_0 &= |E_S|^2 + |E_R|^2 \\ \varepsilon &= \frac{E_R^* E_S}{|E_S|^2 + |E_R|^2} \end{aligned} \tag{3.4}$$

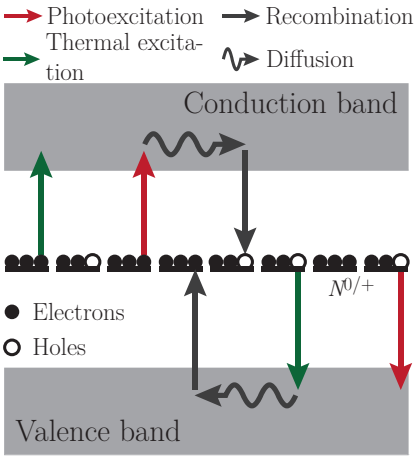

Figure 3.4 – Schematic of the band transport model.

In the following, it will be considered that the reference beam is much more powerful than the signal beam – which is typically the case in acousto-optic imaging. Given this hypothesis, the average irradiance is approximately equal to $|E_R|^2$ and the modulation depth is given by:

$$\varepsilon \sim \frac{E_S}{E_R} \tag{3.5}$$

Such an interference pattern creates a photoinduced electric field which can be approximated to $\mathbf{E}_{loc} = \mathbf{E}_{loc,0} + \mathcal{R}\left(\mathbf{E}_{loc,1} \exp\left(i\Delta\mathbf{k}\cdot\mathbf{r}\right)\right)$. The modulated part of this field is, in steady-state:

$$\mathbf{E}_{loc,1} = \varepsilon \mathbf{E}^{\text{sc}} \tag{3.6}$$

where $\mathbf{E}^{\text{sc}}$ is called the space-charge field and is a parameter of the crystal that only depends on the geometry of the illumination. The establishment of this steady-state is responsible for the photorefractive response time τ_{PR}. Its expression is given by (see appendix A):

$$\frac{1}{\tau_{\text{PR}}} = \frac{\Phi_0 e^2}{\epsilon k_B T}\left(\alpha_n + \alpha_p\right)\left(\frac{\Delta k^2}{k_D^2} + 1\right) \tag{3.7}$$

where ϵ is the dielectric permittivity of the material, e is the electron charge and k_D is called the Debye wave-vector and is expressed as:

$$k_D^2 = \frac{e^2}{\epsilon k_B T} N_{eff} \tag{3.8}$$

where N_{eff} is the effective density of centres:

$$N_{eff} = \frac{N^0 N^+}{N^0 + N^+} \tag{3.9}$$

In steady-state, the modulated part of the photoinduced electric field is given by:

$$\mathbf{E}_{loc,1} = -i\left\langle\varepsilon\right\rangle_{\tau_{\text{PR}}} \frac{k_B T}{e} \xi_0 \frac{\Delta\mathbf{k}}{1 + \dfrac{\Delta k^2}{k_D^2}} \tag{3.10}$$

where "$\langle\rangle_{\tau_{\text{PR}}}$" stands for the average value over the photorefractive response time: moving fringes are "blurred" by the crystal if moving faster than τ_{PR}. Interestingly, the photorefractive response time is inversely proportional to the average light irradiance so that the higher it is, the faster the

crystal is. ξ_0 is called the hole-electron competition factor the value of which is between –1 and 1 depending on the wavelength among others. This latter coefficient is here to take into account the fact that displacements of electrons and holes have opposite influence on the local electric field. If $\xi_0 = 1$, only electrons are photoexcited whereas if $\xi_0 = -1$ only holes are. If the two phenomena are equivalent, the hole-electron competition factor is equal to zero and there is no photoinduced electric field. The presence of the factor i means that the photoinduced electric field is phase-shifted by $\pi/2$ compared to the illumination pattern. In this case, the photorefractive effect is referred to as a "non-local" phenomenon. By applying an external electric field, it is possible to compensate this phase-shift.

The photoinduced electric field generates a modulation Δn of the refractive index:

$$\Delta n = n_1 \sin\left(\Delta \mathbf{k} \cdot \mathbf{r}\right) \tag{3.11}$$

where $n_1 = -\frac{1}{2} n_0^3 r_{eff} \mathcal{R}\left(i E_{loc,1}\right)$. Here r_{eff} is the effective electrooptic coefficient seen by the beams that depends on the crystal orientation, the fringes wave-vector direction and the polarization of the two beams. In the manuscript, the crystal I use is cut so that the effective electrooptic coefficient sign changes by π-rotating the crystal along its vertical axis.

3.2.2 Two-wave mixing process

The two beams that created the refractive index grating will diffract on it. As a direct consequence, the Bragg condition is automatically verified. Part of the reference will diffract in the direction of the signal beam and reciprocally. In case of small modulation, diffraction by an index grating leads to a $\pi/2$ phase-shift for diffracted beams. Because the refractive index grating is phase-shifted compared to light the two beams have a additional phase-shift of $\pm\pi/2$ depending on the incoming direction and the sign of the effective electrooptic coefficient. As a consequence, the diffracted beam in a given direction can be either in-phase ($\pi/2 - \pi/2 = 0$, constructive interferences) or out-of-phase ($\pi/2 + \pi/2 = \pi$, destructive interferences) compared to the transmitted one in this same direction. It results in an energy transfer from a beam to the other that can be modelled through coupled equations and solved thanks to a perturbation approach as developed by H. Kogelnik [120]. This phenomenon is called two-wave mixing (TWM) and was represented on figure 2.6 of chapter 2. The figure is also represented hereunder for convenience purpose.

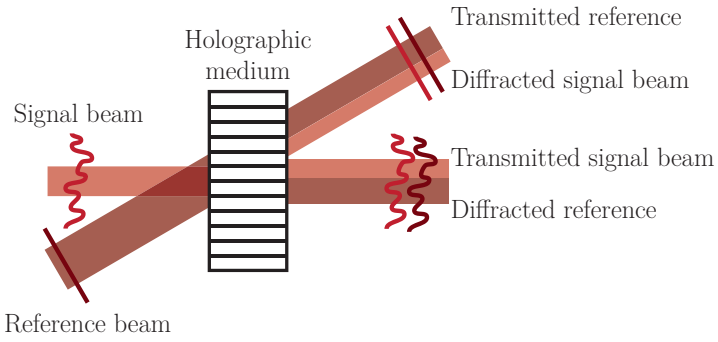

Figure 3.5 – Schematic of TWM process.

For small modulation depths, which is typically the case when working with scattered light, it can be considered that the loss in energy of the reference beam due to TWM is negligible. In this case, the only reference decay is due to absorption and the coupled equations that drive the

TWM process can be simply written as [121, Chapter 4]:

$$\begin{cases} \dfrac{\partial E_S}{\partial z} &= \left(\gamma - \dfrac{\alpha}{2}\right) E_S \\ \dfrac{\partial E_R}{\partial z} &= -\dfrac{\alpha}{2} E_R \end{cases} \tag{3.12}$$

where α stands for the crystal absorption coefficient and γ stands for the photorefractive gain in amplitude defined as:

$$\gamma = \frac{\pi n_0^3 r_{eff}}{2i\lambda \cos\theta} E^{\text{sc}} \tag{3.13}$$

where E^{sc} is the modulus of the space charge field. These equations can be solved and lead to the expression of the irradiance in each direction after the crystal:

$$\begin{cases} \Phi_S(z) &= \Phi_S(0) \exp\left[(\gamma_{\text{PR}} - \alpha) z\right] \\ \Phi_R(z) &= \Phi_R(0) \exp\left(-\alpha z\right) \end{cases} \tag{3.14}$$

where $\gamma_{\text{PR}} = 2\gamma$ is the photorefractive gain in energy that was already mentioned in section 2.4.3 of chapter 2. Under the approximation that high values of average irradiance are used on the crystal so that thermal energy can be neglected, the photorefractive gain is constant and is referred to as the saturated gain. When it is not true, the gain increases with the average irradiance on the crystal as shown in appendix A.

3.2.3 Detecting tagged photons

For small diffraction efficiency and negligible absorption, L.-A. De Montmorillon *et al.* [122] show that the transfer function H of the crystal in terms of amplitude is given by:

$$H(L,t) = \gamma L \frac{\exp\left(-\dfrac{t}{\tau_{\text{PR}}}\right)}{\tau_{\text{PR}}} \tag{3.15}$$

where L is the crystal thickness and τ_{PR} is the photorefractive response time on the crystal surface. Because the ultrasonic pulse propagates through the whole sample over few tens of µs, temporal variation of acousto-optic signal is also of the same order of magnitude. It is then not possible to tune the reference on tagged photons frequency for the hologram changes too fast to be properly engraved. The theoretical study of photrefractive detection can be found in [79] in this case. The electric field after the photorefractive crystal can simply be expressed as:

$$\mathcal{E}_D(\mathbf{r}', t) = \mathcal{E}_S(\mathbf{r}', t) + \mathcal{E}_S(\mathbf{r}', t) * H(L, t) \tag{3.16}$$

where $*$ stands for the convolution product. In such a case, the signal measured on the photodiode is proportional to the light irradiance integrated over a single-detector of surface S:

$$s_{\text{PD}} \propto \int_S \Phi_D(\mathbf{r}', t)\, \mathrm{d}\mathbf{r}' \tag{3.17}$$

which was derived in appendix A:

$$s_{\text{PD}} \propto S E_0^2 \left[(1+\gamma L)^2 - \gamma L \frac{\varepsilon^2(t)}{2}\right] \tag{3.18}$$

The DC-level corresponds to the untagged photons signal that undergoes TWM whereas the AC-component corresponds to the portion of photons that does not properly participate to TWM because they were tagged. Recording the AC-component thus gives the acousto-optic signal proportional to the tagged photons power. Typical shapes of acousto-optic signals change depending on the sign of the photorefractive gain. For positive gain, TWM process is in the so-called amplification regime in which untagged photons signal is amplified and the presence of tagged photons is detected through a decrease of the overall irradiance. Otherwise, the process is in the so-called attenuation regime in which untagged photons signal is attenuated and the presence of tagged photons is detected through the increase of the overall irradiance.

Interestingly, when the absolute value of the gain is high, it is preferable to work in a negative gain regime in which the noisy background is reduced – this remains true as long as the electronic noise can be neglected. In practice, a small amount of the reference beam scatters inside the crystal on defects, surface roughness, index inhomogeneities or impurities for instance. This scattered reference also undergoes TWM so that this unwanted light is also amplified in case photofrefractive gains are positive. This phenomenon is called photorefractive beam fanning [121,123] and increases the unwanted light background. In practice, this effect is the predominant source of noise in photorefractive-crystal-based acousto-optic imaging so that another interest of working in the negative gain regime is that beam fanning is reduced.

3.2.4 Application to acousto-optic imaging

The previous sections showed that the main interest of using photorefractive crystals is that it allows self-adapting interferometry provided that the speckle decorrelates slower than the photorefractive response time. Because the wave-fronts are identical after the photorefractive crystal, the measured modulation increases as the square-root of the number of speckle grains collected within the crystal optical *etendue*. The main criteria driving the choice of the photorefractive crystal are then its spectral range, its photorefractive gain, its response time and its size. A proper crystal should work within the optical therapeutic window with high photorefractive gain and a characteristic response time under 1 ms. In order to measure decent acousto-optic signal, its optical *etendue* should be as large as possible while being as thick as possible in order to ensure big interaction volumes and optimal TWM[1].

The working wavelength of the crystals depends on the impurities and defects that can be found inside. It must be high enough to excite the centres, but under the band-gap wavelength in order not to excite electrons from the valence band directly to the conduction one. This thus defines the working range of the crystals. Regarding acousto-optic imaging, several crystals were considered such as BSO under an DC-electric field (working at 532 nm) [97, 124] or AsGa in infrared (working at 1064 nm) [112]. The main drawback of these materials is that they do not work around the centre of the optical therapeutic window: green light is strongly absorbed by blood whereas infrared is absorbed by water. In order to overcome this difficulty, S. Farahi tested several materials working around 800 nm such as Cu:BGO, V:ZnTe, Mn:ZnTe and Te:SPS [118]. The conclusion of this exhaustive work was that Te:SPS working around 780 nm gave the best compromise in terms of low response time and high gain.

Our SPS crystals are provided by A. A. Grabar from Uzhgorod University in Ukraine. Thanks

[1] In the amplification regime, it exists an optimal crystal thickness for best amplification. When crystal is thick, the decay of the reference due to TWM can not be neglected anymore and the process stops as soon as the reference beam energy is equal to zero. Beyond this point, only absorption remains and all beams start being attenuated. This effect is less inconvenient in the attenuation regime in which one aims at attenuating unwanted beams.

to a frequency shift method previously developed by M. Lesaffre *et al.* [125], I characterized three of these crystals (numbered crystals 1, 2 and 3) in terms of gain and response time in order to select the most appropriate one for a multi-modal imaging device. The results are plotted on figure 3.6. The crystals bandwidth – inverse of the characteristic response time τ_{PR} – and the gain in the diffusion regime (no applied electric field) are plotted as a function of the average irradiance ($W \cdot cm^{-2}$) on the crystal surface. Figure 3.6(a) shows a gain saturation regime beyond 1.6 $W \cdot cm^{-2}$, reaching a high value of about 7 cm^{-1} for crystal 1. According to figure 3.6(b), the photorefractive bandwidth is increasing linearly with the average irradiance on the crystal surface, as predicted by the band-transport model. The photorefractive time τ_{PR} can be as short as 3 ms for crystal 1, almost compatible with correlation time of living tissues. Further study of the physical properties of such crystals is not the point of this manuscript, but a lot of deeper characterizations can be found in papers such as [126] or [127]. In the following, I will use crystal 1 all along the rest of the manuscript. Its thickness is 0.7 cm.

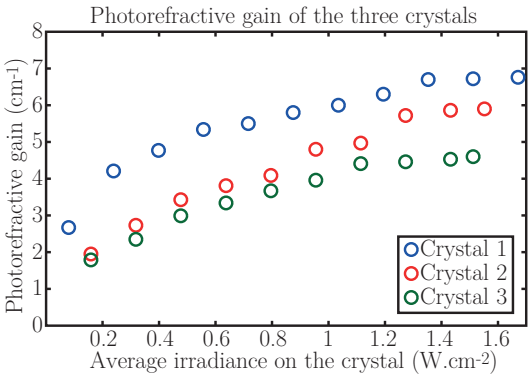

(a) Photorefractive gain

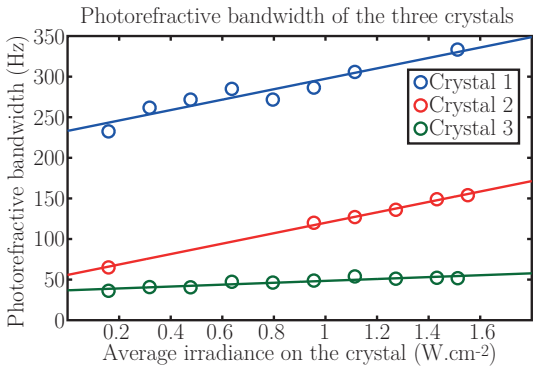

(b) Photorefractive response time

Figure 3.6 – Characterization of the basic properties of our photorefractive crystal according to the method developed by M. Lesaffre *et al.* [125]. (a) Photorefractive gain as a function of the average light irradiance on the crystal. (b) Photorefractive bandwidth as a function of the average light irradiance on the crystal.

3.3 Bimodal imaging of *ex vivo* liver tumours

One of the major fields of application that was thought of for acousto-optic imaging is early-stage cancer diagnosis. It is then no surprise that the first tests that were performed with our bimodal imaging platform concern tumours detection. The bimodal imaging platform is shown on figure 3.7. The first results presented in this section were obtained together with E. Benoit who initiated the development of the platform. This work was performed as part of a collaboration with V. Servois and P. Mariani from the Institut Curie.

Despite improvements in preoperative imaging (Magnetic Resonance Imaging (MRI), Positron Emission Tomography, ultrasound) and surgical techniques, detection of small hepatic tumours - of diameter typically smaller than 5 mm - remains difficult during both preoperative and intraoperative processes. The small contrast in acoustical properties between healthy tissues and small tumours contributes to current detection failures.

3.3.1 Uveal melanoma

Uveal melanoma is the most common ocular tumour in the adult Caucasian population. It is a melanoma that develops inside the pigmented region of the eye so-called uvea. Uvea is the middle layer between the retina and the sclera that contains three parts: the iris, the ciliary body and the choroid. Uveal melanoma leads to liver metastases through mechanisms that are not well understood in 50% of cases after a mean interval of three years. Once hepatic metastases develop, life expectancy is reduced to less than six months even after the eye tumour is destroyed (mostly through radiotherapy). When possible, complete surgical resection of liver lesions is the only way to improve patients' survival [128]. In order to avoid unnecessary invasive surgical procedures, it is fundamental that surgeons benefit from reliable imaging techniques. Currently, they face two major issues. On the one hand, small liver melanoma metastases have very low acoustical contrast so that their location is difficult to assess precisely during intraoperative processes. It results in the resection of liver portions far bigger than needed. On the other hand, detection of small liver sub-capsular lesions – near the liver surface, few centimetres deep inside the human body – during preoperative processes remains difficult for they are located in a noisy region for MRI. Their profusion is consequently often underestimated [129].

In the case of uveal melanoma metastases, tumours are often highly pigmented with a dark colour due to an abnormal presence of melanin deposits – though the variable quantity of melanin may change optical aspect from one tumour to another. This aspect which is visible through naked eyes usually fits the anatomopathological limits of the tumour. It suggests that optical contrast – both absorption and scattering properties – could be of prime interest for tumours detection during both preoperative and intraoperative processes. It has been recently shown that green indocyanine can be used as a contrast agent during surgical procedures in order to enhance optical contrast provided a proper imaging system working in the near-infrared spectral region is used [130]. Thanks to this method, the surgeon detected additional tumours that were not primarily detected through conventional means – naked eye, palpation and intraoperative ultrasound. Thereby, optical-contrast-based techniques could be a good alternative to overcome detection failures of both ultrasound during intraoperative processes and MRI during preoperative imaging. However, such approaches are limited to superficial lesions because of multiple scattering. In this way, optical detection of deeper ones remains a challenging issue and acousto-optic imaging coupled to ultrasound could be a convenient alternative.

3.3.2 Results on liver biopsies

The imaging setup

Our setup is a photorefractive-based acousto-optic imaging setup using crystal 1 defined in the previous section, coupled with a commercial ultrasound scanner (Aixplorer, SuperSonic Imagine, Aix-en-Provence, France). The scanner drives a linear probe – 8 MHz central frequency, 256 elements; 0.2 mm pitch (SL15-4, SuperSonic Imagine, Aix-en-Provence, France) – for multi-modal imaging purpose, providing both optical contrast and ultrasound images. The conventional ultrasound scan called Bmode is directly provided by the commercial mode of the Aixplorer system with a resolution of 200 μm^3.

The acousto-optic sequence is built of consecutive focused lines sequentially emitted in front of each probe transducer, just as it is the case for a conventional Bmode. The number of lines varies depending on the horizontal range of the acousto-optic image, but each line is generally averaged several thousands of times. The probe aperture is set equal to 20 mm while the ultrasonic focal

point is 20 mm deep, leading to a lateral size of the pulse at the focal point of 200 µm (y-axis). Besides, in the elevation direction (perpendicularly to the array, z-axis, corresponding also to the light propagation direction), the probe geometrically focuses the ultrasound at 20 mm giving a typical size of 200 µm at the focal point, thus defining the z-axis resolution (200 µm). The sequence was used with a 4-cycles long emission, giving a 0.5 µs lasting pulse which corresponds to a spatial length of 750 µm (x-axis).

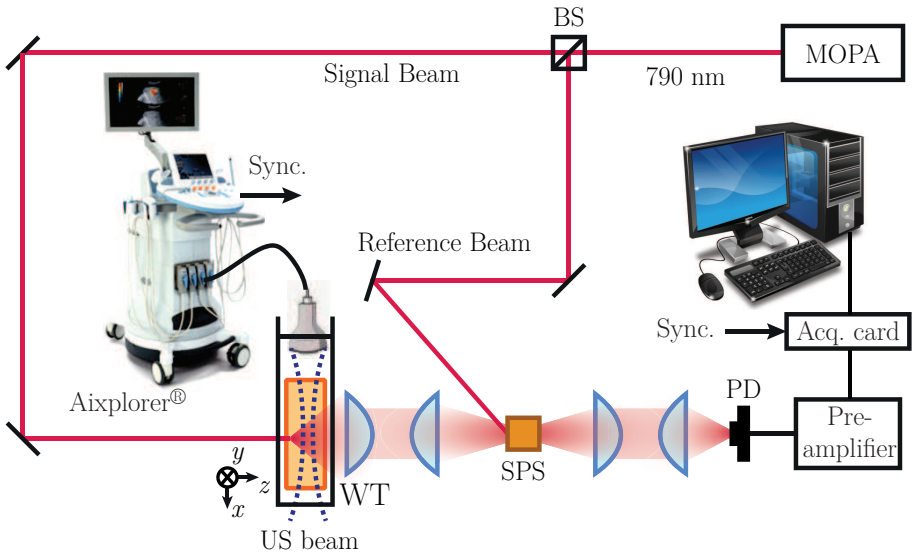

Figure 3.7 – The bimodal ultrasound/acousto-optic imaging platform. WT: Water tank, MOPA: Master Oscillator Power Amplifier, BS: Beam splitter, PD: Photodiode.

The setup is shown on figure 3.7. It consists in a semi-conductor laser diode (LD) emitting at 790 nm, amplified with a 2 W tapered amplifier (TA, Sacher laser technik – GmbH). These two make a Master Oscillator Power Amplifier (MOPA). Amplified light is split into two beams thanks to a polarization beam splitter (PBS): the signal and reference beams. The signal beam goes into a Plexiglas water tank – for acoustical contact – inside which the sample is placed. The transmitted light is collected with high aperture lenses and interferes with the reference beam on a SPS crystal (PRC) in order to build the hologram and perform self-adaptive holography.

The time-varying transmitted beam after the crystal is then measured on a Si-photodiode (PD, Thorlabs PDA 36A-EC) with a detector surface of 10 mm^2, amplified thanks to a large bandwidth pre-amplifier (DHPVA-100, FEMTO Messtechnik - GmbH) and acquired thanks to an acquisition card (Acq. Card, ADLink PCI-9846, 14 bits depth, 40 MHz sample rate). The acquisition rate of the acousto-optic signal is 40 MS/s leading to a pixel size in the acousto-optic image of 37.5 µm along the x-axis whereas it is equal to 200 µm along the y-axis – which is the probe pitch value. The synchronization of this card with the ultrasonic pulse is ensured by the ultrasound scanner (Sync.). Images are then obtained by scanning the ultrasound focus within the sample and stacking the different acousto-optic in-line signals one after another, the lines being spatially separated one from another by the probe pitch. Each line is pulsed 1000 times in a row for averaging purpose. It lasts about 100 ms to acquire one line averaged 1000 times, leading to acousto-optic ultrasound sequence times varying from 10 to 15 s depending on the size of the image. In practice, the buffer of the acquisition card does not allow to store the entire image so that data must be transferred after each line. It results in a complete imaging time of the order of several minutes. However, such an issue can be addressed for instance by streaming the data during waiting delays (ultrasound propagation, hardware and cooling delays...).

The setup was used on *ex vivo* human liver samples containing melanoma metastases. In order to provide a scattering surrounding medium so that this optical contrast was not accessible through naked eyes, biological samples were embedded within a gel matrix mimicking biological tissues. This gel matrix is an agar gel mixed with Intralipid-10%, optical properties of which are provided in [25]. Using the equation the authors derived thanks to Mie theory and assuming agar scattering is weak compared to Intralipid-10%, the concentration of the latter is calculated in order to obtain the required reduced scattering coefficient (10 cm^{-1} in the following). In general, absorption in such gels is negligible (about 0.1 cm^{-1}).

Agar is dissolved into hot water at 90°C and Intralipid-10% is added once the mixture has cooled down to 60°C or less. The liquid gel is then poured on the biological sample at the lowest temperature possible before solidification (that is to say over 45°C) so that it completely embeds the liver piece, placed approximately in the middle, without altering it. For the following sections, the gels dimensions are $4 \times 4 \times 4$ cm^3. The gel fabrication protocol will be the same all along the remaining of the manuscript.

Samples studied in the following were removed from different patients with previous history of uveal melanoma and about whom liver metastases were suspected. Tumours were located near the liver surface and the tumorous nature of tissues was diagnosed and histologically proved by physicians. It is worth being mentioned that all examinations described in the following are part of the usual clinical procedures.

Imaging a wire-shaped microbiopsy

The first sample was obtained thanks to a percutaneous microbiopsy that was removed from a bigger tumour previously located through X-ray scans. It is a 10 mm long and 1 mm large by 1 mm thick wire-shaped microbiopsy with black areas corresponding to melanin deposits inside the tumour. The sample was placed in the middle of a $4 \times 4 \times 4$ cm^3 agar-agar hydrogel mixed with Intralipid-10% as previously described in order to provide a scattering environment and mimic scattering properties of biological tissues.

The liver biopsy sample is observed through classical ultrasound imaging inside the optically scattering gel (figure 3.8(a)). Raw acousto-optic data are presented on figure 3.8(b). This image was obtained using the acousto-optic sequence described in the previous section. Because of scattering, the light irradiance within a transverse cut plane along the (x, y) directions at a given distance from the source presents a diffusion pattern that obeys equation 1.8 given in section 1.3.1 of chapter 1. In the case of a homogeneous scattering medium the scattered light shape is then:

$$\Phi_s(r) \propto \frac{\exp(-\mu_{\text{eff}} r)}{r} \tag{3.19}$$

Since the surrounding medium is mostly homogeneous, a correction envelope of the light scattering pattern can be performed by using the following equation:

$$I_{\text{corr}} = \log\left(\frac{I_{\text{th}}}{I_{\text{AO}}}\right) \tag{3.20}$$

where I_{corr} is the corrected image, I_{th} stands for the theoretical 2D scattered light irradiance profile without any liver sample and I_{AO} stands for the raw acousto-optic image. The optical contrast as it is defined above is then related to a difference of effective attenuation. This correction gives an optical contrast taking the optical properties of the homogeneous gel as a reference. It has to be taken into account that this simple modelling is only suitable for samples embedded within homogeneous media of constant effective attenuation coefficient. For further experiments on real

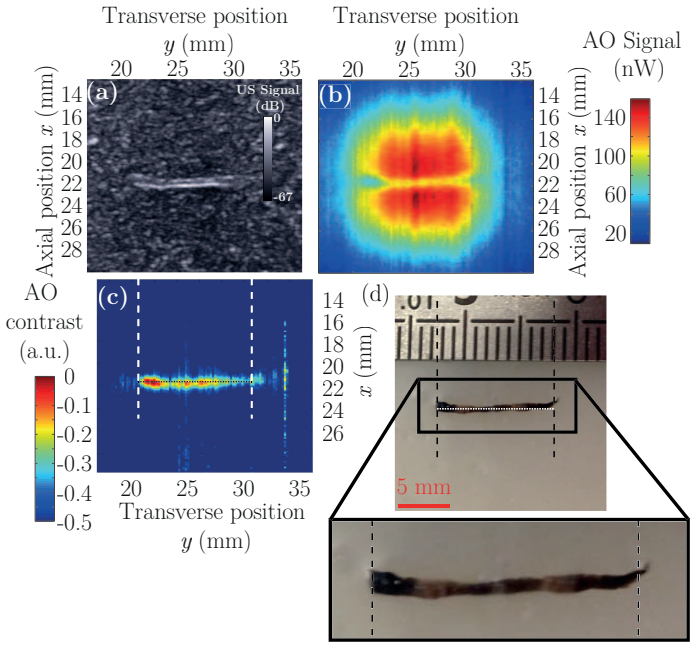

Figure 3.8 – Representation of *ex vivo* results on the wire-shaped microbiopsy (a) Ultrasound image. The different portions composing the microbiopsy are not visible. (b) Raw acousto-optic image. (c) Acoutso-optic image on which the scattered light irradiance profile has been removed. It is now possible to distinguish the different portions. (d) Picture of the sample with zoom on the microbiopsy. It consists in pale portions (healthy liver) and black portions (melanin deposits).

livers, other techniques may be investigated in order to derive a theoretical 2D scattered light profile that takes into account inhomogeneity or anisotropy, such as Monte Carlo algorithm [131]. Moreover, this optical contrast contains both scattering and absorption effects for we are not technically able to discriminate one from another yet as it was explained in the previous chapters.

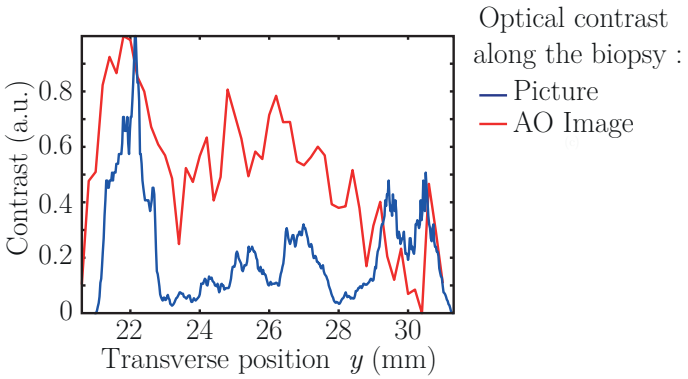

Figure 3.9 – Profile along the microbiopsy between the dashed lines on the picture (blue) and on the acousto-optic image (red). These curves confirm the consistency of the acousto-optic image with the picture.

The acousto-optic image in which the scattered light irradiance profile has been removed thanks to the correction envelope given above is presented on figure 3.8(c). Contrary to what is displayed on the ultrasound image, different portions are clearly appearing with a resolution of the order of one millimetre and correspond to the melanin deposits visible on figure 3.8(d). A profile along the sample has been plotted on figure 3.9 in order to ensure that these regions are consistent with the microbiopsy. The red and blue lines are plotted along the horizontal dotted lines visible on

figure 3.8(c) and 3.8(d) and correspond respectively to the acousto-optic and the picture profiles. The profile from the picture was obtained by using the negative grayscale picture that only retains luminance information and both profiles were normalized in order to ease comparison. One can see that the two curves follow the same tendency, which shows the consistency of the acousto-optic result.

Imaging a thicker biopsy

The tumours on this second sample were close to the surface enough so that they were detected through naked eyes and surgically resected. This is a thicker biopsy sample of dimension $2 \times 1 \times 1$ cm^3 containing two visible spherical black melanoma metastases with a diameter of about 2 mm. Each of them was diagnosed as tumorous tissues through histology.

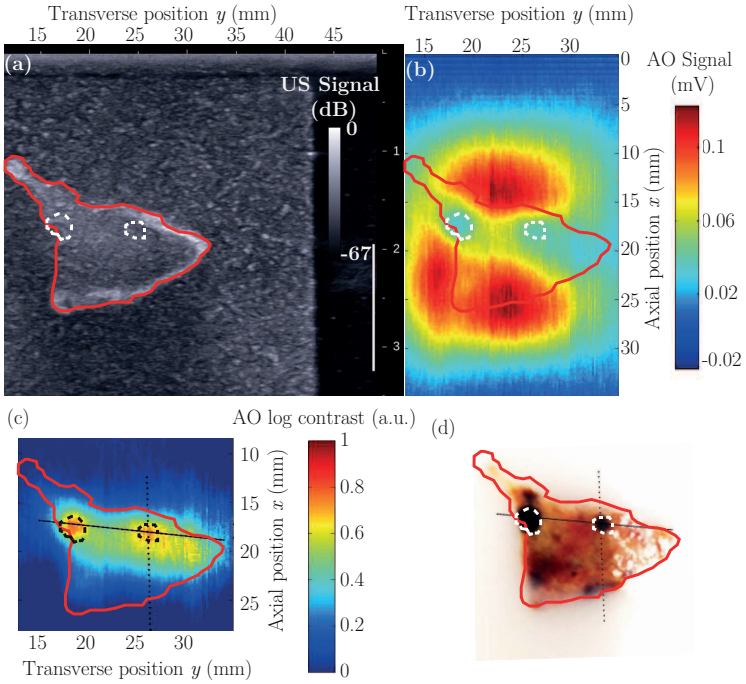

Figure 3.10 – Representation of *ex vivo* results. The tumours are circled with a white dashed line and reported on the different images. (a) is the ultrasound image; acoustical contrast inside the liver sample is not significant. The liver extent has been delimited in red and reported on the other images. (b) is the acousto-optic image; the optical contrast is not easily interpreted but it seems that several regions appear. (c) is the optical contrast; the scattered light irradiance profile has been removed and the two tumours appear. (d) is a picture of the liver sample showing the black tumours.

The ultrasound image of this biopsy embedded in the same kind of optically scattering gel matrix as before (also $4 \times 4 \times 4$ cm^3) is presented on figure 3.10(a). Figure 3.10(b) presents the corresponding acousto-optic image. The biopsy sample is delimited by the red solid line. The acousto-optic image was corrected the same way as before, resulting in a contrast enhancement, and displayed on figure 3.10(c). White dashed circles report the position of the two metastases visible on the photograph (figure 3.10(d)) on the other pictures for easier location.

The acousto-optic section that was plotted in arbitrary units from the plain black line on figure 3.10(c) and 3.10(d) is presented on figure 3.11(a). Images were rescaled in order to match dimensions. Figure 3.11(a) exhibits higher acousto-optical losses at the tumours positions (pointed out with black arrows) thus ensuring that the tumours that are not visible through ultrasound

were detected. Figure 3.11(b) presents the vertical profile (black dotted line on figure 3.10(d) and 3.10(c)) of the second tumour. It seems here that the vertical resolution is degraded compared to what was expected according to the ultrasound parameters. It may be due to the photodiode bandwidth, narrower than the ultrasound pulse one. The photodiode bandwidth is intrinsically linked to its gain. It was increased up to 30 dB here due to the sample being thicker than the microbiopsy, thus corresponding to a 260 kHz bandwidth at –3 dB. The corresponding degraded resolution is not straightforward to derive for the exact shape of the frequency response is not known but it can be estimated to about 4 to 5 mm. It is to be noted that the horizontal resolution of the second tumour (on the right on figure 3.11(a)) seems to be also degraded. It may be due to several reasons. Among others, it may be possible that it does not exactly follow the picture profile. Here for instance, there is a reflection on the picture in this area, leading to an artificial increase of the luminance. It may also be due to the fact that the end of the liver is located near an edge of the scattered light profile. The corrected image is therefore obtained through a low theoretical background divided by a low acousto-optic signal so that the result is mostly noise in this region.

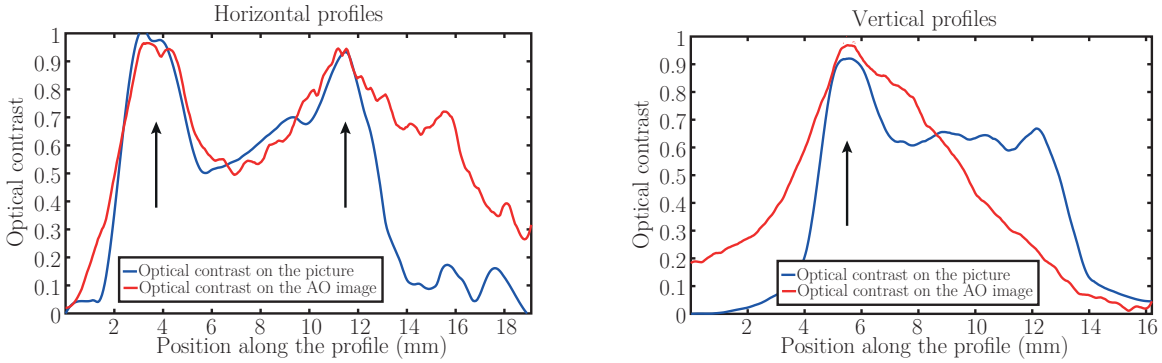

(a) Horizontal profile (b) Vertical profile

Figure 3.11 – Profiles along the black lines shown on the two pictures on figure 3.10(c) and 3.10(d). (a) exhibits profiles along the plain line. The blue profile is plotted from the photograph, the red one from the acousto-optic image; both profiles are plotted from left to right. (b) vertical profiles along the dotted line from top to bottom. The colours are the same as for (a).

In order to verify the depth-resolution capabilities of the technique, a 3D image was reconstructed by stacking several planes of the biopsy one after another. The imaged planes were taken every 0.5 mm along the z-axis from the surface up to 7 mm inside the biopsy. A section of the left tumour along the plane constituted by the ultrasound and light propagation axes – (y, z) plane – is represented on figure 3.12. The extent of the tumour inside the liver can be estimated from such a section (to about 2 mm from the full width at half maximum for instance). Such depth-resolved images can not be obtained through conventional optical imaging and show the main advantage of using acousto-optic imaging in order to better target areas to remove in the three-dimensions.

A light tumour

The third sample of this section was also surgically removed. The interesting point about this biopsy is that the tumour has a light aspect contrary to the previous ones, probably because of lower amount of melanin deposits (see the picture on figure 3.13(d)). Though the naked-eyes aspect of the tumour can not be easily correlated to the real optical properties, this tumour is *a priori* less absorbing than the previous ones and its white milky aspect could be associated to a

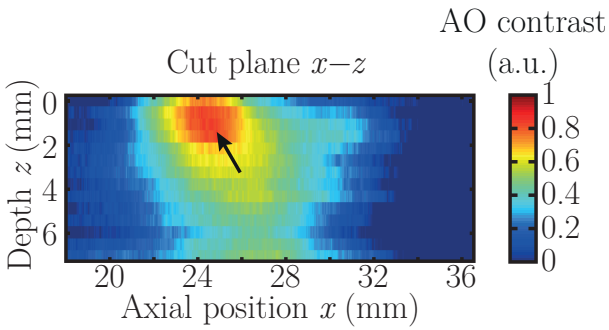

Figure 3.12 – Section of the left tumour along the plane constituted by the ultrasound and light propagation axes. The tumour is appearing and its extent inside the liver can be estimated to about 2 mm.

more scattering region. The liver biopsy is about $2 \times 0.5 \times 0.5$ cm^3 and embedded inside the same kind of gel as before. Figure 3.13(a) shows the corresponding ultrasound scan. By coincidence, the acoustical contrast between the tumorous region and the gel matrix is weak so that the tumour is not easily seen – though a physician's trained eye would probably detect it. Figure 3.13(b) shows the acousto-optic image of the biopsy. Here the whole sample is clearly appearing because optical contrast between the sample and the gel matrix is significant. Figure 3.13(c) shows the acousto-optical contrast extracted from the acousto-optic image in which the scattered light background has been removed. The tumorous region is appearing here as a region of higher contrast.

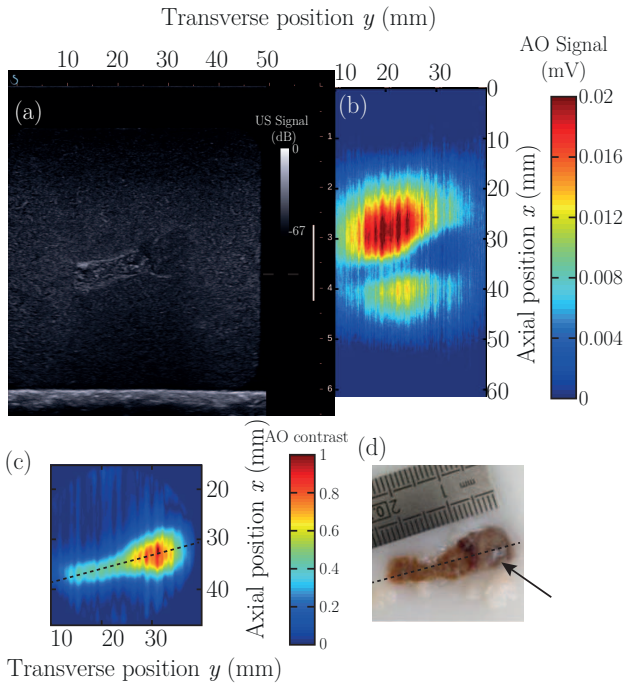

Figure 3.13 – Representation of *ex vivo* results. The tumour is the light region pointed out with a black arrow. (a) is the ultrasound image; by coincidence, the acoustical contrast is not very significant between the tumour and the gel matrix so that the tumour is hardly visible. (b) is the acousto-optic image; the whole liver sample, tumour included, is clearly appearing because of optical contrast between the liver and gel matrix. (c) is the optical contrast; the scattered light irradiance profile has been removed and the tumour appears as a region of higher optical contrast. (d) is a picture of the liver sample showing the light tumour (black arrow).

A profile of the acousto-optical contrast and the negative grayscale picture of the biopsy is presented on 3.14. The blue curve corresponds to the picture profile whereas the red one cor-

responds to the normalized acousto-optic contrast. The blue curve was scaled so that the level of signal corresponding to the healthy liver are equivalent in both profiles. The tumorous region clearly appears through the increase of acousto-optical contrast. Interestingly, the tumour does not appear on the profile of the grayscale picture of the biopsy.

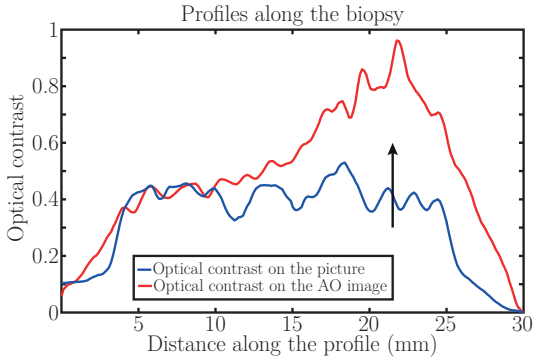

Figure 3.14 – Profile along the dashed lines on the picture (blue) and on the acousto-optical contrast image (red). The tumorous area is clearly appearing through the increase of acousto-optical contrast. The light tumour does not appear on the profile of the negative grayscale picture.

3.3.3 A discussion about acousto-optic imaging and uveal melanoma

It has to be considered that these first results are optical contrast images and do not provide a quantitative value for optical properties. This issue is quite similar to what one faces with ultrasound scans that do not return quantitative measurements of sound velocity within the different regions of a medium but interfaces between regions of different sound velocities, which is somehow a sound velocity contrast. Here, regions of different optical properties are imaged though a quantitative value for these properties is not provided. Since the surrounding sample is homogeneous here, it is easier to use it as a reference for optical contrast.

Liver samples were embedded within homogeneous gel matrices providing a scattering environment. The chosen optical properties of the gels here are usually used to mimic breast tissues, but, as human liver is surrounded by perihepatic structures composed with fat and connective tissues, this choice is also relatively relevant here. Nevertheless, gels homogeneous characteristics are not representative of real hepatic surroundings and issues will probably appear when dealing with real livers due to the very high vasculature of this region.

In these first results, tumours that presented optical contrast observable through naked eyes were also observed thanks to acousto-optic imaging. Though ultrasound scans fail to detect the tumours, they are useful in order to locate the liver sample and make consistencies between optical contrast seen through naked eyes and acousto-optical one. The study presented in this section was performed in a transmitted light configuration for it *a priori* enables collecting more tagged photons. Obviously, this configuration is not suitable for clinical applications so that a back-scattered light configuration may be preferred in the future. Further long-term studies may provide more complete results on more diverse samples in order to assess the limit of detection, the sensitivity and the specificity of the technique.

These first *ex vivo* results show that acousto-optic imaging is able to access optical contrast in biological samples far beyond the transport mean free path of the surrounding medium. Acousto-optic images provide complementary information to ultrasound images, though the main results showed that they are not easy to interpret alone. Acousto-optic imaging was able to locate regions

that were not ultrasonically detected so that this bimodal platform may offer a complementary imaging solution in case of ultrasound detection failure.

In the case of uveal melanoma, multi-modal acousto-optic/ultrasound imaging may provide an efficient non-invasive technique that would help physicians to carry their diagnoses out. It could therefore be possible to adjust treatments to patients thanks to a better detection. Patients with few metastases may be surgically treated whereas patients with a lot of them may be treated thanks to chemotherapy or targeted therapy. These results draw the very first step toward clinical acousto-optic imaging. For medical purpose, *i.e.* better treatment of uveal melanoma metastases, the long-term goal is to detect small tumours (with a diameter of 5 mm or less) in the liver using a back-scattered light configuration so that their number can be precisely estimated.

3.4 What next for bimodal imaging?

The previous promising results gave a good idea of the capabilities and areas of improvement of such a multi-modal platform. I suggest to discuss a few other options that were explored during my PhD in this section. Though the next experiments are just at the state of very first proofs of concept and a lot of points are still needed to be fully understood, they make a few suggestions of directions to explore in the future.

3.4.1 Quantitative imaging

It appeared during the uveal melanoma study that the scattered light shape makes acousto-optic images very hard to interpret and sometimes contributes to undetected objects. In the previous section, this issue was overcome by removing the scattered light envelope through a fit of its predicted behaviour. However, such an approach is obviously limited to small objects embedded inside homogeneous matrices or needs full modelling of light propagation inside complex biological structures. Such results then brought into light the necessity of improving the image reconstruction technique and converging toward quantitative imaging. The resolution of the acousto-optic inverse problem in order to recover both absorption and scattering coefficients is currently being explored [132] but the resolution of this problem inside a complex scattering medium such as biological tissues is not easy. Awaiting such promising developments, other methods to get rid of this unwanted light envelope may be explored.

One possible way could be to perform acousto-optic imaging at several wavelengths in order to extract only spectral features, independent from the value of the local light irradiance. This approach was suggested by C. Kim and L. V. Wang in 2007 [133]. Another way that can easily be set on a commercial ultrasound scanner was suggested by P. Lai *et al.* [134] and consists in using two different ultrasound pressures – a more complete description of the technique can be found in the PhD thesis of P. Lai [135]. It can be easily deduced from what was shown in chapter 2 that the ratio between two acousto-optic images obtained by using two different ultrasound pressures only depends on the optical properties of the sample and the chosen pressures. The authors suggest in their paper that such a contrast may mostly depend on the transport mean free path in the sample and developed a technique that measured quantitative reduced scattering coefficients in purely scattering media after calibration. Though the influence of the inclusion absorption still needs to be clarified, such an approach is a simple way of removing the scattered light shape from acousto-optic images.

Figure 3.15 shows an example of pressure contrast imaging performed with our multi-modal imaging platform. The sample is an absorbing cross in which Intralipid-10% was diluted into an

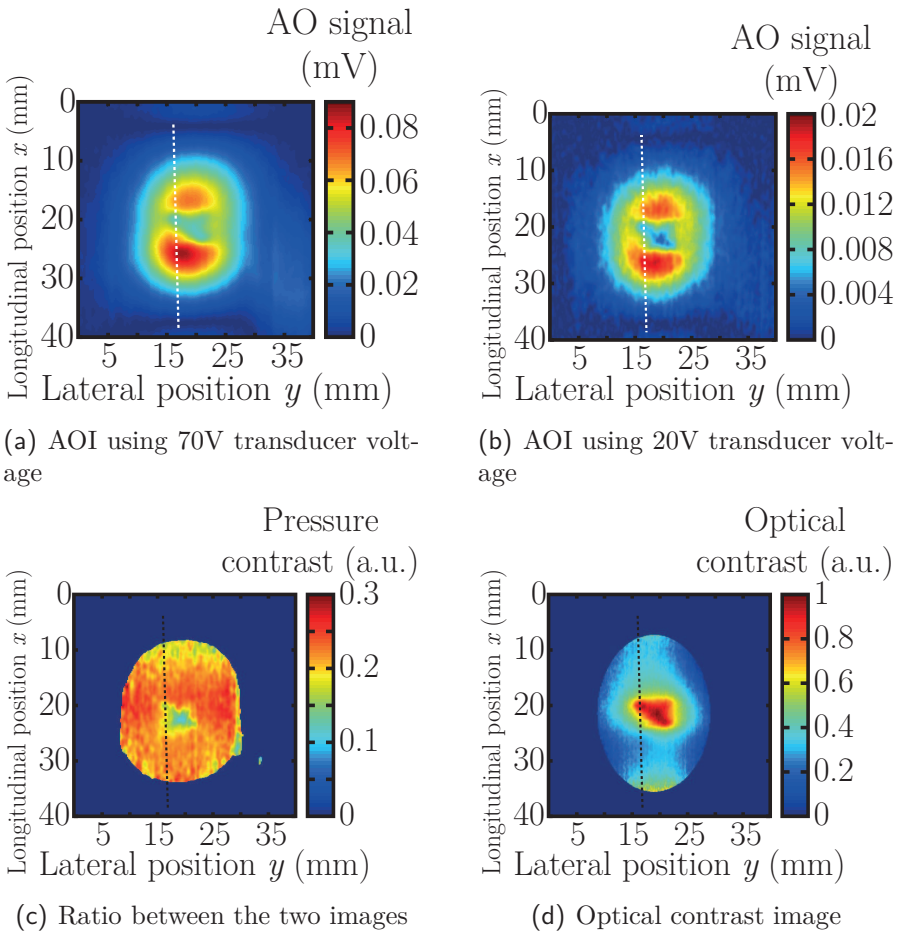

(a) AOI using 70V transducer voltage

(b) AOI using 20V transducer voltage

(c) Ratio between the two images

(d) Optical contrast image

Figure 3.15 – Example of pressure contrast imaging on an absorbing and less scattering inclusion. (a) Acousto-optic image with 70V transducers voltage. (b) Acousto-optic image with 20V transducers voltage. Because the noise in the pressure contrast image increases very fast with the noise of the different images, each one was horizontally and vertically smoothed over 1 mm. The ratio between the two images is presented on (c). The scattered light dependence is removed and the cross is visible on a flat background. Interestingly the four branches of the cross are visible whereas only three of them were on the raw acousto-optic images. This is confirmed by the profiles plotted on figure 3.16 along the vertical dashed line. (d) Image of the corresponding optical contrast obtained by removing the light envelope the same way as for the previous liver biopsies.

ink solution so that the cross is more absorbing but less scattering than the surrounding. The cross was embedded inside a scattering gel of dimension $4 \times 4 \times 3$ cm^3 and of reduced scattering coefficient $\mu_s' = 9$ cm^{-1}. The point here is not to perform quantitative imaging, but just to show that such an approach can be used to remove the scattered light background without assuming anything about the optical properties of the sample, contrary to what was done in the previous section. As a consequence, nor the absorbing and scattering coefficients, nor the acoustic pressures were calibrated here.

In [134], the authors state that in order to have the highest amount of pressure contrast signal, it must be considered working with the highest pressure difference possible, the high pressure being limited by the safety limits whereas the weak one being limited by the detection limit. Considering this point, the acousto-optic sequence was composed of two sequences using a 6 MHz probe (SL10-2) that allows greater pressures than the 8 MHz probe (SL15-4) previously used. Each sequence consisted in 4-cycles pulses averaged 2000 times and focused at 20 mm. The first

image was obtained using a transducers voltage of 70 V (figure 3.15(a)), whereas the second one was obtained using a transducers voltage of 20 V (figure 3.15(b)). Because the pressure contrast image is very sensitive to the noise in the acousto-optic images, each one was smoothed over 1 mm in both direction in order to reduce the amount of noise while keeping a decent resolution.

The ratio between these two images is displayed on figure 3.15(c). It is visible here that the pressure contrast image is not sensitive to the light irradiance anymore and the background of the image is flat. I left the DC-background level here in order to highlight the fact that this value depends on the optical properties of the surrounding medium. Assuming that, as it is stated in [134], the pressure contrast mostly comes from the scattering properties, the decrease of signal in the cross on the ratio image is consistent with what is observed in the paper of P. Lai *et al.* For comparison purpose, the optical contrast image obtained by removing the scattered light background the same way as for the liver biopsies is shown on figure 3.15(d). Though in arbitrary units, this image provides information about the effective attenuation of the sample. Here again assuming that the pressure contrast mainly depends on the scattering properties, the differences with the optical contrast image may come from ink that diffused inside the gel matrix.

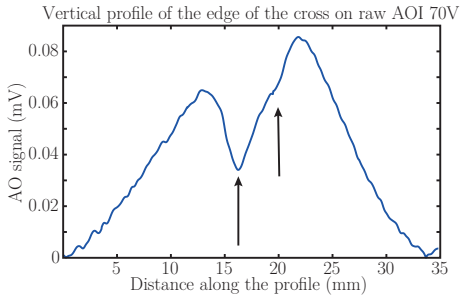

(a) Profile on the AOI using 70V

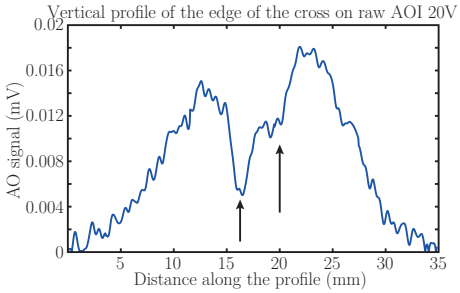

(b) Profile on the AOI using 20V

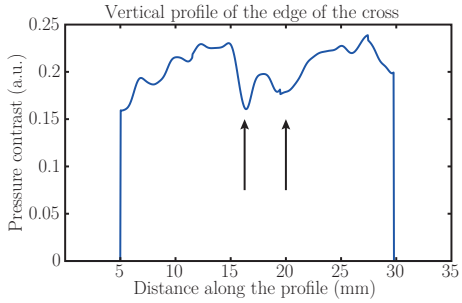

(c) Profile on the pressure contrast image

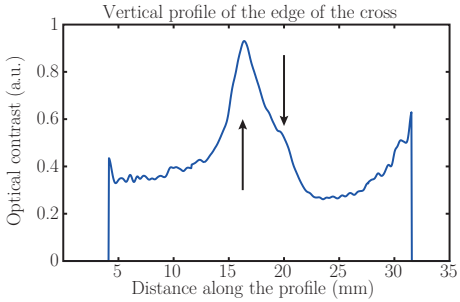

(d) Profile on the optical contrast image

Figure 3.16 – Profiles along the vertical dashed lines on the three figures of 3.15. The fourth branch which is not well-separated on the raw acousto-optic images and the optical contrast image can be clearly seen on the pressure contrast.

Interestingly, only three branches of the cross are visible on the acousto-optic images. The fourth branch is slightly visible on the profiles plotted on figures 3.16(a) and 3.16(b) through the small drop of signal pointed out by the black arrow but it can not be interpreted easily for the two branches are not well separated. It appears that the fourth branch is visible and well separated on the pressure contrast image as shown on the profile on figure 3.16(c) even if it is still not the case on the optical contrast profile of figure 3.16(d). A DC-level is also visible on the optical contrast profile probably coming from a mismatch between the fitted envelope and the real one.

The goal of this section was not to demonstrate the efficiency of pressure contrast imaging, but only to suggest an alternative technique in order to get acousto-optic images that do not depend

on light irradiance inside the scattering sample. As suggested by P. Lai *et al.* [134], this approach may lead to quantitative measurement of optical properties of biological samples.

3.4.2 Functional brain imaging

As I showed in chapter 1, one of the main interest of using optical imaging is the spectral information it carries about the chemical nature of biological species. Because of light scattering, most of optical techniques nowadays are NIR spectroscopy techniques that measure a global physiological parameter integrated over the entire illuminated area. In section 1.1, I showed that NIR light can be used to measure blood oxygenation and, in section 2.1.2, I showed that acousto-optic imaging could be used in order to increase the spatial resolution of such techniques. A natural direction of exploration for a multi-modal platform is then mapping of blood oxygenation and functional brain imaging. Coupled with ultrasound Doppler imaging which is a powerful tool for measuring blood perfusion, acousto-optics may bring useful complementary information about brain activity.

As a preliminary study, several washed *ex vivo* rat brains[1] were studied in order to get a first idea of how light scatters in simple conditions. This study is being performed in collaboration with I. Cohen from the Neuroscience department of Institut de Biologie de Paris and experiments were done with Baptiste Blochet during his internship. Though still under investigation, I will show an example of the very first results that were obtained, the goal of which are to understand how acousto-optic images behave in a rat brain.

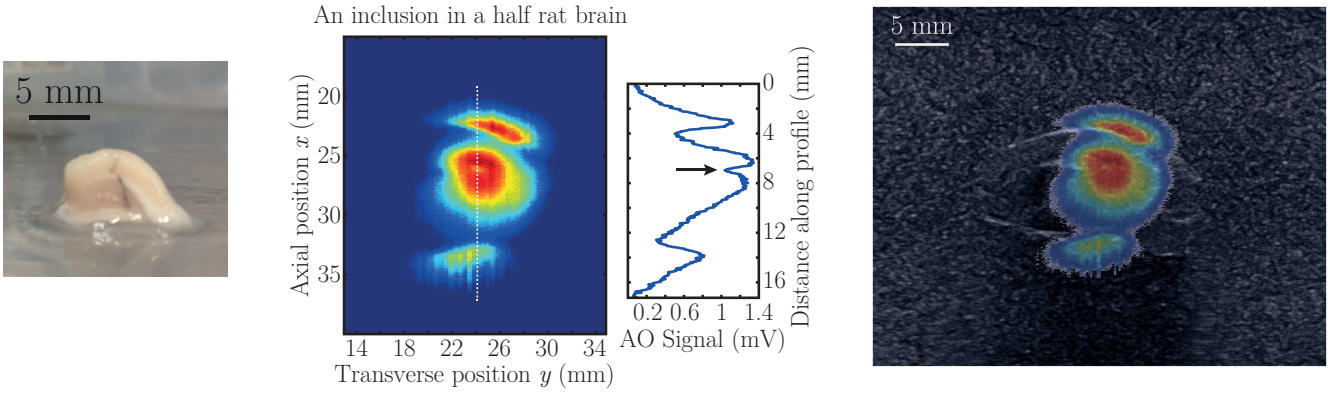

(a) Picture of the bain

(b) Acousto-optic image of the inclusion

(c) overlay of AOI and ultrasound scan

Figure 3.17 – Acousto-optic imaging of a rat brain with an ink inclusion. (a) Picture of the rat brain hemisphere with the ink inclusion. It is an elongated inclusion of width under 1 mm coarsely modelling a blood vessel. (b) Acousto-optic image of the hemisphere approximately 2 to 3 mm deep inside the brain sample. The inclusion is appearing here as confirmed by the vertical profile along the dashed line. Here the long dimension of the inclusion is oriented along the z-axis – along the light propagation direction – so that the acousto-optic image shows a transverse section in the (x, y) plane. (c) overlay of the ultrasound scan and the acousto-optic image showing to what extent the light information fits the structure of the brain.

In order to ensure a good resolution, the probe was a 8 MHz probe sending only 2-cycles long pulses at its resonance frequency resulting in a longitudinal resolution of 400 µm. For unclear reasons, it was very hard to collect decent acousto-optic signals through a whole rate brain. All current results were obtained in the middle of brain hemispheres only. The hemispheres were

[1]By washed brain, it must be understood that all blood has been removed from the vessels and replaced by a salt solution.

embedded within a transparent gel the role of which is just to hold the sample. The upper interface of hemispheres was approximately located at 20 mm under the probe. Ultrasound pulses are focused at 25 mm deep so that the focus is approximately located in the middle of the brain. The result I show here is an elongated ink inclusion of width under 1 mm crossing the whole brain thickness and coarsely modelling a blood vessel (see picture on figure 3.17(a)). The long dimension of the inclusion is oriented along the z-direction – the light direction – so that the transverse section of the cylinder is inside the (x, y) plane – the acousto-optic image one. The corresponding acousto-optic image is shown on figure 3.17(b). It can be seen here that because the rat brain is nor homogeneous nor isotropic, the scattered light profile is distorted compared to what was obtained earlier. The inclusion is appearing here and its presence is confirmed by the profile along the white dashed line. Figure 3.17(c) shows the overlay of the acousto-optic image and the conventional ultrasound scan in order to locate the light information inside the brain structure.

As I showed in the previous section, the scattered light envelope leads to an inconvenient curved background. Most of other images were just scattered light patterns in blank samples the goal of which is to build a library of typical light envelope shapes. Such washed brain images could be integrated to further imaging or modelling in order to extract relevant blood information.

3.4.3 Sketches of *in vivo* imaging

As it was the case for liver imaging, a transmission configuration is not suitable for functional brain imaging either. In order to confront the multi-modal platform to *in vivo* imaging, a backscattering configuration was installed together with Clement Dupuy at the beginning of his PhD. The optimization of the position of the light source and detector was studied in a cylindrical geometry by S. Gunadi *et al.* [136], but a lot of work is still to be performed in terms of relative position of the light source or detection and the ultrasound probe. The experimental setup was fibred in order to authorize several configurations.

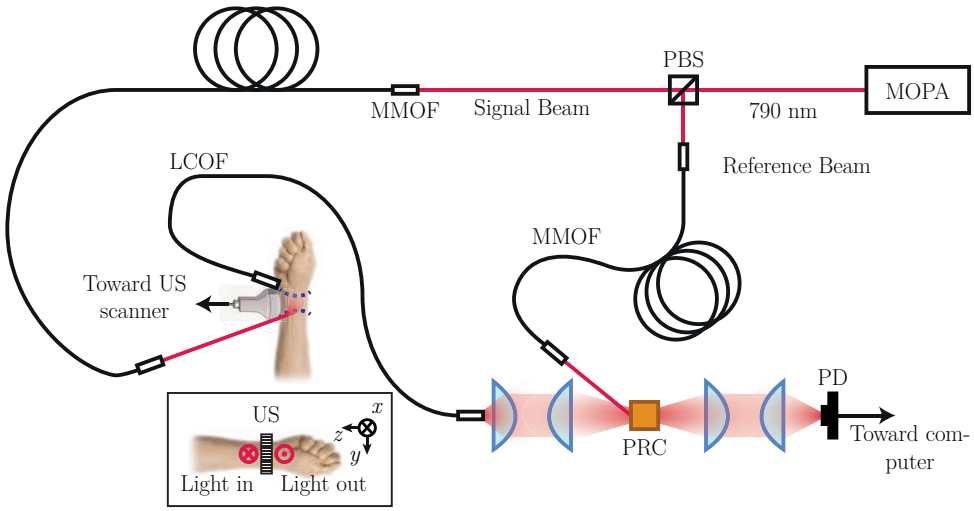

Figure 3.18 – Experimental setup in order to acquire acousto-optic images in the wrist of a male volunteer. LCOF: Liquid Core Optical Fibre, MMOF: Multi-Mode Optical Fibre, PBS: Polarization Beam Splitter, PRC: Photorefractive Crystal, MOPA: Master Oscillator Power Amplifier, PD: Photodiode.

The setup was tried on the wrist of a male volunteer just to see if it is possible to measure acousto-optic signals *in vivo*. The configuration that was used is presented on figure 3.18. The

arm was tied to the optical breadboard in order to limit at maximum unwanted motion. The acousto-optic sequence is generated by a commercial ultrasound scanner and the light power was decreased so that both ultrasound and light parameters were within the safety limits. A typical acousto-optic image obtained in the motionless arm is shown on figure 3.19(a). The image was superimposed to the ultrasound scan in order to locate the optical information inside the biological structures measured by ultrasound. It is impossible to extract any biological information here and it was not the goal of the experiment, but interestingly it is still possible to measure acousto-optic signals over shallow depths. Indeed, though response times of SPS crystals are a bit long to completely follow the speckle decorrelation *in vivo*, a blurred hologram can still be engraved. In this case, the acousto-optic sequence was pulsed over several tens of seconds so that it is very hard to remain static over times that long. Figure 3.19(b) shows another acousto-optic image obtained with similar conditions but for which the volunteer slightly moved during the scan. It can be seen here that acousto-optic signal almost vanished.

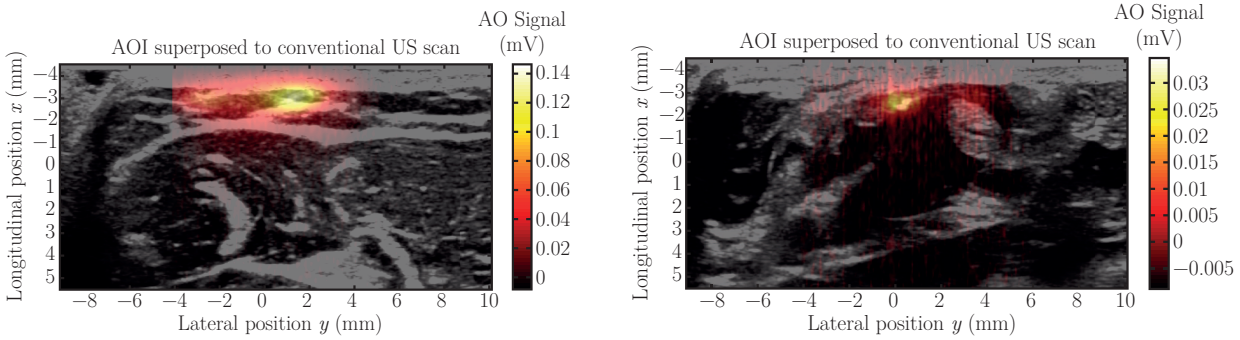

(a) Acousto-optic image in the wrist

(b) Acousto-optic image in the wrist

Figure 3.19 – Acousto-optic image in the wrist *in vivo*. (a) The wrist remained static during the imaging time. (b) The wrist moved during the imaging time.

The goal of this section was actually not to give a proof of concept of *in vivo* acousto-optic imaging but to highlight the limitations of the current technique and give an insight of further necessary developments.

3.5 Bimodal imaging limitations

Self-adaptive wave-front holography is a dynamical process that allows correcting the reference wave-front in order to overcome the random nature of speckle patterns. This dynamical process has an intrinsic response time of the order of several milliseconds. In this chapter, I showed that, because it works with large-area single detectors, such an approach allows performing time-resolved acousto-optic imaging over the ultrasound propagation. It is then possible to acquire a whole line of the final acousto-optic image with a single ultrasound pulse.

This feature makes the coupling of self adaptive wave-front holography with conventional ultrasound natural. These last years, we developed a multi-modal acousto-optic/ultrasound platform working with SPS crystals. Beside having high photorefractive gains and response times almost compatible with *in vivo* speckle decorrelation, such crystals have the important feature of working around 800 nm, inside the optical therapeutic window. Such a platform offers the advantage of matching optical information to structures provided by conventional ultrasound and gave very

promising *ex vivo* results. More importantly, these very preliminary studies gave an insight of further essential developments in order to switch to *in vivo* and clinical imaging.

Quantitative imaging It was shown up to now that acousto-optics was sensitive to light irradiance and not directly to optical properties. It appeared that the scattered light envelope makes it difficult to interpret images as soon as the sample becomes more complex than a small inclusion inside a homogeneous sample. The liver results benefited from the fact that the embedding matrix was a homogeneous medium in which the shape of scattered light can be easily predicted. Once this scattered light envelope is removed, it is possible to recover optical properties images. Obviously, such a basic approach can not be applied to more complex samples, as shown by the rat brain results. Even though I showed that some direct approaches exist such as measuring spectral information through multi-wavelengths imaging or recovering scattering properties through pressure contrast, it highlighted the necessity of working on forward models and inverse problems in order to extract optical properties from acousto-optic measurement.

Backscattering configuration All previous results showed that clinical imaging does not fit a transmission configuration. In the very first sketches of *in vivo* imaging I presented here, we tested a backscattered configuration in which the probe is placed between the illuminating and collecting fibres. The basic issue here is that the shape of the illuminated region can not be easily controlled for it is defined by light scattering. It is then necessary to further study the light distribution inside a scattering medium and the resulting acousto-optic signal as a function of the shape, size, position or number of light illumination and collection areas – through simulations and experimental tests on blank samples for instance.

Sensitivity to speckle decorrelation As explained above, the response time of SPS crystals is of the order of several milliseconds which is a bit higher for *in vivo* imaging for which speckle patterns decorrelate over a characteristic time under 1 ms. This decorrelation can mainly occur due to blood flows, breathing, heart beating or global motion of the patient. It results that photorefractive detection is limited in terms of SNR – because the hologram can not be fully engraved – and imaging depth – because the deeper one goes, the faster speckle decorrelates.

Low imaging rate As explained in the conclusion of chapter 2, the robustness to speckle decorrelation is to be distinguished from the imaging rate, the latter mainly depending on the number of ultrasound pulses that are used to obtain the image. The previous results showed that acousto-optic images are obtained in typically several tens of seconds. Beside the fact that any movements that occur during this amount of time participate to speckle decorrelation and loss of acousto-optic signal, low imaging rates will be a major hindrance when imaging dynamical processes.

The first two essential developments are part of Clement Dupuy's PhD since October 2014 and will not be further studied here. I will only focus on the other two in the following, that is to say speckle decorrelation and imaging rate. These two points will be treated separately inside the next two parts. In part III, I will suggest a novel acousto-optic sequence based on the use of ultrasonic plane waves and a tomographic reconstruction in order to increase the imaging framerate up to a factor of 50. In part IV, I will study the possibility of using spectral holeburning as a narrowband filter insensitive to speckle decorrelation that may allow to combine the advantage of time-resolved imaging provided by photorefractive crystals while being insensitive to speckle decorrelation.

Part III

Increasing the imaging rate thanks to ultrasonic plane waves and tomographic reconstruction

CHAPTER 4

Introduction to acousto-optic imaging with ultrasonic plane waves

Table of contents

PART II showed that acousto-optic imaging can be coupled with a commercial ultrasound scanner in order to converge toward clinical imaging. I showed first promising *ex vivo* and *in vivo* results that take part in a general ongoing process toward potential medical applications of acousto-optic imaging. However, one encounters two major difficulties when dealing with clinical imaging. The first one concerns speckle decorrelation in *in vivo* tissues that prevents from using a lot of interferometric techniques and that will be dealt with in Part IV. The second one, that will be dealt with in this Part, concerns the low imaging rate of acousto-optic imaging. In this chapter, I will show that tomography is a natural approach for acousto-optic imaging. I will develop a theoretical and numerical framework of acousto-optic imaging with ultrasonic plane waves in order to derive the main properties of the technique. The following chapter will be dedicated to experimental considerations and proofs of concept of the technique.

4.1 Of low imaging rate in acousto-optic imaging

There are basically two main phenomena that limit the imaging rate of acousto-optic imaging. The first limitation concerns the waiting time between two ultrasound pulses. Conventional commercial ultrasound scanners usually limit the firing rate to 1 pulse of few cycles - 2 or 3 - every 100 µs. This waiting delay comes from several parameters such as ultrasound time-of-flight, hardware delays or cooling delay in order to avoid heat damages of the transducers. In principle, this waiting time is ultimately limited by the the ultrasound time-of-flight across the sample at 1.5 mm $\cdot$ µs^{-1}, of the order of several tens of µs. Classical acousto-optic sequences use focused ultrasound pulses and need about 100 lines, *i.e.* as many pulses, to get an image so that the theoretical framerate using standard ultrasound scanners is of the order 100 frames per second.

Though this theoretical limit is acceptable for video rate display and most of *in vivo* applications, it is drastically reduced by the low amount of useful signal in acousto-optic imaging and the resulting high number of averaging. This second limitation implies that images obtained at few centimetres deep in the light beam direction require several thousands averaging pulses for each line as shown in the previous chapter and in [116] so that the ultrasound firing rate requires at least a few tens of seconds in order to obtain an image.

It appears here that current acousto-optic imaging rates are not compatible with real-time *in vivo* experiments. Since the waiting delay between two pulses can hardly be reduced, it is absolutely necessary to reduce the number of ultrasound pulses before any clinical applications can be thought of. One easily guesses that any techniques improving the signal-to-noise ratio (SNR) will contribute to increase the imaging rate by reducing the number of needed averaging pulses. However, a second approach consists in changing the emitted ultrasound pattern in order to reduce the number of ultrasound pulses needed to obtain an image. These two approaches are independent and can be coupled easily for the first concerns the optical reception as the second concerns the ultrasound emission. As an example, in [137] P. Lai *et al.* used an optimized photorefractive-based detection thanks to, among others, a very high numerical aperture fibre bundle and long ultrasound pulses (from 10 to 100 cycles) in order to decrease the number of averaging down to 64 at the cost of the longitudinal resolution (along the ultrasound propagation

direction). Though this method reaches unprecedented depths, its main drawbacks are that it uses a single element transducer at relatively low repetition rate (100 Hz).

In this part, I will study a new pattern based on ultrasonic plane waves emitted from a transducer array that allows reducing the number of pulses necessary to create an image while maintaining the firing rate at the hardware limit. Coupled with a tomographic reconstruction, this pattern needs about 50 times fewer ultrasound pulses at equal SNR.

4.2 Tomography and multi-waves imaging

Tomography is an imaging technique widely used in all fields in which an object must be reconstructed through its projections along particular directions. The main one is X-rays imaging and in particular CT scanners [138] but tomographic approaches are also used in other medical techniques such as positron emission tomography (PET) [139]. In optics, several imaging techniques are based on similar approaches such as optical projection tomography (OPT) [140], optical equivalent of CT that uses the depth of focus of an in line optical imaging system in order to produce 3D images of a rotating object, or Selective Plane Illumination Microscopy (SPIM) [141], that also produces images of rotating objects by imaging a selected plane illuminated with a 2D light sheet on a camera orthogonal to the illumination axis. It recently appeared that tomographic techniques also suit multi-waves imaging techniques very well. Similar ideas of what is presented in this Part were already suggested for different multi-waves techniques, and in particular, multi-waves techniques coupling ultrasound with another modality.

First proofs of concept of photoacoustic imaging were tomographic images using one or several receiving single-element transducers rotating in a plane orthogonal to the illumination direction [142]. Because it allowed decent images without moving the probe, coupling this approach, so-called photoacoustic tomography, with receiving linear ultrasound arrays allowed increasing the imaging rate and led to embedded multi-modal photoacoustic/ultrasound imaging platforms [50]. Several drawbacks of the linear array brought back tomographic approaches into light. The main one is the limited field of view of a linear probe that can not detect ultrasonic waves emitted along the direction parallel to the probe. It led to the development of circular transducers arrays for applications compatible with tomography, small animal [143] or finger imaging [144] for instance.

In the case of acousto-optic imaging, an experimental demonstration of tomographic approaches was performed in [109] with single-element transducers emitting continuous focused ultrasound waves. Later, the idea was theoretically suggested again in [145] in order to correct problems that may occur due to the focal point of ultrasound being of finite volume. Interestingly, in this paper the authors suggest to use unfocused ultrasound and developed a synthetic focusing method for monochromatic waves. The major drawback of this approach is again that it needs mechanical translations and rotations of the transducer, which is very time-consuming. Considering this drawback, tomographic approaches were left aside in favour of single-side imaging methods with linear ultrasonic probes and focused pulses [116, 117]. However, transducers arrays also allow electronic beam steering so that it can be considered sending plane waves to recover the projections as the ultrasound probe stands still. This idea was already used in other imaging modalities such as acousto-electric imaging [146] but never applied to acousto-optic imaging.

Ultrasonic plane waves are widely used in ultrasound imaging. Because each transducer can measure a backscattered time-resolved echo independently from the other ones, ultrasound images can be obtained with only one pulse, thus allowing very high framerates (up to 10000 fps) [147]. However, the resolution of the final image is degraded because ultrasound are not focused in

emission. Coherent compound imaging [148] was developed to overcome this difficulty: several plane waves propagating with different angles are emitted inside the medium and final images are coherently summed in order to recover emission focusing in post-processing. The mathematical study of this problem is given in [149]. Obviously, in the case of acousto-optic imaging, only one channel is available in reception (the scattered light), so that plane waves imaging will require a tomographic approach. Similarly to ultrafast acousto-electric imaging [146], it will be shown below that high imaging framerates can be performed at the cost of an image distortion and a resulting loss of resolution in the lateral direction, the amplitude of which will be quantified.

4.3 Acousto-optic signal with an ultrasonic plane wave

In the previous section I showed that tomography is a frequent approach in multi-waves imaging. However, when one of the two modalities is ultrasound imaging, tomographic approaches often require a mechanical displacement of the transducer. As a consequence, these techniques were left aside in favour of commercial linear probes that allow electronic linear scans. However, the use of linear probes offers a lot more possibilities than just linear scans. In this part, ultrasonic plane waves generated by a conventional phased-array are used for the first time in acousto-optic imaging. From this section and until the end of the chapter, I will derive a simple theoretical model and numerically predict a few properties of the technique.

4.3.1 From focused acousto-optic imaging to tomography

Let us consider a static sample, with negligible Brownian motion, illuminated by a monochromatic optical wave. The irradiance ($\mathrm{W.m^{-2}}$) inside the scattering medium in a plane perpendicular to the optical beam axis (z-axis) at a fixed depth z, is $\Phi(x,y)$. The aim of acousto-optic imaging is thus to recover $\Phi(x,y)$. The light is modulated by an arbitrary ultrasound wave $P_{US}(\mathbf{r},t)$ propagating along the $\mathbf{r}=(x,y)$ direction in this plane:

$$P_{US}(\mathbf{r},t) = P_0\left(t - \frac{\mathbf{K}_{US}\cdot\mathbf{r}}{\omega_{US}}\right)\sin(\omega_{US}t) \tag{4.1}$$

where I considered the retarded potential. P_0 represents the temporal shape of the ultrasound pulse. In practice, the ultrasound wave is geometrically focused along the z-direction (in the elevation direction) so that I will consider that it propagates within a 2D plane (x,y) at a fixed position z. In chapter 2, it was shown that the tagged photons intensity on a photodetector can be expressed as:

$$\Psi_T \propto \iint \Omega(\mathbf{r},\mathbf{r}')\,\Phi(\mathbf{r})\,P_0^2\left(t - \frac{\mathbf{K}_{US}\cdot\mathbf{r}}{\omega_{US}}\right)\mathrm{d}x\mathrm{d}y \tag{4.2}$$

where $\Omega(\mathbf{r},\mathbf{r}')$ is the probability of having a tagged photon at $\mathbf{r}$ reaching the detector at $\mathbf{r}'$. The $\mathbf{r}'$ variable will not be kept in the subsequent paragraphs by considering that the detector is at a fixed position and defines a certain shape of the scattering envelope. Let us then define $I(\mathbf{r}) = \Omega(\mathbf{r},\mathbf{r}')\,\Phi(\mathbf{r})$ as the image to be recovered that implicitly depends on the real light irradiance inside the medium $\Phi(\mathbf{r})$, the position of the detector and the probability that a photon in $\mathbf{r}$ reaches it. This formula is just expressing the fact that photons are tagged over the entire ultrasound pulse volume and indistinctly counted on the detector.

Let us now consider that the ultrasound pattern we use consists in a plane wave generated by a commercial scanner and propagating within the sample with an angle θ, see figure 4.1 and [148].

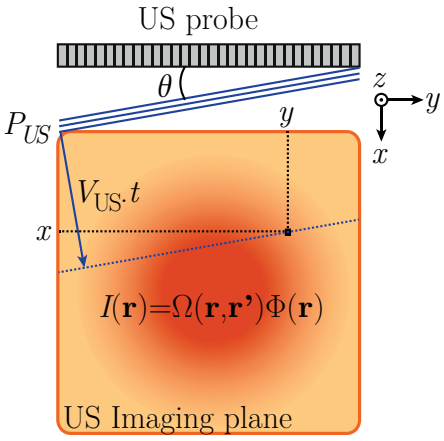

Figure 4.1 – Schematic of the ultrasonic plane wave propagating inside an illuminated sample with an angle θ. Ultrasound are focused along the z-direction so that they propagate in a plane perpendicular to the light propagation direction. This figure represents this section defined by the ultrasound probe position. The three plain blue lines represent the ultrasonic pulse propagating at V_{US}. At time t, the wave is at the position of the dashed blue line. A voxel (black square) is located through its coordinates (x, y). Photons are indistinctly tagged along the entire wave-front so that the signal recorded on a single detector is the integrated light intensity along the dashed line.

As photons are tagged along the entire ultrasound volume, the single detector indistinctly counts all tagged photons coming from the plane wave-front. Here, I use the wave-front adaptive photorefractive crystal-based detection in a negative gain configuration with Te:SPS crystals described in part II in order to record a voltage proportional to the tagged photons intensity on the photodiode. The single-detector records a signal proportional to the light irradiance inside the medium integrated along the ultrasound wave-front:

$$s_{\mathrm{PD}}(t,\theta) \propto \iint I(x,y)\, P_0^2\left(t - \frac{x\cos\theta + y\sin\theta}{V_{\mathrm{US}}}\right) \mathrm{d}x\mathrm{d}y \tag{4.3}$$

where V_{US} is the sound velocity inside the medium. It is possible to re-write equation 4.3 as:

$$s_{\mathrm{PD}}(t,\theta) \propto \iint I(x,y)\left[P_0^2(t) * \delta\left(t - \frac{x\cos\theta + y\sin\theta}{V_{\mathrm{US}}}\right)\right] \mathrm{d}x\mathrm{d}y \tag{4.4}$$

where δ stands for the Dirac distribution and "$*$" stands for the convolution product. Except from the term $P_0^2(t)$, this is very close to the Radon transform of the light irradiance repartition inside the medium. The Radon transform relates an object to its projections on a space of smaller dimension. It is known since 1917 and widely used and studied since the late 50's. The Radon transform is involved in a lot of fields as diversified as astrophysics [150], electron microscopy [151] or optical imaging [152]. However, the greater use of the Radon transform is made in the field of X-rays imaging and more specifically for medical imaging purposes with CT scanners [138]. Acousto-optic imaging with ultrasonic plane waves can thus benefit from what was developed for these purposes during the last 60 years. More specifically, acousto-optic imaging is even equivalent to one of the CT modality: the pencil beam scan [138, Chapter 3] represented on figure 4.2(a). In the following, I will not enter a lot into the details of the Radon transform. I will only use few properties that I quickly justify in appendix B.

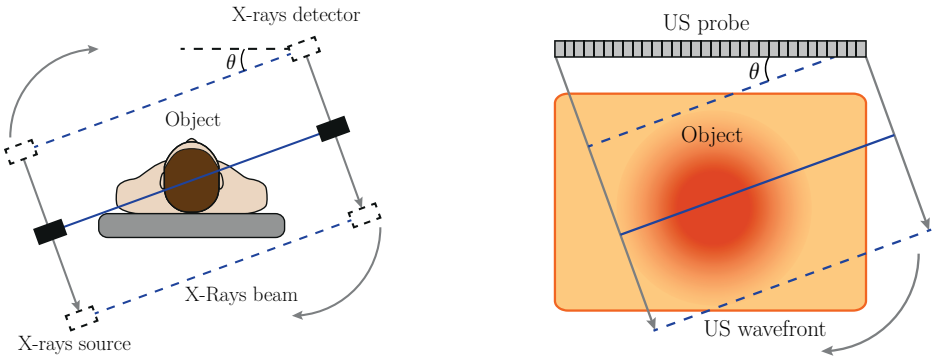

(a) Pencil beam CT scan

(b) AO imaging plane wave scan

Figure 4.2 – AO imaging with plane waves is equivalent to the pencil beam scan that was developed for CT. (a) Principle of the pencil beam CT scan. There is a single X-rays source and a single detector and measurements are incremental. At one position of the couple source/detector, the X-ray beam measures the integrated absorption along the blue line. Two kind of motions are then involved. First the source and detector are moved in a direction perpendicular to the blue line and data are collected for one set of parallel lines. Once the object has been scanned, the couple source/detector is rotated of a small amount and a new linear scan is measured. (b) Principle of AO imaging with ultrasonic plane waves. At one given position of the US wave-front the photodiode records a signal proportional to the integrated irradiance along the blue line. As the US pulse propagates inside the object in the direction perpendicular to the blue line, data are collected for a set of parallel wave-fronts. Once US have explored the object, the emission angle is tilted of a small amount and a new pulse is sent in the medium.

4.3.2 Problem inversion and image reconstruction

The similarity between plane waves acousto-optic imaging and CT principle allows adapting what was already developed in this latter field, and in particular image reconstruction algorithms. The backprojection technique (cf. appendix B) is the most common way of reconstructing a tomographic image. This technique consists in attributing each value of one projection $s_{\mathrm{PD}}(t,\theta)$ along one given angle θ to all potential areas of the sample that may have contributed to this value. The final image can be obtained by scanning the angle of projection over 360° and summing all contributions in order to refine the localization of the different objects. The backprojection principle is shown on figure 4.3(a) in the case of the CT scanner technique and on figure 4.3(b) for its adaptation to acousto-optic imaging. It can be shown mathematically that this very simple reconstruction method gives a blurred version of the final image.

It appears naturally that a projection obtained along a direction θ contains the exact same information than the projection along $\theta+\pi$. In an ideal case then, angles should be scanned over π with carefully chosen steps. The major limitation in acousto-optic imaging with ultrasonic plane waves is that the whole angular domain is not accessible. Elements on commercial ultrasound flat probes have a typical directivity of ±20° so that the angular domain is limited to 40°. As the main goal of using ultrasonic plane waves is to increase the imaging rate, mechanically moving the probe to increase the explored angular domain is to be avoided as far as possible. It will necessarily result in degraded images.

A first proof of principle can be done in these conditions. An absorbing cylindrical inclusion of diameter 2.5 mm is embedded inside a scattering gel matrix of dimensions $4\times4\times3$ cm^3 with a reduced scattering coefficient of $\mu_{\mathrm{s}}'=10$ cm^{-1}. This inclusion is imaged with a photorefrective-crystal-based detection coupled with a commercial ultrasound scanner similar to what was used in part II. The probe is a 6 MHz commercial linear transducers array provided by the company

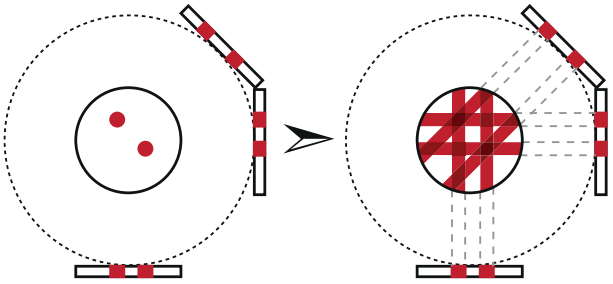

(a) Backprojection principle in the case of the CT scanner

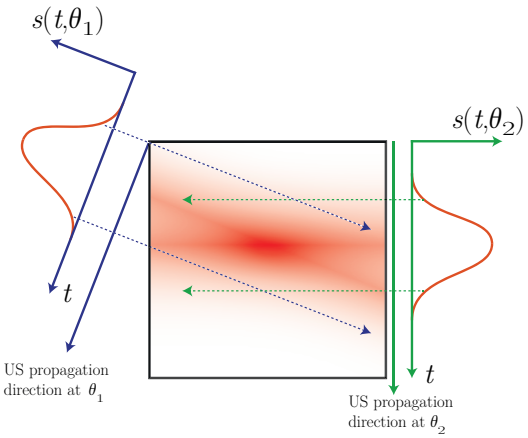

(b) Backprojection principle in the case of AOI

Figure 4.3 – Backprojection principle in the case of (a) the CT scanner (b) acousto-optic imaging. The principle is the same in the two cases and consists in attributing each value of a projection to all points that contributed to this value. The shape of the final object is recovered by superposing all backprojected signals. It can be shown that the resulting image is a blurred version of the real object.

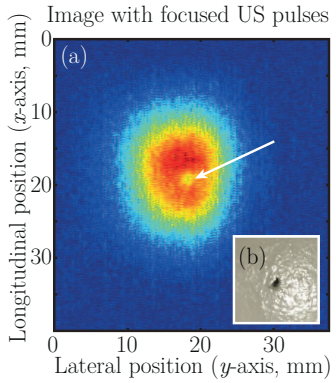

Figure 4.4 – Example of an acousto-optic image of an absorbing inclusion embedded in a scattering gel obtained with 2-cycles focused pulses.

SuperSonic Imagine with 192 elements of 0.2 mm pitch. For comparison purposes, the image obtained with 2-cycles focused pulses is displayed on figure 4.4 and the inclusion is pointed out with a white arrow. The same inclusion was imaged with plane waves from $-20°$ to $20°$ with $1°$ angular steps. The final image was reconstructed with a simple backprojection algorithm and is shown of figure 4.5(a). The first observation that can be made here is that the image is distorted in the lateral direction and this comes from the limited angular scan. The second observation is that the inclusion is almost invisible. Two sections of this image along respectively the longitudinal (black dashed line) and lateral (white dashed lines) dimensions are plotted on figures 4.5(b) and 4.5(c). It appears here that the contrast – ratio between the depth of the inclusion signal compared to the maximum value of the scattered light envelope – is very low due to both the intrinsic blurring of the backprojection algorithm and the limited angular range.

Other reconstruction methods give more accurate images and will be detailed later on. The goal of next sections is then to theoretically study the acousto-optic signal and image reconstruction in order to discuss the degradations due to angular range limitation and reconstruction issues.

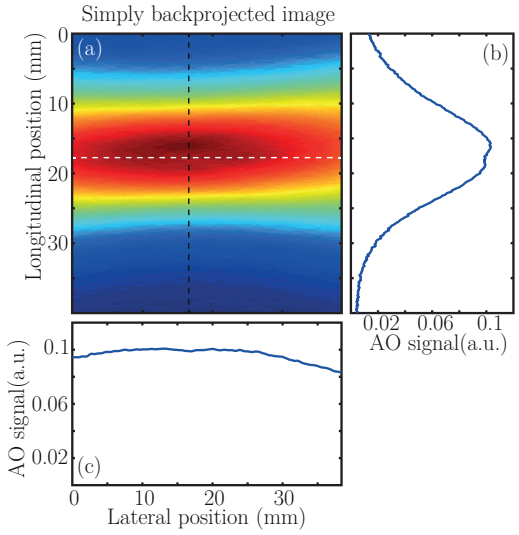

Figure 4.5 – Example of a plane wave acousto-optic image of an absorbing inclusion embedded in a scattering gel obtained by scanning angles from $-20°$ to $20°$ with $1°$ angular steps and reconstructing with a simple backprojection algorithm. (a) The backprojected image. (b) A longitudinal section of the image along the black dashed line showing the inclusion. (c) A lateral section of the image along the white dashed line.

4.4 Theoretical study of the acousto-optic signal

4.4.1 Analytical inversion

As I showed previously, a simple backprojection gives a blurred version of the final image and the limited field of view of a linear probe degrades the resolution. In order to quantify the degradations due to limited angular exploration, I will first study the analytical inversion of the problem. I showed in appendix B that the analytical inversion can be expressed through the spatial Fourier transform of the image thanks to the projection-slice theorem. This property of the Radon transform states that the temporal Fourier transform of a projection $\widetilde{s_{\mathrm{PD}}}(\nu,\theta)$ is equal to a slice along θ of the final image spatial Fourier transform $\widehat{I}\left(\frac{\nu}{V_{\mathrm{US}}}\cos\theta, \frac{\nu}{V_{\mathrm{US}}}\sin\theta\right)$:

$$\begin{aligned}\widetilde{s_{\mathrm{PD}}}(\nu,\theta) &= \widehat{I}\left(\tfrac{\nu}{V_{\mathrm{US}}}\cos\theta, \tfrac{\nu}{V_{\mathrm{US}}}\sin\theta\right)\\ &= \widetilde{P_0^2}(\nu)\iint I(x,y)\exp\left(-2i\pi\nu\frac{x\cos\theta + y\sin\theta}{V_{\mathrm{US}}}\right)\mathrm{d}x\mathrm{d}y\end{aligned} \tag{4.5}$$

where $\widetilde{P_0^2}$ stands for the temporal Fourier transform of P_0^2. In the following, the notation "$\widetilde{g}$" will denote 1D Fourier transforms (time here) whereas "$\widehat{g}$" will stand for 2D Fourier transforms (space in our case). In order to simplify notations, $\widetilde{P_0^2}$ will be denoted as $\widetilde{P}$. The exact inversion of the problem can then be obtained by iteratively reconstructing the 2D Fourier plane back through a summation over θ. The final image can then be expressed through the inverse spatial Fourier transform of this reconstructed Fourier plane. The projection-slice theorem is represented on figure 4.6.

In order to take into account the electronic system beyond the photodiode that may alter the tagged photons signal $s_{\mathrm{PD}}(t,\theta)$, let us introduce the frequency response $\widetilde{R}(\nu)$ of the detection

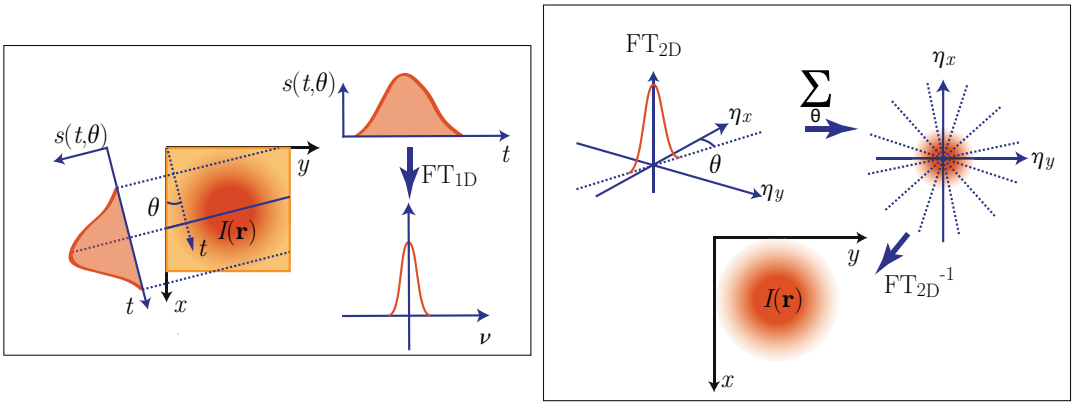

(a) Temporal Fourier transform (b) Spatial Fourier transform

Figure 4.6 – Illustration of the projection-slice theorem. (a) The temporal Fourier transform of a projection recorded on the photodiode at θ... (b) ...is equal to a slice of the spatial Fourier transform of the final image along θ. The slice is placed back in its rightful place in the spatial Fourier space and summed over all angles. The inverse spatial Fourier transform of the reconstructed Fourier space gives the expected image.

scheme. In terms of spatial frequencies, it gives:

$$\widetilde{s_{\mathrm{PD}}}\left(\eta,\theta\right)=\widetilde{R}\left(\eta\right)\widetilde{P}\left(\eta\right)\widehat{I}\left(\eta\cos\theta,\eta\sin\theta\right) \tag{4.6}$$

where $\eta=\frac{\nu}{V_{\mathrm{US}}}$ is the radial spatial frequency. Let us then define the spatial frequencies along the x- and y-directions $\eta_x=\eta\cos\theta$ and $\eta_y=\eta\sin\theta$ such as $\eta=\sqrt{\eta_x^2+\eta_y^2}$.

In the following, I will define the reconstructed image $\mathcal{I}\left(x,y\right)$ and its spatial Fourier transform $\widehat{\mathcal{I}}\left(\eta_x,\eta_y\right)$. The reconstructed image is then obtained through inverse Fourier transform of the reconstructed Fourier space:

$$\widehat{\mathcal{I}}\left(\eta_x,\eta_y\right)=\sum_{\theta}\widetilde{s_{\mathrm{PD}}}\left(\eta,\theta\right)=\widetilde{R}\left(\eta\right)\widetilde{P}\left(\eta\right)\times\sum_{\theta}\widehat{I}\left(\eta_{x,\theta},\eta_{y,\theta}\right) \tag{4.7}$$

The quality of the reconstructed image is then influenced by:

- The receiving bandwidth of the optical detection scheme. In order not to degrade the image, it is important that the system can follow the propagation of the plane wave pulse. Ultimately, this bandwidth is limited by the sampling rate of the acquisition system.
- The shape of the ultrasound pulse. The broader it is, the lower the resolution is.
- The angles used for the reconstruction. This is the most critical parameter. The spatial Fourier plane must be assessed precisely in order to ensure images of good quality. For instance, limited field-of-view leads to the absence of information in some regions of the Fourier space and alters the final image.

4.4.2 Point-spread function and limited angular range

Previous section gave an analytical expression of the reconstructed image. As it was stated in section 4.3.2, the angular range is limited to typically $\pm20°$ due to the transducers directivity on a linear commercial probe. In this section, I will derive an exact expression for the point-spread function (PSF) with a limited angular range. Let us consider that the spatial Fourier

transform of the image is now truncated by a limited angle exploration range $\pm\theta_m$. It means that all angles outside the domain $[-\theta_m, \theta_m]$ are not physically accessible through the system. The direct consequence is that the Fourier space can only be reconstructed within a cone of angular extension $\pm\theta_m$. Using the exact inversion formalism derived above, the reconstructed spatial Fourier transform of the image is:

$$\widehat{\mathcal{I}}(\eta_x, \eta_y) = \sum_{\theta\in[-\theta_m,\theta_m]} \widetilde{s_{\mathrm{PD}}}(\eta, \theta) \tag{4.8}$$

In order to assess the PSF of the system, let us consider a point object $\delta(x, y)$, where δ stands for the Dirac distribution. The spatial Fourier transform of the PSF can be expressed as:

$$\widehat{PSF}(\eta_x, \eta_y) = \widetilde{R}(\eta)\,\widetilde{P}(\eta) \sum_{\theta\in[-\theta_m,\theta_m]} \widehat{\delta}(\eta_{x,\theta}, \eta_{y,\theta}) \tag{4.9}$$

where $\widehat{\delta}(\eta_x, \eta_y)$ is the spatial Fourier transform of a Dirac distribution and is equal to 1 all over the Fourier plane. The receiving and emitting bandwidths $\widetilde{R}(\eta)$ and $\widetilde{P}(\eta)$ limit the maximum frequency modulus accessible so that the accessible portion of the Fourier plane is a segment of finite radius η_m between $\pm\theta_m$. Figure 4.7 represents the limited accessible region of the Fourier space. As $\widetilde{R}(\eta)$ and $\widetilde{P}(\eta)$ result in an homogeneous broadening in both x- and y-directions, they will be left aside in the following and taken into account in first approximation in a finite radius η_m of the Fourier spectrum.

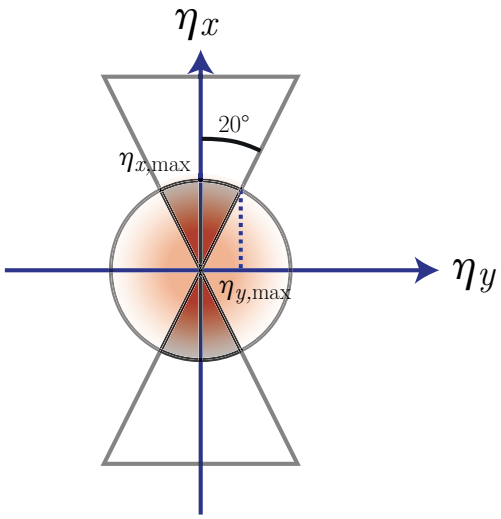

Figure 4.7 – The receiving and emitting bandwidths limit the highest accessible frequency modulus and the probe limits the angular range so that the accessible region is limited to a segment of the Fourier plane (darker gray portion).

In order to find an analytical solution, the problem will be simplified by replacing the discrete sum over θ by a continuous integral. The problem is then equivalent to the estimation of the effect of a polar truncation of the Fourier space between $\pm\theta_m$. From figure 4.7, it is possible to qualitatively describe the expected deformation of the PSF. In the longitudinal direction (x-axis), the maximum accessible spatial frequency is given by the emitting and receiving bandwidth η_m: the resolution in this direction is thus expected to be the same as with focused ultrasound. In the lateral direction (y-axis), the maximum accessible spatial frequency is now $\eta_m \sin\theta_m$: the resolution in this direction is thus expected to be degraded by a factor of $\frac{1}{\sin\theta_m} \sim 3$ in the case of an angular limitation of 20°.

In order to analytically express the PSF, let us switch to polar coordinates where the coordinates of the real space are r and φ and their corresponding transform variables η and θ. Inverse Fourier transform of equation 4.9 thus leads:

$$PSF\left(r,\varphi\right)=\int_{-\eta_m}^{\eta_m}\int_{-\theta_m}^{\theta_m}\widehat{\delta}(\eta,\theta)\exp\left[2i\pi\eta r\cos(\theta-\varphi)\right]|\eta|\mathrm{d}\eta\mathrm{d}\theta \tag{4.10}$$

where $\theta_m \leq \pi/2$. This expression could be used as is to compute the PSF with MATLAB. Yet, as polar Fast Fourier Transform (FFT) algorithms are not easily available, it takes a lot of time to compute the double integral. For a single line in a given φ direction of the final image, it typically takes between 10 and 20 seconds to compute the corresponding section of the PSF over ± 2 mm with the integral tools of MATLAB. This analytical formula took almost 7 minutes to compute a 2D image of the PSF over ± 2 mm with a poor angular sampling over φ (12° steps). Consequently, it is expected to take over 1 h to compute a PSF with an angular resolution of 1°. It is thus interesting to work on an approximate expression of the PSF that would be faster to compute.

4.4.3 Approximate expression of the PSF

The expression of equation 4.10 can be decomposed as a sum of Bessel functions of the first kind:

$$PSF\left(r,\varphi\right)=\sum_{n=-\infty}^{+\infty}e^{in\left(\frac{\pi}{2}-\varphi\right)}\int_{-\theta_m}^{\theta_m}e^{in\theta}\mathrm{d}\theta\int_{-\eta_m}^{\eta_m}J_n\left(2\pi\eta r\right)|\eta|\mathrm{d}\eta \tag{4.11}$$

where J_n is the n^{th} order Bessel function of the first kind. When the integral over θ is calculated:

$$PSF\left(r,\varphi\right)=\sum_{n=-\infty}^{+\infty}\frac{2}{n}\sin(n\theta_m)e^{in\left(\frac{\pi}{2}-\varphi\right)}\int_{-\eta_m}^{\eta_m}J_n\left(2\pi\eta r\right)|\eta|\mathrm{d}\eta \tag{4.12}$$

The PSF can then be developed as follows thanks to the substitution $\eta=\eta_m u$:

$$\begin{aligned}PSF\left(r,\varphi\right)=2\theta_m\eta_m^2\int_{-1}^{1}J_0\left(2\pi\eta_m r u\right)|u|\mathrm{d}u+\\ \eta_m^2\sum_{n=1}^{+\infty}\frac{2}{n}\sin(n\theta_m)\left(e^{in\left(\frac{\pi}{2}-\varphi\right)}+(-1)^n e^{-in\left(\frac{\pi}{2}-\varphi\right)}\right)\int_{-1}^{1}J_n\left(2\pi\eta_m r u\right)|u|\mathrm{d}u\end{aligned} \tag{4.13}$$

Due to the parity of the Bessel functions, all odd orders are equal to zero. The PSF is then equal to:

$$\begin{aligned}PSF\left(r,\varphi\right)=4\theta_m\eta_m^2\int_{0}^{1}J_0\left(2\pi\eta_m r u\right)|u|\mathrm{d}u+\\ \eta_m^2\sum_{p=1}^{+\infty}\frac{4}{p}(-1)^p\sin(2p\theta_m)\cos(2p\varphi)\int_{0}^{1}J_{2p}\left(2\pi\eta_m r u\right)|u|\mathrm{d}u\end{aligned} \tag{4.14}$$

As expected, if the angular range is $\pm\frac{\pi}{2}$, *i.e.* the whole angular domain is scanned, only the first term remains. As the integral of the 0^{th} order Bessel function can be rewritten thanks to the properties of the Bessel functions, the PSF is in this case:

$$\frac{PSF\left(r,\varphi\right)}{4\theta_m\eta_m^2}=\frac{J_1\left(2\pi\eta_m r\right)}{2\pi\eta_m r} \tag{4.15}$$

This is the Airy disk and the spreading is due to bandwidth limitation η_m. Another way of writing the PSF is then:

$$\frac{PSF\left(r,\varphi\right)}{4\theta_m\eta_m^2} = \frac{J_1\left(2\pi\eta_m r\right)}{2\pi\eta_m r} + 2\sum_{p=1}^{+\infty}(-1)^p \mathrm{sinc}(2p\theta_m)\cos(2p\varphi)\int_0^1 J_{2p}\left(2\pi\eta_m r u\right)|u|\mathrm{d}u \tag{4.16}$$

Equation 4.16 above can be numerically assessed. As the integral over J_{2p} also takes few seconds to be computed, it is interesting to use the properties of the Bessel functions to derive an inductive relationship between the different orders. The PSF can be expressed eventually as (see Appendix C):

$$\frac{PSF\left(r,\varphi\right)}{4\theta_m\eta_m^2} = \mathscr{A}\left(r\right) + \sum_{p=1}^{\infty}\mathscr{B}_p\left(r,\varphi\right) + \sum_{p=1}^{\infty}\mathscr{C}_p\left(r,\varphi\right) \tag{4.17}$$

in which each term can be separately assessed and obeys the following relationships:

$$\begin{cases} \mathscr{A}\left(r\right) = \frac{J_1(2\pi\eta_m r)}{2\pi\eta_m r} \\ \mathscr{B}_p\left(r,\varphi\right) = 2(-1)^{p+1}\mathrm{sinc}(2p\theta_m)\cos(2p\varphi)\frac{J_{2p-1}(2\pi\eta_m r)}{2\pi\eta_m r} \\ \mathscr{C}_p\left(r,\varphi\right) = \frac{2p(-1)^p}{\pi\eta_m r}\mathrm{sinc}(2p\theta_m)\cos(2p\varphi)c_p\left(r\right) \end{cases} \tag{4.18}$$

where $c_p\left(r\right)$ can be calculated by recursion thanks to the following relationships:

$$\begin{cases} c_0\left(r\right) = \frac{J_0(2\pi\eta_m r)-1}{2\pi\eta_m r} \\ c_{p+1}\left(r\right) = c_p\left(r\right) - \frac{1}{\pi\eta_m r}\left(J_{2p}\left(2\pi\eta_m r\right) - J_{2p}\left(0\right)\right) \end{cases} \tag{4.19}$$

These relationships above are much faster to compute than the integral.

4.5 Influence of angular exploration

4.5.1 Behaviour of the inductive terms

The advantage of using inductive relationships lies in the fact that the functions $\frac{J_{2p}(2\pi\eta_m r)}{2\pi\eta_m r}$ decrease very fast with p and r. They rapidly become negligible around the center of the PSF so that higher orders affect regions further from the center as shown on figure 4.8. On this figure, the first three orders of $\mathscr{B}_p\left(r,\varphi\right) + \mathscr{C}_p\left(r,\varphi\right)$ are plotted over a radius of 4 mm with a sampling of 7 µm and an angular resolution of 1°. The other interesting property is that each inductive term also decrease with p as $\mathrm{sinc}(2p\theta_m)$, it is then expected that a few orders are necessary to compute a good approximation of the PSF over a finite area.

Interestingly, it only takes less than a hundred of milliseconds to compute one order with an angular sampling much more refined than with the analytical solution. The main issue is then to find out how many orders are necessary to compute a decent 2D PSF over a given area. A way of estimating this number consists in monitoring the error that one makes when summing over a finite number of orders compared to the analytical solution. Because the analytical 2D PSF is very long to compute, this study was done only along the two directions we are interested in – $\varphi = 0°$ (x-axis) and $\varphi = 90°$ (y-axis). The integrated error $e\left(N\right)$ along a 4 mm radius section was computed as a function of the number N of orders taken into account.

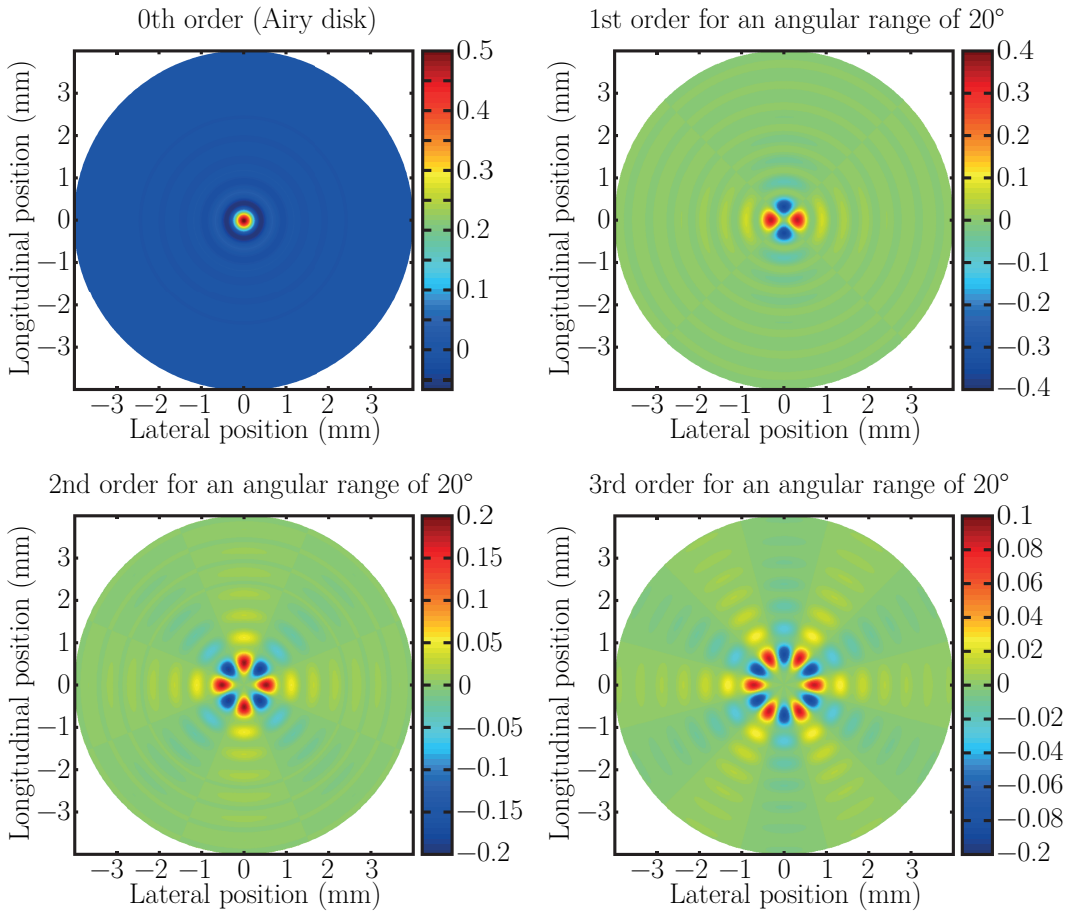

Figure 4.8 – The first three orders of $\mathscr{B}_p(r,\varphi) + \mathscr{C}_p(r,\varphi)$ are plotted. One can notice that highest orders are likely to affect regions further from the center.

The error $e(N)$ was calculated as:

$$e(N) = \| \frac{PSF(r,\varphi)}{4\theta_m \eta_m^2} - \mathscr{A}(r) - \sum_{p=1}^{N} \mathscr{B}_p(r,\varphi) + \mathscr{C}_p(r,\varphi) \| \tag{4.20}$$

where $\|\|$ stands for the 2-norm and φ is either 0° or 90°. This error was divided by $\| \frac{PSF(r,\varphi)}{4\theta_m \eta_m^2} \|$ so that the error is given in percent of the expected section. The results are plotted on figure 4.9. One can see that only few tens of orders are enough to obtain a good approximation, with a global error of less than 0.1%, of the PSF on a disk area of 4 mm diameter.

4.5.2 Study of the 2D PSF

Now we have a criterion over the necessary number of orders to compute a good approximation of the PSF, the latter was computed for several angular ranges. For information purposes, it took less than 700 ms to compute the whole PSF over a 4 mm range with 1° steps and the first 30 orders. Figure 4.10(a) shows the PSF for a range of ±20° which is a typical range for commercial linear probes. The bandwidth BW was taken equal to 4 MHz, which is a relevant value for usual pulses, *e.g.* 2 cycles at 8 MHz. One can see that the finite range distorts the PSF in the lateral direction as expected. A slice along the $\varphi = 0°$ and $\varphi = 90°$ directions are plotted respectively on figures 4.10(b) and 4.10(c). The full width at half maximum (FWHM) of the main lobe in each direction was assessed thanks to these two plots and it was found that the lateral size is about

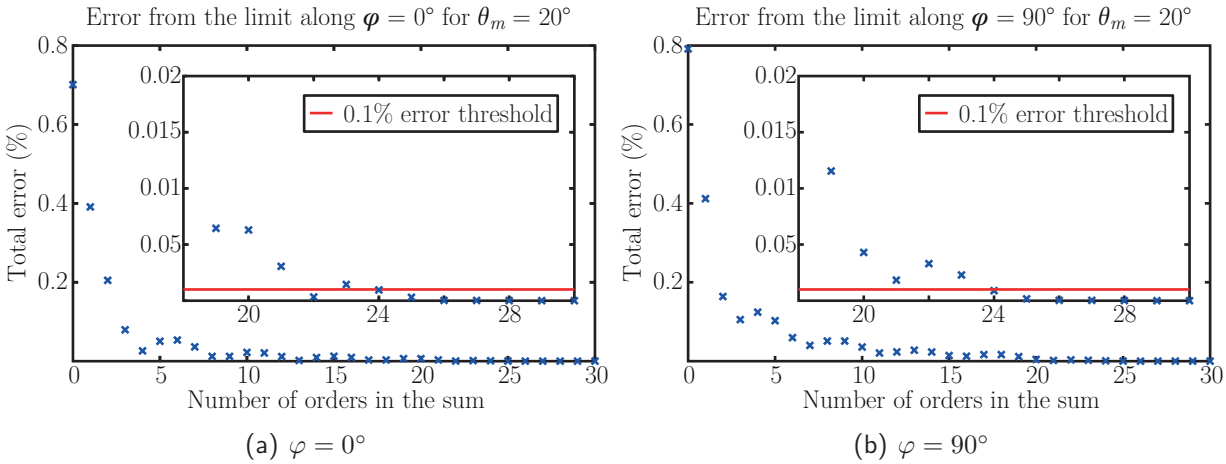

(a) $\varphi = 0°$ (b) $\varphi = 90°$

Figure 4.9 – Computed integrated error between the approximated section and the exact PSF as a function of the number of orders N used for calculation. Because the calculation of the exact PSF is long, the comparison was done only along the two directions of interest: (a) $\varphi = 0°$ and (b) $\varphi = 90°$. The error is given as a fraction of the 2-norm of the exact section.

3 times larger than the longitudinal one. One retrieves the scaling that was done in section 4.4.2 thanks to the Fourier plane represented in figure 4.7: the maximum spatial frequency accessible in the x-direction (ultrasound propagation axis, $\varphi = 0°$) is η_m given by the system bandwidth. In the y-direction however ($\varphi = 90°$), the maximum η_y accessible is $\eta_m \sin\theta_m$ which is approximately equal to $0.34\eta_m$ in the case of an angular range of $\pm 20°$.

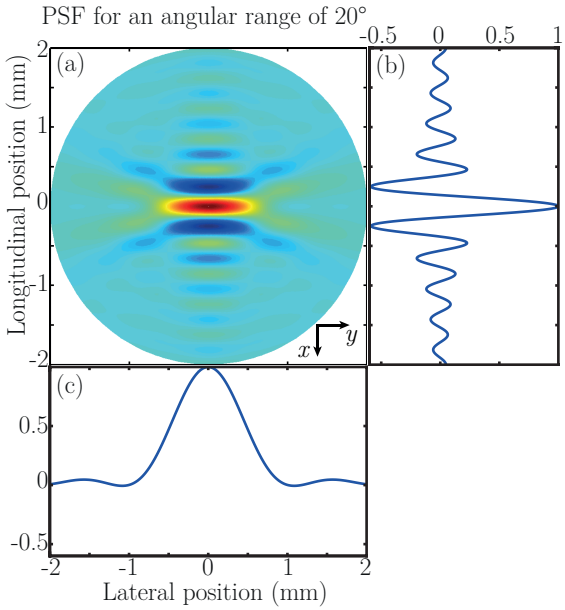

Figure 4.10 – (a) PSF for an angular range of $\pm 20°$ which is the typical range for a commercial linear ultrasound probe. One can see here that the limited angular range degrades the lateral resolution. (b) Slice along the $\varphi = 0°$ direction (x-axis). (c) Slice along the $\varphi = 90°$ direction (y-axis).

4.5.3 Resolution as a function of the angular range

The radial PSF in the longitudinal and lateral directions can be computed for different angular ranges so that the resolution is assessed in both directions and plotted on figure 4.11. The green

and blue crosses respectively correspond to the computed values of the lateral and longitudinal resolutions. A simple way of physically understanding the evolution of the two curves is to assimilate the 1D PSF to a section of an Airy disk corresponding to a Fourier space of radius respectively $\eta_{x,m}$ and $\eta_{y,m}$, where $\eta_{x,m}$ and $\eta_{y,m}$ are the maximum spatial frequency values accessible in the Fourier plane in each direction. The FWHM of the primary lobe is given in this simple case by:

$$\begin{cases} \Delta x = \frac{0.7}{\eta_m} \\ \Delta y = \frac{0.7}{\eta_m \sin\theta_m} \end{cases} \tag{4.21}$$

This simple model was plotted in plain lines on figure 4.11 and is in good agreement with the computed values of the resolution. It is interesting to notice that the lateral FWHM is even more degraded compared to an isotropic case, but its evolution is consistent. The fact that the 1D PSF is not perfectly an Airy function is also appearing in the longitudinal direction along which the secondary lobes are important. In this case the computed FWHM is below the predicted value and increases with the angular range to fit the isotropic PSF radius. This does not mean that the resolution is improved but simply that the final images will also be slightly distorted in the longitudinal direction leading to an image sharper in this direction. The deviation from the simple model above can be quantified for the lateral resolution through a fitting curve of same equation as in equation 4.21 but in which the factor of 0.7 is now an adjustable parameter. The resulting fit is shown in dashed line on figure 4.11. The fitted coefficient is now 0.88 instead of 0.7, leading to a correction coefficient of about 1.3. For angles $\theta_m < 60°$ for which the fit works well, the real expected resolution can then be estimated by multiplying the factor $\frac{1}{\sin\theta_m}$ by this correcting factor.

Here it is important to notice that, because of the cone shape of the Fourier domain, the lateral spatial cut-off frequency of the process depends on the spectral content of the object – contrary to the diffraction limit case for instance. It will result in an object-dependent distortion and not a simple anisotropic blurring, though this distortion also implies a loss of resolution in the lateral direction obviously.

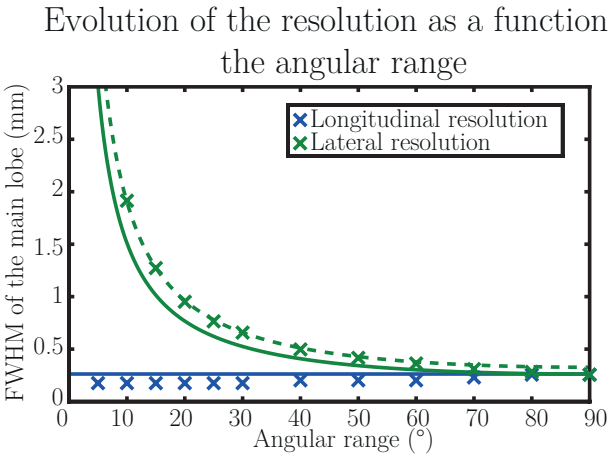

Figure 4.11 – Plot of the resolution (FWHM) along both directions as a function of the angular range. Crosses stand for computed values. Plain lines correspond to the FWHM of the main lobe assuming the 1D PSF is a section of an Airy disk. Dashed line is the previous model with a correcting factor of 1.3.

4.6 Intermediary conclusion

In this chapter, I introduced the idea of using ultrasonic plane waves and a tomographic reconstruction in order to recover acousto-optic images. I developed a simple model for the acousto-optic signal that highlighted a lot of similarities between acousto-optic imaging with plane waves and CT. This suggested that a lot of techniques that were developed in this field can be adapted to our case, and in particular the backprojection algorithm that gives a method to reconstruct the acousto-optic image. A first proof of concept showed that a simple backprojection leads to poor images because of:

- the algorithm in itself. It can be shown (cf. appendix B) that the backprojection algorithm gives a blurred version of the real image.
- the limited field of view of a linear probe, the elements of which usually emit inside a $\pm 20°$ cone.

These two observations led to the development of an analytical inversion of the problem in order to find more adapted reconstruction methods. The numerical study of this inversion allowed quantifying the expected degradations that will affect the final image due to the limited field of view of a linear probe. In the next chapter, I will show further proofs of concept and show that such sequences may lead to an increase in imaging speed.

CHAPTER 5

Ultrafast acousto-optic imaging with ultrasonic plane waves

Table of contents

In the previous chapter, I showed that, though tomography is a natural approach for multi-waves imaging techniques in which ultrasound is one of the involved modality, it was often left aside because of the need for mechanical displacement of ultrasound transducers. Coupling acousto-optic imaging with commercial ultrasound scanners and linear probes offers the possibility of using ultrasonic plane waves and a tomographic approach without physically moving the probe. I showed previously that, due to the limited field of view of linear probes, this leads to a distortion of the final images that decreases the lateral resolution. The goal of this chapter is then to demonstrate that plane waves acousto-optic imaging is effectively increasing the imaging rate. I will show first proofs of concept on simple samples that I will compare to focused acousto-optic imaging in order to characterize few experimental properties of the technique. It will be shown that the gain in imaging rate can be up to almost a factor of 50, in particular thanks to an increase of SNR that comes along with the use of ultrasonic plane waves. The end of this chapter will be devoted to develop a very preliminary idea that may allow to recover the lateral resolution.

5.1 Reconstruction method

It appeared in chapter 4 that acousto-optic imaging with ultrasonic plane waves is a physical problem very close to the CT scanner technique. It is known that several tomographic methods can then be used in order to recover the final image. As I showed in section 4.3.2, a simple backprojection algorithm leads to a blurred image with very poor contrast. In order to overcome this difficulty, I developed an exact inversion based on an inverse polar spatial Fourier transform. However, polar FFT algorithms are not easy to implement numerically and often need to interpolate the polar Fourier transform on a square grid, which leads to increased computation time. In appendix B, I showed that calculating the inverse spatial Fourier transform is mathematically equivalent to a backprojection algorithm in which each projection has been preliminarily filtered thanks to a ramp filter. This alternative algorithm is called the filtered backprojection [153] and is usually preferred. Other approaches were developed along with advances in the field of computer sciences. These are iterative methods [138, Chapter 11 and 12] that can take into account *a priori* knowledge such as known object shapes or sparsity, but these techniques will not be considered in this manuscript.

The filtered backprojection works exactly as a simple backprojection algorithm, the only difference being that each projection is filtered with the Jacobian matrix of polar coordinates switch $|\eta|$. In practice, this filtering step is critical due to the presence of noise in projection signals. In order not to overweight high frequencies dominated by white noise, this filter is usually multiplied by a rectangle function with a width corresponding to the bandwidth of the image. In order to smooth the image, the ramp is sometimes also windowed so that remaining high frequencies are attenuated (for instance cosine, sinc or hamming windows). The resulting filter is noted $f(\eta)$.

In the case of acousto-optic imaging, each acousto-optic signal $s_{\mathrm{PD}}(t = r/V_{\mathrm{US}}, \theta)$ is filtered by the correcting filter $f(\eta = \nu/V_{\mathrm{US}})$. The filtered signal $s^f_{\mathrm{PD}}(r, \theta)$ is then backprojected in real space using a delay-and-sum beamforming algorithm very similar to what is used in conventional ultrasound. For each voxel of the image, the one-way time of flight of the ultrasonic plane wave

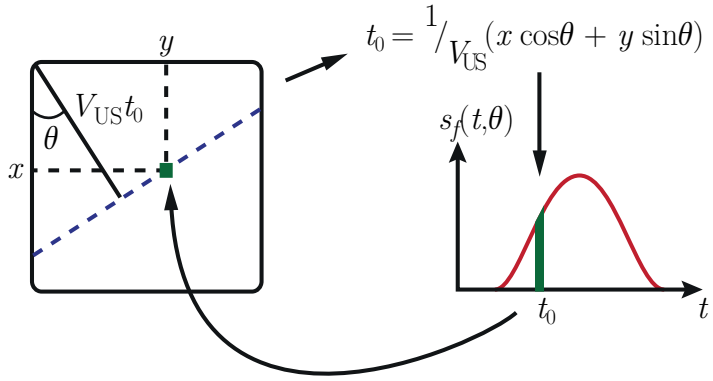

Figure 5.1 – Schematic of the filtered backprojection applied to acousto-optic imaging. Each projection is preliminary filtered by the filter $f(\eta)$. For a given plane wave angle and each voxel of coordinates (x, y) of the image, the one way time of flight t_0 of the ultrasonic plane wave is calculated. Note that all voxels on the dashed blue line correspond to the same t_0. This time of flight targets a portion of the corresponding filtered projection that defines the value of the voxel. Once all voxels of the image plane have been filled, the same is done for another angle. The backprojected filtered projections are then summed in order to recover the acousto-optic image.

is calculated as shown in appendix D. This time of flight targets a portion of $s_{\mathrm{PD}}^{f}(t,\theta)$ which defines the value of the corresponding voxel. The different values of the voxels defined by the different angles are then summed in order to recover the final image. The principle of the filtered backprojection is illustrated on figure 5.1. In our case, each projection was filtered with the following filter:

$$f(\eta) = |\eta| \cos\left(\frac{\pi\eta}{2\eta_m}\right) \mathrm{rect}_{\eta_m}(\eta) \tag{5.1}$$

where $\mathrm{rect}_{\eta_m}(\eta)$ represents the rectangle function which value is 1 over $[-\eta_m, \eta_m]$ and 0 elsewhere. In practice, $\eta_m = \dfrac{\mathrm{BW}}{V_{\mathrm{US}}}$ where BW is the temporal bandwidth of the detection scheme, limited either by the ultrasound pulses or the electronic detection bandwidth.

5.2 Study of a single inclusion

The previous section gave a more adapted tomographic reconstruction compared to the simple backprojection. However, the limited angular range accessible for commercial ultrasound probes degrades the lateral resolution by a factor of the order of $\dfrac{1}{\sin\theta_m}$. The goal of this section is to experimentally assess the capability of this method in terms of contrast and framerate.

5.2.1 Experimental setup

The setup used in this section is described on figure 5.2. The laser source is a semiconductor laser diode coupled to a 2 W tapered amplifier in order to have a MOPA (Master Oscillator Power Amplifier) system (Sacher Lasertechnik GmBH). The wavelength is 790 nm. The light beam is split into two beams thanks to a beam splitter. The signal beam is collected in a Thorlabs multimode optical fibre through a commercial collimator and guided to the scattering sample leading to an illuminating power of the order of 1.2 W on a disc area with a 1 cm diameter.

The scattered light is collected through a liquid core optical fibre with a collection area of 1 cm^2 and 0.4 NA and guided to the SPS photorefractive crystal. The reference beam (few dozens of mW) is used to perform two-wave mixing and decrease the untagged photons background. The acousto-optic signal is measured on a photodiode and processed on a computer. The acousto-optic imaging setup is coupled with a commercial ultrasound scanner (Aixplorer, SuperSonic Imagine, Aix-en-Provence, France). The ultrasound probe is a commercial ultrasound transducer array (SL10-2, 192 elements, 0.2 mm pitch, SuperSonic Imagine) with a central frequency of 6 MHz. The temporal bandwidth is 5 MHz and was chosen in order to be the lowest possible without degrading the shape of the inclusion.

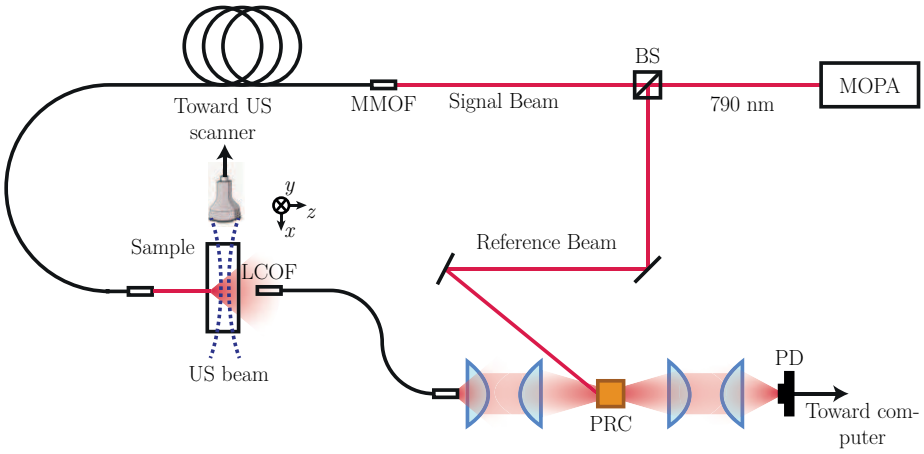

Figure 5.2 – Schematic of the experimental setup. The laser source is a laser diode added to a 2 W tapered amplifier in order to have a MOPA system (Sacher Lasertechnik GmBH). The wavelength is 790 nm. Light is split into two beams thanks to a polarization beam splitter (PBS). The signal beam is collected in a Thorlabs multimode optical fibre (MMOF) through a commercial collimator and guided to the scattering sample. The scattered light is collected through a liquid core optical fibre (LCOF) with a collection area of 1 cm^2 and 0.4 NA and guided to the SPS photorefractive crystal (PRC). The reference beam (few dozens of mW) is used to perform two wave mixing and decrease the untagged photons background. The acousto-optic signal is measured on a photodiode (PD) and processed on a computer.

The sample studied here is the same as the one presented in section 4.3.2. It is an absorbing ink inclusion embedded within a scattering gel matrix. The embedding gel is $4 \times 4 \times 3$ cm^3 with a reduced scattering coefficient $\mu_s' = 10$ cm^{-1} and negligible absorbing properties. The cylindrical inclusion is located approximately in the middle of the gel. It has a diameter of 2.5 mm and an absorption coefficient of the order of 5 cm^{-1}.

5.2.2 Focused ultrasound reference image

A first image was taken using 2-cycles pulses at 6 MHz focused at a depth of 20 mm along the ultrasound propagation beam (x-axis). The whole image needed 188 lines and each line was averaged 2000 times, thus leading to a total of 376000 ultrasound pulses. Therefore, the ultrasound sequence lasts typically 40 s at 100 µs pulsing rate. The corresponding image is shown on figure 5.3(a) with a picture of the real inclusion at the bottom. The inclusion is pointed out thanks to a white arrow. A vertical profile along the inclusion was plotted on figure 5.3(b). The acousto-optic profile was fitted thanks to a sum of two Gaussian curves:

$$\Sigma = \Sigma_{diff} - \Sigma_{incl} \tag{5.2}$$

where Σ_{diff} represents a Gaussian fit of the envelope and Σ_{incl} a Gaussian fit of the inclusion. This represents a good approximation of an absorbing inclusion in the middle of a diffused light pattern [114]. The size of the inclusion can be measured from the FWHM of Σ_{incl} and has a value of 2.5 mm which is the expected value. Let us define the image contrast as the ratio between the inclusion signal depth and the profile max value. With focused ultrasound, we find a contrast of 0.34 for the inclusion. The contrast-to-noise ratio (CNR) is defined as the ratio between the inclusion signal depth and the amount of noise in the image. This definition physically comes from the fact that the presence of an inclusion is detected through a decrease of the acousto-optic signal compared to the diffuse light envelope. Here, the inclusion is detected with a CNR of 9.

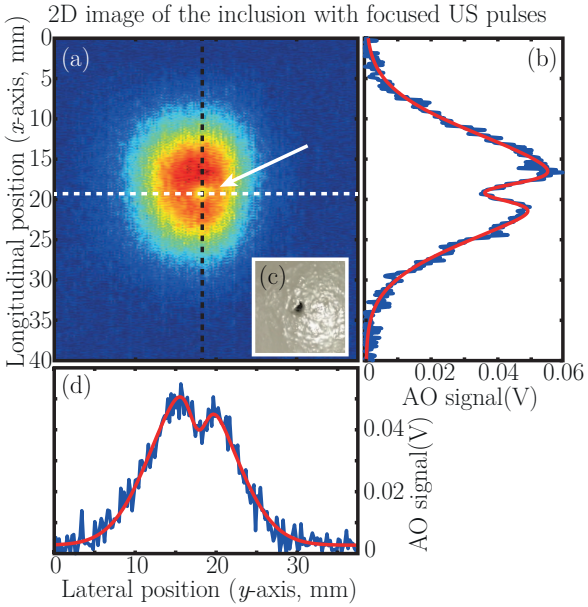

Figure 5.3 – (a) AO image using focused pulses. The white arrow points to the inclusion. (b) 1D vertical profile along the black dashed line. (c) Picture of the inclusions taken before it was embedded. (d) 1D horizontal profile along the white dashed line.

In the following, the image obtained with focused pulses will be compared to images obtained with plane waves and will act as a reference image.

5.2.3 Improvement of imaging speed

The plane waves are also 2-cycles pulses at 6 MHz. The plane waves angles range from $-20°$ to $20°$ with $1°$ steps (41 angles) and each projection was also averaged over 2000 pulses, thus decreasing the number of pulses needed by almost a factor of 5. The bandwidth of the ramp filter was defined in post-processing and set to 1 MHz. The image is presented on figure 5.4(a). As expected, the horizontal resolution is degraded compared to the focused one. A vertical profile along the black dashed line and a horizontal one along the white dotted line are respectively plotted on figure 5.4(b) and 5.4(c). It is visible here that the vertical profile is sharper than what was obtained with focused pulses. This is due to the small distortion that also occurs in the longitudinal direction and that was noticed in section 4.5.3. The size of the inclusion can be calculated in both directions thanks to the same kind of fit as presented in equation 5.2. One finds then a vertical size of the inclusion of 2 mm, which is still relevant with the expected size, though a bit smaller. The horizontal size is about 9 mm, which is relevant with the expected distortion ($> 3 \times 2.5$ mm). The contrast can be measured the same way as for focused waves.

Here we find 0.49 which is higher than in the focused wave image. The CNR is here equal to 24, almost 3 times higher. This suggests that, in order to obtain an image with equivalent CNR as with focused ultrasound pulses, the number of averaging can be divided by almost 10.

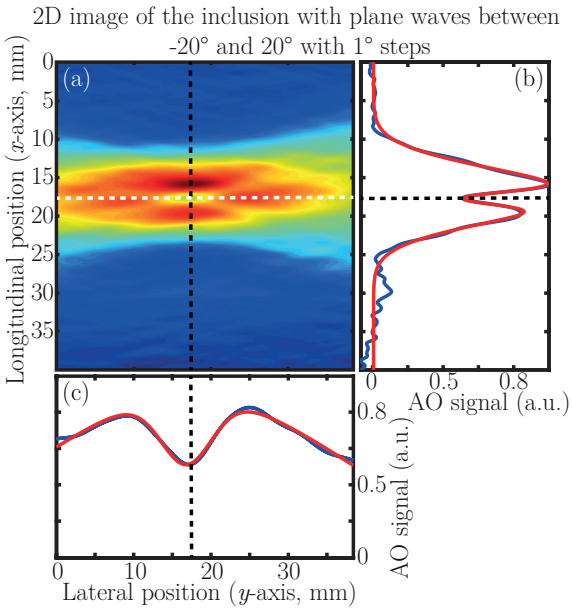

Figure 5.4 – (a) AO image using plane waves ranging from $-20°$ to $+20°$ with $1°$ steps. (b) vertical profile along the black dashed line. (c) horizontal profile along the white dotted line.

In order to confirm this hypothesis, the number of averaging was decreased down to 1000, 200 and 100 pulses and the CNR was calculated in each case. It was plotted on figure 5.5 and shows the intuitive and expected evolution as a square root of the number of averaging pulses. As expected, at equivalent CNR, only 200 averaging pulses are needed with plane waves. The corresponding plane waves image is displayed on figure 5.6. The inclusion is still visible here. Its size in both directions was measured thanks to images profiles and it was found that it is now about 8.6 mm in the lateral direction and 1.7 mm in the longitudinal one, still relevant with what was measured on figure 5.4. The ultrasound sequence in itself needed only 8200 pulses and lasts 0.82 s at 100 µs pulsing rate, which is almost 50 times faster than a focused wave sequence. The computation time must be added in order to have an idea of the overall time to get an image. In the reported example here, it took 1.8 s to compute the image using MATLAB, leading to an overall imaging time of 2.6 s. However, the computation time can be drastically reduced with parallel computation through the use of the GPU provided in the ultrasound scanner for instance.

Another interesting point to the use of plane waves is the decrease of the mechanical index (MI) of the sequence. MI is defined as the ratio of the peak negative pressure (PNP, in MPa) in tissues to the square root of the frequency (in MHz) and quantifies the risk of creating cavitation bubbles. The US Food and Drug Administration (FDA) guidelines limit the mechanical index to 1.9 for medical applications. The PNP in water was measured for our two sequences thanks to an optical interferometer and a calibrated membrane. In the case of ultrasonic focused waves the corresponding MI in tissues is 1.14, much higher than with ultrasonic plane waves, for which the MI is only 0.43, way below FDA guidelines. Interestingly, the acoustic pressure can be increased up to the safety limits if necessary, leading to an increase of acousto-optic signal - as the square of the pressure increase - much higher for plane waves than focused ones. This could contribute to further improve the imaging speed.

This increased CNR that allows decreasing the number of averaging pulses can be interpreted

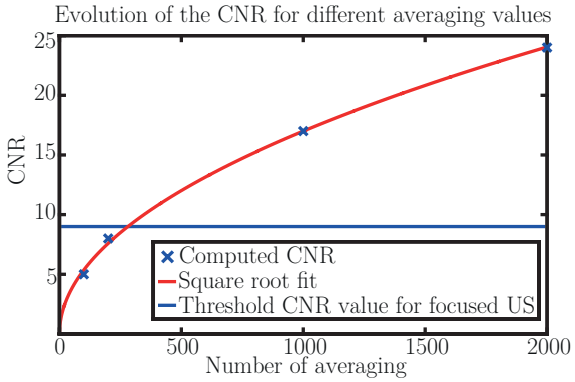

Figure 5.5 – Evolution of the CNR as a function of the averaging. The CNR level for focused US averaged 2000 times is indicated by the blue line for comparison purpose.

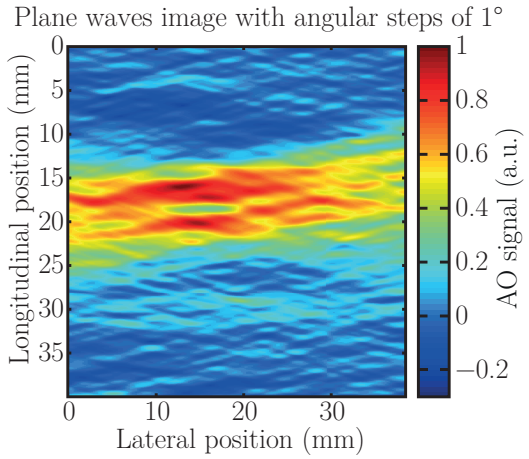

Figure 5.6 – Plane waves image with only 200 averaging per projection. The inclusion is still visible here. Its size in both directions was measured thanks to images profiles and it was found that it is now about 8.6 mm in the lateral direction and 1.7 mm in the longitudinal one, still relevant with what was measured on figure 5.4.

by considering the amount of ultrasound energy delivered to the sample. Due to the high MI of focused sequences and the directivity of the transducers, only small apertures of few tens of transducers can be used to produce focused ultrasound. On the contrary, plane waves sequences use the whole probe: the number of pulsing transducers is increased by a factor of almost 5, and so is the ultrasound energy delivered to the system. Another approach consists in noticing that the ultrasound tagging volume is much bigger with plane waves than with focused waves as the ultrasonic pressure is only 2.5 times weaker in the first case. With focused waves, the tagging volume is of the order of the impulse size at focus, that is to say of the order of $\Lambda^3 \sim 2 \cdot 10^{-2}$ mm^3, where Λ stands for the ultrasonic wavelength. For plane waves, the tagging volume extent is of the order of Λ in the x- and z-directions but is the length of the probe in the y-direction which is about 150 times the wavelength: the tagging volume is thus of the order of 2 mm^3. Hence the number of tagged photons that is expected to be higher with plane waves than with focused waves.

5.2.4 Further considerations on plane waves images

Effect of the filter

Due to the presence of noise in acousto-optic signals, the final image quality is very sensitive to the filtering parameters in filtered backprojection. In order to smooth high frequencies often coming from noise, the ramp filter is usually windowed with a cosine or a sinc function. Figure 5.7 shows typical shapes of these filters as an example. The expression for the three examples given on figure 5.7 are:

$$\begin{cases} f(\eta) = |\eta| \text{rect}_{\eta_m}(\eta) \ \text{(raw ramp filter)} \\ f(\eta) = |\eta| \text{sinc}\left(\frac{\pi\eta}{2\eta_m}\right) \text{rect}_{\eta_m}(\eta) \ \text{(with sinc window)} \\ f(\eta) = |\eta| \cos\left(\frac{\pi\eta}{2\eta_m}\right) \text{rect}_{\eta_m}(\eta) \ \text{(with cosine window)} \end{cases} \tag{5.3}$$

These filters are to be adapted to the amount of noise in the projections and the typical size of the objects to be imaged. In practice, the effect of each filter is not straightforward to predict. In the following, I suggest to explore a little bit further the effect of the filtering parameters for the three examples of figure 5.7 in order to justify the choice that was made in section 5.2.3.

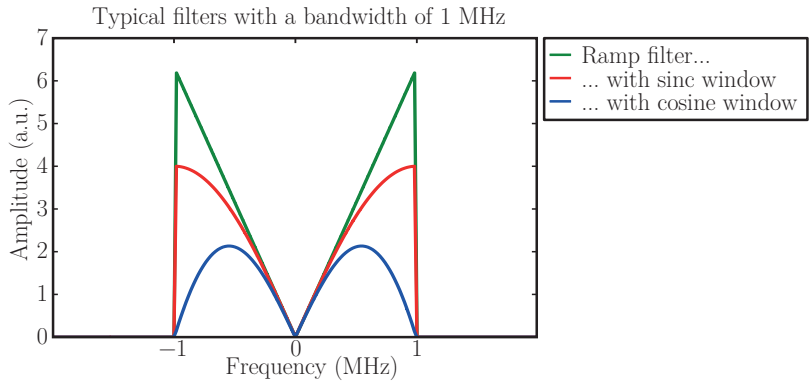

Figure 5.7 – Example of filters used in the filtered backprojection algorithm.

The plane waves image presented on figure 5.4(a) was recontructed with different windows and bandwidths. As a reminder, the filtering bandwidth BW, given in MHz because temporal signals are filtered, is related to η_m through the relation: $\eta_m = \text{BW}/V_{\text{US}}$. Profiles of the inclusion along the longitudinal and lateral direction (the same dashed lines of figure 5.4(a)) are used to measure its size. Results are displayed on figure 5.8(a) for the raw ramp filter, the sinc window and cosine window. As expected, at equivalent bandwidth, inclusion is bigger as high frequencies are smoothed by the window. However, these variations are very small compared to the total size of the inclusion so that the filtering bandwidth appears to be the most critical parameter for a relevant inclusion shape. On the other hand, because high frequencies are amplified, the filtering bandwidth is also a significant parameter in terms of noise. If low filtering bandwidths necessarily degrade the shape of the inclusion, high ones drastically increase the amount of noise on the final image. The direct consequence of both effects is a decrease of CNR. Figure 5.8(b) shows the measurement of the CNR of the inclusion as a function of the bandwidth for the different kinds of filters. As expected, the CNR is very sensitive to the bandwidth value, and this influence is sharper as the window lets high frequencies through.

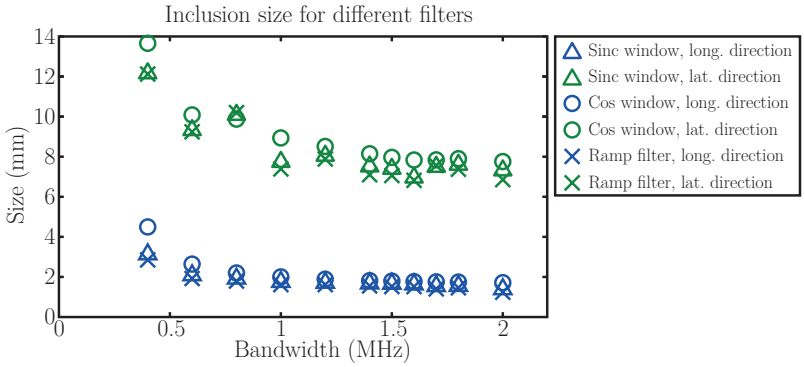

(a) Size of the inclusion

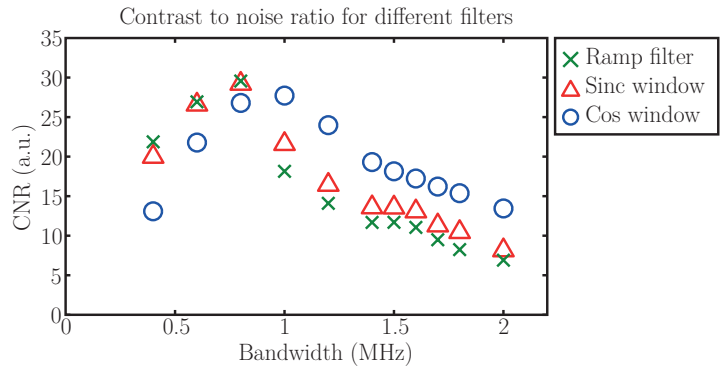

(b) Contrast-to-noise ratio

Figure 5.8 – Effect of the filter parameters for different shapes of filters. (a) Longitudinal and lateral sizes of the inclusions as a function of the filtering bandwidth. (b) Evolution of the CNR as a function of the filtering bandwidth.

Figure 5.8 gives a good idea of the influence of the filter on the final image. Here, a cosine window with a bandwidth of 1 MHz appears to be a good compromise in terms of CNR and inclusion shape though the latter is a little bit degraded. It appears that a raw ramp filter or a sinc window with a bandwidth of 0.8 MHz gives comparable results, but the cosine window seems to be less sensitive to the amount of noise in acousto-optic signals as shown by the higher CNR at high bandwidths.

The angular exploration

The distortion of the final image directly comes from the radiation pattern of the transducers for which most of energy is emitted inside a 40° cone. Figure 5.9 shows the measured projections for different plane waves angles, known as the sinogram of the image. Plane waves are emitted up to ±30°. It can be seen first that the sinogram is not symmetrical compared to 0°, due to the scattered light pattern not being perfectly centred compared to the probe – as can be seen from the focused and plane waves images. It can also be observed that the amount of acousto-optic signal is higher for one projection (max. 120 mV) than for focused ultrasound (max. 60 mV, see figure 5.3). As explained in section 5.2.3, this comes from the fact that the tagging volume is much bigger for a plane wave than a focused pulse. Despite acoustical pressure is lower for plane waves, the ratio between the two leads to higher acousto-optic signal in the first case. As the amount of noise in photorefractive detection comes from the untagged photons and scattered reference beam (beam fanning), the latter does not vary between focused or plane waves. This justifies the increased CNR on plane waves images.

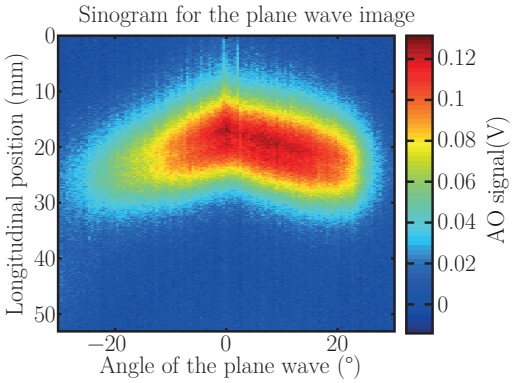

Figure 5.9 – Sinogram of the plane waves image with angles up to 30°. The sinogram is not symmetric to zero, due to the fact that the scattered light is not perfectly centred compared to the probe. Beyond 20°, the acousto-optic signal vanishes very rapidly. This is a consequence of the radiation pattern of the transducers for which most of energy is emitted within a 40° cone.

Interestingly, beyond 20° the acousto-optic signal rapidly vanishes probably due to two main reasons. The first one is purely geometry and comes from the fact that, because of the finite length of the ultrasonic wave-front, higher angles explore shallower depths and may not cross the illuminated area. The other one comes from the acoustic pressure of the ultrasound wave that decreases with angles similarly to the transducers directivity pattern so that acousto-optic signals associated with high angles decrease as the pressure squared. It is to be noticed here that the ±20° limit is not a strict limit for it appears here that there is still significant acousto-optic signal up to ±25°. The resolution may then be improved a bit by increasing the maximum angle. Figure 5.10 shows a plane waves image for different angular ranges. The improvement of lateral resolution with the increase of angular range is appearing here. The angular range of 25° also gives a small improvement of the lateral resolution (most visible thanks to the shrinking of the scattered light pattern) but this case will not be considered in the following for the gain in resolution is not significant. If one measures the lateral size of the inclusion on each figure, it appears that it decreases with the angular range indeed but not as fast as expected from what is predicted in section 4.5.3. One possible explanation may lie in the radiation pattern of the transducers. As already stated above, projections corresponding to high angles – and thus that contribute to decrease the size of the inclusion – are weaker than low angles projections because radiated energy decreases as θ increases. It could then be imagined to measure the radiation pattern of the transducers and correct each projection by the emitted pressure squared in order to recover the right contribution of each projection.

Number of angles

Previous images were obtained using angular steps of 1°. However, it is interesting to question this choice, particularly in terms of signal-to-noise ratio. Increasing the number of angles is expected to take part in the increase of signal-to-noise ratio on the same level as averaging each projection individually. However, it can be easily guessed that in case of angular oversampling the amount of useful new information brought by a new angle may be low compared to the global noise and adding projection may mostly contribute to noise. It is not straightforward thus that the influence of the number of angles on the signal-to-noise ratio is equivalent to the number of averaging of each projection. Figure 5.11 shows the same image as displayed on figure 5.4 with smaller angular steps. It is no surprise that global noise seems a bit reduced as the overall number of pulses is

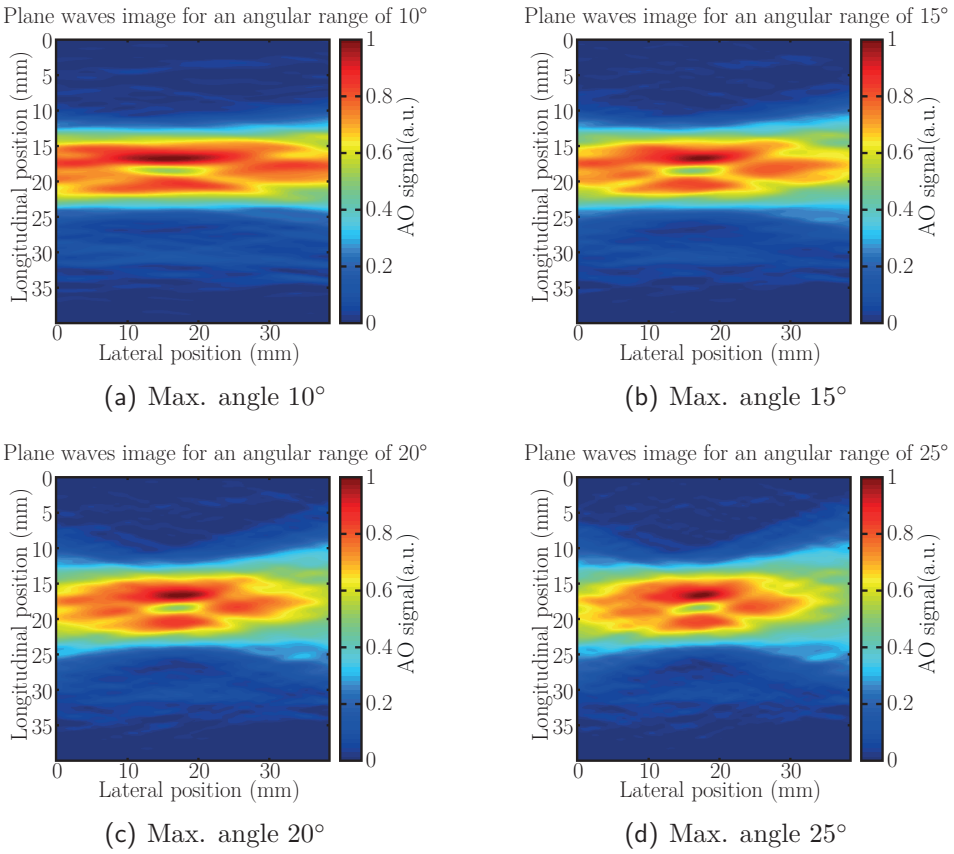

(a) Max. angle 10°

(b) Max. angle 15°

(c) Max. angle 20°

(d) Max. angle 25°

Figure 5.10 – Effect of the angular range on the reconstructed image. A maximum angular range of 25° gives a small improvement of the lateral resolution (most visible thanks to the shrinking of the scattered light pattern) but this case was not considered in the following.

increased. However, if comparing two images obtained using the exact same number of ultrasound pulses, but in which the ratio between the number of angles and the number of averaging of each projection is different, it appears that averaging each projection is not equivalent to increasing the number of angles in terms of noise. Figure 5.12(a) shows an image using 1° angular steps and 200 averaging per projection. This image is the image it was referred to in section 5.2.3. Figure 5.12(b) shows the same image using twice as many angles but averaged two times less. It can be seen that this latter image is of poor quality compared to figure 5.12(a). At given angular range, the influence of the number of angles appears not to be equivalent to the averaging of the different projections. In this case smaller angular steps do not increase the CNR for they add more noise than useful new information. In terms of imaging speed, a compromise must then be found between the number of averaging for each projection and the number of angles. Further characterisation and study of this problem are still to be performed right now.

5.3 Influence of absorbers

Previous section gave a good idea of typical images obtained with ultrasonic plane waves. However, these images were obtained on a simple symmetric inclusion, which is not very representative of the kind of objects that can be found. This section aims at studying few different objects in order to assess the capabilities of plane waves acousto-optic imaging in more complex configurations.

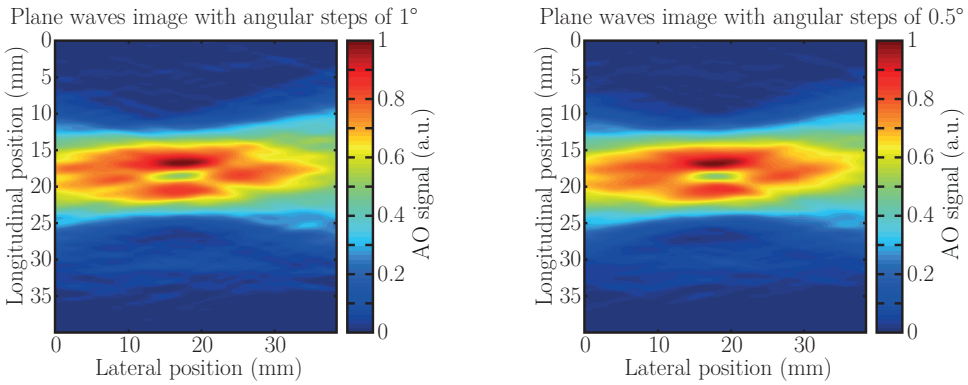

(a) 2000 averaging, 1° steps (b) 2000 averaging, 0.5° steps

Figure 5.11 – Effect of the angular step on the plane wave image. Each projection is averaged 2000 times and the number of angles is doubled from (a) to (b). It is no surprise that the noise seems reduced as the number of angles is increased.

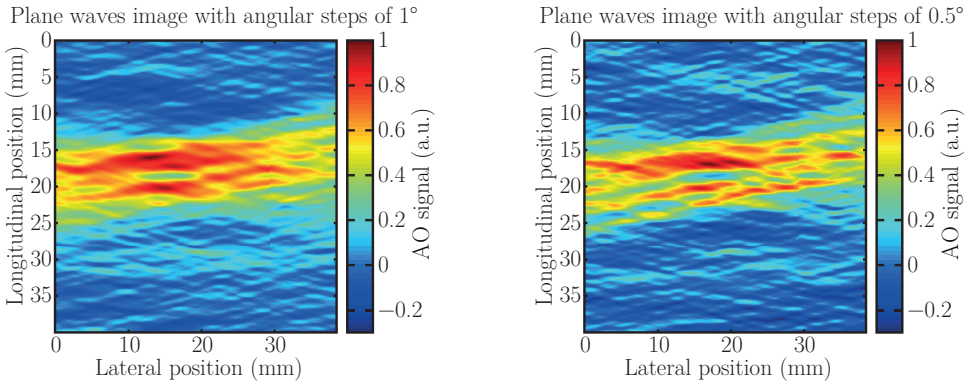

(a) 200 averaging, 1° steps (b) 100 averaging, 0.5° steps

Figure 5.12 – Two plane waves images using the same number of pulses.(a) Image using 1° angular steps and 200 averaging per projection. (b) Image using twice as many angles but averaged two times less. This latter image is of poor quality compared to the previous one. Here, smaller angular steps do not increase the CNR for they add more noise than useful new information.

5.3.1 Robustness to ultrasound artefacts

An advantage of acousto-optic imaging with plane waves is that it insonates the sample from various directions, contrary to focused pulses. As a matter of fact, areas that reflect or absorb ultrasound have less impact on the final image. Figure 5.13(a) shows a focused acousto-optic image of a black electric cable plastic sheath embedded within a scattering gel of dimensions $4 \times 4 \times 2$ cm^3 with scattering coefficient $\mu_s' = 10$ cm^{-1}. The sheath is a 1 mm diameter, 5 mm length cylinder. This cylinder is hollow in the center where the copper wire was removed. Aside from absorbing light, the plastic sheath also absorbs and reflects ultrasound: there are as many impedance losses as the number of interfaces – *a priori* 4 of them – and the plastic envelope is a visco-elastic solid – probably more absorbing than the gel matrix mostly made of water. There is no point discussing the exact acoustic properties of the inclusion, only the effect will be considered: focused pulses are weakly transmitted by the inclusion and there is a loss of acousto-optic signal underneath.

As a consequence, the inclusion shape may be badly interpreted for it is impossible to say whether the loss of acousto-optic signal is due to light absorption or absence of ultrasound. This

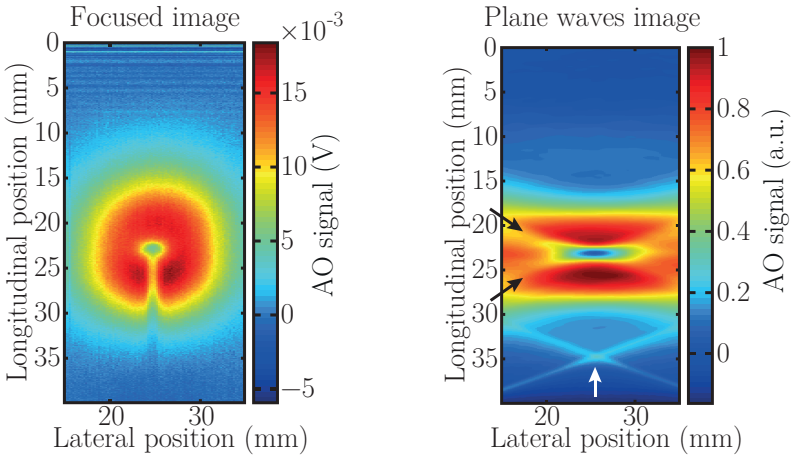

(a) Focused image (b) Plane waves image

Figure 5.13 – Image of an inclusion that also interacts with ultrasound. (a) Focused ultrasound image. The pulse is reflected and absorbed by the inclusion so that the ultrasound energy below is weak. The inclusion shape may be badly interpreted and the presence of another inclusion in this area may be undetected. (b) Plane waves image with plane waves ranging from $-20°$ to $20°$ with angular steps of $0.5°$. The shadow disappeared. Other predictable and correctable artefacts appeared.

uncertainty may be removed thanks to an ultrasound scan on which the absence of ultrasound is visible through the absence of echoes, but the presence of another light-absorbing inclusion below an ultrasound-absorbing inclusion may be undetected. Because it insonates the sample from various directions, this shadow can be removed on plane waves acousto-optic images. Figure 5.13(b) shows the same inclusion imaged with plane waves ranging from $-20°$ to $20°$ with angular steps of $0.5°$. The filter used here is the same as defined in section 5.1 with a bandwidth of 2 MHz. As expected, the shadow disappeared, but it was replaced by a cross-shaped artefact – pointed out by the two black arrows – around the inclusion induced by the limited angular range. This artefact was already visible on the PSF displayed on figure 4.10 of section 4.5.2. The main difference between this latter artefact on plane waves image and the previous one with focused pulses is that the first one comes from the imaging sequence – its behaviour is predictable and potentially correctable – as the second is *a priori* unknown. The white arrow points to another artefact appearing between 30 and 40 mm on the plane wave image. This artefact comes from the length of the projections which is too short to cover the entire diagonal of the final image and is easily corrected by increasing the length of each projections.

5.3.2 Towards more complex objects

Previous examples studied simple-shaped objects. In this section, I will show an example on a more complex object. The inclusion is a crossed-shaped inclusion embedded inside a $4 \times 4 \times 3$ cm^3 scattering gel of scattering coefficient $\mu_s' = 9$ cm^{-1}. The focused image is given on figure 5.14(a) and a picture of the inclusion is showed on the bottom of the image. The corresponding plane waves image is shown on figure 5.14(b). The inclusion is clearly appearing but the distortion due to the limited view makes it impossible to see a cross.

The lateral distortion of the image and resulting loss of resolution will make it difficult to recognize the shape of an object. However, the increased CNR and imaging speed of plane waves imaging allows locating areas of interest very easily. I can thus be imagined using these distorted

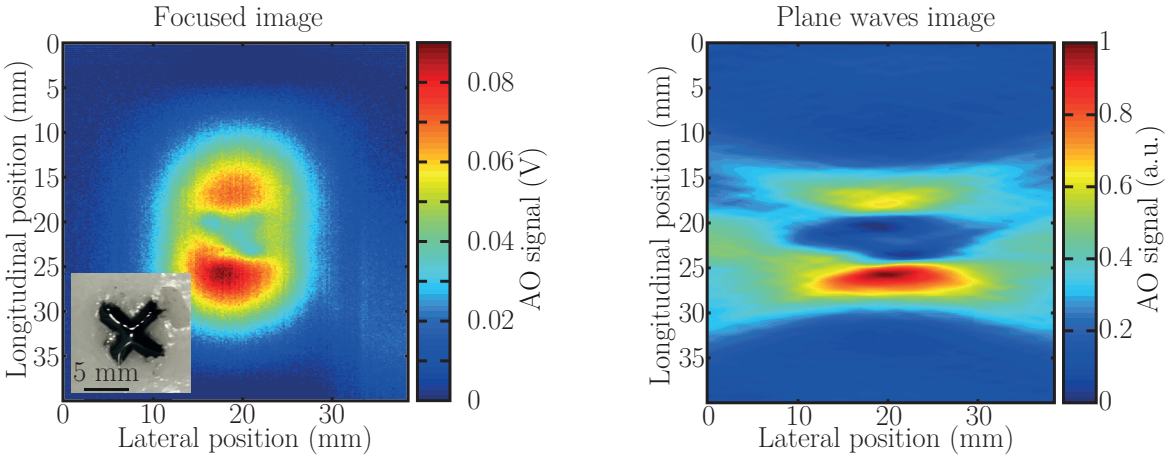

(a) Focused image (b) Plane waves image

Figure 5.14 – Image of cross object. (a) Focused pulses image. (b) Plane waves image.

images for fast preliminary imaging and detection of suspicious regions before using slower and more precise techniques. However, if one wishes to use plane waves acousto-optics as an imaging technique, previous examples showed that it is of prime interest to recover the lateral resolution. In this case, reconstruction with *a priori* knowledge of the objects can be thought of in order to correct this distortion. This ill-posed limited view problem was already studied in the field of computerized tomography and this kind of approaches were already suggested. A review of several possible – mostly iterative – approaches is given in [154]. As an example, Sato *et al.* suggested a technique in [155] that uses known information about the boundary of the object in order to iteratively correct the Fourier space after reconstruction. In the case of acousto-optic imaging, this *a priori* knowledge could be extracted from classical ultrasound scans for instance.

5.4 Two probes imaging

A simple way of recovering the lateral resolution is to return to tomographic approaches in which the ultrasound array encompasses the sample. Obviously, transducer arrays distributed over more than 180° are not easily available. A decent alternative just consists in using two orthogonal linear probes. By decreasing the imaging rate by a factor of about two, this approach may recover the lateral resolution.

A proof of principle was realized with another sample with two inclusions disposed one beside the other in the same imaging plane. This sample is $4 \times 4 \times 4$ cm^3 with a scattering coefficient $\mu_s' = 10$ cm^{-1}. The two inclusions have a diameter of 2 mm and are separated by about 5 mm. A schematic of the experiment is presented on figure 5.15. The two inclusions are close enough so that they overlap on plane waves images using probe number 1 and are impossible to distinguish. Probe number 2 is added perpendicularly to probe number 1 and is also used to perform plane waves acousto-optic imaging. Figure 5.16(a) presents a picture of the two inclusions. The focused ultrasound acousto-optic image using probe number 1 is presented on figure 5.16(b) and the two inclusions are visible and well separated. The plane waves acousto-optic image using probe number 1 and an angular range of ±20° with 1° steps is presented on figure 5.16(c). As expected according to the sample design, the two inclusions are too close one from another to be separated. It then seems to be only one big inclusion. The plane waves acousto-optic image obtained from the two

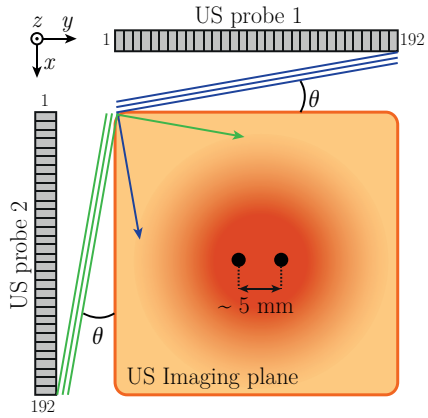

Figure 5.15 – Schematic of the sample with two inclusions and the positions of the two probes. Numbers 1 and 192 on each probe represent the locations of the first and last elements. The two inclusions are close enough so that they can not be distinguished in the plane wave image using only probe 1.

probes and the same angular domain as above is presented on figure 5.16(d). It appears that few distortions still remain due to the absence of information along the diagonal of the sample but the two inclusions are clearly appearing.

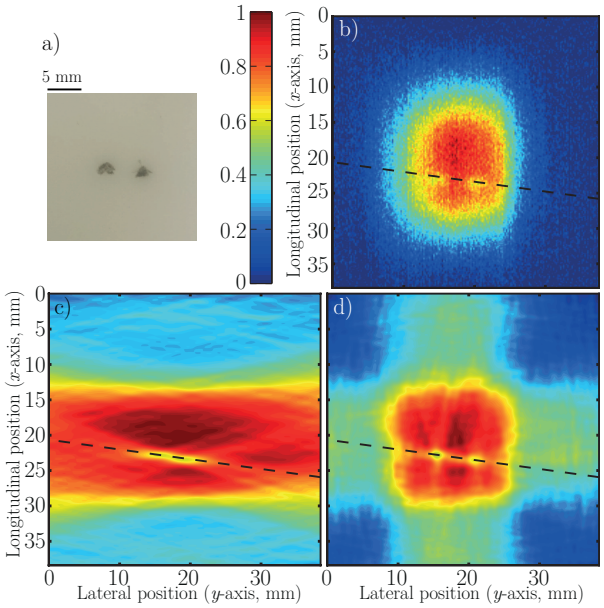

Figure 5.16 – Two probes plane waves results. The colorbar is the same for each AO image and is showed on the left side of (b). The black dashed line on each image is the line along which the profiles of figure 5.17 were plotted. (a) Picture of the gel with the two black inclusions. (b) AO image using focused US. (c) AO image using plane waves from one probe. (d) AO image using plane waves from two perpendicular probes.

Profiles along the black dashed lines visible on figure 5.16(b), 5.16(c) and 5.16(d) are plotted on figure 5.17. The expected positions of the inclusions are pointed out with two black arrows. The green profile corresponds to the inclusions on the focused ultrasound acousto-optic image which are well separated. The red profile corresponds to the inclusions on the plane waves image using only probe number 1 and confirms that the two inclusions are not separated. The distortion of the image is clearly appearing here since the scattered light envelope is almost flat though it is expected to be Gaussian-shaped as explained in equation 5.2 and visible on the green profile. The

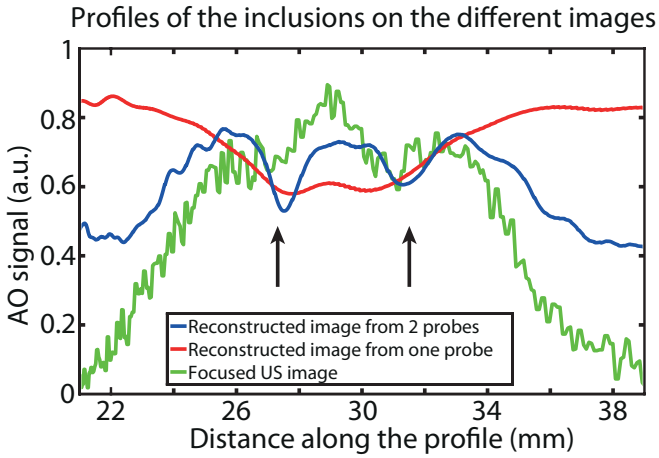

Figure 5.17 – Profiles along the black dashed lines of figure 5.16. The black arrows point the positions of the two inclusions. As expected, with one probe, it is impossible to distinguish the two inclusions as they clearly appear with 2 probes.

blue profile corresponds to the inclusions on the plane waves acousto-optic image using two probes and confirms that the two inclusions are well separated. The DC level on this profile is a residual distortion due to the fact that it still misses information in the diagonal directions of the image. Indeed, the cross shape of the image responsible of this DC level can be understood as a remaining of the elongated shape of the scattered light envelope that is not properly compensated as angles are not scanned over 180°. It is appearing here that the two inclusions on the two-probes image are slightly shifted compared to their position in the image obtained with focused ultrasound. This may be due to a small inaccuracy in the determination of the position of probe number 2 in relation to probe number 1, a wrong estimation of which would directly affect the lateral position of the inclusions. This issue can easily be addressed by using a rigid structure that could hold the two probes in the same imaging plane at fixed and controlled positions.

5.5 Prospects for acousto-optic imaging with plane waves

In the previous two chapters, I showed that ultrasonic plane waves may be used in acousto-optic imaging. By doing so, I showed that it is possible to gain at least one order of magnitude in terms of imaging speed. However, I predicted and experimentally demonstrated that this increased imaging speed is obtained at the cost of a lateral distortion of final images. This issue comes from the transducers directivity that limits emitted angles within a ±20° cone. This distortion severely degrades the shape of imaged objects but several advantages come along with this new type of sequences.

Decreased mechanical index A measurement of the peak negative pressure for focused pulses and plane waves showed that the mechanical index is over two times weaker with plane waves – and far below the FDA limits. Interestingly, the pressure can be increased up to the focused pulses value for instance, thus multiplying the acousto-optic signal by at least a factor of 4 – as the pressure squared. It might allow decreasing the number of averaging even more for example.

Increased contrast-to-noise ratio The same directivity issue that influences the plane waves also affects focused pulses: transducers that are over 20° from focal point poorly participate to

focusing. As a matter of fact, only small apertures of few tens of elements are used to focus ultrasound where the whole probe is used to generate plane waves. It results in higher acousto-optic signal in this latter case for equivalent amount of noise. I experimentally demonstrated that, despite the lower acoustical pressure, plane waves images have a better contrast-to-noise ratio compared to focused pulses images.

Robustness to ultrasound absorption Because it insonates the sample from various directions, plane waves images are more robust to interactions between ultrasound and inclusions. In the case of focused acousto-optic images, the absence of acousto-optic signal due to the absorption of pulses may lead to undetected objects below the ultrasound-absorbing inclusion.

Plane waves acousto-optic imaging could then be used for fast preliminary detection of suspicious area before using slower and more precise techniques. Moreover, several directions can be considered in order to improve images quality, depending on the kind of targeted applications. For applications that need a single-side access, plane waves images can be improved by correcting the projections with the radiation pattern of the transducers and using iterative reconstruction algorithms integrating *a priori* knowledge. It is also possible to use higher directivity transducers or slightly bent probes in order to increase the angular range and improve the lateral resolution a bit more. Obviously, in such applications, the imaging depth decreases as the maximum angles increase. A way of addressing this issue would be to use diverging waves as it is the case in CT. On the other hand, I showed that, for applications that allow two-sides access, a second probe can be used in order to recover the lateral resolution. Plane waves acousto-optic imaging might lead to reconsider tomographic applications such as small animal or breast imaging.

Part IV

Robustness to speckle decorrelation: acousto-optic imaging with spectral holeburning

CHAPTER 6

Basic principle of spectral holeburning

Table of contents

In Part II, I presented the main limitations of a photorefractive detection. I showed that the characteristic response time of a photorefractive detection is higher than the decorrelation time of speckle *in vivo*. In such a case, the hologram can not be fully engraved and it results in a decrease of the SNR and the accessible imaging depth. It then appears that a detection scheme based on a direct measurement of the *flux* of tagged photons would overcome this difficulty. However, it was brought out in Part I that the very small frequency shift of tagged photons compared to light frequency makes such a filter difficult to implement. The goal of this chapter is to introduce the principle of spectral holeburning (SHB) and show how this phenomenon can be useful for acousto-optic imaging. This work is in the continuity of what was introduced by S. Farahi in [118]. I will first study several potential techniques in order to justify the choice of spectral holeburning as a detection scheme. After presenting a few essential properties of Tm^{3+} doped YAG (Yttrium Aluminium Garnet, $Y_3Al_5O_{12}$) crystals and spectral holeburning, I will study this technique from the point of view of acousto-optic imaging in order to enlighten the main limitations.

6.1 Spectral filtering techniques for tagged photons

In chapter 2, I showed that parallel processing of speckle patterns can be made robust to speckle decorrelation *in vivo* through the use of tandem nanosecond pulses for instance [89]. However, current imaging framerates of conventional cameras are too low to time-resolve ultrasound propagation. As a consequence, as many pulses as the number of required pixels in the final image are usually to be used. In order to overcome this difficulty, people developed analogical holographic techniques that allow using single-detectors, the bandwidth of which is broad enough to time-resolve ultrasound propagation. As explained previously, the characteristic response time of photorefractive crystals is too long for enabling such a process to follow speckle decorrelation. As a matter of fact, two approaches were thought of. The first one consisted in finding faster holographic materials such as gain media [103, 104] whereas the second consisted in developing ultra-narrowband spectral filters in order to discriminate tagged from untagged photons.

The idea of using direct spectral filtering on Doppler shifted photons is not new and was already suggested by J.-P. Monchalin in 1985 [106] in order to image unpolished vibrating surfaces. In this paper, the author suggests to use a stabilized confocal Fabry-Perot interferometer. He claims that such an approach is less influenced by surface parasitic vibrations and works from any distance from the object because it is sensitive surface velocity – contrary to conventional Michelson interferometers that are sensitive to surface displacement. This approach was applied to acousto-optic imaging by S. Sakadžić and L. V. Wang in 2004 [107] and G. Rousseau *et al.* few years later [156]. Such approaches use high finesse and long stabilized interferometers (50 cm in [107], 1 m in [156]) so that angles of acceptance are small. As a consequence, the optical *etendue* of such detection schemes is weak ($0.1\ mm^2 \cdot sr$ in [107], $0.38\ mm^2 \cdot sr$ in [156]) which is damageable for scattered light and speckled wave-fronts in which photons directions are random.

In order to overcome this difficulty, Li *et al.* suggested to use spectral holeburning [108] that theoretically have a much greater optical *etendue*. Basic principle of spectral holeburning will be detailed in the following sections. Briefly, it consists in burning a narrow transparency window

inside the transmission of an inhomogeneously broadened spectral line. This hole can be very narrow (from few hundreds of kHz to few MHz) so that is is possible to have untagged photons being fully absorbed by the crystal as tagged photons are mostly transmitted. In [108] authors used a Tm^{3+} doped YAG crystal of dimensions $10 \times 10 \times 1.5$ mm^3 with a 2 at.% substitution rate that has the advantage of having an absorption line at 793 nm, right in the middle of the therapeutic window. Using such a filter, authors achieved tagged photons filtering – 5 MHz ultrasound frequency – with an improvement of the crystal transparency of 14 dB – meaning that the resulting filter increases the transmission of tagged photons by a factor of 25. Though such techniques only work at cryogenic temperatures, they allow increasing the optical *etendue* by at least two orders of magnitude – the authors estimate the optical *etendue* of the order of 31 mm$^2\cdot$sr, limited by the numerical aperture (NA) of the cryostat windows. Independently from these works, spectral holeburning was explored at the Institut Langevin by S. Farahi during her PhD [118] but was left aside because the cryostat at this time did not allow low enough temperatures.

Recent results obtained with the bimodal platform highlighted limitations of a photorefractive detection and led to reconsider spectral holeburning filtering for acousto-optic imaging. In the next two chapters, I will work on the same kind of crystals as used by Li *et al.* . Our crystal is a Tm^{3+}:YAG crystal of dimensions $10 \times 10 \times 2$ mm^3 with a 2 at.% substitution rate. It is important to notice that, though cryogenic temperatures seem to be a big drawback of the technique, similar conditions are used in MRI for which big supraconductive coils are continuously immersed in liquid helium.

6.2 Choice of Tm^{3+}:YAG crystals

In section 6.1, it was shown that spectral holeburning could be a convenient filtering technique. I pointed out a few expected properties of an efficient filter and showed a first proof of concept. In this section I suggest to explore the physical justifications for the choice of the crystal that was used earlier. It is not aimed at giving a complete description in this section, but only to give a few essential features. A complete study of rare-earth ions in crystal lattices can be found in [157] and a more precise description of the properties of Tm^{3+} in a YAG crystal lattice is given in French in [158].

6.2.1 Tm^{3+} ions in a YAG matrix

Rare-earth-doped crystals have a few ideal characteristics for ultra-narrowband filters. Rare earth elements are the 14 elements that follow lanthanum in the periodic table, among which is thulium. They have the following electronic structure :

$$[\mathrm{Xe}]4f^n5d^16s^2 \tag{6.1}$$

where n is an integer varying from 1 for cerium to 13 for ytterbium. When ionized, they usually lose the electrons in the subshells of highest energy, that is to say the two electrons in the $6s$ and the electron in the $5d$ orbitals. The typical stable oxidation state of these elements is then +III. In the xenon electron configuration the highest two occupied subshells are $5s$ and $5p$, that are further away from the center – though less energetic – than the optically active $4f$ subshell. As a matter of fact, $4f$ – $4f$ transitions are partially screened by the $5s$ and $5p$ orbitals, resulting in low influence of the environment. A direct consequence is that rare-earth ions behave in crystal lattices almost as free ions so they have very sharp energy levels [159, Chapter 8]. A review of the

properties and applications of rare-earth in crystal lattices can be found in [160].

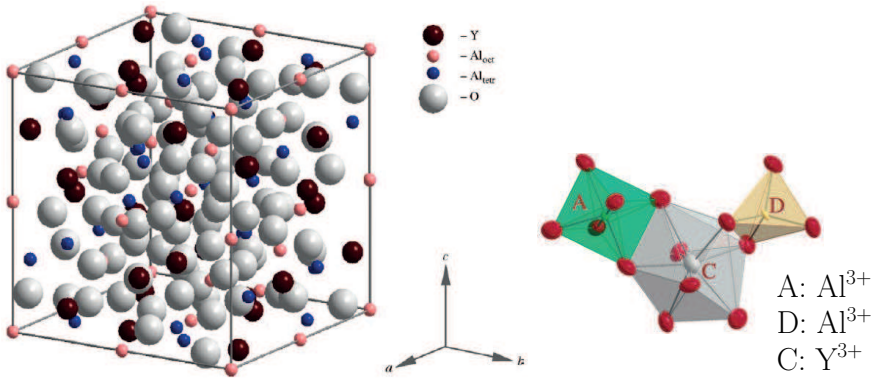

(a) Structure of YAG crystal (b) Yttrium site

Figure 6.1 – Structure of YAG crystal. (a) General structure of a unit cell of the lattice. Figure extracted from [161]. (b) Zoom over the Yttrium site. Figure extracted from [162]. A and D corresponds to Al^{3+}sites and C to Y^{3+}. Tm^{3+} is substituted to Y^{3+} ions so that it is noticeable here that they are surrounded by two non-equivalent Al^{3+} sites – A is in an octahedral environment as D is in a tetrahedral one. The local electric field around Tm^{3+} sites is not isotropic resulting in a dipole moment.

Let us focus now on thulium ions Tm^{3+}, for which $n = 12$. Tm^{3+} doped YAG are crystals in which some yttrium ions in low symmetry centres have been substituted by Tm^{3+} ions. The symmetry group of garnet crystals, among which is YAG, is given in [163] and the structure is shown on figure 6.1(a). A zoom over the Y^{3+} site is shown on 6.1(b). It appears that the local electric field around each Tm^{3+} ion is not isotropic [161] so it results that each site has a dipole moment. Due to the geometry of YAG lattice and rotation invariance, thulium ions can be found in 6 different crystallographic sites [164] represented on figure 6.2. The dipole moment of each site is oriented along the long dimension of each rectangle on figure 6.2. A complete demonstration of the existence of these sites through symmetries invariance is given in [158]. It will be admitted here that, even if these sites are not equivalent in relation to light polarization when light is propagating along $[1\bar{1}0]$, the resulting absorption coefficient is independent of the polarization direction of the electric field – for one given polarization, the strength of the interactions with the electric field is compensated by the number of excited atoms [158].

The transitions that are considered here are the $4f - 4f$ transitions. These transitions, yet forbidden in the free ion due to the Laporte selection rule, may be made possible in a crystal lattice. A complete description of the energy levels and possible transitions in Tm^{3+}:YAG is given in [165] but there is no point entering this level of details here. I will focus on levels involved in holeburning process. A schematic of these levels is presented on figure 6.3. The transition I consider is the transition from the ground state $^3H_6$ ($|g\rangle$) to the excited state $^3H_4$ ($|e\rangle$) around 793 nm. An important parameter of the transition is its oscillator strength f that characterizes how strong is the transition response to an excitation. It was evaluated by G. Gorju *et al.* [166] in a 0.5 at.% substitution rate crystal to about 1.8×10^{-6}. The oscillator strength can be used to evaluate a lot of other parameters such as the Einstein coefficients [167].

From the excited state, ions can either decay back to the ground state through radiative transfer or decay into two other states, $^3H_5$ and $^3F_4$, through non-radiative relaxation. Non-radiative transfer can also occur from the $^3H_5$ state to the $^3F_4$ state, and eventually atoms can transfer back to the ground state from $^3F_4$ through non-radiative relaxation also.

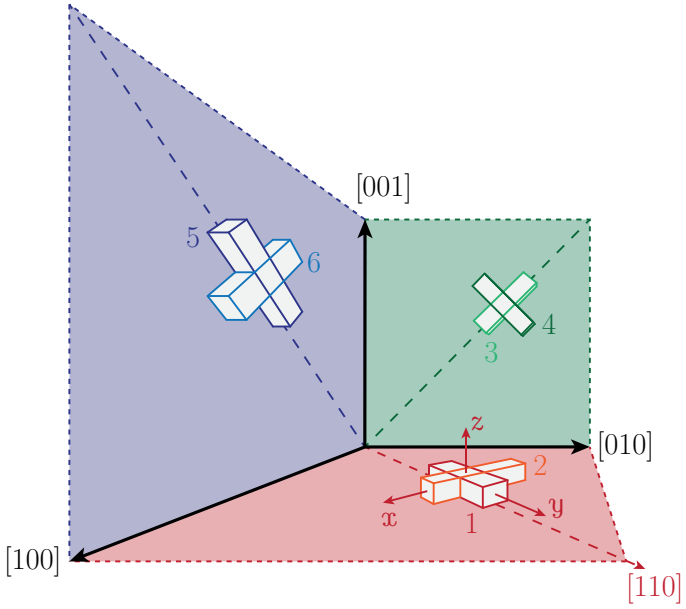

Figure 6.2 – Representation of the different possible sites for Tm^{3+}. Each rectangle represents the D_2 symmetry of the crystal field. x, y and z axes are the local axes of the sites. The dipole of each site is oriented along the longest dimension of each rectangle, *i.e.* y-axis oriented along $[110]$. In the following, I will consider a crystal cut along the $[110]$ axis and light propagates along the $[1\bar{1}0]$ axis (the x-axis represented here).

6.2.2 Linewidth broadening

As explained above, the main advantage of rare earth ions is the narrow linewidth of the transitions $4f - 4f$. Mechanisms responsible for linewidth broadening can be sorted into two main categories: *homogeneous* and *inhomogeneous* broadening.

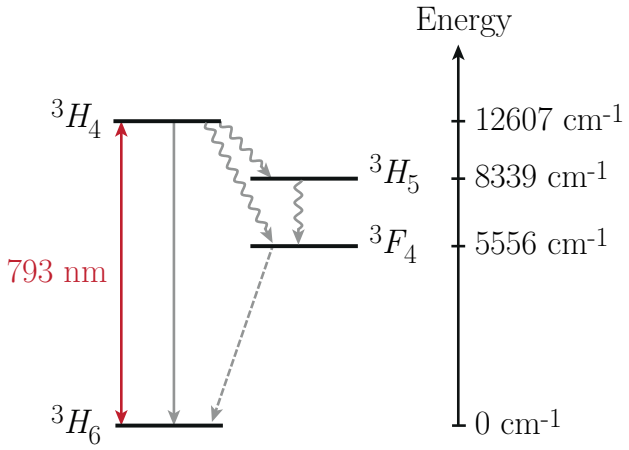

Figure 6.3 – In order to make the problem simpler, only the levels involved in SHB are considered here. A schematic representation is shown here.

Homogeneous linewidth

The homogeneous linewidth Γ_h is the linewidth that would be measured if working with only one ion, that is to say the FWHM of the Lorentzian absorption line of one transition $^3H_6 - {}^3H_4$. This

linewidth is directly related to the lifetime of the coherences associated to the transition T_2:

$$\Gamma_h = \frac{1}{\pi T_2} \tag{6.2}$$

This lifetime is ultimately limited by the lifetime of the excited state of an atom in vacuum, that is to say the characteristic time an atom remains in the excited state before relaxing to the ground state through spontaneous emission. This lifetime is noted T_1.

$$\Gamma_h = \frac{1}{\pi T_{2,max}} = \frac{1}{2\pi T_1} \tag{6.3}$$

One can then easily understand that in order to have a homogeneous linewidth as narrow as possible, long excited state lifetimes are necessary. Because the $4f - 4f$ transitions are forbidden, the transition probability is weak and the lifetime of the excited state is long, making rare earth elements good candidates.

Up to now, only one atom was considered. However, it must be taken into account that one is rather working on a population of atoms in a given environment, assumed identical for all atoms. These atoms can interact incoherently with the surroundings through collisions or spin exchange for instance. This is a dynamic effect that reduces the lifetime of coherences and broadens the linewidth. It can be expressed as follows [168, Chapter 3]:

$$\frac{1}{T_2} = \frac{1}{T_{2,max}} + \frac{1}{T^*} \tag{6.4}$$

where T^* is a characteristic time that denotes the decrease of coherences compared to the lifetime of the excited state.

A complete description of the mechanisms involved in homogeneous broadening in crystal lattices is given in [157]. Three main mechanisms can possibly occur: ion-phonon, ion-ion and ion-lattice couplings. It can be shown that coupling between ions and lattice vibrations is the dominant source of broadening at temperatures above 5 K. However, it rapidly becomes negligible around 2 – 3 K so that ion-ion and ion-lattice couplings become the main sources of linewidth broadening. This phenomenon enlightens the main difficulty of a detection scheme based on spectral holeburning: it works efficiently at cryogenic temperatures. It is stated in [158] that ion-ion coupling, that is to say Tm^{3+} coupling with other Tm^{3+} in the crystal, is negligible at low doping concentration (0.01 at.%). In very absorbing crystals, 2 at.% Tm^{3+} here, this contribution is expected to be more important and not necessarily negligible. The ion-lattice coupling is mainly due to magnetic spin flips between Tm^{3+} and crystal lattice ions through two processes shown in figure 6.4. The first process is a direct process in which spins flip through the exchange of one or several phonons. The second one is a *flip-flop* process in which spin flips are synchronous at constant energy, which makes them particularly efficient.

Inhomogeneous linewidth

In the previous paragraph, I studied the linewidth of one transition of a population of ions in a given environment and how it may be broadened by interactions with the surroundings. In practice, the environment is not strictly identical for all populations of ions so that the resulting line is not a homogeneous spectral line but a superposition of several ones corresponding to different spectral classes of atoms with slightly shifted resonant transitions. Its width is called the inhomogeneous linewidth and is noted Γ_{inh}. This is the linewidth that can be measured through a spectrometer.

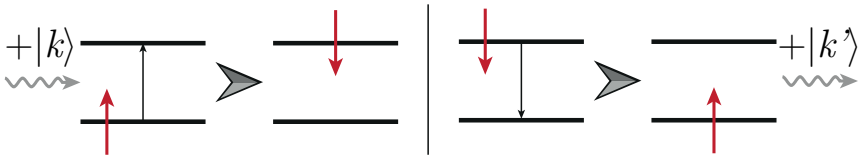

(a) Direct process

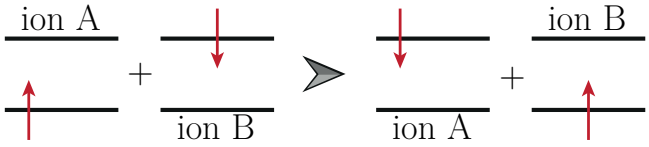

(b) *flip-flop* process

Figure 6.4 – Schematic of spin flips processes

Inhomogeneous broadening occurs in several kinds of media. For instance, in gases, the distribution of molecules velocities due to thermal energy leads to an inhomogeneous broadening through Doppler effect: the transition of each population of same velocity is shifted of the corresponding Doppler frequency. In crystals, inhomogeneous broadening comes from impurities, strains or defects in the crystal lattice structure that slightly modifies the local crystal field around Tm^{3+} ions. It results in shifted transitions that are inhomogeneously distributed over the spectral domain Γ_{inh} as shown on figure 6.5. The shape of the inhomogeneous line is not straightforward as it mainly depends on the defects statistical distribution [169]. In the case of gases for instance, the velocity distribution obeys a Maxwell-Boltzmann law so that the resulting line is Gaussian-shaped. In solids, this line is often approximated to a Gaussian curve also but, in the following, I will use a Lorentzian shape approximation that stands as long as holeburning process occurs around the the centre of the line. The FWHM of this Lorentzian curve defines the linewidth Γ_{inh}.

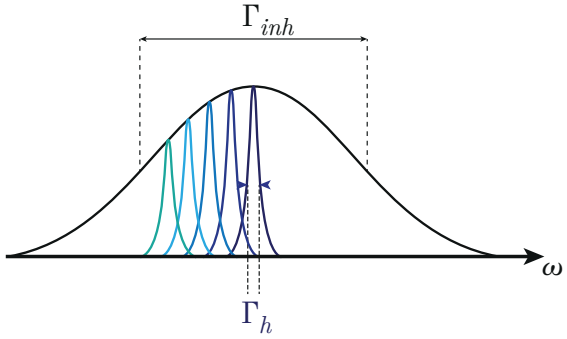

Figure 6.5 – Schematic of an inhomogeneous linewidth. This is the superimposed contribution of several shifted homogeneous linewidths.

6.2.3 Characterization of the linewidths

The experimental setup presented on figure 6.6 was installed at Institut de Recherche de Chimie Paris in Philippe Goldner's team in order to further characterize the properties of our crystal. It consists in a semi-conductor laser diode (Toptica DL pro) emitting about 30 mW around 793 nm coupled through a polarization-maintaining optical fibre with a semi-conductor 2 W fibred amplifier (Sacher Lasertechnik GmbH). The output beam of the amplifier is sent into a double pass acousto-optic modulator in order to precisely control light frequency without deflecting the beams.

The beam is focused in the crystal thanks to a 200 mm focal length lens and collected on a photodiode (Thorlabs PDB150A ~ 1 mm^2). A small part of the light is sent into a lambdameter. The crystal is a $10 \times 10 \times 2$ mm^3 2 at.% Tm^{3+}:YAG. Let $\alpha(\lambda)$ stand for the wavelength-dependent absorption coefficient in cm^{-1} and L stand for the thickness of the crystal.

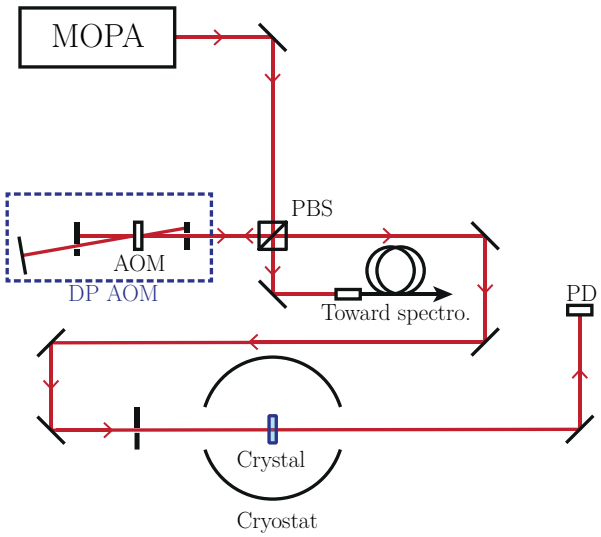

Figure 6.6 – The characterisation setup. MOPA: Master Oscillator Power Amplifier composed of a master fibred semi-conductor laser diode (LD) feeding a fibred tapered amplifier. PBS: Polarization Beam Splitter. AOM: Acousto-Optic Modulator in a double-pass configuration (DPAOM). PD: Photodiode. The beam is focused on the crystal with a 200 mm focal length lens.

The inhomogeneous linewidth is the linewidth returned by a spectrometer. At temperatures under 4 K, the homogeneous linewidth is very small compared to the inhomogeneous linewidth so that the latter does not vary with temperature in these conditions. The inhomogeneous linewidth Γ_{inh} is of the order of 20 GHz. For instance, G. Gorju *et al.* [170] reported an inhomogeneous linewidth of 25 GHz at 4.5 K for 0.5 at.% Tm^{3+}:YAG crystals. In our case, the inhomogeneous linewidth of our 2 at.% crystal was measured at 3 K by scanning the wavelength of the laser diode over $\pm$ 40 GHz ($\sim$ $\pm$ 0.1 nm) around the central wavelength of the transition (12604.32 cm^{-1}, 793.3788 nm). The total attenuation $\alpha(\lambda) L$ was probed thanks to short and weak light pulses (200 µs , 2 µW) at 10 Hz repetition rate. The absorption line is plotted on figure 6.7 and the linewidth Γ_{inh} was estimated to about 36 GHz through a Lorentzian fit.

As explained in chapter 2, the tagged photons over untagged photons ratio is very weak so that noise is ultimately dominated by untagged photons. It is thus fundamental to use a very absorbing crystal in order to have the highest possible tagged/untagged photons ratio. On figure 6.7, the maximum absorption of the crystal $\alpha_m L$ is about 3.1. Here α_m stands for the maximum absorption coefficient of the spectral line. For comparison purposes, A. Louchet measured an absorption $\alpha_m L = 0.7$ in a 0.1 at.% and 5 mm-thick crystal [158] and Li *et al.* state that $\alpha_m L \sim 4$ for their 2 at.% - 1.5 mm thick crystal [108]. An order of magnitude of the expected $\alpha_m L$ of our 2 at.% - 2 mm thick crystal is thus estimated between 5 and 6. It then appears that the measured absorption is not as high as expected. The absorption may mainly be underestimated due to broadband Amplified Spontaneous Emission (ASE) coming out of the fibred amplifier. The emission spectrum given in its specifications is shown on figure 6.8. It is noticeable here that the ASE baseline is about 30 dB under the emission line but is about 20 nm wide, where the Tm^{3+}:YAG absorption linewidth is only of the order of 0.07 nm. As a consequence, ASE contributes to a DC level of light going through the sample without being absorbed. Moreover, the crystal being

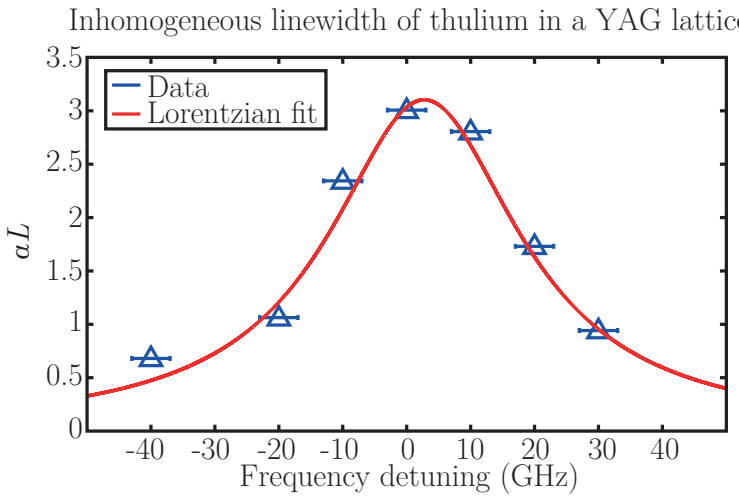

Figure 6.7 – The inhomogeneous linewidth of the crystal at 3 K. The inhomogeneous linewidth was estimated thanks to a Lorentzian fit and is of the order of 36 GHz. The crystal maximum absorption $\alpha_m L$ is of the order of 3 as it is expected to be at least of the order of 5. This may be due to ASE being transmitted through the crystal without being absorbed (see figure 6.8).

very absorptive – about 20 to 25 dB expected –, this DC level may be of the order or even higher than the absorbed light on the photodiode, thus potentially drastically decreasing the estimated value of the absorption[1].

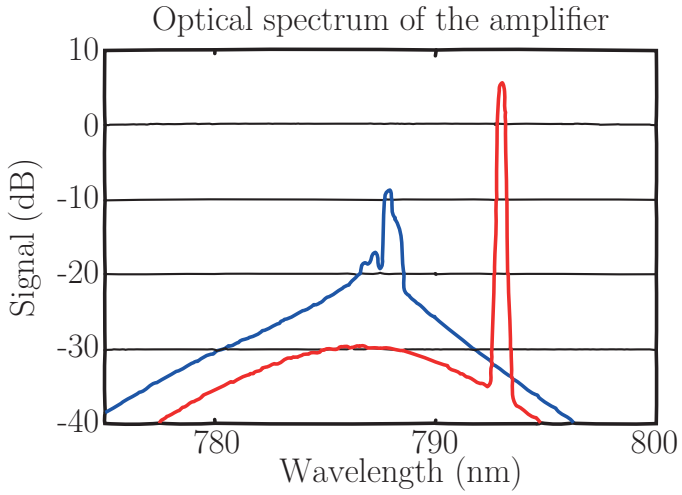

Figure 6.8 – The emission spectrum of the fibred amplifier digitized from the specifications documentation provided by the supplier. The blue curve corresponds to the optical spectrum without the master laser, the red curve corresponds to the spectrum with the master laser. Feeding current is not specified.

If the inhomogeneous linewidth is quite easy to measure, it is not as straightforward to obtain the homogeneous linewidth. If only one population of atoms was probed, the homogeneous linewidth could theoretically be measured by exciting the atoms with a short light pulse – shorter than the coherence lifetime – and measuring the decay time of the resulting macroscopic atomic dipole radiation. However, because of inhomogeneous broadening, dipoles oscillate at different frequencies and add incoherently, resulting in a macroscopic dipole decaying much faster than the expected

[1]It is furthermore possible that the probing beam also slightly burns a hole while probing so that the crystal may appear more transparent than expected

time. A robust method to measure the homogeneous linewidth is to measure the decay time of a photon echo. The phenomenon of photon echo is described in [168, Chapter 9] and its complete study is out of the scope of this manuscript. The principle of photon echo phenomenon is very similar to spin echoes that are used in MRI. Inhomogeneous broadening induces a fast decay of the macroscopic polarization induced by a light pulse because all dipoles have slightly different frequencies. Because this decay is due to the dephasing of the different microscopic dipole moments, it can be time-reversed by a second light pulse. The rephasing of the dipole moments re-induces a macroscopic polarization and a light emission called photon echo. The area of the photon echo signal is proportional to the number of moments that have been rephased. Interestingly, atoms that lost their coherence between the two pulses because of homogeneous broadening do not participate to photon echo. It then appears that the decay of photon echo along with the delay between the two pulses is proportional to the coherence lifetime and gives information about the homogeneous linewidth.

R. M. MacFarlane measured a homogeneous linewidth for the $^3H_6$ - $^3H_4$ transition of 4 kHz at 1.5 K [171] and studied its thermal behaviour [172] in a 0.17 at.% Tm^{3+}:YAG crystal. In our case, the photon echo decay was measured at 3 K and is plotted on figure 6.9. As shown in [168, Chapter 9], the photon echo decay time T_{PE} is related to the homogeneous linewidth Γ_h through the relationship:

$$\Gamma_h = \frac{1}{4\pi T_{\mathrm{PE}}} \tag{6.5}$$

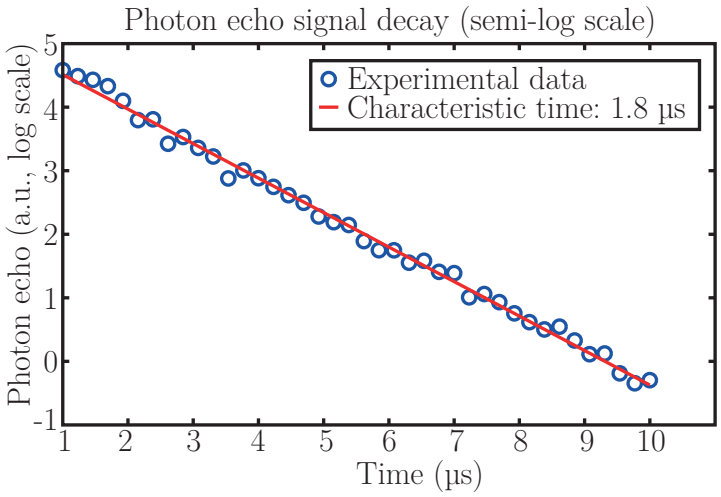

Figure 6.9 – Photon echo decay in logarithmic scale. The photon echo intensity is the number of atoms that were involved in the echo generation and is measured thanks to the echo signal area. It is plotted as a function of the delay between the first and the rephasing optical pulses and gives a decay time of 1.8 µs.

The measured photon echo characteristic decay time was $T_{\mathrm{PE}} = 1.8$ µs, resulting in a homogeneous linewidth of 44 kHz. Based on [172], the homogeneous linewidth increases fast with temperature (*e.g.* 1 MHz at 6 K). Beside temperature considerations, the linewidth may be broadened through ions-ions interactions that are more important in the 2 at.% crystal than in the 0.17 at.% crystal used in [171].

6.3 Principle of spectral holeburning

The previous section presented a few useful general features of Tm^{3+}:YAG crystals in order to understand spectral holeburning process. The goal of this section is to describe the basic principle of spectral holeburning and a few experimental considerations about holes properties, with respect to acousto-optic imaging requirements.

6.3.1 General idea

Let us consider the transition studied in section 6.2.1. The lifetime of the $^3H_4$ state is of the order of 800 µs for an isolated ion as shown in [173]. In this paper, authors studied the lifetime of this excited state as a function of Tm^{3+} concentration, among others. They showed that this lifetime is reduced due to cross relaxation between Tm^{3+} ions and measured a value of the order of 400 µs at 8 K in 2 at.% crystals. Direct relaxation from $^3H_4$ to $^3H_6$ is weak so that $^3H_4$ preferentially decays into $^3F_4$ through multiphonon emission via $^3H_5$, the lifetime of which is short enough to neglect this level. The lifetime of $^3F_4$ is of the order of 10 ms, significantly longer than the excited state lifetime. $^3F_4$ is called the metastable state due to this long lifetime and noted $|m\rangle$. A simplified representation of the levels in which $^3H_5$ was omitted is shown on figure 6.10. In the following $^3H_6$ and $^3H_4$ will be respectively referred to as $|g\rangle$ and $|e\rangle$.

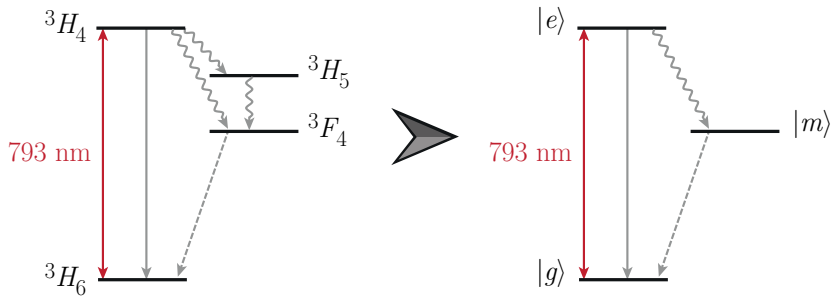

Figure 6.10 – As the lifetime of level $^3H_5$ is very short compared to the other three, it is not taken into account in the holeburning process. The system is now considered as a three-levels system composed of $|g\rangle$, $|e\rangle$ and $|m\rangle$.

The spectral holeburning process is based on two main steps : the burning and the probing sequences. A schematic of the process is represented on figure 6.11 and 6.12 as the two different steps are detailed below. Spectral holeburning is a particular case of *saturated absorption* that also occurs in gases [168, Chapter 6].

Burning sequence

A burning sequence is represented schematically on figure 6.11. The burning sequence consists in a narrowband light beam at ν_b within the inhomogeneous linewidth, lasting a time T_b. T_b is supposed very long compared to the coherence lifetime so that it optically pumps the spectral classes of atoms with a resonant transition close to ν_b. Ions in the ground state are excited in $|e\rangle$ and may non-radiatively decay in the metastable state $|m\rangle$, in which they stay about 10 ms. Provided the burning irradiance Φ_b and the burning time T_b are high enough, it is theoretically possible to almost empty the ground state and place all ions in $|e\rangle$ and $|m\rangle$.

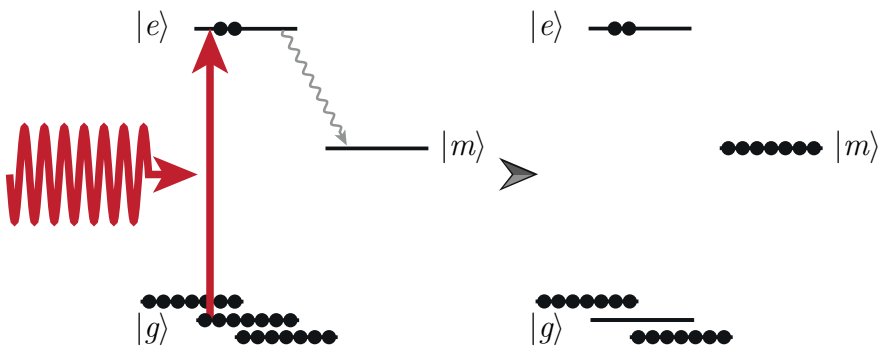

Figure 6.11 – Scheme of a burning sequence. A powerful optical beam is sent on the crystal. It is tuned on a specific frequency so that it optically pumps the corresponding level while not interacting with the others in first approximation. If the burning sequence is powerful enough, it is possible to almost empty the ground state of the excited transition.

Probing sequence

A probing sequence is represented schematically on figure 6.12. After the burning sequence, a weak beam ($\Phi_p \ll \Phi_b$) at ν_p and lasting T_p is sent through the crystal. By weak beam, it is to be understood here that the probing sequence should not move ions populations. If ν_p is equal to the burning frequency ν_b, the probing beam coincides with a transition that has been pumped: the absorption has been saturated by the burning sequence and the crystal is almost transparent. If ν_p is "sufficiently" different from ν_b, the probing beam coincides with a transition that did not interact with the burning sequence and crystal absorption is unchanged. Here, the populations that interact with the burning light are populations for which ν_b is in the homogeneous linewidth. "Sufficiently" then means that ν_p must be different from ν_b of at least Γ_h: $|\nu_b - \nu_p| > \Gamma_h$. A hole is then burnt in the absorption line of the crystal, the FWHM of which is of the order of $2\Gamma_h$.

In the absence of light, the two states $|e\rangle$ and $|m\rangle$ both decay back to the ground state over time so that the transparency vanishes as the ground state population starts increasing. The hole disappearance occurs in two phases: first a fast decrease over a few hundreds of µs corresponding to $|e\rangle$ decaying to $|m\rangle$, followed by a slow one over a few tens of ms as $|m\rangle$ is depopulated.

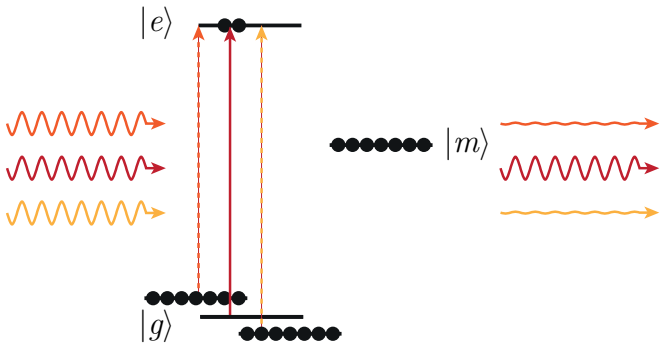

Figure 6.12 – Scheme of a probing sequence. A second weak optical beam is sent on the crystal after the burning sequence is turned off. If the probing sequence frequency corresponds to the burning frequency, it corresponds to an empty transition so that it is not absorbed. If the probing sequence is detuned, it corresponds to a transition that did not interact with the burning beam and absorption is unchanged.

There is a necessary delay between the burning and the probing beam. This delay can vary from about 100 µs to 1 or 2 ms depending on the configuration of the setup. Obviously, the longer

this delay the shallower the probed hole will be. This delay is thus a fundamental parameter that shall be the shortest possible.

Influence of light polarization

Careful attention must be paid to light polarization. If the crystal overall absorption is independent of light polarization, its influence on a hole shape is not straightforward. First, the burning efficiency depends on the orientation of the electric field in the sites local axes and all sites are not necessarily equivalent. Second, if the probing beam is not polarized in the same direction, it may probe sites that did not interact with the burning beam, thus changing the hole shape. In order to neglect such considerations, it will be considered in the following that both probing and burning beams have the same polarization oriented along [001], direction along which sites 1 and 2 do not interact with light and the other four are all equivalent.

6.3.2 Simple model for spectral holeburning

In section 6.3.1, I gave a qualitative description of holeburning process. The goal of this section is to derive the results presented in 6.3.1 in a more quantitative way thanks to a simple model based on the population equations of the three-level system presented above.

Steady state study

Let us consider the schematic presented on figure 6.13. Let us consider also a system with three levels numbered {1} ($|g\rangle$), {2} ($|e\rangle$) and {3} ($|m\rangle$). The absorption cross section from $|g\rangle$ to $|e\rangle$ is denoted σ. The spontaneous emission rate from $|e\rangle$ to $|g\rangle$ is denoted w. The decay rate from $|e\rangle$ to $|m\rangle$ is denoted β and the decay rate from $|m\rangle$ to $|g\rangle$ is denoted γ. In order to make a connection with the quantities given before, the lifetime of $|e\rangle$ is given by $(w+\beta)^{-1}$ and is of the order of 400 µs. The lifetime of $|m\rangle$ is given by γ^{-1} and is of the order of 10 ms. The transition cross section σ directly depends on the radiative decay rate w [174, Chapter 7]. The latter is also the Einstein coefficient $A_{|e\rangle\rightarrow|g\rangle}$, which was computed at room temperature in [175] and found of the order of 110 s^{-1}. At room temperature, the transition cross section is of the order of 10^{-20} cm^2 [176], however it increases at low temperatures as the homogeneous linewidth decreases. Using the value of $\Gamma_h = 44$ kHz measured in section 6.2.3, we derive that the transition cross section is of the order of 10^{-13} cm^2 at 3 K. The details of the following calculations are presented in appendix E, only the main results will be recalled here.

In steady state, it can be shown that populations in the three states are given by:

$$\begin{cases} N_1 = \dfrac{\gamma\left(\sigma\phi + w + \beta\right)}{\left(2\gamma+\beta\right)\sigma\phi + \gamma\left(w+\beta\right)} N \\ \\ N_2 = \dfrac{\gamma\sigma\phi}{\left(2\gamma+\beta\right)\sigma\phi + \gamma\left(w+\beta\right)} N \\ \\ N_3 = \dfrac{\beta\sigma\phi}{\left(2\gamma+\beta\right)\sigma\phi + \gamma\left(w+\beta\right)} N \end{cases} \tag{6.6}$$

where ϕ is the number of photons per unit of time and surface. A natural consequence of these equations is that in case an infinite light *flux* is used, the populations in $|g\rangle$ and $|e\rangle$ are equal:

$$N_2 = N_1 \propto \frac{\gamma}{\beta} N \tag{6.7}$$

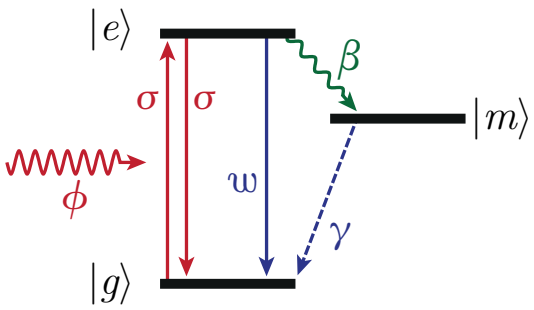

Figure 6.13 – Levels involved in holeburning process. From ground state $|g\rangle$, atoms can be excited to the excited state $|e\rangle$ thanks to a photons number per unit of time and surface ϕ. The absorption cross section of the transition is σ in cm^2. From the excited state, atoms can decay back to the ground state through spontaneous emission with a rate w (s^{-1}) or to the metastable state $|m\rangle$ through non radiative decay with a rate β (s^{-1}). From the metastable state, atoms can decay back to the ground state through radiative decay with a rate γ (s^{-1}). In the following it will be assumed that $\beta \gg w$ and $\beta \gg \gamma$.

where $N = N_1 + N_2 + N_3$. It appears that the crystal tends to become transparent.

Absorption coefficient of the crystal

In first approximation, the crystal absorption can be expressed as (see appendix E):

$$\alpha(\nu_p) = \sigma_h N \frac{\Gamma_h}{\Gamma_{inh}} \left[1 - \frac{\sqrt{1+\frac{\phi_b}{\phi_s}} - 1}{\sqrt{1+\frac{\phi_b}{\phi_s}}} \frac{1}{1+\left(\frac{\nu_p-\nu_b}{\Gamma_{\mathrm{HB}}/2}\right)^2} \right] \tag{6.8}$$

where σ_h is the homogeneous cross section, of the order of 10^{-13} cm^2. Γ_h and Γ_{inh} are the homogeneous and inhomogeneous linewidths respectively, and it is assumed that $\Gamma_h \ll \Gamma_{inh}$. ϕ_b is the photon number per unit of time and surface of the burning beam. ϕ_s is the saturation number of photons per unit of time and surface that creates a population difference of $\frac{N}{2}$ between $|g\rangle$ and $|e\rangle$. Γ_{HB} is the FWHM of the hole. The expressions of Γ_{HB} and ϕ_s are:

$$\Gamma_{\mathrm{HB}} = \Gamma_h \left(1 + \sqrt{1 + \frac{\phi_b}{\phi_s}} \right) \tag{6.9}$$

and

$$\phi_s = \frac{\gamma(w+\beta)}{(2\gamma+\beta)\sigma_h} \tag{6.10}$$

In case $\beta \gg \gamma$ and $\beta \gg w$, ϕ_s only depends on γ. If $\phi_b \gg \phi_s$, the crystal is transparent. The FWHM of the hole starts at twice the homogeneous linewidth, as qualitatively explained in section 6.3.1 and increases as the square root of ϕ_b. Here the laser linewidth was assimilated to a Dirac distribution. In order to be more realistic this linewidth should be convoluted to the Lorentzian laser linewidth during both burning and probing steps. The real FWHM is rather:

$$\Gamma_{\mathrm{HB}} = \Gamma_h \left(1 + \sqrt{1 + \frac{\phi_b}{\phi_s}} \right) + 2\Gamma_l \tag{6.11}$$

where Γ_l is the FWHM of the laser linewidth. Because of conservation of excited ions, *i.e.* the area under the Lorentzian curve, the hole is not as deep as expected and it is more difficult to burn holes.

Spatial variations of absorption

Here absorption was assumed to be constant along the thickness of the crystal. However, this assumption is not realistic since the burning pulse is absorbed as it propagates through the crystal, thus causing a decrease of the saturation. Considering the spatial variation of the flux leads to a strongly non-linear steady-state differential equation that can be solved numerically on a slice between z_0 and $z_0 + \Delta z$ thanks to the following inductive relationships:

$$\begin{cases} \phi_b(0) = \phi_b^0 \\ \alpha(\nu_p, z_0) = \sigma_h N \frac{\Gamma_h}{\Gamma_{inh}} \left[1 - \frac{\sqrt{1+\frac{\phi_b(z_0)}{\phi_s}}-1}{\sqrt{1+\frac{\phi_b(z_0)}{\phi_s}}} \frac{1}{1+\left(\frac{\nu_p-\nu_b}{\Gamma_{\mathrm{HB}}(z_0)/2}\right)^2} \right] \\ \phi_b(z_0+\Delta z) = \phi_b(z_0) \exp\left(-\alpha(\nu_p, z_0)\Delta z\right) \end{cases} \tag{6.12}$$

Dynamics considerations

The analytical study of the transient formation of a hole is not straightforward due to absorption of the burning pulse while propagating in the crystal and coherent processes at short times that lead to a system of non-linear differential equations. I will not theoretically study this point in this manuscript. However, it is interesting to study the dynamics of hole erasure after the burning sequence is switched off.

In the simple case in which the burning flux is very high and $\beta \gg w$ and $\beta \gg \gamma$, the population difference between $|g\rangle$ and $|e\rangle$ is given by:

$$N_1 - N_2 = N\left[1 - \left(1+\frac{\gamma}{\beta}\right)e^{-\gamma t} - \frac{\gamma}{\beta}e^{-\beta t}\right] \tag{6.13}$$

At $t = 0$ the crystal is transparent and it slowly recovers its absorption over time. It is noticeable that the decrease of the population difference occurs in two phases. A first fast decay occurs over a time scale of the order of β^{-1} concerning a small amount of atoms ($N\frac{\gamma}{\beta}$) corresponding to the atoms decaying from $|e\rangle$. It is followed by a slow one over γ^{-1} corresponding to the atoms returning to $|g\rangle$.

Here β^{-1} is of the order of a few hundreds of µs. After this characteristic time, $N\frac{\gamma}{\beta}$ atoms have returned back to the ground state. If the probing beam is switched on after this time – which is typically the case – the crystal has recovered $100 \times \frac{\gamma}{\beta}$ % of its original absorption. Considering the orders of magnitude given in the previous sections, this proportion is of the order of 4% of ions. Given that the expected absorption is of the order of $\alpha_m L = 5$, only 80% of the incident *flux* is transmitted after a few hundreds of µs. A way of limiting this issue is to use atomic systems for which the proportion of ions in $|e\rangle$ is lower, *i.e.* the lifetimes ratio is smaller.

6.3.3 Acousto-optic imaging with spectral holeburning

A theoretical study of the measurement of tagged photons through spectral holeburning was done by Li *et al.* in [177]. In this section, I suggest to derive the acousto-optic signal on the photodiode after the crystal using the simple model previously derived. Let us recall here the expression of the modulated scattered spectral power density with ultrasound obtained in section 2.3.2 in which I leave aside the probability $\Omega(\mathbf{r}, \mathbf{r}')$ of having a photon tagged at $\mathbf{r}$ and reaching the detector

at $\mathbf{r}'$. In a single speckle grain:

$$\Psi_S(\tau,\nu) = \Psi_{UT}(\tau) * \delta(\nu-\nu_0) + \frac{1}{2}\Psi_T(\tau) * \delta(\nu-\nu_0-\nu_{US}) + \frac{1}{2}\Psi_T(\tau) * \delta(\nu-\nu_0+\nu_{US}) \quad (6.14)$$

where $\Psi_{UT}(\tau)$ and $\Psi_T(\tau)$ are given by:

$$\begin{cases} \Psi_{UT}(\tau) &= \Psi_0\left[1-\beta\int\Phi(\mathbf{r})\,P_0^2\left(\tau-\dfrac{\mathbf{K}_{US}\cdot\mathbf{r}}{\omega_{US}}\right)\mathrm{d}\mathbf{r}\right] \\ \Psi_T(\tau) &= \Psi_0\beta\int\Phi(\mathbf{r})\,P_0^2\left(\tau-\dfrac{\mathbf{K}_{US}\cdot\mathbf{r}}{\omega_{US}}\right)\mathrm{d}\mathbf{r} \end{cases} \quad (6.15)$$

where I used the retarded potential for the acoustic pressure, ν_0 and ν_{US} are the light and ultrasound frequencies, β is a proportionality coefficient, Ψ_0 the overall light power and $\Phi(\mathbf{r})$ is the irradiance at $\mathbf{r}$ inside the scattering medium. In its most general expression, the transmitted scattered power is:

$$\Psi_S^{\text{out}}(\tau,\nu) = \Psi_S(\tau,\nu)\exp\left[-\int_0^L\alpha(\nu,z)\,\mathrm{d}z\right] \quad (6.16)$$

If one neglects the z dependence and expresses the absorption $\alpha(\nu)$ as $\alpha_m - \Delta\alpha(\nu)$ where:

$$\begin{cases} \alpha_m &= \sigma_h N\dfrac{\Gamma_h}{\Gamma_{inh}} \\ \Delta\alpha(\nu) &= \alpha_m\dfrac{\sqrt{1+\frac{\phi_b}{\phi_s}}-1}{\sqrt{1+\frac{\phi_b}{\phi_s}}}\dfrac{1}{1+\left(\frac{\nu-\nu_b}{\Gamma_{\text{HB}}/2}\right)^2} \end{cases} \quad (6.17)$$

The power spectral density after the crystal is:

$$\Psi_S^{\text{out}}(\tau,\nu) = \Psi_S(\tau,\nu)\exp(-\alpha_m L)\exp[\Delta\alpha(\nu)\,L] \quad (6.18)$$

Let us assume that the pressure is a Dirac distribution so that the tagged and untagged photons spectra are infinitely narrow. If the burning beam matches one of the side-bands (let us say the band at $\nu_0+\nu_{US}$) the tagged photons power is given by:

$$\begin{aligned} \Psi_T^{\text{out}}(\tau) &= \Psi_T(\tau)\exp(-\alpha_m L)\exp[\Delta\alpha(\nu_0+\nu_{US})\,L] \\ &= \Psi_T(\tau)\exp(-\alpha_m L)\exp\left[\alpha_m L\frac{\sqrt{1+\frac{\phi_b}{\phi_s}}-1}{\sqrt{1+\frac{\phi_b}{\phi_s}}}\right] \end{aligned} \quad (6.19)$$

while the untagged photons power is:

$$\Psi_{UT}^{\text{out}}(\tau) = \Psi_{UT}(\tau)\exp(-\alpha_m L)\exp\left(\alpha_m\frac{\sqrt{1+\frac{\phi_b}{\phi_s}}-1}{\sqrt{1+\frac{\phi_b}{\phi_s}}}\frac{1}{1+\left(\frac{\nu_{US}-\nu_b}{\Gamma_{\text{HB}}/2}\right)^2}\right) \quad (6.20)$$

Assuming that the hole is narrow compared to the ultrasound frequency, the ratio between tagged and untagged power thus increases as $\exp\left[\alpha_m L\frac{\sqrt{1+\frac{\phi_b}{\phi_s}}-1}{\sqrt{1+\frac{\phi_b}{\phi_s}}}\right]$. In this case, the SNR in a

single speckle grain assuming that the detector is shot-noise limited is given by:

$$\begin{aligned} SNR &\propto \frac{\Psi_T^{\text{out}}}{\sqrt{\Psi_T^{\text{out}} + \Psi_{UT}^{\text{out}}}} \\ &\propto \frac{\Psi_T \exp\left(-\alpha_m L\right) \exp\left[\Delta\alpha\left(\nu_0 + \nu_{US}\right) L\right]}{\sqrt{\Psi_T \exp\left(-\alpha_m L\right) \exp\left[\Delta\alpha\left(\nu_0 + \nu_{US}\right) L\right] + \left(\Psi_0 - \Psi_T\right) \exp\left(-\alpha_m L\right)}} \end{aligned} \tag{6.21}$$

Assuming that $\exp\left[\Delta\alpha\left(\nu_0 + \nu_{US}\right) L\right] \gg 1$ – *i.e.* the hole is deep – but that the ratio between tagged and untagged photons is still small after the crystal – *i.e.* the crystal is not absorbing enough so that the amount of untagged photons always remain very high compared to the amount of tagged photons – it comes that:

$$SNR \propto SNR_0 \exp\left(-\frac{\alpha_m}{2} L\right) \exp\left[\Delta\alpha\left(\nu_0 + \nu_{US}\right) L\right] \tag{6.22}$$

where $SNR_0 = \Psi_T / \sqrt{\Psi_0}$ is the signal-to-noise ratio before the crystal. This is the typical value that is obtained when simply measuring the modulation of a single speckle grain with a single-detector of small area. Here, without the burning beam, the main effect of the crystal is to decrease the SNR since it basically absorbs light. Interestingly, in order to see an improvement of the SNR through spectral holeburning, the burning beam must be powerful enough to burn a hole at least as deep as $\frac{\alpha_m}{2}$. Contrary to coherent techniques that measure the modulation, spectral holeburning measures the *flux* of tagged photons so that the random phase from a speckle grain to another does not influence the SNR. Here, it then naturally comes out that the SNR increases as the square root of the collected number of speckle grains.

6.4 Characterization of a hole

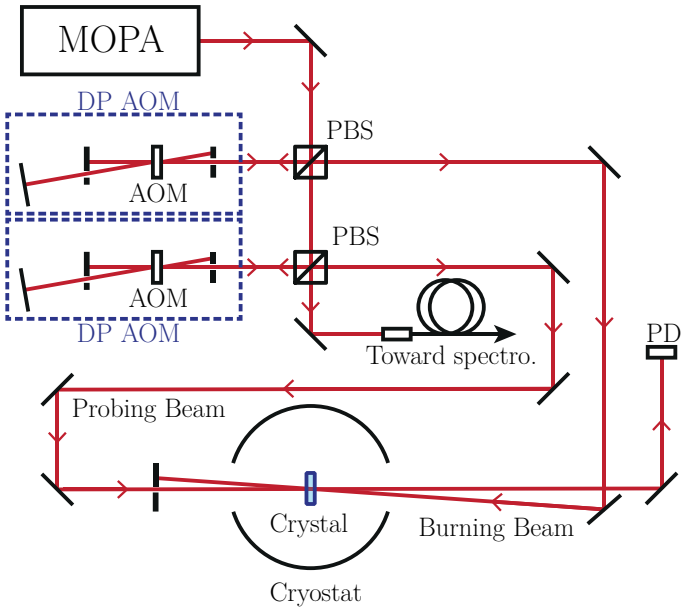

Figure 6.14 – The characterisation setup for holeburning experiments. MOPA: Master Oscillator Power Amplifier composed of a fibred semi-conductor laser diode (LD) feeding a fibred tapered amplifier. PBS: Polarization Beam Splitter. AOM: Acousto-Optic Modulator in a double-pass configuration (DPAOM) (AA Optoelectronics AA MT80, 80 MHz central frequency). PD: Photodiode.

In the previous section, I predicted a few properties of a hole. In this section, I will quantify some of these in order to picture the main challenges of acousto-optic imaging with spectral holebunring. I will study the behaviour of a hole as the different physical parameters vary in order to give an idea of the future properties of the final imaging modality. The experimental setup used here is very similar to what was used in section 6.2.3 and is pictured on figure 6.14. The burning beam is collimated and has a diameter of typically 3 mm whereas the probe is focused on the crystal thanks to a 200 mm focal length lens, leading to a probe diameter of the order of 100 µm. Temperature is around 3 K. The probe frequency can be scanned over several MHz thanks to acousto-optic modulators (AOM). The spectral hole results in an increase of the transmitted probe power that can be measured on a photodiode:

$$\Psi_p(\nu) \propto \exp\left[-\left(\alpha_m - \Delta\alpha(\nu)\right) L\right] \text{ with } \Delta\alpha(\nu) > 0 \tag{6.23}$$

Using $\Psi_p^0 \exp(-\alpha_m L)$ as a baseline and taking the natural logarithm of the probe signal, it is then possible to measure the variations of absorption $\Delta\alpha(\nu)$ due to the burning process.

The two beams are counter-propagating in order not to blind the photodetector with the burning beam. This way, it is possible to avoid using optical shutters that may increase the necessary delay between the probing and burning beams. However, a small amount of burning light is reflected on the cryostat and reaches the detector anyway. In order to prevent overlapping between the probing beam and electronic remainder of the burning beam, the delay between the two sequences is 500 µs in the following.

6.4.1 Study of a hole

A first hole is burnt using a burning power of 15 mW ($\Phi_b \sim 50$ mW $\cdot$ cm^{-2}) during 10 ms and probed with a chirp of power of the order of 3 µW ($\Phi_b \sim 8$ mW $\cdot$ cm^{-2}) scanning 20 MHz around the burning frequency over 200 µs[1]. The temperature is 3.5 K. The repetition rate of the two sequences is 10 Hz so that the hole is erased from a pulse to another.

Shape of the hole

The corresponding hole is presented on figure 6.15(a) and fitted with a Lorentzian shape as predicted by the model of section 6.3.2. It is to be noticed here that the feet of the Lorentzian curve do not perfectly fit the hole shape. It may be due to a laser frequency jitter. Indeed, in addition to the intrinsic finite linewidth of the emitted spectral line (~ 50 kHz), the laser diode exhibits a frequency jitter – *i.e.* a random deviation of the central frequency of the laser line over time – due to several noise sources such as thermal noise or vibrations in the laser head or the injection fibre between the laser diode and the tapered amplifier. The burning beam then pumps several homogeneous linewidths as its central frequency randomly changes over the burning time. The final hole is then a superposition of several Lorentzian holes slightly shifted one from another. Beside the fact that the shape is not completely Lorentzian, the consequences are that the hole is larger and not as deep as expected. As the burning efficiency is lower than expected, higher light irradiance is necessary in order to burn at equivalent depth. A way of supporting this point is to reduce the burning duration so that the laser spectral line does not have time to jump very

[1]Here the probe power does not seem to be in agreement with the orders of magnitude given in appendix E. However, beside the fact that the saturation irradiance is probably underestimated, it must be kept in mind that, due to the high chirping rate of 100 kHz $\cdot$ µs^{-1}, the probing beam spends a very short time in a homogeneous linewidth.

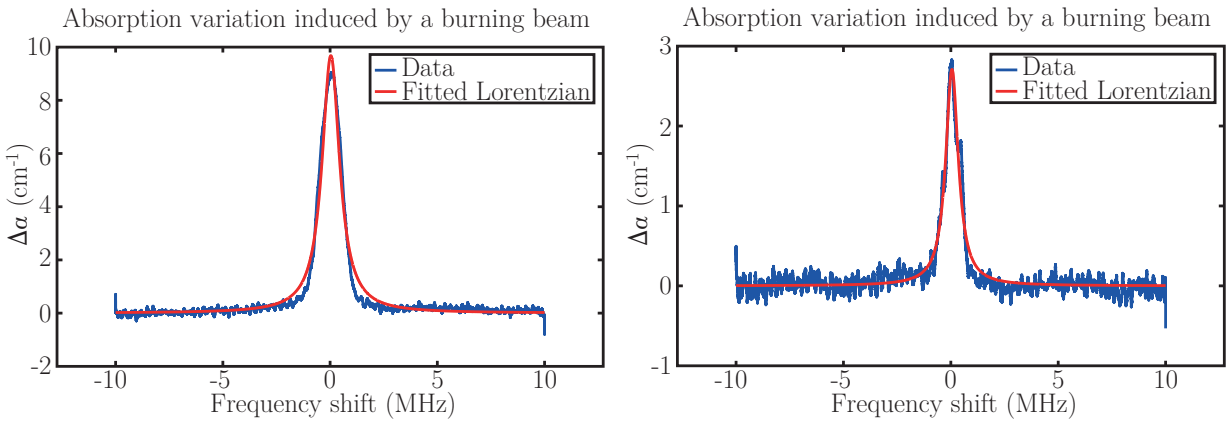

(a) Burning power 15 mW during 10 ms, width is 1 MHz

(b) Burning power 15 mW during 1 ms, width is 700 kHz

Figure 6.15 – Shape of a hole with a burning power of 15 mW ($\sim 50\ \mathrm{mW \cdot cm^{-2}}$). The plot represents the absolute value of the variation of absorption generated by the burning sequence. (a) The hole was burnt during 10 ms and fitted by a Lorentzian curve as predicted by the theoretical model. Here it can be noticed that the feet of the Lorentzian do not completely fit the hole shape, probably because of laser jitter. (b) The hole was burnt during 1 ms, laser jitter is reduced so that the hole shape closer to a Lorentzian curve.

far. Another hole was burnt using the same burning power but during only 1 ms and shown on figure 6.15(b). It can be seen here that, since laser jitter was reduced, the hole converges towards a Lorentzian curve, as predicted by the model.

Laser jitter

Since laser frequency jitter influences the shape of a hole, the latter was characterized by acquiring 300 realizations of the same holeburning sequence. The burning sequence lasts 10 ms with a power of 3 mW, rather low in order to have a sharp hole. The delay before probing is 500 µs. Laser jitter during the burning sequence contributes to the broadening of the hole, however, measuring the center frequency of the hole is a way of estimating the frequency deviation between the probe and the mean frequency of the burning beam. The position of the hole center frequency was measured and the corresponding histogram is plotted on figure 6.16. The frequency jumps distribution was fitted with a normal distribution the standard deviation of which gives an order of magnitude of the laser frequency jitter which is 200 kHz over 500 µs.

Lifetime of a hole

An important parameter for acousto-optic imaging is the lifetime of the metastable state $|m\rangle$ since it defines how long the hole stands and thus how often the burning sequence must be repeated. One easily understands that the future imaging rate of an acousto-optic imaging technique based on a spectral holeburning detection scheme will be mainly limited by the burning repetition rate. The lifetime of the hole was estimated by measuring the proportion of atoms in $|m\rangle$ – that is to say the area of the hole in the crystal absorption – as the delay between the burning and probing sequences is increased gradually. The erasure of the hole as a function of this delay is plotted on figure 6.17. One retrieves the expected exponential decay predicted in section 6.3.2. Here only the slow decay in γ^{-1} is visible for the fast one mainly occurs before the first point is taken. The measured hole lifetime is 7.4 ms here, thus retrieving the expected order of magnitude.

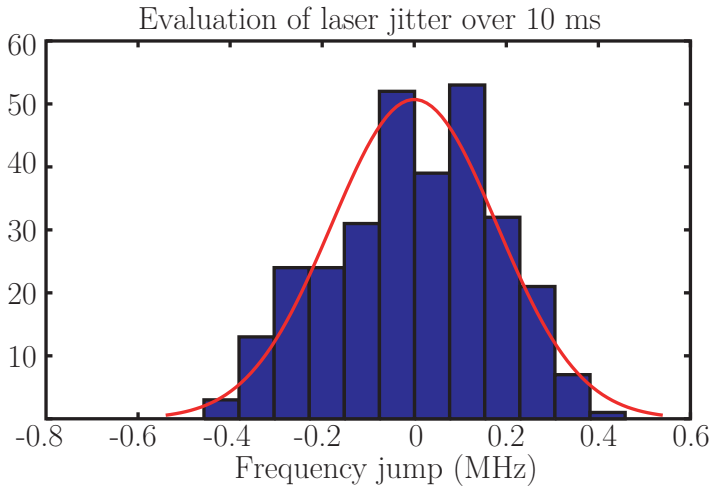

Figure 6.16 – Estimation of laser jitter. 300 realizations of the same holeburning sequence are recorded and the center frequency of each hole is measured. The burning sequence is weak in order to have a sharp hole and lasts 10 ms. The delay before probing is 500 µs. The histogram represents the distribution of frequency jumps and is fitted by a normal distribution with a standard deviation of about 200 kHz.

6.4.2 Influence of the burning beam

In the previous section, a few properties of the holes were experimentally demonstrated and were in good agreement with what was theoretically predicted by the simple model of section 6.3.2. In order to get a step further, it is interesting to explore the behaviour of the hole as the parameters of the burning beam vary. The idea is to try to predict the requirements of the future burning sequence in acousto-optic imaging.

Effect of the burning power on the hole depth

The study of the hole depth as a function of the burning beam power is of interest for it is related to the tagged photons filtering efficiency. Using the same experimental setup, the power of the burning beam was changed while keeping its duration equal to 10 ms[1]. The maximum value of the absorption variation – *i.e.* logarithm of the transmitted power divided by the crystal thickness – is measured as a function of the burning power Ψ_b and fitted with the expression predicted by the model of section 6.3.2:

$$\Delta\alpha\left(\Psi_b\right) = \alpha_m - \alpha\left(\nu_b\right) = \sigma_h N \frac{\Gamma_h}{\Gamma_{inh}} \frac{\sqrt{1+\frac{\Psi_b}{S_b\Phi_s}}-1}{\sqrt{1+\frac{\Psi_b}{S_b\Phi_s}}} \tag{6.24}$$

where S_b is the beam section on the crystal and Φ_s the saturation irradiance in $\mathrm{W}\cdot\mathrm{cm}^{-2}$. The results are plotted on figure 6.18. Figure 6.18(a) shows the hole depth behaviour as the burning power is increased up to 120 mW ($> 400\ \mathrm{mW}\cdot\mathrm{cm}^{-2}$). Data were fitted thanks to equation 6.24 so that it is possible to extract experimental values of the parameters defined in the holeburning model of 6.3.2. A zoom over low powers is displayed on figure 6.18(b) showing that the model seems to be in good agreement with the experimental data. Here the maximum absorption measured

[1]It is *a priori* not necessary to burn over a time longer than the lifetime of $|m\rangle$ because atoms start decaying back to $|g\rangle$ after. However, I will show later that this does not ensure that steady-state is reached so that high saturation irradiances are measured. The main issue here is that laser jitter prevents from burning efficiently during long times, at risk of burning very broad and shallow holes.

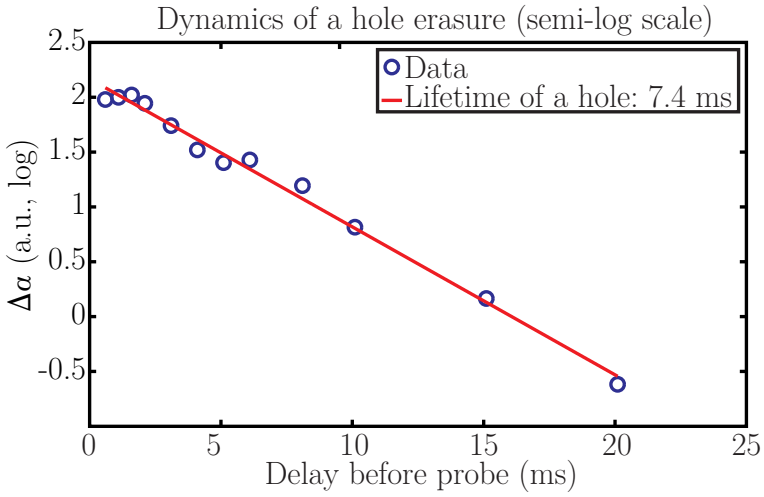

Figure 6.17 – Measurement of the hole lifetime. The area of the hole absorption (log) is plotted as a function of the delay between the burning and probing sequences. It exhibits the expected exponential decay with a characteristic decay time $T_1 = \gamma^{-1}$. The fast decay due to the excited state $|e\rangle$ is not visible here for it concerns few atoms and mainly occurs before the first point was taken.

thanks to the fitting curve is $\alpha_m = 16.2$ cm^{-1}. This value is in good agreement with the predicted order of magnitude and the measured absorption of section 6.2.3. It must be kept in mind that due to the hole erasure, the measured absorption decreased of about 7% during the 500 µs delay between the burning and the probing sequence. As in 6.2.3, the maximum absorption is not as high as expected (to be compared to expected $\alpha_m L = 5$). From what was discussed earlier, this may be mainly due to the ASE background that produces light transmitted through the crystal. The saturation irradiance Φ_s can also be estimated and is about 15 mW $\cdot$ cm^{-2}. This saturation irradiance corresponds to the irradiance needed to move half the ions in the metastable state. It is then an effective parameter that depends on the saturation number of photons per unit of time and surface ϕ_s (which is an intrinsic parameter of the transition) but also takes into account other experimental parameters such as finite burning time, spatially inhomogeneous burning irradiance, burning beam absorption, laser linewidth or laser jitter. It thus appears that, despite all experimental deviations, the simple holeburning model seems to work provided that one defines an effective saturation irradiance that quantifies the burning efficiency. An interesting benchmark is that, due to the square root increase, at $\Phi_b = 10\Phi_s$ only 70% of the total hole depth is reached and one needs up to $100\Phi_s$ to reach 90% of the total depth.

One can see that there is a deviation from the model at high burning powers. First causes come from the model itself. Here the data were fitted thanks to a model that assumes laser linewidth is infinitely narrow, which is obviously not the case. As stated above, the fact that the model used to fit the data does not take into account both the burning beam absorption in the crystal thickness and the Gaussian shape of all beams is also to be highlighted here. The measured hole is an averaged hole over the crystal thickness and the beam transverse profile so that the derived expression does not perfectly hold.

Other deviation sources can be suggested, the influence of which is not straightforward to quantify. It is possible that the amplifier introduces instabilities at high powers so that the burning efficiency decreases. It is also possible that high burning power slightly increases the local temperature within the crystal so that the homogeneous linewidth increases. A third possibility concerns cross-relaxations that may occur between close ions [174, Chapter 30]. Cross-relaxation is likely to transfer energy from the saturated transition to the other unsaturated ones. The

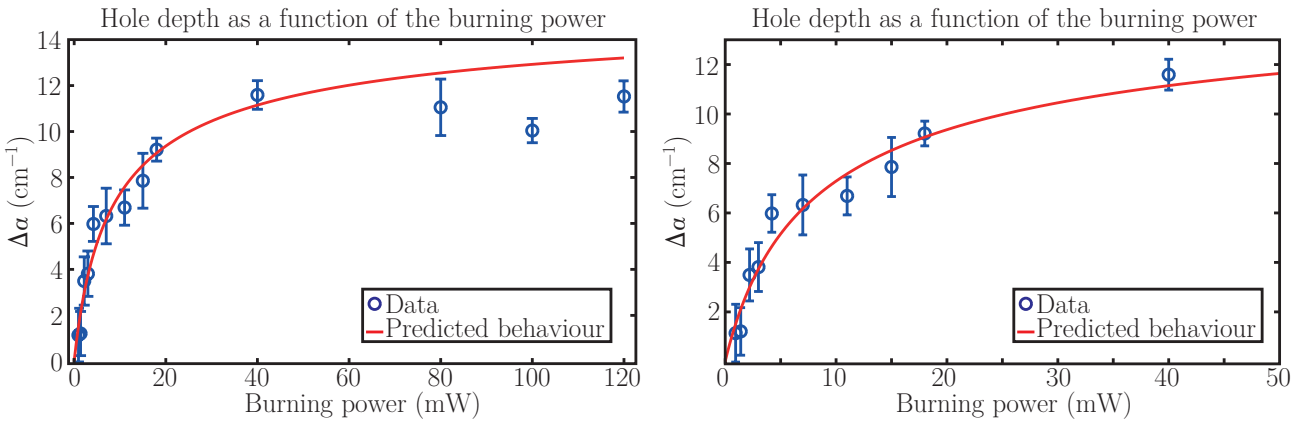

(a) Burning during 10 ms up to 120 mW

(b) Same data up to 40 mW

Figure 6.18 – Evolution of the absorption hole depth as a function of the increasing burning power. (a) Power increased up to 120 mW. It seems that there is a deviation from the predicted behaviour at high burning power. (b) Zoom over the low burning powers. The model seems to be in good agreement with experimental data up to 40 mW.

effect on the hole is that the background slightly increases as the surrounding transitions are turning transparent and the hole depth is underestimated. The higher the pumping rate, the more important this phenomenon is. This third hypothesis is all the more likely as the crystal we use has a high Tm^{3+} concentration.

Effect of the burning power on the hole linewidth

Based on the same data as used above, it is possible to plot the hole linewidth as a function of the burning power. The result is shown on figure 6.19. In red is plotted the predicted linewidth behaviour using the measured saturation irradiance from the fitting curve of figure 6.18, the expected homogeneous linewidth of 40 kHz at 3 K and assuming that, at low burning power, the hole linewidth is dominated by laser linewidth and jitter. The first observation that can be made here is that holes rapidly become very wide ($\sim 7-8$ MHz) compared to typical ultrasound frequencies so that the risk of letting untagged photons through is high. It then seems very important to decrease the saturation irradiance so that thinner holes can be burnt. It also appears here that the model totally fails at describing the behaviour of the hole linewidth. Beside the model weaknesses described in the previous section, this may point to two potential deviation sources: the homogeneous linewidth can increase due to local temperature raise within the crystal or the amplifier can induce instabilities as the power is increased.

6.5 Laser stabilization

6.5.1 Of laser stabilization necessity

It was stated previously that a lot of experimental issues come from two main phenomena. First, the ASE background leads to a wrong estimation of the maximum absorption of the crystal as it contributes to light passing through the crystal without being absorbed. Unfortunately, this background will also be present in acousto-optic imaging since the amplifier is necessary to illuminate the scattering medium with enough light *flux*. However, in order to have a better

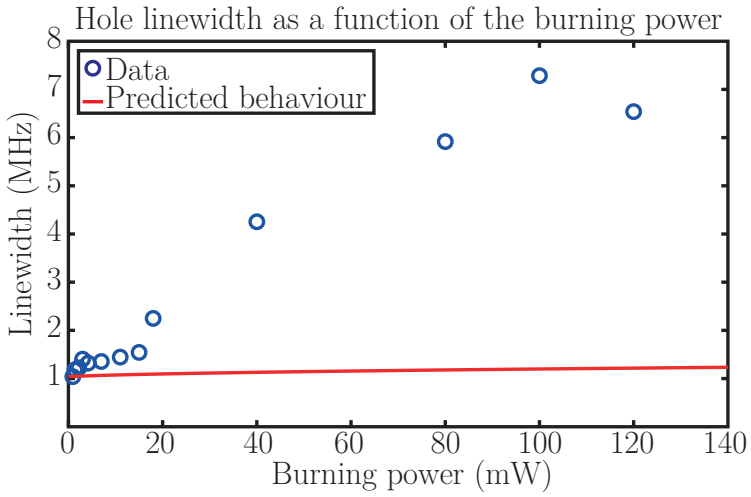

Figure 6.19 – Evolution of the hole linewidth as a function of the burning power. In red is the predicted behaviour using the saturation irradiance derived from the fitting curve of figure 6.18, the expected homogeneous linewidth of 40 kHz at 3 K and assuming that at low burning power, the hole linewidth is dominated by laser linewidth and jitter. If the simple spectral holeburning model seemed in good agreement with the hole depth behaviour, it totally fails at describing the behaviour of the hole linewidth.

estimation of the crystal capabilities, it is interesting to use a laser source with a lower ASE background.

The second main issue comes from the laser linewidth and jitter. Beside the fact that the fitting model does not take into account the laser linewidth, laser jitter results in poor burning efficiency. Higher power must be used in order to burn at equivalent depth and several problems may occur. First, because of the high crystal absorption, temperature may raise locally, thus involving an increase of the homogeneous linewidth. It is also possible that a higher power comes along with amplifier instabilities. Eventually, using a higher burning power may also involve cross relaxation effects that may decrease the measured absorption. All these effects contribute to small burning efficiency. On the other hand, the hole linewidth rapidly becomes too broad for acousto-optic imaging. A stabilized laser source is then expected to help burning thinner holes.

Section 6.4 showed important deviations from the predicted behaviour. In order to discriminate error sources coming from the model hypotheses from errors coming from the experimental issues described above, the laser was actively controlled in order to decrease both linewidth and jitter. The setup was moved to Anne Chauvet and Thierry Chanelière's lab at Laboratoire Aimé Cotton in Orsay. The new laser source will not be studied here but is completely described in the appendices of [178]. It is a semi conductor laser diode locked on an external Fabry-Perot cavity under vacuum thanks to a Pound-Drever-Hall (PDH) method [179, 180]. Further considerations on the laser source is not the point of this manuscript. The new corresponding setup is shown on figure 6.20. Once locked, the laser linewidth is of the order of 10 Hz over 1 ms with a drift of a few $\mathrm{kHz} \cdot \mathrm{s}^{-1}$, which is now much narrower than the homogeneous linewidth.

6.5.2 Shape of a hole

Here again, the delay between the burning and the probing sequences is 500 µs. In order to compare the effects of the two different lasers, a hole was burnt using a burning power of 1 mW during 10 ms. The burning beam is a Gaussian beam of waist of the order of 500 µm. The probing beam has a waist of about 200 µm, its power is of the order of a few µW and chirps 9 MHz over

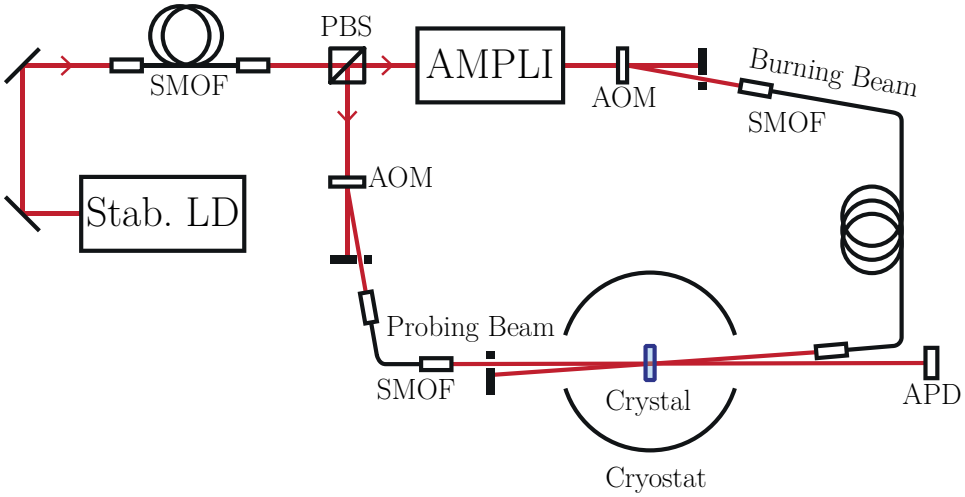

Figure 6.20 – Schematic of the characterization setup with a stabilized laser diode (Stab. LD). SMOF: Single-Mode Optical Fibre, PBS: Polarization Beam Splitter, AOM: Acousto-Optic Modulator (AA Optoelectronics AA MT80, 80 MHz central frequency), APD: Avalanche Photodiode Hamamatsu C5460. The burning beam is amplified (AMPLI) by a succession of two slave lasers: Eagleyard Photonics Laser Diode and Toptica BoosTA 500 mW maximum output power.

200 µs. A hole at 1.5 K is plotted on figure 6.21. Given these parameters, the burning irradiance was estimated to be of the order of 130 $\mathrm{mW \cdot cm^{-2}}$. One can notice here that the shape of the hole is in quite good agreement with the Lorentzian shape predicted by the model and that the hole is deeper and much narrower than any hole burnt with the DL pro laser diode.

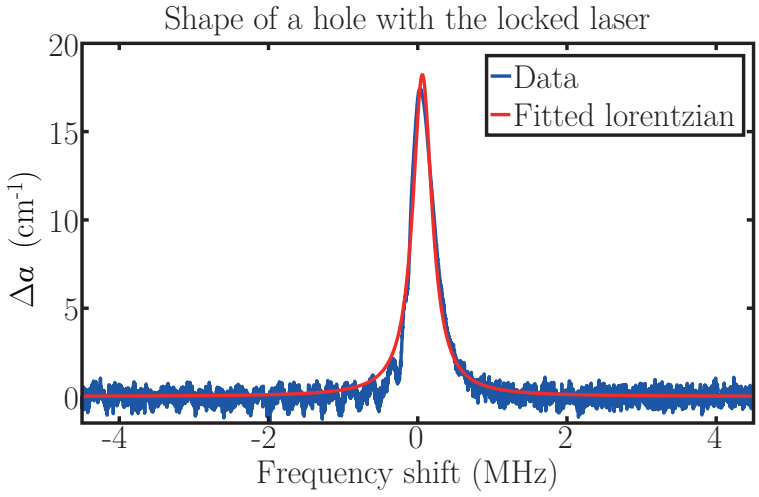

Figure 6.21 – Hole shape with the stabilized laser. The burning irradiance is of the order of 130 $\mathrm{mW \cdot cm^{-2}}$. One can notice here that the hole shape is in good agreement with the Lorentzian shape predicted by the model. The hole is deeper and much narrower than any hole burnt with the DL pro laser diode.

6.5.3 Influence of the burning power

The same experiments as performed in section 6.4 can be performed with the stabilized laser. First, the evolution of the hole depth as a function of the burning irradiance is plotted on figure 6.22. The burning time was 10 ms here and the temperature was 1.5 K. Data were fitted using the

model derived in section 6.3.2 and the latter seems in good agreement with the actual behaviour. The fitting curve predicts an absorption coefficient of 22.8 cm^{-1}, which is closer to the expected absorption of the crystal. This is due to the fact that the probing beam comes directly from the laser instead of being a portion of the amplified beam. The ASE background is then expected to be much lower.

The saturation irradiance was also estimated thanks to the fitting curve. Here it was found $\Phi_s = 9.4\ mW \cdot cm^{-2}$. As expected, stabilizing the laser led to easier burning. One can notice here that, in spite of having a lower saturation irradiance, it is of same order of magnitude as with the DL Pro laser diode. However, now the laser linewidth is very small compared to the homogeneous linewidth, it is expected that deviations come from the model hypotheses. As it was the case in section 6.4, the steady-state hypothesis upon which the entire model is based is not straightforwardly verified as the burning time is only of the order of the metastable state lifetime. However, it is now possible to burn during very long times without degrading the hole shape. The same experiment was performed with burning times of 50 ms, 100 ms and 500 ms, long enough compared to the hole lifetime so that populations can be assumed in steady-state. The saturation irradiances in these cases were all of the order of $\Phi_s = 5.2\ mW \cdot cm^{-2}$. This is to be compared to the value predicted by the simple model of $\Phi_s = 300\ \mu W \cdot cm^{-2}$. As the burning and probing beams have comparable sizes, a probable origin for this difference may lie in the spatially inhomogeneous burning irradiance due to the Gaussian beams and absorption along the crystal thickness. In the model, it was assumed that the probing beam probes a homogeneously burnt area of the crystal. As stated previously when it is not the case, the latter probes an averaged hole over the burning and probing wave-fronts and crystal thickness. In the case of a Gaussian beam, holes are very deep and broad near the center and becomes thinner and shallower near the edges of the wavefront. As the burning beam is absorbed during its propagation, holes are also susceptible to become shallower as one looks deeper inside the crystal. The direct consequence is that one needs higher burning powers to burn equivalent transparency and the saturation irradiance increases.

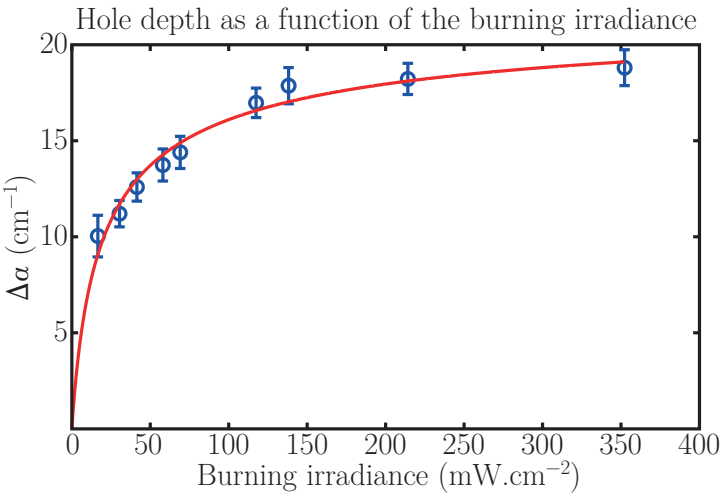

Figure 6.22 – Depth of the hole as a function of the burning irradiance with a burning time of 10 ms. Data were fitted using the predicted behaviour of section 6.3.2.

The hole linewidth estimation is not easy at low burning powers for it is very narrow. Using a burning time of 10 ms, the hole linewidth was estimated and plotted on figure 6.23. A fitting curve, in red on figure 6.23, showed that the evolution of the linewidth is compatible with the expression derived in appendix E using a homogeneous linewidth of 40 kHz, a laser linewidth of 10 Hz and a saturation irradiance of 4.3 $mW \cdot cm^{-2}$. Though a bit different, the saturation

irradiance is compatible with what was predicted from the evolution of the hole depth.

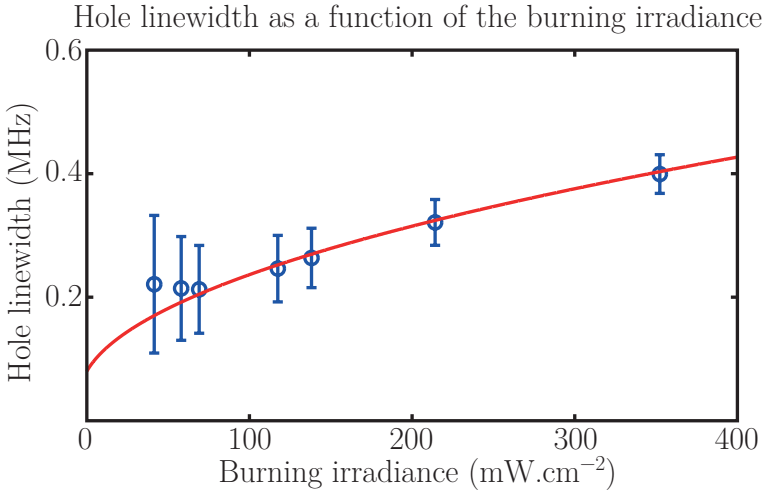

Figure 6.23 – Hole linewidth as a function of the burning irradiance with a burning time of 10 ms. Data were fitted using the predicted behaviour of section 6.3.2. Data are compatible with a homogeneous linewidth of 40 kHz, a laser linewidth of 10 Hz and a saturation irradiance of $4.3\ \mathrm{mW \cdot cm^{-2}}$.

6.6 Experimental limitations of spectral holeburning

In this chapter, I gave a brief glimpse at the principle of spectral holeburning. I developed a simple model that describes the behaviour of a hole in order to predict and tailor acousto-optic sequences and verified that it is in relatively good agreement with the actual behaviour of a hole. I experimentally characterized a few properties of spectral holes in order to quantify the filtering capabilities of such a technique. For instance, for further acousto-optic imaging applications with a stabilized laser diode, a good filtering efficiency is expected to involve a burning power of the order of $400\ \mathrm{mW \cdot cm^{-2}}$ during 10 ms. This burning power can be reduced by increasing the burning time, but this may decrease the imaging rate. The holeburning sequence for acousto-optic imaging must then be a balance between the burning power and the imaging rate: the higher the burning power, the higher the imaging rate.

However, this chapter highlighted several limitations of spectral holeburning for acousto-optic imaging techniques. Beside the main experimental difficulty of working at cryogenic temperatures, it appeared that a lot of other parameters play an important role in the phenomenon.

Amplified Spontaneous Emission background It appeared that the laser amplifier generates a background of ASE. Though this background is very weak compared to the laser emission line – about 30 dB lower – it is considerably broader than the inhomogeneous linewidth – 20 nm to be compared to the ~ 0.1 nm of the inhomogeneous linewidth. The laser emission line being strongly absorbed by the crystal – expected about 20 dB – the ASE background, which is mostly transmitted, may become comparable to the transmitted probe signal. It results in a wrong estimation of the crystal absorption. This issue is expected to remain in further acousto-optic imaging implementations for they require a high light *flux* on the scattering medium. It can be considered decreasing this unwanted background by using a Bragg filter for instance in order to remove as much ASE as possible. For characterization purposes, a simple way of decreasing this background consists in probing the crystal with light coming directly from the non-amplified laser

diode. Thanks to this, it was possible to have a better idea of the crystal absorption which is of the order of $\alpha_m L = 5$.

Laser linewidth and frequency jitter The different characterizations of the behaviour of a hole showed that the simple model fails at describing the physics of the phenomenon in case the burning efficiency is low. In this case, higher burning irradiance is needed in order to burn at equivalent depth and several unwanted effects appear such as hole depth decreasing at very high burning power or unexpected hole broadening. I showed that an active frequency control reduces the laser linewidth and ensures that frequency jitter remains inside a single homogeneous linewidth. A laser locking helps burning deeper holes and brings a lot of advantages for acousto-optic imaging.

Hole lifetime The hole lifetime was measured and is of the order of 10 ms. This lifetime is an important limiting factor for further acousto-optic imaging implementation for two main reasons.

- After the burning sequence ends, atoms first leave the excited state $|e\rangle$ over a characteristic time of a few hundreds of µs. Given the order of magnitude of the lifetime of $|m\rangle$ and the high crystal absorption, it amounts to a decrease of about 20% of the transmitted *flux* in a few hundreds of µs. The longer the storing state lifetime is, the lower this effect is supposed to be.
- As the hole lifetime is shorter than the imaging time, the burning sequence must be repeated every 10 ms at least, which may drastically decrease the imaging rate.

An important issue then consists in increasing the storing state lifetime in order to increase the crystal transparency and potentially increase the imaging rate.

CHAPTER 7

Acousto-optic imaging using spectral holeburning under a magnetic field

Table of contents

In chapter 6 I presented the principle of spectral holeburning and first properties that are involved in acousto-optic imaging. It was shown that a non-stabilized laser diode (DL Pro, 50 kHz linewidth, coupled with a Sacher LaserTechnik Tapered amplifier) burns either narrow and shallow or broad and deep holes. It appeared that laser stabilization allows a high burning efficiency so that deeper and thinner holes can be burnt. This was achieved by using a laser locked on an external Fabry-Perot cavity thanks to a Pound-Drever-Hall locking method. However, the short lifetime of the metastable state $^3F_4$ ($|m\rangle$) – of the order of 10 ms – limits the capabilities of such a system in terms of both filtering efficiency and imaging rate. In part III, I worked on a means of increasing the imaging rate. However, even with the shortest imaging time reached – *i.e.* 0.82 s – it is necessary to repeat the burning sequence many times in order to maintain a decent hole. As a consequence, a short lifetime drastically limits the imaging rate. A natural prospect is then to find a way of increasing the lifetime of the storing level. This can be achieved by adding an external magnetic field in order to remove the degeneracy of the ground state $^3H_6$ ($|g\rangle$). The magnetic field creates a splitting between the two nuclear magnetic spin orientations of Tm^{3+} ions. Once an atom is placed in one of the Zeeman levels, processes responsible for atoms decay are spin flip processes that are very weak in absence of phonons so that the lifetime of these levels is potentially very long.

7.1 Tm^{3+}:YAG under a magnetic field

It was reported by Ohlsson *et al.* [181] that the application of a magnetic field drastically increases (3 orders of magnitude) the storage time of spectral features in Tm^{3+}:YAG crystals. The goal of this section is to give some essential qualitative properties of the effects of an external magnetic field on Tm^{3+} in YAG structure. The complete theoretical study of Tm^{3+} interactions with a magnetic field is not the point of this manuscript. A theoretical background can be found in [182], an experimental study of the resulting properties of Tm^{3+} can be found in [183] and [184].

The presence of an external magnetic field $\mathbf{B}_0$ removes the nuclear spin degeneracy and splits energy levels as shown on figure 7.1. In the following, effects of the magnetic field on the metastable state $|m\rangle$ will be often omitted. The Zeeman splitting of the ground state and the excited state are respectively noted δ_g and δ_e in kHz.G^{-1}. As it will be shown later, δ_g is about 5 times larger than δ_e and of the order of a few tens of kHz.G^{-1}. The energy levels splitting directly depends on the effective magnetic field seen by each site – *i.e.* the projection of the magnetic field on the site local axes. The effective levels splitting in kHz are noted Δ_g and Δ_e. Figure 7.2 represents the magnetic field and the sites local axes. An interesting case occurs when the magnetic field is oriented along [001]. In this case, sites 1 and 2 are orthogonal to the magnetic field so that they undergo a weak energy levels splitting whereas the other four sites are all equivalent of same splitting. Another particular direction would be [111] in which sites 2, 4 and 6 have a weak splitting whereas sites 1, 3 and 5 are all equivalent. In the following, only the case in which the magnetic field is along [001] will be considered. In this case, for magnetic fields up to several hundreds of Gauss, the ground state splitting is very small compared to the thermal agitation k_BT – of the order of 40 GHz at 2 K – so that $|g,+\rangle$ and $|g,-\rangle$ populations are initially equal. As in chapter 6, interactions

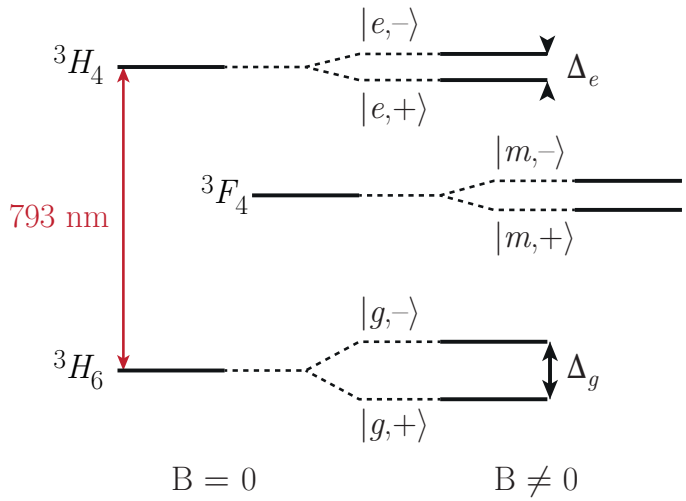

Figure 7.1 – Energy levels of Tm^{3+} under a magnetic field. The three levels $^3H_6$ ($|g\rangle$), $^3H_4$ ($|e\rangle$) and $^3F_4$ ($|m\rangle$) are split in respectively $|g,+\rangle$ and $|g,-\rangle$, $|e,+\rangle$ and $|e,-\rangle$, $|m,+\rangle$ and $|m,-\rangle$. The splitting of the ground state is Δ_g ($= \delta_g \times B_0$), the splitting of excited state is Δ_e ($= \delta_e \times B_0$).

between sites, magnetic field and light strongly depend on light polarization. As an example, let us consider two particular light polarizations [001] (along magnetic field) and [110] (orthogonal) as light propagates along $[1\bar{1}0]$.

- If light is polarized along [001], sites 1 and 2, that have a weak splitting, do not interact with light. The other four sites are all equivalent against both light and magnetic field.
- If light is polarized along [110], sites 3, 4, 5 and 6 are still equivalent against the magnetic field and, in a different way, against light. Site 2 still does not interact with light, but site 1, that have a different splitting now fully interacts with light.

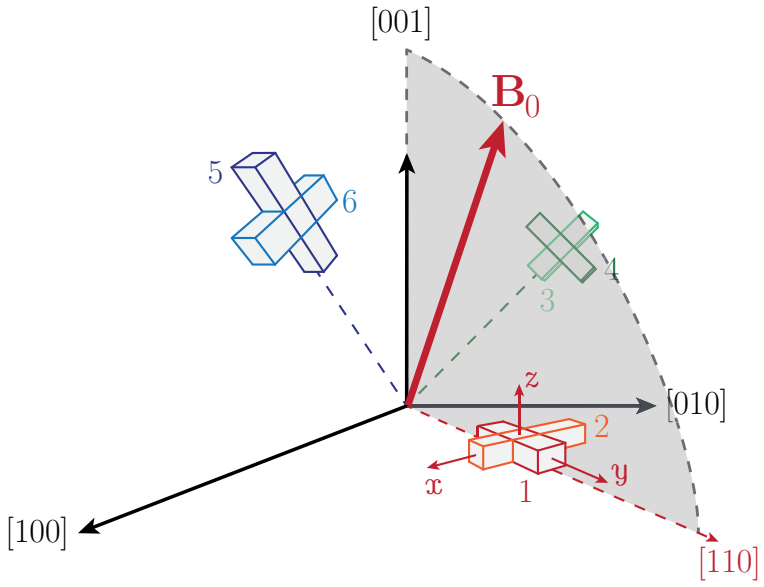

Figure 7.2 – Representation of the magnetic field and the Tm^{3+} sites axes.

In case $\mathbf{B}_0$ is oriented along [001], the selection rules of the optical transition $|g\rangle$ to $|e\rangle$ that can not flip spins imply that transitions from $|g,+\rangle$ to $|e,-\rangle$ and $|g,-\rangle$ to $|e,+\rangle$ are forbidden [182][1]. If considering only these four states, one has two independent systems. Holeburning experiment carried out on such systems should not be any different from the zero-magnetic-field case. In practice, the results presented in [181] suggest that this rule can be overcome. Spin flips may occur during the decay back to $|g\rangle$ through the metastable state $|m\rangle$, due to non-radiative components. The metastable state is thus essential to couple the two split ground levels. Ions that decay back to $|g,-\rangle$ instead of $|g,+\rangle$ are trapped until spin flips in order to decay back to $|g,+\rangle$. As a matter of fact, mechanisms responsible for relaxation from $|g,-\rangle$ to $|g,+\rangle$ are spin-flips mechanisms resulting in potentially very long lifetimes. The first type of these are phonon based mechanisms such as described on figure 6.4(a) in section 6.2.2. A direct consequence of these phenomena is that temperature plays a very important role on the lifetime of the Zeeman levels which is very long in absence of phonons. The second type of mechanisms are temperature-independant mechanisms such as spin flip-flops shown on figure 6.4(b). The impact of these mechanisms increases with dopant concentration.

7.2 Spectral holeburning under a magnetic field

In the previous section, the effect of an external magnetic field on Tm^{3+} ions was qualitatively described. The goal of this section is to study the consequences on spectral holeburning. It must be related to section 6.3 of chapter 6. The principle is the same, this section aims at picturing the main differences.

7.2.1 General principle

The burning and probing sequences are basically identical to what was described in section 6.3.1. Figure 7.1 shows the levels involved in spectral holeburning, splitting of the metastable state will be omitted.

Burning sequence

A burning sequence under magnetic field is represented schematically on figure 7.3. The burning sequence consists in the same light beam at ν_b with a duration T_b as described in 6.3.1. Ions in the ground state $|g,+\rangle$ can only be excited to $|e,+\rangle$ due to selection rules. From $|e,+\rangle$, atoms can non-radiatively decay to the metastable state $|m\rangle$, in which they stay about 10 ms. Then from $|m\rangle$, they can decay to either $|g,+\rangle$ or $|g,-\rangle$ depending on whether the spin flipped during the decaying process back from $|e,+\rangle$ or not. Atoms decaying back to $|g,+\rangle$ can be excited again as atoms decaying in $|g,-\rangle$ stay for a characteristic time of the order of 1 s. As for the zero-magnetic-field case, it is possible to almost empty the ground state $|g,+\rangle$ and move all atoms in the Zeeman level $|g,-\rangle$. It is important to notice that, since the inhomogeneous linewidth is large compared to the different splittings, this phenomenon also occurs for the class of atoms for which the transition $|g,-\rangle$ to $|e,-\rangle$ matches the burning frequency. The storing level is $|g,+\rangle$ in this case (see figure 7.4).

[1] It can be shown that some directions of the magnetic field allow transitions from $|g,+\rangle$ to $|e,-\rangle$ and $|g,-\rangle$ to $|e,+\rangle$ [182, 183], but these cases will not be studied here.

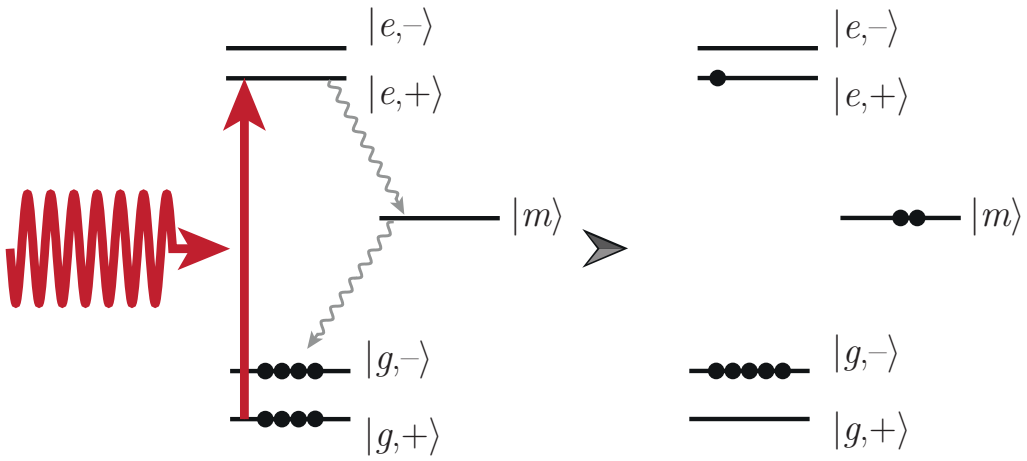

Figure 7.3 – Burning sequence under a magnetic field. Instead of accumulating atoms in the metastable state, the burning beam stores atoms in the Zeeman state $|g,-\rangle$ in which they can remain several seconds.

Probing sequence

In the following, it will be considered that the transition that was burnt is $|g,+\rangle$ to $|e,+\rangle$. In the Zeeman level $|g,-\rangle$, the population can be now up to twice its initial population. If the probing beam is tuned on the transition $|g,-\rangle$ to $|e,-\rangle$ of this class of atoms, the absorption increases – up to twice as absorptive. This absorption increase is called an *anti-hole*. There are four atoms populations that have a transition – forbidden or not – tuned on the burning frequency. These four populations are shown on figure 7.4. Transitions in red corresponds to forbidden transitions, transitions in green are possible. In theory, only cases 5 to 12 did see the burning sequence. The expected shape of the hole should then consist in a hole corresponding to transitions 5 and 9 with two symmetric anti-holes corresponding to transitions 6 and 10. In practice, the magnetic field may not be perfectly oriented along [001]. The consequence is that the forbidden transitions are very weak but possible so the absorption profile is more complex.

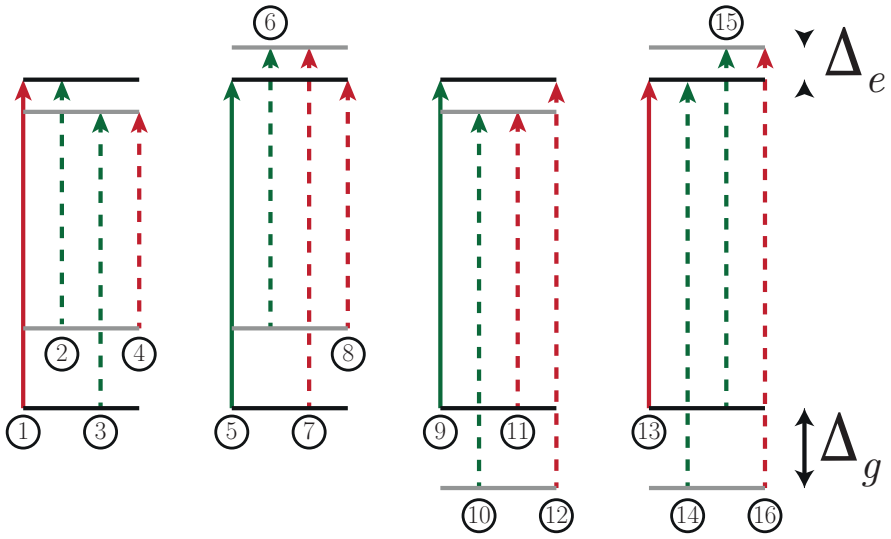

Figure 7.4 – Representation of the four types of populations with a transition at the burning frequency ν_b. Depending on the probing frequency several transitions may occur, red transitions are forbidden, green ones are possible. In practice the forbidden transitions are very weak but possible. A plain arrow corresponds to the transition tuned on the burning sequence frequency.

n°	Frequency	Transparency	Strength	n°	Frequency	Transparency	Strength
1	ν_b	Transp.	w	9	ν_b	Transp.	S
2	$\nu_b - \Delta_g$	Abs.	S	10	$\nu_b + \Delta_g - \Delta_e$	Abs.	S
3	$\nu_b - \Delta_e$	Transp.	S	11	$\nu_b - \Delta_e$	Transp.	w
4	$\nu_b - \Delta_g - \Delta_e$	Abs.	w	12	$\nu_b + \Delta_g$	Abs.	w
5	ν_b	Transp.	S	13	ν_b	Transp.	w
6	$\nu_b - \Delta_g + \Delta_e$	Abs.	S	14	$\nu_b + \Delta_g$	Abs.	S
7	$\nu_b + \Delta_e$	Transp.	w	15	$\nu_b + \Delta_e$	Transp.	S
8	$\nu_b - \Delta_g$	Abs.	w	16	$\nu_b + \Delta_g + \Delta_e$	Abs.	w

Table 7.1 – Table of the different possible transitions involved in spectral holeburning under a magnetic field with their corresponding frequency and strength (Strong or weak). See figure 7.4.

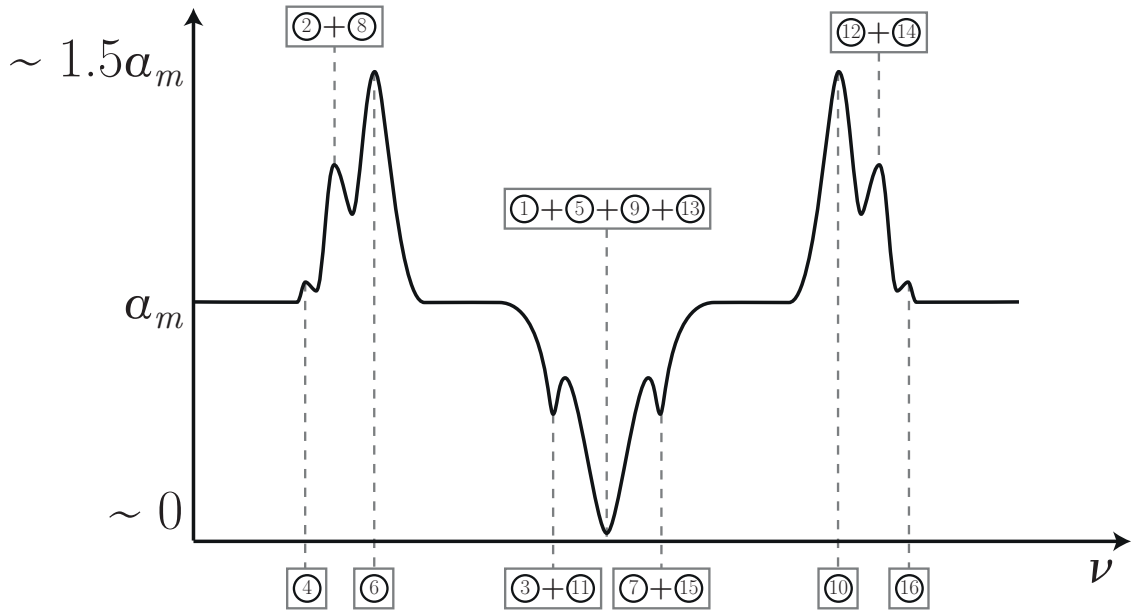

Figure 7.5 – Schematic of a typical absorption profile. In practice peaks corresponding to transitions 4 and 10 are not visible for they corresponds to very weak interactions with both burning and probing sequences.

Table 7.1 gives a summary of the different transitions represented on figure 7.4. Transitions 1, 5, 9 and 10 are the transitions tuned on the burning frequency and all contribute to the main hole at ν_b. Transitions 3 and 11 (resp. 7 and 15) contribute to a smaller hole shifted of $-\Delta_e$ (resp. $+\Delta_e$). The main anti-holes are due to transitions 6 and 10 respectively shifted of $\Delta_e - \Delta_g$ and $\Delta_g - \Delta_e$. Transitions 2 and 8 (resp. 12 and 14) are responsible for a secondary anti-hole shifted of $-\Delta_g$ (resp. $+\Delta_g$). In theory, a third anti-hole should appear on each side of the main hole due to transitions 4 and 16, but it is not visible in practice for it comes from both burning and probing along a weak transition whereas all other spectral features are either burnt or probed along a strong one. A schematic of the expected absorption profile is plotted on figure 7.5 and experimental examples can be found in [184] and [185]. It must be noticed that although the transition absorption increases up to a factor of two on an anti-hole, it does not mean that the total crystal absorption is doubled at this frequency. Indeed, the anti-hole transition only contributes to half the total absorption, the other half being held by the class of atoms for which an optical transition matches the anti-hole frequency. The latter did not interact with the burning beam so that its absorption remains unchanged. Qualitatively, crystal absorption can not increase above $\frac{3}{2}\alpha_m$ on an anti-hole.

In the presence of an external magnetic field, the hole erasure is now expected to occur in three steps, the first two being the same as the zero-magnetic-field case. The first very fast decay occurs over a characteristic time of the order of a few hundreds of microseconds and corresponds to the excited states decay to the metastable state. The second one occurs over about 10 ms and corresponds to the metastable state decaying back to the ground state. The third one is much longer. It occurs over a time of the order of 1 s and corresponds to the time taken by atoms in the Zeeman level $|g,-\rangle$ (resp. $|g,+\rangle$) to flip their spin and return to ground state $|g,+\rangle$ (resp. $|g,-\rangle$).

Of light polarization

Similarly to the zero-magnetic-field case, the presence of the external magnetic field *a priori* induces a light polarization dependence of the hole. As explained in section 7.1, all sites do not see the same effective magnetic field so that their energy levels do not undergo the same splitting. For instance, if the burning beam is polarized perpendicularly to the magnetic field, part of its energy will be used to burn a hole on site 1 that experiences a weak splitting. Similarly, a probing beam polarized perpendicularly to the burning beam may probe sites that did not interact with the burning beam. In order to neglect these considerations in the following, both the burning and the probing beams will be polarized along the magnetic field direction [001], as it was the case in chapter 6.

Summary

In this section I showed that, in the presence of an external magnetic field, the phenomenon of spectral holeburning still holds with a few differences compared to the zero-magnetic-field case. Instead of being accumulated in the metastable state of lifetime of the order of 10 ms, ions are stored from $|g,+\rangle$ in the Zeeman level $|g,-\rangle$ (resp. $|g,-\rangle$ from $|g,+\rangle$, both cases are possible) of lifetime of the order of one second. The first consequence is that the hole remains for much longer durations. The second consequence is that if the probing sequence is tuned on a transition from the storing level to an excited state, the crystal absorption is increased. This increase in absorption is called an anti-hole.

7.2.2 Simple model for spectral holeburning under a magnetic field

Using the same formalism developed in appendix E for the zero-magnetic-field case, the absorption can also be derived in the presence of an external magnetic field. More details are presented in appendix F, only the main hypotheses and results will be recalled here. The levels involved in the holeburning process are presented in figure 7.6. Subscripts {1}, {2}, {3}, {4} and {5} respectively stand for the ground states $|g,+\rangle$ and $|g,-\rangle$, the excited states $|e,+\rangle$ and $|e,-\rangle$ and the metastable state $|m,+\rangle$. The Zeeman splitting of the metastable state was neglected here. It is assumed that the different decay rates are equal, whether they concern a transition of spin $+1/2$ or $-1/2$. The magnetic field is assumed to be oriented along [001] so that optical transitions that involve a spin flip are considered as forbidden transitions.

The hypotheses that were made for the zero-magnetic-field case still hold. Here the transition rate between the two Zeeman ground states is assumed very small compared to the other ones: $\beta \gg \gamma \gg \kappa$ and $\beta \gg w \gg \kappa$. Contrary to the zero-magnetic-field case, it can be shown that only $\frac{4\kappa}{\beta}N$ atoms are left in the excited state – instead of $\frac{\gamma}{\beta}N$. Given these hypotheses it is also possible

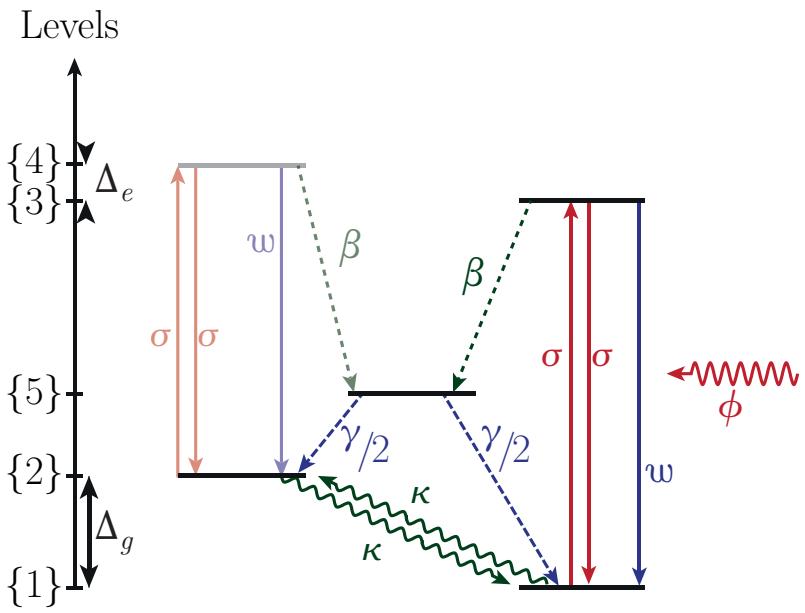

Figure 7.6 – Simplified model of the levels involved in holeburning process under a magnetic field.

to derive the absorption profile of the crystal under a magnetic field:

$$\alpha\left(\nu_p\right) = \sigma_h N \frac{\Gamma_h}{\Gamma_{inh}} \left[1+ \frac{\sqrt{1+\frac{\phi_b}{\phi_s}}-1}{\sqrt{1+\frac{\phi_b}{\phi_s}}} \left(\frac{1}{2}\frac{1}{1+\left(\frac{\nu_p-\nu_b+\Delta_g-\Delta_e}{\Gamma_{\mathrm{HB}}/2}\right)^2} - \frac{1}{1+\left(\frac{\nu_p-\nu_b}{\Gamma_{\mathrm{HB}}/2}\right)^2} + \frac{1}{2}\frac{1}{1+\left(\frac{\nu_p-\nu_b-\Delta_g+\Delta_e}{\Gamma_{\mathrm{HB}}/2}\right)^2} \right) \right] \tag{7.1}$$

where ϕ_s and Γ_{HB} are defined:

$$\phi_s = \frac{1}{\sigma\zeta_B} \text{ with } \zeta_B = \frac{2\kappa+\beta}{4\kappa\left(w+\beta\right)} \sim \frac{1}{4\kappa} \tag{7.2}$$

$$\Gamma_{\mathrm{HB}} = \Gamma_h\left(1+\sqrt{1+\frac{\phi_b}{\phi_s}}\right) \tag{7.3}$$

The expression stands as long as the spectral overlapping between the hole and anti-holes is negligible. Indeed, this expression was derived assuming that the burning beam does not interact with both Zeeman transitions at the same time. This hypothesis is not true for large burning number of photons per unit of time and surface (resp. small Zeeman splitting). Assuming the laser is infinitely narrow, the burning photon number must verify:

$$\phi_b \ll \frac{1+\left(\frac{\Delta_g-\Delta_e}{\Gamma_h/2}\right)^2}{\sigma_h\zeta_B} = \left[1+\left(\frac{\Delta_g-\Delta_e}{\Gamma_h/2}\right)^2\right]\phi_s \tag{7.4}$$

Under a magnetic field, using a lifetime of the Zeeman levels of the order of 1 s, the saturation irradiance under a magnetic field is of the order of 10 $\mu\mathrm{W}\cdot\mathrm{cm}^{-2}$. For a Zeeman splitting $\delta_g - \delta_e = 23\ \mathrm{kHz}\cdot\mathrm{G}^{-1}$ and a magnetic field of 84 G, it gives that the burning irradiance must verify $\Phi_b \ll 80\ \mathrm{mW}\cdot\mathrm{cm}^{-2}$. The calculated absorption coefficient was plotted on figure 7.7 and compared with the no-magnetic-field case, assuming laser line is a Dirac distribution. The burning irradiance was 800 $\mu\mathrm{W}\cdot\mathrm{cm}^{-2}$ in order to ensure that the interaction between the burning beam

and the anti-holes is negligible. One retrieves here the behaviour predicted in section 7.2.1 with a hole flanked by two anti-holes. As the saturation number of photons per unit of time and surface is much smaller in the presence of an external magnetic field, holes can be burnt more easily and are broader.

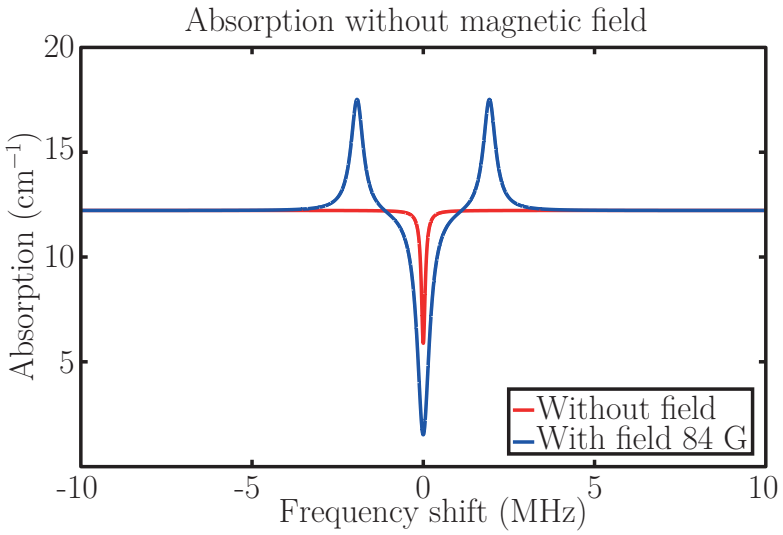

Figure 7.7 – Absorption profile with and without magnetic field at 800 $\mu W \cdot cm^{-2}$ burning irradiance.

Once the burning beam has been shut off, the hole is progressively erased along time according to the following dynamics:

$$\alpha(\nu_b, t) = \sigma_h N \frac{\Gamma_h}{\Gamma_{inh}} \left[1 - \left(1 - \frac{2\kappa}{\gamma} - \frac{6\kappa}{\beta} \right) e^{-2\kappa t} - \left(\frac{2\kappa}{\gamma} + \frac{2\kappa}{\beta} \right) e^{-\gamma t} - \frac{4\kappa}{\beta} e^{-\beta t} \right] \tag{7.5}$$

Here, it was considered that the burning irradiance was infinite in order to simplify the expression and I implicitly neglected the spontaneous decay rate from the excited state. As it was qualitatively guessed in section 7.2.1, the hole erasure now occurs in three stages. The first decay occurs over a time β^{-1} and corresponds to ions leaving the excited states $|e,+\rangle$ and $|e,-\rangle$. The second decay occurs over a characteristic time γ^{-1} corresponding to atoms leaving the metastable state. After this time, only $\left(\frac{2\kappa}{\gamma} + \frac{2\kappa}{\beta}\right) N$ ions return back to the ground states. The rest of the ions returns back to $|g,+\rangle$ – respectively $|g,-\rangle$ – over a characteristic time $(2\kappa)^{-1}$ as they leave $|g,-\rangle$ – respectively $|g,+\rangle$.

It appears from this simple model that the behaviour of the main hole under a magnetic field is identical to the no-magnetic-field one, at the only difference that the saturation irradiance is now smaller. The hole is flanked by two anti-holes that correspond to an increase of the crystal absorption. Through conservation of the number of atoms, they are twice as shallow and behave the same way as the hole. One of the main advantages of using an external magnetic field is the increase of the lifetime of the hole which is now of the order of 1 s.

7.2.3 Towards acousto-optic imaging

In the previous section the main properties of a hole under a magnetic field were theoretically described. It is then natural to wonder why this evolution of properties is interesting for acousto-optic imaging.

The main point justifying the use of a magnetic field is that the hole lasts several seconds with significant depth, whereas it was only lasting a few tens of milliseconds without. It can now be considered burning only one time and performing the whole image at once, which may drastically increase the imaging rate. An interesting side effect is that the delay between the burning and the probing beams has less influence on the hole depth. On the other hand, anti-holes can be used to increase the untagged photons absorption. In order to have a few quantitative values, Li *et al.* [108] use 3.3 ms long pulses with very high power in order to efficiently engrave a hole. Because the burning power is very high, they are forced to use an optical shutter (Uniblitz, VS14S2S1) in order to avoid blinding their detector with reflected remainder of the burning light. This shutter takes at least 1.5 ms to fully open. According to the model developed in appendix E and assuming they burnt transparent holes, by the time the shutter fully opens, about 17% of the atoms have already returned back to the ground state. As they report an absorption coefficient of $\alpha_m L = 4$, it comes that the hole is expected to have lost $\exp(-0.17 \times 4) = 50\%$ of its transmission. If we now assume that ultrafast acousto-optic sequences lasting 0.8 s are used, it comes that the burning sequence must be repeated optimistically at least 100 times. About 500 ms must then be added to the total imaging sequence so that the imaging rate is almost divided by two with a filtering efficiency that is at maximum 50% of what it is expected to be. In the presence of an external magnetic field, with a lifetime of the Zeeman level of 1 s, by the time the shutter fully opens, only 0.7% of the atoms have returned back to the ground state so that, with $\alpha_m L = 4$, the hole depth is still 97% of what it is expected to be. Once a hole is engraved, it can be considered pulsing the whole sequence at once. In terms of imaging rate, the question is then to quantify the duration of a burning beam for acceptable transparency.

7.3 Quantification of hole properties

The goal of this section is to experimentally quantify, and tailor if need be, the hole properties in view of the requirements of an acousto-optic imaging system. The results obtained here are meant to be compared with the no-magnetic-field case. The setup is the same setup as described in figure 6.20. In the following, the magnetic field is generated by two Helmoltz coils that carry a current of several amperes and is assumed oriented along [001] and so are the burning and probing beams polarisations. The coils are calibrated so that they generate a magnetic field of $7\ \mathrm{G} \cdot \mathrm{A}^{-1}$.

7.3.1 Hole and anti-holes

Shape of a hole

A hole is burnt under a magnetic field in order to compare its shape with the predicted one. As the crystal is very absorbing, the anti-holes are difficult to see within the crystal transmission for they are often very broad and comparable to the noise level. The laser was detuned on purpose of 30 GHz from the central frequency in order to decrease the crystal absorption and see the anti-holes easily. The burning power is about $30\ \mathrm{mW} \cdot \mathrm{cm}^{-2}$ during 10 ms. The delay between the burning sequence and the probing sequence is only 10 µs. The hole at about 2 K and 98 G is shown on figure 7.8. The first observation that can be made here is that the hole and anti-holes present several peaks, meaning that optical transitions involving spin flips are partly allowed, probably due to the magnetic field not being perfectly aligned with [001]. The main hole can be fitted with a Lorentzian curve rather well, as predicted by the simple model derived in section 7.2.2 and is about twice as high as the anti-holes.

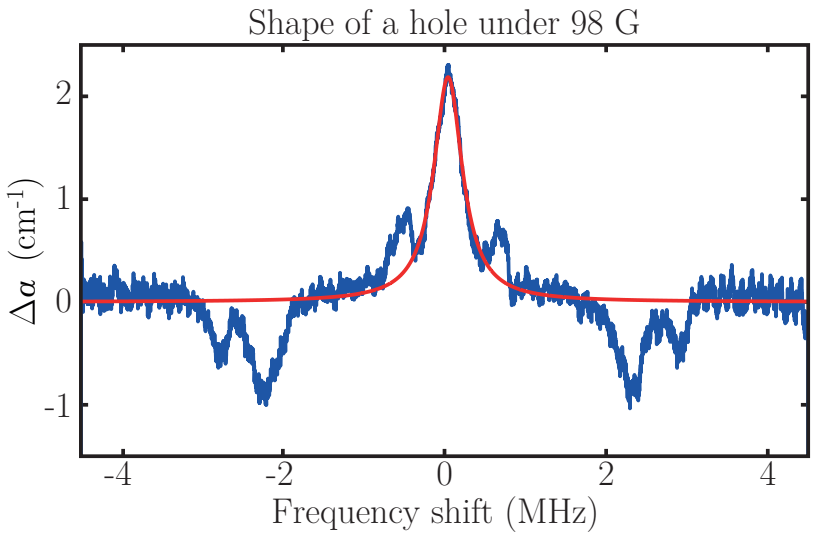

Figure 7.8 – Absorption profile under 98 G at about 30 $\mathrm{mW \cdot cm^{-2}}$ burning irradiance during 10 ms. The anti-holes are clearly visible and one can notice here that holes and anti-holes present several peaks, meaning that optical transitions involving spin flips are not completely forbidden.

Influence of the magnetic field

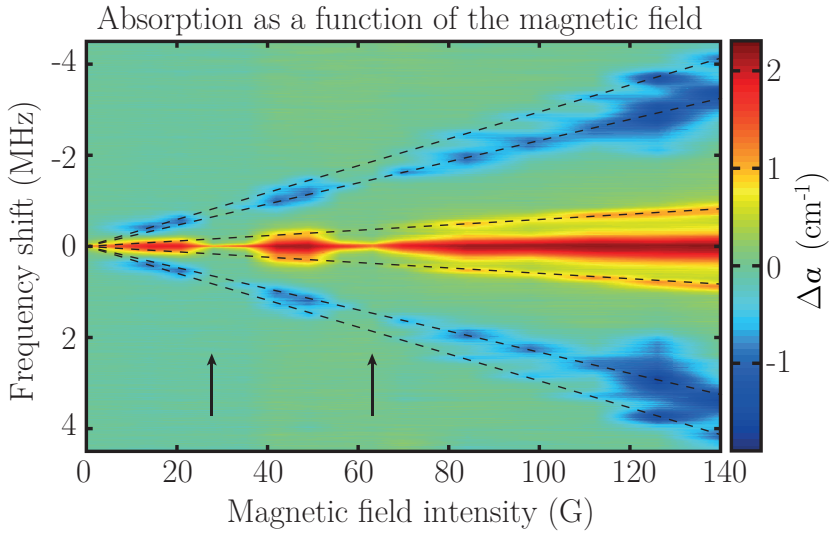

Figure 7.9 – Absorption profile as a function of the magnetic field. Dashed lines are guidelines for the secondary holes and the anti-holes. The position of the holes and anti-holes maxima can be accurately pointed out in order to recover the splittings δ_e and δ_g. The two arrows point to two particular regions in which the effect of the magnetic field seems to cancel.

Keeping in mind the idea of using the anti-holes as a means of increasing the untagged photons absorption, it is interesting to probe the position of the anti-holes as a function of the magnetic field so that the right magnetic field value can be chosen depending on the ultrasound frequency. Several absorption profiles were acquired for different values of the magnetic field and plotted on figure 7.9. Dashed lines were added as guidelines for the positions of the different holes and anti-holes. The position of the holes and anti-holes maxima was accurately pointed out and plotted in order to recover the splitting values. The positions of the main anti-holes maxima are reported on figure 7.10. According to section 7.2.1 and table 7.1, these anti-holes corresponds to strong transitions shifted from the main hole of respectively $\Delta_e - \Delta_g = (\delta_e - \delta_g) \times B_0$ and

$\Delta_g - \Delta_e = (\delta_g - \delta_e) \times B_0$. A linear fitting curve leads to $\delta_g - \delta_e = 23$ kHz $\cdot$ G^{-1}. The same can be done for the secondary anti-holes corresponding to the weak transitions at Δ_g and it leads to a ground state splitting of $\delta_g = 30$ kHz $\cdot$ G^{-1}. From these measurements, the excited state splitting can be deduced and is equal to $\delta_e = 7$ kHz $\cdot$ G^{-1}, consistent with the measured positions of the secondary holes at high field values and in perfect agreement with [183].

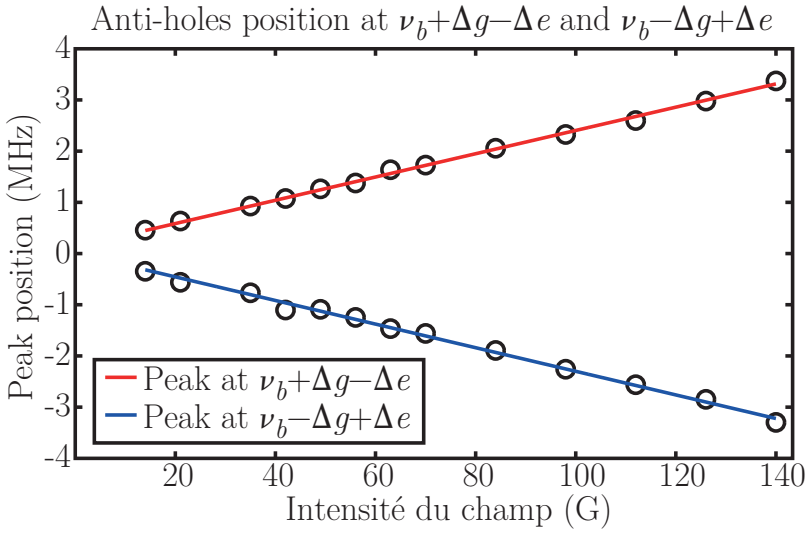

Figure 7.10 – Position of the main anti-holes as a function of the magnetic field. According to section 7.2.1 and table 7.1, these anti-holes correspond to strong transitions at $\Delta_g - \Delta_e$ and $\Delta_e - \Delta_g$. A linear fit leads to $\delta_g - \delta_e = 23$ kHz $\cdot$ G^{-1}.

It is of interest to notice here that the effect of the magnetic field seems to cancel around 30 and 60 G (pointed out by the two arrows on figure 7.9). This effect was reported by R. Ahlefeldt *et al.* in [186] and corresponds to a cross-relaxation effect between Tm^{3+} and Al^{3+} ions. For some magnetic field intensities, the splitting of the Tm^{3+} ground state corresponds to a transition of Al^{3+} so that spin *flip-flop* (see figure 6.4(b)) can occur between the two species. This kind of relaxation is very efficient for it occurs at constant energy. The consequence is that the lifetime of the Zeeman states is drastically reduced and the effect of the magnetic field disappears. R. Ahlefeldt *et al.* report three possible particular values of the splitting for which this cross-relaxation occurs for an external magnetic field oriented along [001]: $\Delta_g = 0.9$ MHz ($\sim$ 30 G), $\Delta_g = 1.8$ MHz ($\sim$ 60 G) and $\Delta_g = 2.7$ MHz ($\sim$ 90 G). It is also reported that the third splitting at $\Delta_g = 2.7$ MHz corresponds to very weak cross-relaxation. Only the first two transitions have a visible effect on the holes and their positions are consistent with the predicted values.

Hole lifetime

Choosing a value of the magnetic field around 84 G, the hole lifetime at about 1.5 K was quantified for a burning power of 750 µW during 1 s. The waist of the burning beam is of the order of 500 µm while the waist of the probing beam is about 200 µm. The delay between the burning and probing sequences was increased up to 3 s and the area of the hole was measured. Due to the repetition rate of the sequence (10 Hz) being higher than the decay rate of the hole under a magnetic field, the holeburning process in this case is in a regime in which atoms can be accumulated in the storing level from a burning sequence to another even if the burning time is short compared to the lifetime of the Zeeman levels. In practice, the atomic system can be assumed to tend toward steady-state after several burning sequences. Data with a magnetic field are thus acquired several seconds after

the first burning sequence. The hole area was then measured after accumulating enough of them so that it is the case. The corresponding result is shown on figure 7.11. A fast decay occurs at the beginning corresponding to atoms leaving the metastable state. The amount of this decay is small, letting think that, as expected, there are few atoms in the metastable state. After a few hundreds of milliseconds, a very slow decay occurs corresponding to the atoms leaving the storing Zeeman level. The lifetime was measured through a linear fit and was estimated of the order of 7 s. It is important to notice that since this decay occurs through spin-flip processes, the hole lifetime is very dependent on the temperature. Given this measured lifetime, the corresponding saturation irradiance can be estimated to about 1.4 $\mu W \cdot cm^{-2}$.

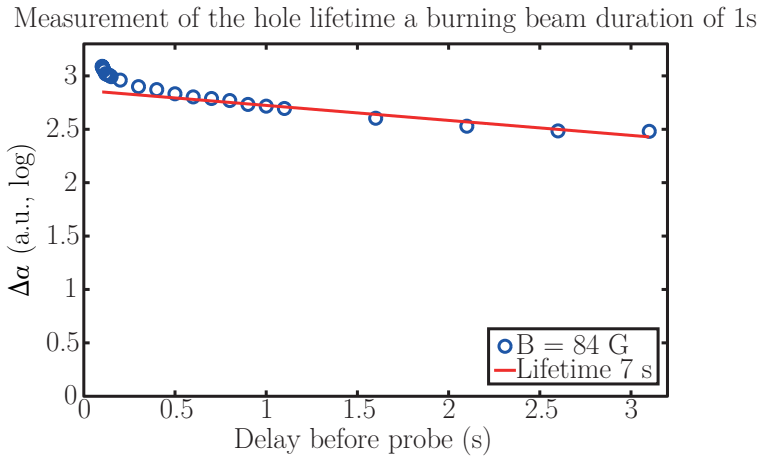

Figure 7.11 – Hole area in logarithmic scale as a function of the delay between the burning and probing sequences. One observes a fast decrease at the beginning corresponding to atoms leaving the metastable state, followed by a slow decrease over a characteristic time of the order of 7 s corresponding to atoms leaving the storing Zeeman state.

This long lifetime is the main justification of the use of a magnetic field. Once the system is in steady-state, several seconds are available to perform the entire imaging sequence. However, it is important to notice that laser stability is of prime importance at this time-scale. If a drift of few kHz over 1 s is negligible for zero-magnetic field holes for which lifetimes are very short, it is no longer the case when working with several seconds lifetimes. The risk is that the laser reaches an anti-hole after slowly drifting for long enough.

7.3.2 Influence of the burning power

On the hole depth

In order to further quantify the effect of the magnetic field, the same characterisation as in section 6.5.1 of chapter 6 can be performed with an external magnetic field. The experimental setup is described in section 6.5.1 and the experimental conditions are identical. As a reminder, the temperature is about 1.5 K, the delay between the burning and the probing sequences is 500 µs and the burning beam is a Gaussian beam of diameter of the order of 500 µm. The probing beam has a diameter of about 200 µm, its power is of the order of a few µW and chirps 9 MHz over 200 µs. The hole depth is measured as a function of the burning irradiance and compared to the zero-magnetic-field case in the same conditions. The hole is still burnt in an accumulation regime and the hole depth is measured after several seconds in order to be as close as possible to steady-state. Resulting data are plotted on figure 7.12 for a burning duration of 500 ms. The blue

curve corresponds to data under a magnetic field as the red one corresponds to data in the same conditions without magnetic field. As a matter of fact, the results for the zero-magnetic-field case shown here are the results that were used in section 6.5.3 to measure the saturation irradiance of 5.2 $\mathrm{mW \cdot cm^{-2}}$. A fit of data under a magnetic field using the model derived in section 7.2.2 leads to a saturation irradiance of 0.8 $\mathrm{mW \cdot cm^{-2}}$. As expected, the burning efficiency is higher with a magnetic field. However, the saturation irradiance is not as small as expected in the presence of a magnetic field as shown from the previous estimations. Two hypotheses may justify this deviation. The first one concerns laser stability and drifts. Indeed, now the lifetime of holes is of the order of several seconds, the atomic system is much more sensitive to laser stability: it is necessary to ensure small laser jitter and drifts over characteristic times of several seconds instead of few tens of milliseconds. For instance, during the time it takes for steady-state to establish, it is possible that laser drifts and excites atoms in the anti-holes thus decreasing the hole depth. The second possible origin of this deviation is the spatial inhomogeneity of the burning beam. Similarly to what was noticed in the zero-magnetic field case, the burning and probing beams have comparable sizes so that the probed hole is an averaged hole over the Gaussian beams and crystal thickness. As the burning irradiance decreases, holes become thinner and shallower so that it takes higher irradiances to burn equivalent transparency, the consequence of which is that the saturation irradiance increases.

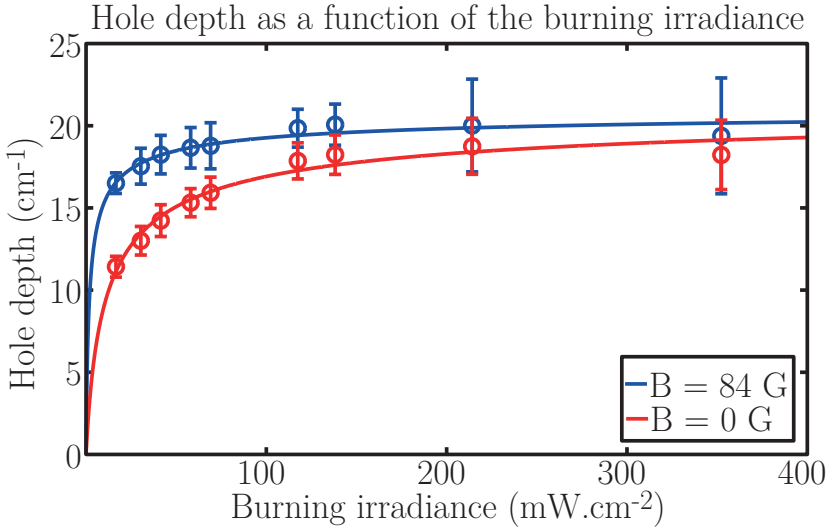

Figure 7.12 – Hole depth as a function of the burning irradiance. The blue curve corresponds to the averaged hole over the probing and burning beams areas under a magnetic field of 84 G, the red curve corresponds to the averaged hole over the probing and burning beams areas without external magnetic field. The saturation irradiance was measured thanks to fitting curves. It is equal to 5.2 $\mathrm{mW \cdot cm^{-2}}$ without magnetic field, 0.8 $\mathrm{mW \cdot cm^{-2}}$ in the presence of an external magnetic field. As expected it is easier to burn holes under a magnetic field.

Another experiment was performed in better conditions in several aspects under 98 G with optimized injection in the laser amplifiers and pumped Fabry-Perot cavity in order to limit laser drifts and instabilities. The burning duration was 10 ms. The burning beam was expanded up to a diameter of the order of 3 to 5 mm (not estimated precisely) whereas the probing beam had similar size compared to the previous case so that the burning beam is now much larger than the probe and the latter probes a crystal area with almost homogeneous burning irradiance. In order to decrease the effects of the hole erasure at maximum, the delay between the burning and probing beams was decreased down to 10 µs. The hole depth as a function of the burning power

is plotted on figure 7.13. Here the maximum absorption is estimated to about 28 cm^{-1} leading to a $\alpha_m L = 5.6$ as expected from the first estimations of section 6.2.3. Given the inaccuracy over the burning beam surface, the fitting curve leads to a saturation irradiance between 2 and 6 $\mu W \cdot cm^{-2}$, in good agreement with the predicted order of magnitude. Because of the very high burning efficiency, this measurement gives the best available estimation of the absorption of the crystal up to now. Here, the hole depth decreases at high burning powers. This probably corresponds to the burning beam starting to burn both Zeeman transitions at the same time – *i.e.* the burning beam starts erasing the anti-holes – as described in section 7.2.2. It is interesting to notice that this effect is not visible on the averaged hole of figure 7.12 because the decrease of the holes depth near the center of the Gaussian beam is partially compensated by the increase of transparency of holes on the edges, but it also explains why the fitted burning irradiance is not as low as expected: when the burning power increases, holes in the center start being erased. Eventually, this suggests that the crystal transparency under a magnetic field will not be as close to 1 as expected in the case of averaged holes, no matter how powerful the burning beam is.

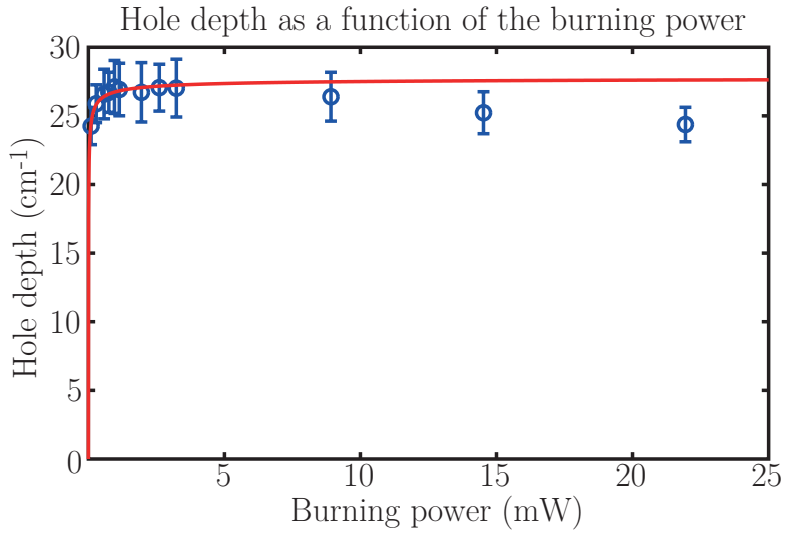

Figure 7.13 – Hole depth as a function of the burning power at 98 G under different experimental conditions such as optimized injection in the amplifiers, pumped stabilizing cavity and expanded burning beam. The saturation irradiance is estimated of the order of a few $\mu W \cdot cm^{-2}$ more compatible with the predicted order of magnitude.

On the hole linewidth

In the same conditions that gave the results presented on figure 7.12, the hole linewidth was measured as a function of the burning irradiance under a magnetic field for a burning duration of 500 ms. The corresponding result is plotted on figure 7.14 and compared to the same case without magnetic field. The hole linewidth follows a square root evolution but it seems to be no saturation irradiance difference between the two curves. This probably comes from the spatial inhomogeneity of the burning irradiance. Holes become thinner as the burning power decreases while being absorbed inside the crystal or near the edges of the Gaussian beam so that the averaged linewidth is difficult to estimate precisely. Another interesting point is that in order to have a decent fit in the presence of a magnetic field, the offset containing the laser linewidth had to be increased. This observation tends to confirm that the hole under a magnetic field is more sensitive to laser instabilities. Laser drifts that are rather small over the few tens of milliseconds lifetime without magnetic field become more important over several seconds.

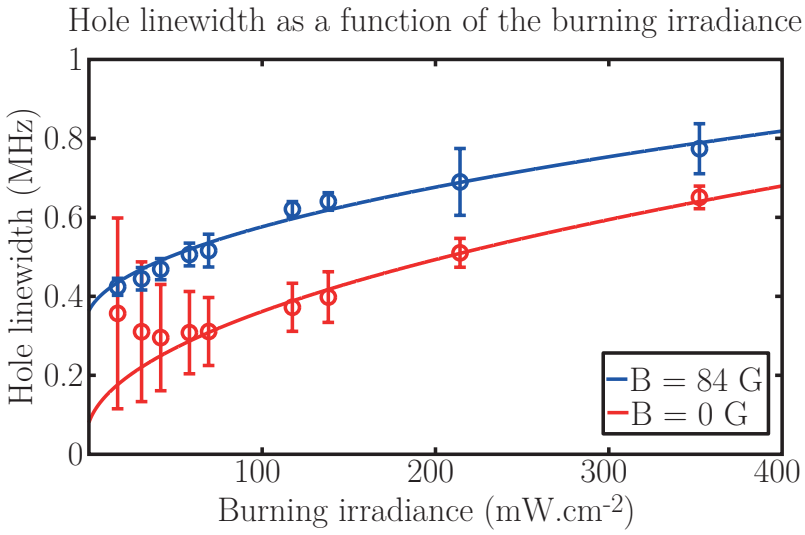

Figure 7.14 – Hole linewidth as a function of the burning irradiance. The predicted square root shape seems in good agreement with experimental data but the values of the fitted parameters do not stick to the predicted ones. This is a probable consequence of the spatially inhomogeneous burning irradiance.

7.4 Transposition to tagged photons

At this point of the manuscript, holes properties were theoretically derived and experimentally studied. I studied the evolution of the hole depth and width as the burning irradiance increases. Experiences have shown that even in ideal conditions it is not straightforward to tend toward optimal filtering properties. However, they gave an idea of potential capabilities of spectral hole-burning under a magnetic field as a filtering technique for acousto-optic imaging. The absorption of the crystal was eventually estimated thanks to holeburning sequences under a magnetic field in optimized conditions and is at least $\alpha_m L = 5.6$. The lifetime of the hole was measured around 7 s at 1.5 K.

The filtering efficiency depends on the burning efficiency through the lifetime of the storing level and the number of atoms stored in it. I showed that the hole is influenced a lot by the number of atoms that remained in the intermediate levels of shorter lifetimes. The saturation irradiance is a parameter that can be used in order to quantify the burning efficiency in given experimental conditions. It is an effective parameter that takes into account several experimental considerations such as the burning duration, light spatial repartition on and within the crystal or laser stability. I showed that in order to get ideal filtering:

- the atomic system must be in steady-state at the end of the burning beam so that the highest number of atoms are stored in the Zeeman states.
- the burning beam should be homogeneous at the scale of the probing beam so that probed holes are identical over the whole probed crystal area.
- the burning irradiance should not be too high at the risk of erasing the anti-holes or other unwanted effects.
- polarization of the burning and probing beam should be aligned with the magnetic field.
- the laser should be as stable as possible so that the burning efficiency is optimal and holes are not too broad.

Obviously, these conditions are difficult to satisfy, and even impossible for some of them, in acousto-optic imaging. Indeed, imaging rate limitations make steady-state difficult to reach. Due to the speckle property of scattered light, a good signal collection implies that the whole crystal surface is illuminated. It is then difficult to consider having a homogeneous burning irradiance at the scale of the probing speckle pattern. These two limitations will necessarily involve higher burning powers. Due to the speckle pattern of scattered light again, the polarization of the probing beam is random so that a portion of light will be absorbed by the crystal anyway. As the scattering medium has to be illuminated with high powers, powerful slave lasers must be used as light amplifiers. As a consequence, they can induce instabilities and ASE background. On the other hand, tagged photons to be filtered have a broader spectrum – several MHz due to the ultrasound pulses bandwidth – so that a decrease of the hole depth may be compensated by an increase of the hole linewidth. As a consequence of these reasons, it is not straightforward to transpose the ideal case to scattered light.

The goal of this section is to experimentally study the behaviour of the crystal in an acousto-optic imaging situation. I will work on tagged photons in a particular configuration for acousto-optic imaging. If the results obtained here depend on the chosen configuration, the degraded capabilities can often be interpreted in the light of the above.

7.4.1 Acousto-optic imaging setup

The acousto-optic imaging system is very similar to what was used in [108] and is presented on figure 7.15. The light coming from the stabilized laser diode is amplified a first time by a slave amplifier Eagleyard Photonics Laser Diode (AMPLI 1) and split into two beams thanks to a polarization beam splitter: the signal and burning beams. The signal beam is amplified a second time by a Sacher LaserTechnik fibred tapered amplifier (AMPLI 2) and sent on the scattering sample placed within a water tank (WT). An acousto-optic modulator (AOM) is used to pulse the probing light in order to prevent scattered light from burning unwanted holes. Scattered light is collected through a liquid core optical fibre (LCOF) and 3 inches thick lenses (TL) and guided through the crystal to a 1 mm^2 Hamamatsu avalanche photodiode (APD). Ultrasound pulses (US) are sent inside the sample along the y-axis direction thanks to single-element transducer Olympus Panametrics NDT A307S (5 MHz, 1" diameter, 2" focal length). The burning beam is also amplified a second time by a Toptica BoosTA slave laser (AMPLI 3). Due to the in-line windows of the cryostat being obstructed by the thick lenses, it is difficult to control the burning beam in a counter-propagating configuration. The Tm^{3+}:YAG crystal is polished on its six faces so that an acceptable alternative consists in burning from the orthogonal windows on the side of the crystal through a cylindrical lens (CL). In order to prevent the photodiode from being blinded by reflected burning stray light, an optical shutter Uniblitz VS14S1T1 (not shown on figure 7.15) controlled by a VCM-D1 controller is placed in front of the APD and only opens when scattered light is on. The APD signal is sent through electronic band-pass filters and acquired with an acquisition card.

The magnetic field is still oriented along [001]. At first, imaging rate considerations will be left aside. The idea is to check the feasibility of acousto-optic imaging with spectral holeburning with and without external magnetic field. The burning sequence will be repeated before every ultrasound pulse so that in the presence of an external magnetic field atoms can be accumulated in the Zeeman state though the burning time is much shorter than the lifetime of the Zeeman levels. The corresponding acousto-optic sequence is represented on figure 7.16. The burning beam lasts 10 ms and the shutter starts opening just at the end for 4.5 ms. The probing light is sent 1.5 ms

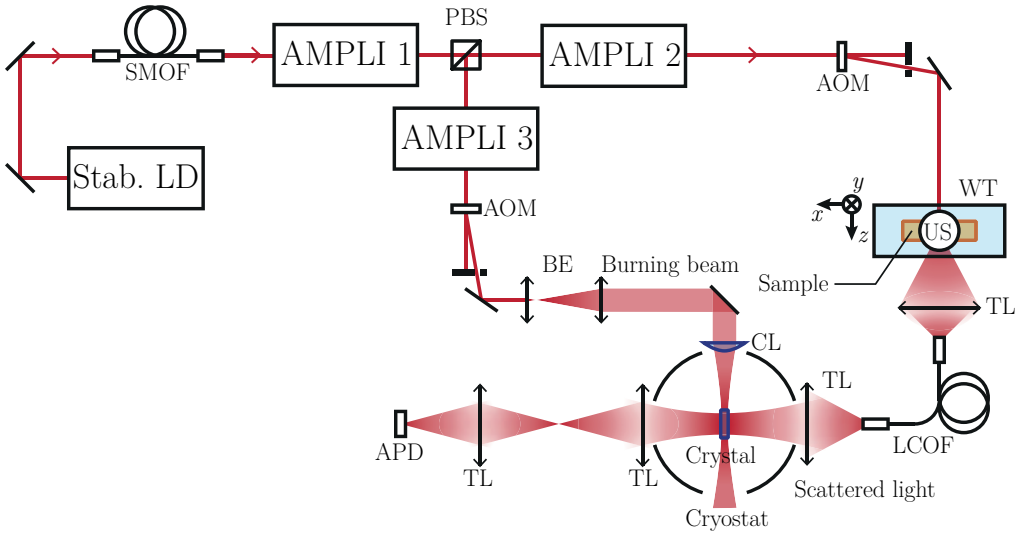

Figure 7.15 – Acousto-optic imaging setup. The light coming from the stabilized laser diode is amplified a first time by a slave amplifier (AMPLI 1). The signal beam is amplified a second time by a fibred tapered amplifier (AMPLI 2) and sent on the scattering sample placed within a water tank (WT). The scattered light is collected by a liquid core optical fibre (LCOF) and thick lenses (TL) of 3 inches diameter. Ultrasound pulses (US) are sent within the sample along the y-axis direction thanks to single-element transducer. The burning beam is amplified a second time by a Toptica BoosTA slave laser (AMPLI 3). The burning beam is sent through the orthogonal windows on the side of the crystal through a cylindrical lens (CL). The acousto-optic signal is measured on an avalanche photodiode (APD). PBS: Polarization Beam Splitter, BE: Beam Expander, SMOF: Single-Mode Optical Fibre, AOM: Acousto-Optic Modulator.

after the beginning of the shutter opening, characteristic time for the shutter to fully open. The probing sequence consists in a light beam shifted from the burning frequency of the ultrasound frequency and lasts few hundred of µs (typically 200 µs). The ultrasound pulse is sent after a variable delay, typically 100 µs, and the probing light remains on for a time long enough to let the ultrasound pulse explore the sample. The sequence is repeated with a 10 Hz rate.

7.4.2 Of burning beam shape and absorption

Because the in-line windows of the cryostat are obstructed by thick lenses, it is more comfortable to burn on the edge of the crystal through the orthogonal windows. The burning beam is polarized along the magnetic field direction. However, it is to be remembered that the burning beam is absorbed while propagating inside the crystal. If the absorption of the burning beam is often neglected when working with a crystal thickness of 0.2 cm, it shall not be the case if the burning beam comes from an edge for which the thickness is 1 cm. It is interesting to estimate the burnt area within the crystal. The absorption coefficient of the crystal was computed as a function of the depth inside the crystal using the thickness dependent model of appendix E, assuming steady-state is reached and neglecting the spatial variations of irradiance in the other directions – *i.e.* the edge of the crystal of surface 0.2 cm^2 is assumed to be homogeneously illuminated. The chosen lifetimes here were 9 ms for the metastable state and 2.5 s for the Zeeman levels. The maximum absorption of the crystal was chosen so that $\alpha_m L = 5.3$. The computed absorption is the absorption at $\nu_p = \nu_b$ and, in the case of the presence of an external magnetic field, the anti-hole erasure at high burning powers was not considered. The absorption variation as a function of the depth inside the crystal is plotted on figure 7.17 for three burning powers at the illuminated face: 100 µW, 1 mW and

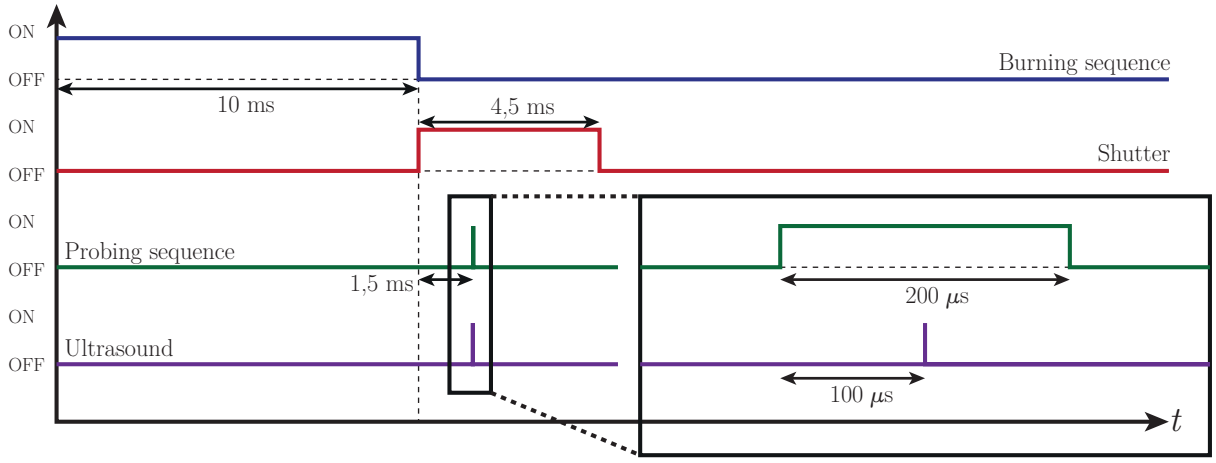

Figure 7.16 – Acousto-optic sequence.

10 mW. It is to be remembered here that, because of light scattering, the acousto-optic image shape is only driven by the ultrasound pulses so that the spatially inhomogeneous absorption inside the crystal does not distort the final image.

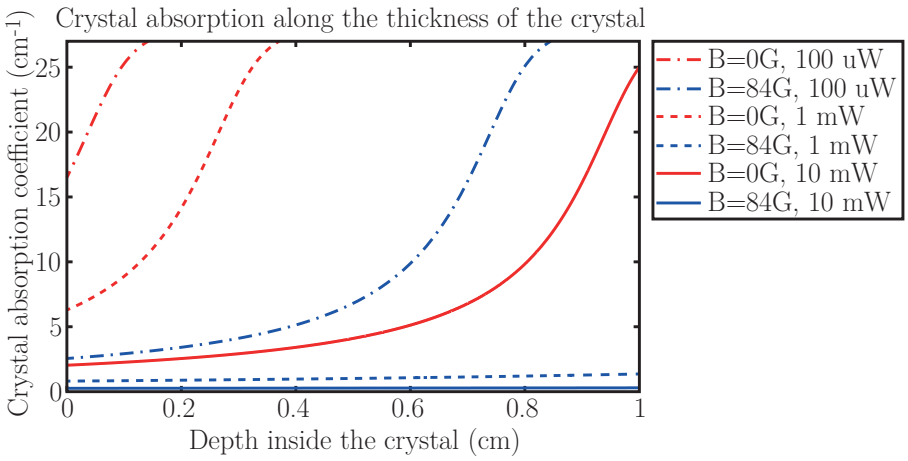

Figure 7.17 – Absorption repartition within the thickness of the crystal when burning from an edge for three burning powers at the illuminated face: 100 µW, 1 mW and 10 mW. The whole surface of the edge of the crystal is assumed homogeneously illuminated. The anti-hole erasure at high burning powers is neglected.

This absorption repartition within the crystal can be integrated in order to derive the global crystal transmission. This integrated transmission was computed for several illumination powers on the edge. The result was plotted in dashed lines on figure 7.18. Here the edge of the crystal is still assumed homogeneously illuminated. In order to take into account the burning beam shape, the same was performed assuming that the burning beam which is focused through a cylindrical lens is homogeneous in the vertical dimension and Gaussian-shaped in the orthogonal direction. By discretizing this latter dimension, it is possible to compute an integrated transmission that takes into account the inhomogeneous burning in the two dimensions. This was performed using a Gaussian waist of 500 µm and plotted in plain lines on figure 7.18. The interesting point here is that, if the anti-holes erasure at high burning irradiances is neglected, the transmitted light through the crystal is expected to be at least about 20% higher with a magnetic field. Here, the hole erasure after the end of the burning sequence was not taken into account but the latter is expected to increase this signal difference even more.

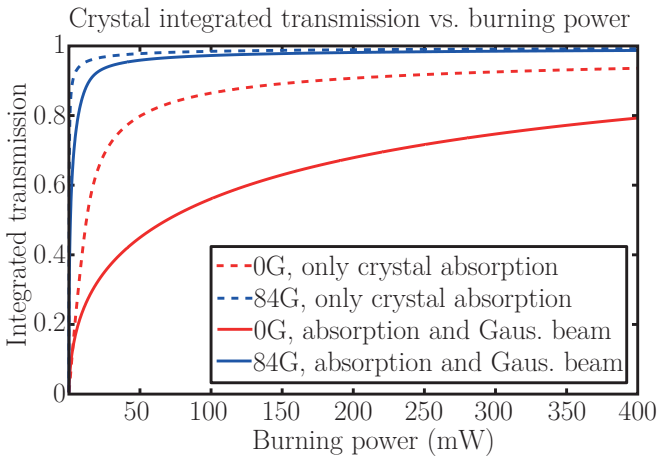

Figure 7.18 – Integrated transmission of the crystal as a function of the burning power. Dashed lines correspond to a homogeneous illumination on the whole edge of the crystal. Plain lines correspond to the integrated transmission of the crystal for a focused beam through a cylindrical lens assumed homogeneous in the vertical dimension and Gaussian-shaped in the other with a waist of 500 µm

7.5 A proof of concept

In this section, I will present the proof of concept of spectral holeburning as a narrowband filter for acousto-optic imaging through the study of 1D acousto-optic signals. In the following, the acousto-optic signal was optimized without any external magnetic field and compared to the signal obtained with an external magnetic field in the same conditions. The same sequence is then compared with and without magnetic field. In view of what was observed in the previous sections, it is to be kept in mind that the sequence is not optimized for the presence of an external magnetic field. The optimization of the acousto-optic sequence in this case is not the point of this proof of concept. I will not consider imaging rate and anti-holes issues in the following.

7.5.1 Acousto-optic signal

Let us now converge step by step towards acousto-optic imaging. At first, I will work on tagged ballistic light in order to have a simple case with a lot of tagged photons. The tank is filled with clear water, light is directly tagged by ultrasound pulses. The speckle pattern of scattered light is provided by the propagation through the multi-mode liquid core optical fibre. The burning beam power is 350 mW during 10 ms so that the acousto-optic signal without magnetic field is maximum. Due to the repetition rate of the burning sequence being higher than the decay rate of the hole under a magnetic field, atoms can be accumulated in the Zeeman level. Data in the presence of an external magnetic field are acquired after a time long enough to tend towards the steady-state (several seconds). The probing beam power is of the order of 200 µW before the liquid core fibre, considerably higher than what is usually collected after a scattering medium. Ultrasound pulses of 10 cycles at 5 MHz are sent inside the water tank at 10 Hz repetition rate, which corresponds to a 3 mm long pulse. They are generated by an Arbitrary Waveform Generator (AWG) and amplified by a RF power amplifier. There is no optical shutter here and the delay between the burning and probing beams is 1 ms. The acousto-optic signals are averaged 512 times and plotted on figure 7.19. The acousto-optic signal is about twice as high with a magnetic field.

The pressure response of the system constituted of the AWG followed by the RF power amplifier

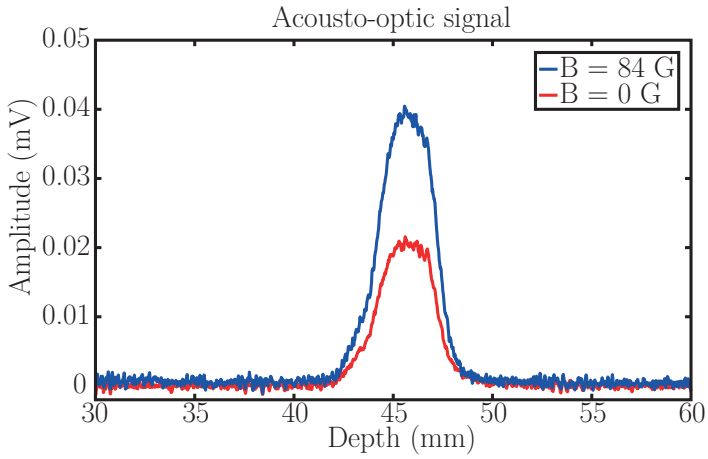

Figure 7.19 – Acousto-optic signal obtained when tagging ballistic light so that a lot of photons are tagged. The increase of acousto-optic signal is of the order of a factor of 2.

and the transducer was not calibrated. However, figure 7.20 shows the evolution of the acousto-optic signal as the input voltage of the RF amplifier is increased. At low voltages, the curves follow the expected quadratic evolution of the acousto-optic signal as a function of the acoustic pressure. Acousto-optic signal reaches a plateau at high AWG output voltages, probably due to the RF amplifier output saturating. In the following, the output voltage of the AWG will always be in the saturation region of the amplifier.

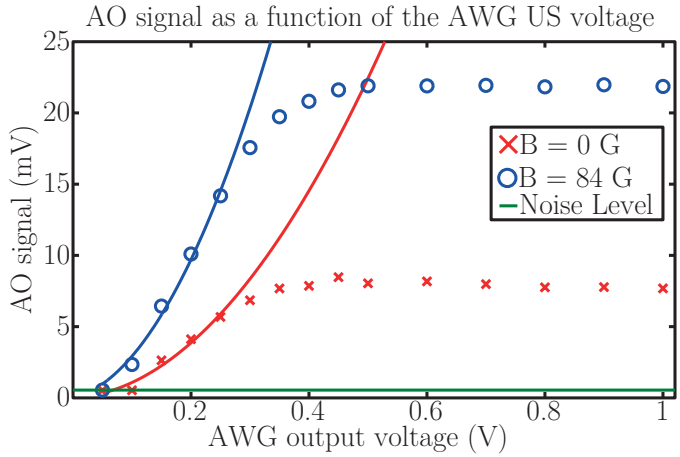

Figure 7.20 – Acousto-optic signal as a function of the AWG output voltage in the RF amplifier. At low voltages, the acousto-optic signal is quadratic as expected. At higher voltages, the acousto-optic signal reaches a plateau, probably due to the RF amplifier output saturating. Red curve corresponds to the acousto-optic signal under zero magnetic field, blue curve corresponds to the acousto-optic signal in the presence of an external magnetic field at 84 G, green line is the global noise level of signal. Signals higher than this line are considered as detected acousto-optic signal.

7.5.2 Behaviour of the acousto-optic signal

The behaviour of the tagged photons signal was explored as the magnetic field varies. Results are plotted on figure 7.21. As expected, the effect of the magnetic field vanishes at 35 and 70 G, corresponding to the coupling with the two transitions of Al^{3+} ions described in section 7.3.1.

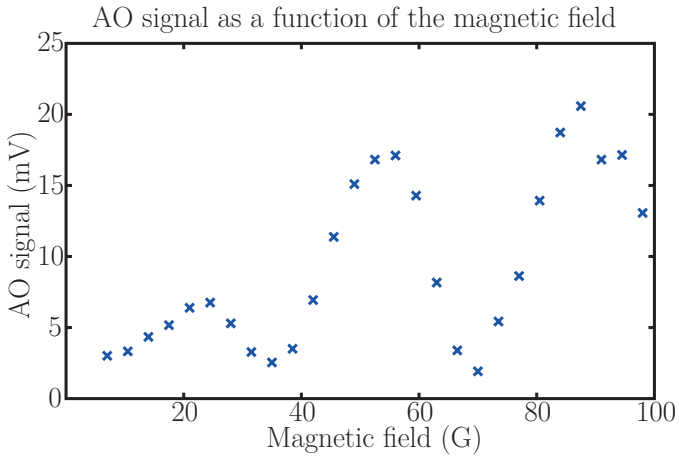

Figure 7.21 – Acousto-optic signal as a function of the magnetic field. The effect of the magnetic field vanishes around 35 G and 70 G as shown in section 7.3.1. It appears here that the effect of the third Al^{3+} transition around 105 G is visible with the acousto-optic signal as it was not when working on holes.

Interestingly, it seems that the third transition at 105 G that was not visible while working with holes is appearing here. When working with anti-holes in the future, it will be important to avoid using ultrasonic frequencies around 800 kHz, 1.6 MHz and 2.4 MHz. Frequencies over 3 MHz do not create any difficulties, whereas optimal effects of the magnetic field under 3 MHz are obtained for frequencies between 1.2 and 1.3 MHz and between 1.9 and 2 MHz. In the following, I will not work with anti-holes so that the magnetic field will be chosen around 84 G, value at which the effects of the magnetic field are close to optimum.

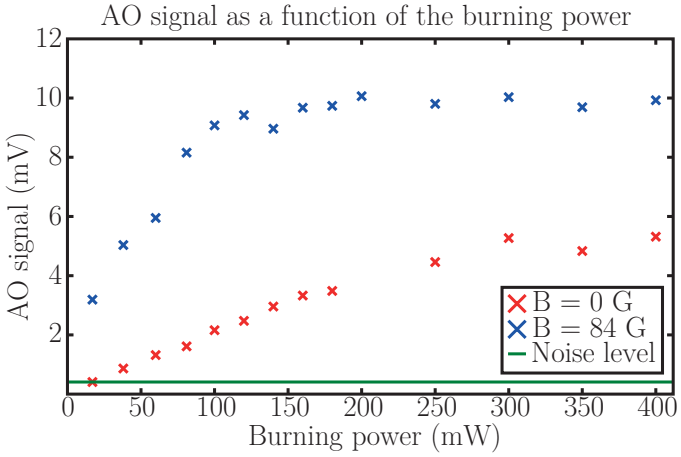

Figure 7.22 – Acousto-optic signal as a function of the burning power. Red curve corresponds to the acousto-optic signal under zero magnetic field, blue curve corresponds to the acousto-optic signal in the presence of an external magnetic field at 84 G, green line is the global noise level of signal. The shape of the curve is difficult to predict analytically, however, a plateau is reached at high burning power for the two curves. A possible explanation would be that the crystal is transparent at the end of the burning sequence for the two cases.

In the previous sections, the hole was mostly characterized through the behaviour of its maximum depth and its linewidth. This allowed probing the behaviour of the absorption in ideal cases and measuring a few intrinsic parameters of the crystal. Most of the previous hypotheses can not be verified in the case of acousto-optic imaging with an orthogonal burning beam because high

and spatially inhomogeneous burning irradiances are used. Moreover, tagged photons probe an integrated absorption over the entire crystal volume, the shape of which is not exactly known. Their spectrum is at least a few megahertz wide due to the bandwidth of the ultrasound pulses, much larger than the laser linewidth and of same order of magnitude than the hole linewidth. Therefore, the shape of the acousto-optic signal curve as a function of the burning power is not easily predicted. Acousto-optic signal was measured in the same conditions as before as the burning power was decreased. Result is plotted on figure 7.22. It is noticeable here that both curves seem to reach a plateau at high burning powers and this plateau is about twice as high with a magnetic field.

The physical origin of this factor of two is not straightforward. In section 7.4.2, I computed an expected decrease of crystal transparency of at least 20% without magnetic field if the burning waist is of the order of 500 µm. This decrease is expected to be higher as the hole gets erased faster without magnetic field. The increase of acousto-optic signal when adding an external magnetic field is then of relevant order of magnitude. However, the burning beam shape is not known precisely here so that it is difficult to estimate the exact expected increase of acousto-optic signal from these computed data, especially because tagged photons are more likely to probe the entire hole area instead of the only absorption at ν_b.

Another possibility of explaining this factor of 2 is to notice that if both curves seem to reach a plateau, it may mean that the crystal is almost transparent at the end of the burning sequence in the two cases. The difference of acousto-optic signal would then only come from the hole erasure that is faster without magnetic field. In this case, calculations of appendices E and F suggest that after 1 ms, the population difference increased up to about 16% of the total population without a magnetic field as it is under 0.1% in the presence of a magnetic field. As a consequence, only 40% of the tagged photons *flux* is transmitted in the first case as almost 99% are still transmitted in the second one. After 1 ms, starting from a transparent crystal in steady-state in both cases, the ratio between the acousto-optic signals is then expected to be of the order of 2.5. These calculations were made using a metastable lifetime of 8 ms as measured in chapter 6, a Zeeman ground states lifetime of 7 s as measured in section 7.3.1, an excited states lifetime of 400 µs and a crystal absorption of $\alpha_m L = 5.6$. In this case, the fact that the enhancement is a little bit lower than predicted by this quick scaling would come from the anti-hole erasure that occurs at high burning irradiances and that increases the crystal absorption by replacing atoms in the ground or metastable states.

Probing the hole erasure along time is a good way of probing the population repartition in the different levels. However, it is difficult to extract quantitative information from these data here because of potential ASE background. This measurement allows estimating the characteristic times that will be involved in the imaging process though. Holes were burnt in these conditions at 140 mW during 10 ms, the areas of which were measured and plotted as a function of the delay between the burning and probing sequences. The results are plotted on figure 7.23. Red curve concerns the zero-magnetic-field case and a linear fit leads to a lifetime of 9 ms. Blue curve was obtained under a magnetic field of 84 G. The two decay times are visible. Under a magnetic field, it appears that the metastable state lifetime is longer equal to 33 ms. The lifetime of the hole is 1.44 s once the metastable state is empty. The decay of the hole is to be compared to what was measured in the ideal case of section 7.3.1 for which the lifetime was longer. Here it is to be noticed that the proportion of atoms in the metastable state seems to be higher here suggesting that the high burning power is exciting atoms in the Zeeman states back to the metastable state indeed. This may justify the lower lifetime measured here and the factor of 2 instead of 2.5 in the acousto-optic signal increase.

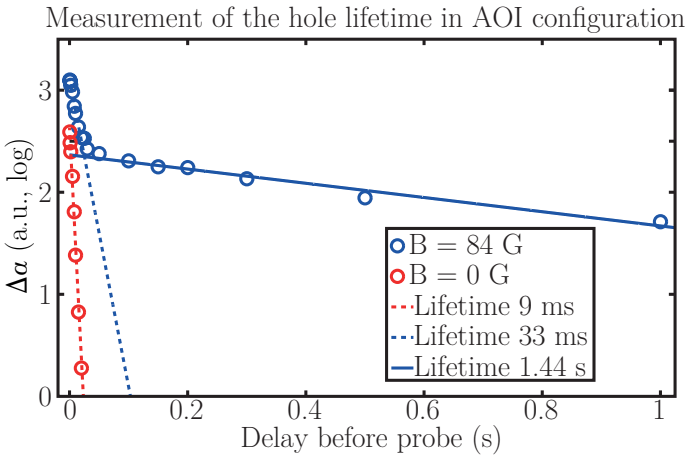

Figure 7.23 – Lifetime of a hole in the acousto-optic imaging configuration for the two cases. The area of the hole is measured as the delay between the burning and probing beam is increased and plotted in semi-logarithmic scale. Red curve concerns the zero-magnetic-field case and a linear fit leads to a lifetime of 9 ms. Blue curve was obtained under a magnetic field of 84 G. The two decay times are visible. Under a magnetic field, the metastable state lifetime is a bit longer and is 33 ms. The lifetime of the hole is 1.44 s once the metastable state is empty. Note that this hole lifetime is half the lifetime of the Zeeman states.

7.5.3 Towards scattering media

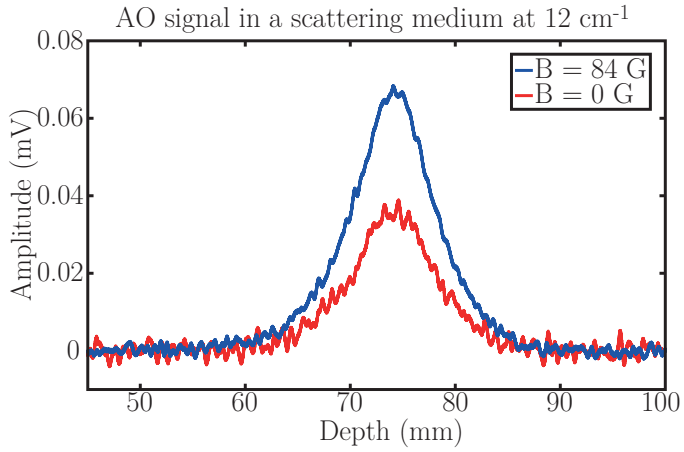

Figure 7.24 – Acousto-optic signals in the middle of a 1.5 cm-thick scattering medium of reduced scattering coefficient $\mu_s' = 12$ cm^{-1}.

In order to converge toward acousto-optic imaging, a proof of concept was done in a scattering medium. Intralipid-10% was gradually added in the water tank in order to quantify the capabilities of the setup in terms of imaging depth. The tank is 1.5 cm thick and acousto-optic signals are measured around the middle of the tank. The probing beam power is 200 mW before the scattering medium, the burning beam is 110 mW during 10 ms. Ultrasound pulses are 10 cycles long and averaged 300 times. Figure 7.24 shows two acousto-optic signals in the middle of this medium with a reduced scattering coefficient $\mu_s' = 12$ cm^{-1}. Figure 7.25 shows the evolution of the acousto-optic signal scaled by the probing light power as a function of the concentration of intralipid c_i. The corresponding scattering coefficients calculated thanks to the equations given in [25] are also presented for information purposes. Assuming that absorption mainly comes from Intralipid-10%, it is possible to deduce the expected shape of this curve. If (x_m, y_m, z_m) are the spatial coordinates

in the scattering sample of the maximum point of the measured acousto-optic signal, the acousto-optic signal at this point is supposed to obey the following equation:

$$s_{\mathrm{PD}}\left(x_m, y_m, z_m\right) \propto \exp\left(-\mu_{\mathrm{eff}}\sqrt{x_m^2 + y_m^2 + z_m^2}\right) \text{ where } \mu_{\mathrm{eff}} = \sqrt{3\mu_{\mathrm{a}}\mu_{\mathrm{s}}'} \tag{7.6}$$

Assuming that the scattering coefficient μ_{s}' and the absorption coefficient μ_{a} are proportional to the Intralipid-10% concentration c_i, it comes that the acousto-optic signal obeys an exponential decay given by:

$$s_{\mathrm{PD}}\left(x_m, y_m, z_m\right) \propto \exp\left(-\xi c_i\right) \tag{7.7}$$

where ξ is a proportionality factor. The exponential fit is also plotted on figure 7.25 and confirms the predicted shape. It is interesting to notice that acousto-optic signal can still be measured with 26 and 46 SNR respectively at almost 10 transport mean free paths. The exponential fit predicts that, in the same conditions, acousto-optic signal can be measured with a SNR of at least 10 up to 16 and 30 transport mean free paths respectively with and without magnetic field. It is to be noticed that the probing power is only 200 mW here and could be increased in order to improve the SNR.

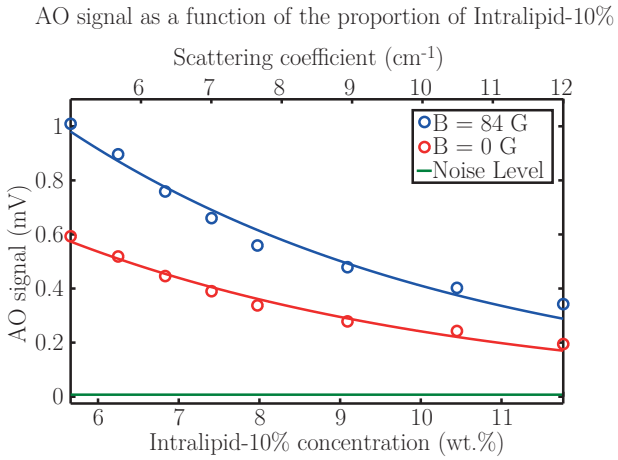

Figure 7.25 – Acousto-optic signal in the middle of a 1.5 cm-thick scattering medium as a function of the concentration of Intralipid-10%. The corresponding reduced scattering coefficient μ_{s}' is represented on the top for information purpose.

7.6 Conclusions and prospects

In the previous chapter, I showed that one of the main limitations of spectral holeburning for acousto-optic imaging is the short lifetime of the metastable state. Here, I showed that the presence of an external magnetic field increases the lifetime of the hole by at least two orders of magnitude by storing atoms in the Zeeman levels instead of the metastable state. I showed that several difficulties appear along with the presence of an external magnetic field:

- The setup is more sensitive to laser stability. Without magnetic field, it is necessary to ensure a good laser stability over a few tens of milliseconds. In the presence of an external magnetic field, the same level of stability should be reached over several seconds. Among the unwanted consequences of laser drifts, it is possible that after a few seconds, the laser excites atoms stored in the Zeeman level and erases the hole.

- The technique is sensitive to high burning powers. The laser has an intrinsic linewidth so that, because the burning efficiency is very high, it is possible that powerful burning beams excite both Zeeman levels and erase the hole.

- Because the burning beam is not spatially homogeneous (Gaussian beam, burning from a side), the crystal transparency is averaged over the probing beam area. If the probing beam is very small compared to the burning beam, it probes a homogeneous hole. However, if it is not the case, which typically arises with scattered light, it probes an averaged hole over deep and broad holes around the center of the burning beam and shallow and narrow holes near the edges. The crystal transparency is then lower than expected. As a consequence of the previous point, increasing the burning power in order to deepen holes near the edges erases holes around the center.

However, the presence of an external magnetic field brings several advantages:

- Because the lifetime is two orders of magnitude longer, it can be considered burning less frequently thus increasing the imaging rate.

- As a consequence of the increased lifetime also, the burning efficiency is higher so that lower burning irradiances burn deeper and broader holes.

- In case mechanical shutter must be used, the transmission of the crystal by the time shutters fully open is higher than without a magnetic field.

- The burning beam creates anti-holes. If the probing beam frequency is tuned on a transition from a storing level to an excited state, the beam potentially undergoes increased absorption.

In this chapter, I gave a very first proof of concept of acousto-optic imaging with spectral holeburning under an external magnetic field. In this proof of concept, the burning beam was sent from the orthogonal windows so that the absorption is very inhomogeneous inside the crystal. I showed that adding a magnetic field increases the transparent volume inside the crystal. Here it is to be remembered that work still remains in terms of optimization of the acousto-optic sequence. The sequence that was used in this chapter maximized the amount of acousto-optic signal without a magnetic field. In these conditions, I showed that an increase of acousto-optic signal by a factor of the order of two can be expected with a hole lifetime of the order of 1.5 s. I did not study the influence of anti-holes yet but highlighted a few values of the magnetic field that induces the loss of its effects on the hole.

Short-term studies should then focus on the development of an efficient acousto-optic sequence under a magnetic field that takes advantage of the presence of anti-holes. The experimental study of the dynamics of hole formation under a magnetic field should provide typical burning duration and power in order to ensure a decent hole with only one burning sequence. The idea would be to provide a sequence that prepares the crystal once and performs the whole imaging sequences with potential short intermediary burning sequences to maintain the hole.

In future works, close-cycle cryostats could be considered in order to converge toward a more transportable setup. It is interesting to notice at this point that even if cryogenic instrumentation seems inconvenient, it is not more complex that what is currently used in MRI in which an expensive superconducting coil is continuously immersed inside liquid helium. Laser stabilization issues may be addressed by stabilizing the laser on a hole instead of an external Fabry-Perot cavity. Such an approach could potentially offer a stabilization that would be more robust to thermal drifts or changes in the optical paths from laser to crystal for instance.

Conclusions and prospect

Optical contrast is of prime interest in medical imaging for it can bring both structural and spectral imaging. The major issue concerning optical techniques at depth compatible with medical imaging requirements comes from multiple light scattering that scrambles information after few millimetres. Several techniques exist that allow overcoming this difficulty such as DOT, but the latter requires long and complex computations. Alternative techniques are light/ultrasound coupling techniques such as acousto-optics. These techniques benefit from the ballistic propagation of ultrasound up to few tens of MHz in biological tissues and use it to localize optical information otherwise lost through scattering.

When propagating through an illuminated area, ultrasound generates tagged photons shifted from the light carrier frequency by the ultrasound one. Acousto-optic imaging is sensitive to both absorption and scattering properties and modulated light has three main properties that play an important role on the technique. First, the number of tagged photons is proportional to the light irradiance integrated over ultrasound volume. Second, the acousto-optic signal is proportional to the pressure-squared. Third, modulated light presents a speckle pattern and is spatially uncorrelated to untagged light. The challenge in acousto-optic imaging lies in measuring the amount of modulated light for the latter is very weak and, because of the speckle wave-front of scattered light, classical interferometric techniques with a plane wave reference lead to poor SNR.

Several detection schemes were developed in order to overcome this difficulty that can be sorted into three categories. The first kind of techniques are camera-based techniques that allow parallel processing of all speckle grains separately. The second kind is wave-front adaptive interferometry that makes scattered light and reference beam interfere coherently all over large-area single detectors. The third one is ultra-narrowband filtering that allows directly measuring the *flux* of tagged photons.

Framerates of common cameras are too low to follow ultrasound propagation whereas ultra-narrowband filtering techniques suffer from inconvenient instrumentation. As a consequence, people focused on wave-front adaptive holographic techniques that allow working with ultrasound pulses. The development of schemes based on SPS crystals working around 800 nm led to the setup of a multi-modal platform coupling acousto-optic imaging with conventional ultrasound. Such a platform showed very promising *ex vivo* results on melanoma metastases in liver biopsies. These results showed the main limitations of such a bimodal device.

The first issue of the technique comes from the fact that acousto-optic imaging is sensitive to light irradiance instead of optical properties directly. The scattered light envelope makes it

usually difficult to interpret acousto-optic images in complex media. In order to recover optical properties, it is thus necessary to work on quantitative imaging in order to remove the irradiance distribution dependence. Several direct techniques can be considered such as spectral imaging with different wavelengths or pressure contrast imaging. The scattered light irradiance can also be simulated through Monte-Carlo in carefully modelled biological tissues. It is also possible to work on the forward model and inverse problem in order to find quantitative optical properties from acousto-optic images.

The second issue concerns the optimization of a backscattering configuration. Current transmitted-light configuration are not compatible with clinical requirements. However, because of scattering, it is difficult to control the illuminated area in the sample as a function of the number of sources and detectors, their positions and sizes. It is thus of prime interest to further optimize such a configuration.

The third issue is the low framerate of acousto-optic imaging because of the high necessary number of averaging. Typical images need several tens of second which does not fit clinical imaging requirements. It is possible to increase the imaging speed by using ultrasonic plane waves. The study of the PSF of the technique shows that the problem is very similar to the CT scanner technique. A tomographic approach recovers the final image with an increased SNR that allows increasing the framerate by a factor up to fifty. This increased imaging rate is possible at the cost of the lateral resolution because of the limited emission angle of linear arrays. This resolution can be recovered by adding another probe orthogonally to the first one. This approach suggests that tomography could be reconsidered for some applications such as breast imaging or small animals.

The fourth and last one is due to speckle decorrelation *in vivo* that strongly limits the use of photorefractive detection. The use of spectral holeburning at cryogenic temperatures provides a way of performing direct *flux* measurement insensitive to speckle decorrelation. Since the lifetime of holes is short, the technique was left aside because of inconvenient instrumentation. In the presence of an external magnetic field, the lifetime of the hole is increased by two orders of magnitude so that burning is easier and less frequent and holes potentially remain during the whole imaging sequence. Interestingly, a close-cycle cryostat and laser stabilization on the hole can be considered in order to increase robustness to thermal drifts or vibrations of the cryostat. In the end, the use of a cryostat in spectral holeburning is not very different from MRI instrumentation in which a superconductive coil is immersed in liquid helium.

Future works in acousto-optic imaging may then lead to a more compact and transportable all-fibred device. The use of acousto-optic imaging as a complementary tool for ultrasound may increase the accuracy of current diagnoses processes. Several applications are currently under investigations such as blood oxygenation mapping or functional imaging, therapy (HIFU) monitoring, localization of fluorescence signal inside scattering media or melanoma imaging.

APPENDIX A

The photorefractive effect

In this appendix, I detail the principle of the photorefractive effect as a detection tool for acousto-optic imaging. Because it was already developed in many PhD manuscripts [66, 111, 118] and articles [79, 97, 98, 110], I only recall the major results in the main text. A more detailed version can be found hereunder. Most of what is described in this appendix is more completely detailed in the book of P. Yeh [121] and the PhD thesis of L.-A. de Montmorillon [187].

A.1 The band transport model

A.1.1 Principle

The photorefractive effect is an effect that occurs in materials that are both photoconductive and electrooptic. An often used model to derive the properties of such crystals is the band transport model developed by N. V. Kukhtarev [188]. Photorefractive crystals are often doped or present intrinsic defects so that some energy levels can be found inside the forbidden band. These centres must be found in both neutral and ionized states. Photorefractive crystals also have traps called donors or acceptors in order to ensure electrical neutrality of the material. The presence of a photon of adapted energy induces photoionization of the centres so that charge carriers, electrons or holes, can reach the conductive or valence bands and move inside the crystal. In the presence of a spatially inhomogeneous illumination – an interference pattern for instance – carriers will be mostly excited in regions of high light energy. These carriers move inside the conductive band through thermal energy or the presence of an external electric field and decay into other centres inside the forbidden band. Eventually, a steady-state occurs in which charge carriers are accumulated in regions of low light energy.

In the following I will assume that the crystal is illuminated by a static interference pattern between a signal and a reference plane waves:

$$\begin{aligned} \mathcal{E}_S(\mathbf{r},t) &= E_S \exp\left[i\left(\omega_0 t - \mathbf{k}_S\cdot\mathbf{r}\right)\right] \\ \mathcal{E}_R(\mathbf{r},t) &= E_R \exp\left[i\left(\omega_0 t - \mathbf{k}_R\cdot\mathbf{r}\right)\right] \end{aligned} \tag{A.1}$$

The resulting irradiance is given by:

$$\Phi = \Phi_0\left[1 + \mathcal{R}\left(\varepsilon \exp\left(i\Delta\mathbf{k}\cdot\mathbf{r}\right)\right)\right] \tag{A.2}$$

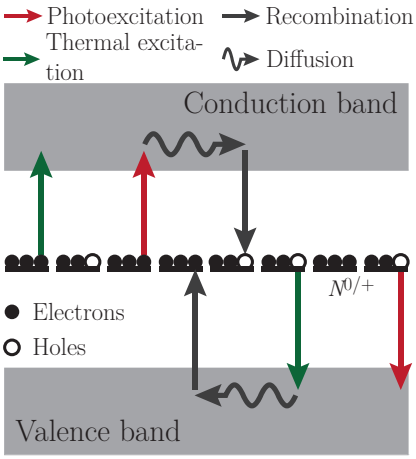

Figure A.1 – Simplified version of the band transport model involving only one kind of centre.

where $\mathcal{R}$ denotes the real part, $\Delta\mathbf{k} = \mathbf{k}_R - \mathbf{k}_S$ is the difference of wave-vectors, Φ_0 is the average value of the irradiance and ε the modulation depth of the fringes:

$$\begin{aligned} \Phi_0 &= |E_S|^2 + |E_R|^2 \\ \varepsilon &= \frac{E_R^* E_S}{|E_S|^2 + |E_R|^2} \end{aligned} \tag{A.3}$$

In the following, it will be considered that the reference beam is much more powerful than the signal beam – which is typically the case in acousto-optic imaging. Given this hypothesis, the average irradiance is approximately equal to $|E_R|^2$ and the modulation depth is given by:

$$\varepsilon \sim \frac{E_S}{E_R} \tag{A.4}$$

A.1.2 The space-charge field

The refractive index modulation is due to the distribution of charge carriers under and inhomogeneous illumination pattern which generates a photoinduced electric field that modulates the refractive index through Pockels effect. The response time τ_{PR} of the photorefractive effect is given by the establishment time of this field. In this section, I will derive the expressions of the photoinduced electric field and the response time.

Main parameters

In practice, there are a lot of different kinds of centres inside the forbidden band, but treating the band transport model with several of them is complex and out of the scope of this manuscript. In the following, the derivations will assume that there is only one kind of centre[1]. I will assume that traps do not participate to photorefractive effect and are only here to ensure electrical neutrality. The simplified version of this model is shown on figure A.1[2].

The centres can be found under both neutral and ionized states. Let then N^0 and N^+ be the respective number of these states per units of volume. Under the presence of light, the irradiance

[1] A model using two different kind of centres can be found in [189] but will not be studied here.

[2] This schematic gives an insight concerning the working wavelength range of the photorefractive effect: it can occur for wavelengths high enough to excite the centres, but under the band-gap wavelength in order not to excite electrons from the valence band directly to the conduction band.

of which is assumed to be high compared to thermal energy[1], centres can free charges. As a consequence, electrons (subscript n) and holes (p) can be freed into respectively the conduction or the valence bands.

Let σ_n and σ_p respectively be the photoexcitation cross-sections of electrons and holes. Let β_n and β_p be the thermal excitation rates of the centres in s^{-1}. Obviously, a photon that excites a charge is necessarily absorbed so that the absorption coefficients of the two phenomena can be defined: $\alpha_n = \sigma_n N^0$ and $\alpha_p = \sigma_p N^+$. Once in one of the two bands, the carriers can move either through thermal diffusion or application of an external electric field. It is then possible to define the charges current density:

$$\begin{aligned} \mathbf{j}_n &= en\mu_n \mathbf{E}_{loc} + \mu_n k_B T \mathbf{grad}\ n \\ \mathbf{j}_p &= ep\mu_p \mathbf{E}_{loc} - \mu_p k_B T \mathbf{grad}\ p \end{aligned} \tag{A.5}$$

where e is the electron charge, n and p are the number of free charges per unit of volume in cm^{-3}, μ_n and μ_p are the moduli of the mobility in $\mathrm{cm}^2 \cdot \mathrm{V}^{-1} \cdot \mathrm{s}^{-1}$, $\mathbf{E}_{loc}$ is the local electric field and **grad** stands for the gradient operator. The term $\mathbf{E}_{loc}$ contains a local component due to the charge repartition inside the material and an external component in case of applied external voltage. In the following, this external contribution will be considered equal to zero. This situation is called the diffusion regime.

Charges decay back with a recombination rate γ_n and γ_p expressed in $\mathrm{cm}^3 \cdot \mathrm{s}^{-1}$. This rate defines the average time after which charges recombine, noted:

$$\begin{aligned} \tau_n &= \frac{1}{\gamma_n N^+} \\ \tau_p &= \frac{1}{\gamma_p N^0} \end{aligned} \tag{A.6}$$

and the average distance carriers can travel through before recombining:

$$\begin{aligned} r_n &= \sqrt{\frac{\mu_n \tau_n k_B T}{e}} \\ r_p &= \sqrt{\frac{\mu_p \tau_p k_B T}{e}} \end{aligned} \tag{A.7}$$

Equations of charges motion

The density of ionized centres obeys the following population equation:

$$\frac{\partial N^+}{\partial t} = (\beta_n + \sigma_n \Phi) N^0 - n\gamma_n N^+ - (\beta_p + \sigma_p \Phi) N^+ + p\gamma_p N^0 \tag{A.8}$$

Once the carriers are in one of the two bands – conduction band for electrons, valence band for holes – they obey a Fick law and move inside the crystal:

$$\begin{aligned} \frac{\partial n}{\partial t} &= \frac{\mathbf{grad} \cdot \mathbf{j}_n}{e} + (\beta_n + \sigma_n \Phi) N^0 - n\gamma_n N^+ \\ \frac{\partial p}{\partial t} &= \frac{\mathbf{grad} \cdot \mathbf{j}_p}{e} + (\beta_p + \sigma_p \Phi) N^+ - p\gamma_p N^0 \end{aligned} \tag{A.9}$$

[1]Thermal energy is unfavourable to photorefractive effect for it excites charges uniformly inside the crystal volume. A threshold irradiance value beyond which the photorefractive effect can occur may then be defined.

As charges move, they create a local electric field according to the Poisson law:

$$\mathbf{grad} \cdot \mathbf{E}_{loc} = -\frac{e}{\epsilon}\left(N_A - N_D + n - p - N^+\right) \tag{A.10}$$

where ϵ stands for the permittivity of the material, N_A and N_D respectively stand for the density of acceptor and donor traps. Solving this system of differential equations is complex, but it is possible to simplify the calculation by assuming that the modulation depth of the interference pattern is weak as in [188]. It is then possible to linearise all variables under the form $x = x_0 + \mathcal{R}\left(x_1 \exp\left(i\Delta\mathbf{k}\cdot\mathbf{r}\right)\right)$. The calculation was done by F. P. Strohkendl *et al.* in [190] and shows that the modulated part of the local field obeys the following equation:

$$\frac{\partial \mathbf{E}_{loc,1}}{\partial t} + \frac{\mathbf{E}_{loc,1}}{\tau_{\mathrm{PR}}} = \varepsilon\frac{\mathbf{E}^{\mathrm{sc}}}{\tau_{\mathrm{PR}}} \tag{A.11}$$

where τ_{PR} is the photorefractive response time, ε the modulation depth of the interference pattern and $\mathbf{E}^{\mathrm{sc}}$ is called the space-charge field. In the diffusion regime, under the assumptions that the modulation period is small compared to the characteristic diffusion length – $1/\Delta k^2 \ll r_n^2$ and $1/\Delta k^2 \ll r_p^2$, where Δk is the modulus of the interference pattern wave vector – and that thermal energy can be neglected, the two parameters can be expressed as:

$$\begin{aligned}\frac{1}{\tau_{\mathrm{PR}}} &= \frac{\Phi_0 e^2}{\epsilon k_B T}\left(\alpha_n + \alpha_p\right)\left(\frac{\Delta k^2}{k_D^2} + 1\right)\\ \frac{\mathbf{E}^{\mathrm{sc}}}{\tau_{\mathrm{PR}}} &= -i\frac{\Phi_0 e}{\epsilon}\left(\alpha_n - \alpha_p\right)\Delta\mathbf{k}\end{aligned} \tag{A.12}$$

where Φ_0 is the average value of the light irradiance on the crystal, ϵ is the permittivity of the material, α_n and α_p are defined above and respectively stand for the absorption coefficients induced by photoexcitation and k_D is called the Debye wave-vector and is expressed as:

$$k_D^2 = \frac{e^2}{\epsilon k_B T} N_{eff} \tag{A.13}$$

where N_{eff} is the effective density of centres:

$$N_{eff} = \frac{N^0 N^+}{N^0 + N^+} \tag{A.14}$$

As can be seen here, the space-charge charge field does not depend on light irradiance and only depends on the geometry of the illumination. This regime is called the saturation regime. In case thermal energy can not be neglected, the photorefractive response time is expressed as:

$$\frac{1}{\tau_{\mathrm{PR}}} = \frac{\Phi_0 e^2}{\epsilon k_B T}\left(\mathcal{A}_n\alpha_n + \mathcal{A}_p\alpha_p\right)\left(\frac{\Delta k^2}{k_D^2} + 1\right) \tag{A.15}$$

where $\mathcal{A}_n = \dfrac{\beta_n + \sigma_n\Phi_0}{\sigma_n\Phi_0}$ and $\mathcal{A}_p = \dfrac{\beta_p + \sigma_p\Phi_0}{\sigma_p\Phi_0}$. In every case, the photorefractive response time is inversely proportional to the average irradiance on the crystal.

Steady-state electric field

In steady state, the complex part of the photoinduced electric field $\mathbf{E}_{loc,1}$ that will modulate the refractive index is equal to $\varepsilon\mathbf{E}^{\text{sc}}$ so that:

$$\mathbf{E}_{loc,1} = -i\varepsilon\frac{k_B T}{e}\xi_0\frac{\Delta\mathbf{k}}{1+\dfrac{\Delta k^2}{k_D^2}} \tag{A.16}$$

where $\xi_0 = \dfrac{\alpha_n - \alpha_p}{\mathcal{A}_n\alpha_n + \mathcal{A}_p\alpha_p}$ is called the hole-electron competition factor and is between -1 and 1 depending on the wavelength among others. This latter coefficient is here to take into account the fact that displacements of electrons and holes have opposite influence on the local electric field. If $\xi_0 = 1$, only electrons are photoexcited whereas if $\xi_0 = -1$ only holes are. If the two phenomena are equivalent, the hole-electron competition factor is equal to zero and there is no photoinduced electric field. In the saturation regime in which the average irradiance is high enough to neglect thermal energy, $\mathcal{A}_n$ and $\mathcal{A}_p$ are equal to 1 so that the photoinduced electric field only depends on the modulation depth. In a given geometry of illumination, the space-charge field $\mathbf{E}^{\text{sc}}$ is an intrinsic parameter of the crystal that depends on its different physical properties in this case. Otherwise, the photoinduced electric field modulus increases as the average irradiance to reach the saturated value. The presence of the factor i means that the photoinduced electric field is phase-shifted by $\pm\pi/2$ compared to the illumination pattern. In this case, the photorefractive effect is referred to as a "non-local" phenomenon. By applying an external electric field, it is possible to compensate this phase-shift.

In practice, if the interference pattern is moving, the photoinduced electric field is given by the average value of the modulation depth over the photorefractive response time:

$$\mathbf{E}_{loc,1} = -i\left\langle\varepsilon\right\rangle_{\tau_{\text{PR}}}\frac{k_B T}{e}\xi_0\frac{\Delta\mathbf{k}}{1+\dfrac{\Delta k^2}{k_D^2}} \tag{A.17}$$

where "$\langle\rangle_{\tau_{\text{PR}}}$" stands for the average value over the photorefractive response time. Moving fringes are "blurred" by the crystal. Interestingly, the photorefractive response time is inversely proportional to the average light irradiance so that the higher it is, the faster the crystal is.

A.1.3 Photoinduced variation of the refractive index

Because the crystal is also electrooptic, the photoinduced electric field will generate a modulation of the refractive index. In the most general case, it exists three axes denoted **a**, **b** and **c** so-called principal axes into which the permittivity tensor can be written as:

$$\underline{\underline{\epsilon}} = \begin{pmatrix} \epsilon_a & 0 & 0 \\ 0 & \epsilon_b & 0 \\ 0 & 0 & \epsilon_c \end{pmatrix} = \begin{pmatrix} n_a^2 & 0 & 0 \\ 0 & n_b^2 & 0 \\ 0 & 0 & n_c^2 \end{pmatrix} \tag{A.18}$$

The impermeability tensor $\underline{\underline{\eta}}$ is defined as the inverse of the permittivity tensor $\underline{\underline{\epsilon}}$ such as $\underline{\underline{\eta}}\,\underline{\underline{\epsilon}} = \epsilon_0$, where ϵ_0 is the dielectric permittivity of vacuum. The elements of the impermeability tensor η_{ii} are related to the elements of the refractive index tensor by: $\eta_{ii} = 1/n_{ii}^2$. Here, i stands for one the three principal axes of the crystal.

Electrooptic tensor

In the following, only non-centrosymmetric crystals will be considered so that Kerr effect is negligible. The presence of a local electric field modulates the impermeability tensor elements such as:

$$\Delta\eta_{ij} = \Delta\left(\frac{1}{n^2}\right)_{ij} = \sum_k r_{ijk} E_k \tag{A.19}$$

where i, j and k stand for either one of the three principal axes, r_{ijk} are the elements of the electrooptic tensor and E_k is the component of the photoinduced electric field on the principal axis k. Because of symmetry considerations, one usually uses the notation r_{lk} where $k = 1,\ 2,\ 3$ for **a**, **b** or **c** and l varies between 1 and 6 so that:

$$\begin{array}{lllll} 1 & = & (aa) & & \\ 2 & = & (bb) & & \\ 3 & = & (cc) & & \\ 4 & = & (bc) & = & (cb) \\ 5 & = & (ca) & = & (ac) \\ 6 & = & (ab) & = & (ba) \end{array} \tag{A.20}$$

The electrooptic tensor is then expressed as:

$$\underline{\underline{r}} = \begin{pmatrix} r_{11} & r_{12} & r_{13} \\ r_{21} & r_{22} & r_{23} \\ r_{31} & r_{32} & r_{33} \\ r_{41} & r_{42} & r_{43} \\ r_{51} & r_{52} & r_{53} \\ r_{61} & r_{62} & r_{63} \end{pmatrix} \tag{A.21}$$

The main point thus consists in measuring the electrooptic tensor in the considered material. The electrooptic tensor for different kind of symmetry groups is given in the first chapter of P. Yeh's book [121]. The particular case of SPS crystals is treated by A. A. Grabar *et al.* in the book of P. Günter and J.-P. Huignard [123]:

$$\underline{\underline{r}} = \begin{pmatrix} r_{11} & 0 & r_{13} \\ r_{21} & 0 & r_{23} \\ r_{31} & 0 & r_{33} \\ 0 & r_{42} & 0 \\ r_{51} & 0 & r_{53} \\ 0 & r_{62} & 0 \end{pmatrix} \tag{A.22}$$

The refractive index modulation in SPS

The modulation of the refractive index is given by:

$$\Delta n_{ij} = -\frac{1}{2} n_0^3 \Delta\eta_{ij} = -\frac{1}{2} n_0^3 \sum_k r_{ijk} E_k \tag{A.23}$$

In general, it can be shown that the modulation of refractive index seen by the two beams can be expressed under the form [191]:

$$\Delta n = -\frac{1}{2} n_0^3 r_{eff} \mathcal{R}\left(E_{loc,1} \exp\left(i\Delta\mathbf{k}\cdot\mathbf{r}\right)\right) \tag{A.24}$$

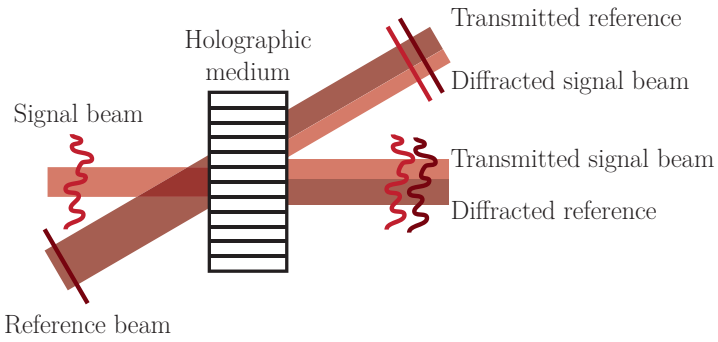

Figure A.2 – Schematic of TWM process.

where r_{eff} is the effective electrooptic coefficient seen by the beams and that depends on the crystal orientation, the fringes wave-vector direction and the polarization vector of the two beams. In the manuscript, the crystal I use is cut so that by π-rotating the crystal along its vertical axis, the effective electrooptic coefficient sign changes. The refractive index variation can then be expressed as:

$$\Delta n = n_1 \sin\left(\Delta \mathbf{k} \cdot \mathbf{r}\right) \tag{A.25}$$

where it was set:

$$n_1 = -\left\langle \varepsilon \right\rangle_{\tau_{\mathrm{PR}}} \frac{r_{eff} n_0^3 k_B T}{2e} \xi_0 \frac{\Delta k}{1 + \dfrac{\Delta k^2}{k_D^2}} \tag{A.26}$$

A.2 Two-wave mixing

The two beams that created the refractive index grating will diffract on it. As a direct consequence, the Bragg condition is automatically verified. Part of the reference will diffract in the direction of the signal beam and reciprocally. In case of small modulation, the diffracted beams acquire a $\pi/2$ phase-shift. Because the refractive index grating is phase-shifted compared to light the two beams have a additional phase-shift of $\pm\pi/2$ depending on the diffraction direction and the sign of the effective electrooptic coefficient. As a consequence, the diffracted beam in a given direction can be either in-phase ($\pi/2 - \pi/2 = 0$, constructive interferences) or out-of-phase ($\pi/2 + \pi/2 = \pi$, destructive interferences) compared to the transmitted one in this same direction. It results in an energy transfer from a beam to the other that can be modelled through coupled equations and solved thanks to a perturbation approach as developed by H. Kogelnik [120]. This phenomenon is called two-wave mixing (TWM). In the following, I will consider that the average irradiance is high enough to neglect thermal energy.

A.2.1 Photorefractive gain

Let us consider the two previous beams propagating along the z-direction with a symmetrical incidence. The system of coupled equations driving the amplitude of the two beams inside the

crystal is given in steady-state by [121, Chapter 4]:

$$\begin{cases} \dfrac{\partial E_S}{\partial z} &= \dfrac{\pi n_0^3 r_{eff}}{2i\lambda\cos\theta} E^{\mathrm{sc}} \langle\varepsilon\rangle_{\tau_{\mathrm{PR}}} E_R - \dfrac{\alpha}{2} E_S \\ \dfrac{\partial E_R}{\partial z} &= \dfrac{\pi n_0^3 r_{eff}}{2i\lambda\cos\theta} E^{\mathrm{sc}*} \langle\varepsilon\rangle_{\tau_{\mathrm{PR}}} E_S - \dfrac{\alpha}{2} E_R \end{cases} \tag{A.27}$$

where θ stands for the incident angle on the crystal and α stands for the crystals absorption coefficient. These equations define the photorefractive amplitude gain γ such as:

$$\gamma = \frac{\pi n_0^3 r_{eff}}{2i\lambda\cos\theta} E^{\mathrm{sc}} \tag{A.28}$$

This gain is *a priori* complex is the general case in which an external field is applied, but in the particular case of the diffusion regime, it appears that this is a real variable. Let us assume for now that the temporal evolution of the interference pattern is slow compared to the response time of the photorefractive crystal. By remembering that, in case the reference is much powerful than the signal beam – implying $\varepsilon \sim \dfrac{E_S}{E_R}$ – it comes simply that:

$$\begin{cases} \dfrac{\partial E_S}{\partial z} &= \left(\gamma - \dfrac{\alpha}{2}\right) E_S \\ \dfrac{\partial E_R}{\partial z} &= -\dfrac{\alpha}{2} E_R \end{cases} \tag{A.29}$$

This means that the amount of diffracted reference beam is weak enough to consider that the main decay comes from absorption. In terms of irradiance, it then comes that:

$$\begin{cases} \Phi_S(z) &= \Phi_S(0) \exp\left[(2\gamma - \alpha) z\right] \\ \Phi_R(z) &= \Phi_R(0) \exp\left(-\alpha z\right) \end{cases} \tag{A.30}$$

This defines the photorefractive gain in energy γ_{PR} that was already mentioned in section 2.4.3 of chapter 2: $\gamma_{\mathrm{PR}} = 2\gamma$. For high value of the average irradiance on the crystal, that is to say when thermal energy is negligible, this gain is constant and referred to as the saturated gain as shown above. When it is not the case, the gain increases with the average irradiance on the crystal in the same manner as the photoinduced electric field.

A.2.2 Transmission of time-modulated signals

In the previous section, it was considered only a static interference pattern that allowed to highlight the light amplification due to two-wave mixing. The study of the transmission of time-modulated signal through a photorefractive crystal can be found in [192], I will just recall the main steps of the derivation here. The dynamic photoinduced electric field obeys the following three equations. The temporal evolution derived thanks to the band-transport model:

$$\frac{\partial E_{loc,1}}{\partial t} + \frac{E_{loc,1}}{\tau_{\mathrm{PR}}} = \varepsilon \frac{E^{\mathrm{sc}}}{\tau_{\mathrm{PR}}} \tag{A.31}$$

and the reformulated coupled equations under the form:

$$\frac{\partial E_S}{\partial z} = \frac{\gamma}{E^{\mathrm{sc}}} E_{loc,1} E_R - \frac{\alpha}{2} E_S \tag{A.32}$$

$$\frac{\partial E_R}{\partial z} = \frac{\gamma}{E^{\text{sc}}} E^*_{loc,1} E_S - \frac{\alpha}{2} E_R \tag{A.33}$$

Under the assumptions that the reference depletion due to TWM is negligible it comes as previously:

$$\Phi_R(z) = \Phi_R(0) \exp(-\alpha z) \tag{A.34}$$

This suggests that the photorefractive response time, inversely proportional to the average light irradiance, will increase along with the thickness of the interaction volume:

$$\tau_{\text{PR}}(z) = \tau_{\text{PR}}(0) \exp(\alpha z) \tag{A.35}$$

The time derivative of equation A.32 gives:

$$\frac{\partial^2 E_S}{\partial t \partial z} = \frac{\gamma}{\tau_{\text{PR}}(z)} E_S - \frac{\gamma}{\tau_{\text{PR}}(z) E^{\text{sc}}} E_{loc,1} E_R - \frac{\alpha}{2} \frac{\partial E_S}{\partial t} \tag{A.36}$$

The term $\frac{\gamma}{E^{\text{sc}}} E_{loc,1} E_R$ can be expressed thanks to equation A.32 again:

$$\frac{\partial^2 E_S}{\partial t \partial z} = \frac{\gamma}{\tau_{\text{PR}}(z)} E_S - \frac{1}{\tau_{\text{PR}}(z)} \frac{\partial E_S}{\partial z} - \frac{\alpha}{2\tau_{\text{PR}}(z)} E_S - \frac{\alpha}{2} \frac{\partial E_S}{\partial t} \tag{A.37}$$

or by replacing the expression of the photorefractive response time:

$$\frac{\partial^2 E_S}{\partial t \partial z} = \frac{\exp(-\alpha z)}{\tau_{\text{PR}}(0)} \left(\gamma - \frac{\alpha}{2}\right) E_S - \frac{\exp(-\alpha z)}{\tau_{\text{PR}}(0)} \frac{\partial E_S}{\partial z} - \frac{\alpha}{2} \frac{\partial E_S}{\partial t} \tag{A.38}$$

This equation was solved by P. Delaye *et al.* [192] assuming that a hologram is already engraved at $t = 0$. I will not give the exact solution here, but in case the time modulation is fast compared to the response time of the photorefractive crystal (*i.e.* the detection occurs over short characteristic times compared to the photorefractive response), the authors show that the latter behaves as a first order low pass filter with an amplification. For small diffraction efficiency and negligible absorption, L.-A. De Montmorillon *et al.* [122] show that the transfer function H of the crystal in terms of amplitude is given by:

$$H(L,t) = \gamma L \frac{\exp\left(-\frac{t}{\tau_{\text{PR}}}\right)}{\tau_{\text{PR}}} \tag{A.39}$$

where L is the crystal thickness and τ_{PR} is the photorefractive response time on the crystal input surface $\tau_{\text{PR}}(0)$ in which the parentheses were dropped for convenience.

A.3 Detection of acousto-optic signals

A.3.1 Small diffraction efficiency

The above development was derived for plane waves but the same kind of reasoning holds with scattered light. Because the ultrasonic pulse propagates through the whole sample over few tens of µs, the temporal variations of acousto-optic signal are also of the same order of magnitude. It is then not possible to tune the reference on tagged photons frequency for the hologram can not be engraved anyway. The photorefractive detection of tagged photons is then very close to the case described above with the reference tuned on untagged photons frequency. The theoretical study

of photrefractive detection can be found in [79] for small diffraction efficiency, I suggest to give the main steps here. Let us consider the expression of the modulated light complex field given in section 2.3.1 of chapter 2:

$$\mathcal{E}_S(\mathbf{r},t) = E_0\left[\mathcal{S}_0(\mathbf{r},t)\,e^{i\omega_0 t} + \mathcal{S}_1(\mathbf{r},t)\,e^{i(\omega_0+\omega_{US})t} + \mathcal{S}_1^*(\mathbf{r},t)\,e^{i(\omega_0-\omega_{US})t}\right] \tag{A.40}$$

where $\mathcal{S}_i(\mathbf{r})$ stands for a random speckle pattern and in which the other light frequency harmonics are omitted. The speckle patterns must verify $|\mathcal{E}_S(\mathbf{r},t)|^2 = E_0^2$ and $|\mathcal{S}_0(\mathbf{r},0)|^2 = 1$. Here the time-dependence of these speckle patterns comes from the ultrasound pulse propagation. As demonstrated in the previous section, the field after the crystal $\mathcal{E}_D(\mathbf{r}',t)$ is given by:

$$\mathcal{E}_D(\mathbf{r}',t) = \mathcal{E}_S(\mathbf{r}',t) + \mathcal{E}_S(\mathbf{r}',t) * H(L,t) \tag{A.41}$$

where "$*$" stands for the convolution product. As derived previously, in case of a fast modulation and neglected absorption inside the crystal, the latter behaves as a first order low-pass filter.

$$\mathcal{E}_D(\mathbf{r}',t) = \mathcal{E}_S(\mathbf{r}',t) + \gamma L\mathcal{E}_S(\mathbf{r}',t) * \left(\frac{\exp\left(-\dfrac{t}{\tau_{\mathrm{PR}}}\right)}{\tau_{\mathrm{PR}}}\right) \tag{A.42}$$

Typical ultrasonic frequencies are of the order of several MHz, where photorefractive response are only of the order of a few milliseconds. As a consequence, all ultrasound frequency harmonics are averaged over a high number of periods and are equal to zero. After the crystal, the diffracted reference only contains the average value of untagged light over the photorefractive response time:

$$\mathcal{E}_D(\mathbf{r}',t) = \mathcal{E}_S(\mathbf{r}',t) + E_0\gamma L\left\langle\mathcal{S}_0(\mathbf{r}',t)\right\rangle_{\tau_{\mathrm{PR}}} e^{i\omega_0 t} \tag{A.43}$$

The light irradiance after the crystal is given by:

$$\begin{aligned}\Phi_D(\mathbf{r}',t) &= |\mathcal{E}_D(\mathbf{r}',t)|^2 = |\mathcal{E}_S(\mathbf{r}',t)|^2 + E_0^2\gamma^2L^2\left|\left\langle\mathcal{S}_0(\mathbf{r}',t)\right\rangle_{\tau_{\mathrm{PR}}}\right|^2 + \\ &\quad \mathcal{E}_S(\mathbf{r}',t)\,E_0\gamma L\left\langle\mathcal{S}_0(\mathbf{r}',t)\right\rangle^*_{\tau_{\mathrm{PR}}} e^{-i\omega_0 t} + c.c.\end{aligned} \tag{A.44}$$

where "*c.c.*" stands for the complex conjugate. From the development of the Bessel function of the first kind $J_0(\varepsilon(t))$, the speckle pattern of untagged photons varies as $1-\dfrac{\varepsilon^2(t)}{4}$, where $\varepsilon(t)$ is the ultrasound modulation depth that is proportional to the acoustic pressure and contains information about the scattered light field inside the medium. It is usually assumed that the number of untagged photons is very big compared to tagged photons and that the modulation depth evolves very fast compared to the photorefractive response time so that nor the hologram nor the untagged photons wave-front are perturbed by ultrasound modulation:

$$\begin{aligned}&\left\langle\varepsilon^2(t)\right\rangle_{\tau_{\mathrm{PR}}} \ll 1\\ &\left\langle\mathcal{S}_0(\mathbf{r}',t)\right\rangle_{\tau_{\mathrm{PR}}} \sim \mathcal{S}_0(\mathbf{r}',0)\\ &\mathcal{S}_0(\mathbf{r}',t) \sim \left(1-\frac{\varepsilon^2(t)}{4}\right)\mathcal{S}_0(\mathbf{r}',0)\end{aligned} \tag{A.45}$$

and the modulation information is contained in the cross terms. Their development leads to:

$$\begin{aligned}\Phi_D(\mathbf{r}',t) = \; & E_0^2\left[1+\gamma^2L^2\right] + 2E_0^2\gamma L\mathcal{R}\left(\langle\mathcal{S}_0(\mathbf{r}',t)\rangle^*_{\tau_{\mathrm{PR}}}\mathcal{S}_0(\mathbf{r}',t)\right) + \\ & 2E_0^2\gamma L\mathcal{R}\left(\langle\mathcal{S}_0(\mathbf{r}',t)\rangle_{\tau_{\mathrm{PR}}}\right)\mathcal{S}_1(\mathbf{r}',t)\,e^{i\omega_{US}t} + c.c.\end{aligned} \tag{A.46}$$

The light irradiance after the crystal then contains a DC-level corresponding to the global transmitted energy, a time varying irradiance corresponding to the signal of untagged photons, and an oscillating term at ω_{US} corresponding to the beating between tagged and untagged photons. The term $\mathcal{R}\left(\langle\mathcal{S}_0(\mathbf{r}',t)\rangle^*_{\tau_{\mathrm{PR}}}\mathcal{S}_0(\mathbf{r}',t)\right)$ can be developed as:

$$\mathcal{R}\left(\langle\mathcal{S}_0(\mathbf{r}',t)\rangle^*_{\tau_{\mathrm{PR}}}\mathcal{S}_0(\mathbf{r}',t)\right) \sim \mathcal{R}\left(\mathcal{S}_0^*(\mathbf{r}',0)\,\mathcal{S}_0(\mathbf{r}',0)\left(1-\frac{\varepsilon^2(t)}{4}\right)\right) \sim \left(1-\frac{\varepsilon^2(t)}{4}\right) \tag{A.47}$$

whereas one also has:

$$\mathcal{R}\left(\langle\mathcal{S}_0(\mathbf{r}',t)\rangle_{\tau_{\mathrm{PR}}}\right)\mathcal{S}_1(\mathbf{r}',t)\,e^{i\omega_{US}t} + c.c. \sim 2\mathcal{R}\left(\mathcal{S}_0(\mathbf{r}',0)\right)\mathcal{R}\left(\mathcal{S}_1(\mathbf{r}',t)\,e^{i\omega_{US}t}\right) \tag{A.48}$$

In the end, the acousto-optic signal is proportional to the light irradiance integrated over a single-detector of surface S:

$$\begin{aligned}s_{\mathrm{PD}} &\propto \int_S \Phi_D(\mathbf{r}',t)\,\mathrm{d}\mathbf{r}' \\ &= S\left[E_0^2\left[1+\gamma^2L^2\right] + 2E_0^2\gamma L\left(1-\frac{\varepsilon^2(t)}{4}\right) + 4E_0^2\gamma L\left\langle\mathcal{R}\left(\mathcal{S}_0(\mathbf{r}',0)\right)\mathcal{R}\left(\mathcal{S}_1(\mathbf{r}',t)\,e^{i\omega_{US}t}\right)\right\rangle_S\right]\end{aligned} \tag{A.49}$$

where "$\langle\rangle_S$" stands for the average value over the detector surface. In principle, the oscillating term is supposed to bring a first order in the modulation depth whereas the rest is of second order. However, the speckle patterns $\mathcal{S}_0(\mathbf{r}',0)$ and $\mathcal{S}_1(\mathbf{r}',t)$ are spatially uncorrelated so that the average value of this term over the surface detector is very weak in practice. By noticing that $1+\gamma^2L^2+2\gamma L$ is equal to $(1+\gamma L)^2$, the signal over the detector is then:

$$s_{\mathrm{PD}} \propto SE_0^2\left[(1+\gamma L)^2 - \gamma L\frac{\varepsilon^2(t)}{2}\right] \tag{A.50}$$

The DC-level corresponds to the untagged photons signal that undergoes TWM whereas the AC-component corresponds to the portion of photons that does not properly participate to TWM because they were tagged. Recording the AC-component thus gives the acousto-optic signal proportional to the tagged photons power:

$$s_{\mathrm{PD}}^{AC} \propto -SE_0^2\gamma L\frac{\varepsilon^2(t)}{2} \tag{A.51}$$

Two cases can then occur. If the photorefractive gain is positive, meaning that the reference is in-phase with the signal beam, the untagged photons signal is amplified. In this case the AC-component is negative because tagged photons do not properly undergo TWM and their signal is not amplified: the presence of tagged photons leads to a decrease of acousto-optic signal. On the other hand, if the gain is negative, meaning that the reference and the signal beam are out-of-phase, TWM implies a decrease of the untagged photons signal and tagged photons are measured through an increase of the acousto-optic signal.

In an ideal case, the noise is mostly driven by the untagged photons signal. For small diffraction efficiency, the SNR is then given by:

$$SNR \propto \frac{\left|SE_0^2\gamma L\frac{\varepsilon^2(t)}{2}\right|}{\sqrt{SE_0^2\left(1+\gamma L\right)^2}} \sim \sqrt{S}E_0\left|\gamma\right|L\frac{\left|\varepsilon\right|^2(t)}{2} \tag{A.52}$$

One retrieves here the effect of the wave-front adaptation through the fact that SNR increases as a square-root of the number of speckle grains. Here, the finite area of the crystal was not taken into account so the detector area is naturally limiting the number of integrated speckle grains. In practice, one is mainly limited by the optical *etendue* of the crystal so that the meaningful parameter is the number of speckle grains on the crystal surface. It is no surprise that the SNR increases linearly with the electric field amplitude (square-root of the irradiance), the photorefractive gain in amplitude and the crystal length. The interesting point here is that the modulation depth is proportional to the acoustic pressure so that the SNR increases as the pressure squared.

A.3.2 Accurate solution

Assuming that the signal is rapidly phase-modulated $E_S(z=0,t) = E_S\exp(\varphi(t))$, P. Delaye *et al.* [192] derived an analytical solution for the electric field amplitude in the signal direction using a more accurate transfer function. Though their development was derived for plane waves, it can be extended to speckles. They show that the electric field can be expressed as:

$$E_S(L,t) = E_S(0,0)\left[\left(e^{\gamma L}-1\right)+e^{i\varphi(t)}\right]\exp\left(-\frac{\alpha}{2}L\right) \tag{A.53}$$

The interesting point here is that the electric field in the direction of the signal beam $\mathcal{E}(L,t)$ is constituted by two components and can be expressed as $\mathcal{E}(L,t) = \mathcal{E}_D(L) + \mathcal{E}_S(L,t)$ where $\mathcal{E}_D(L)$ is the diffracted reference and $\mathcal{E}_S(L,t)$ the transmitted signal beam. The light irradiance after the crystal is given by:

$$\Phi_S(L,t) = \Phi_S(0,0)\left[1+\left|e^{\gamma L}-1\right|^2+2\mathcal{R}\left(\left(e^{\gamma L}-1\right)e^{i\varphi(t)}\right)\right]\exp(-\alpha L) \tag{A.54}$$

The photorefractive gain in amplitude being a purely real number in our case, the development of the light irradiance leads to:

$$\Phi_S(L,t) = \Phi_S(0,0)\left[2+e^{2\gamma L}-2e^{\gamma L}+2\left(e^{\gamma L}-1\right)\cos\varphi(t)\right]\exp(-\alpha L) \tag{A.55}$$

Assuming the modulation is small, the cosine can be developed around zero. The light irradiance after the crystal thus contains a static and a modulated part such as:

$$\Phi_S(L,t) = \langle\Phi_S(L,t)\rangle + \delta\Phi_S(L,t) \tag{A.56}$$

where:

$$\begin{cases} \langle\Phi_S(L,t)\rangle &= \Phi_S(0,0)\,e^{2\gamma L}\exp(-\alpha L) \\ \delta\Phi_S(L,t) &= \Phi_S(0,0)\exp(-\alpha L)\left(1-e^{\gamma L}\right)\varphi(t)^2 \end{cases} \tag{A.57}$$

This result shows that the photorefractive detection of a phase modulated signal is always sensitive to this modulation squared as in a standard interferometer. The previous expression can also be interpreted in terms of tagged/untagged light. The untagged light is at the same

frequency as the reference so that its hologram is static and it can undergo TWM: this is the static component of the light irradiance that exhibits a photorefractive amplification. Tagged light is modulated faster than the photorefractive response time so that its hologram is blurred and it does not undergo a proper TWM: it is not properly amplified as shown by the fact that the modulated part is negative. Obviously, this discussion also holds for negative gains: in this case, untagged light is attenuated by TWM as tagged light is not.

In case the detection is shot-noise limited, the SNR is given by:

$$SNR \propto \frac{\Phi_S \exp\left(-\alpha L\right)\left|1-e^{\gamma L}\right|\left|\varphi\left(t\right)\right|^2}{\sqrt{\Phi_S e^{2\gamma L}\exp\left(-\alpha L\right)}} = \sqrt{\Phi_S}\left|e^{-\gamma L}-1\right|\exp\left(-\frac{\alpha}{2}L\right)\left|\varphi\left(t\right)\right|^2 \tag{A.58}$$

Interestingly, when the absolute value of the gain is high, the term $\left|e^{-\gamma L}-1\right|$ tends to 1 if $\gamma > 0$ as it exponentially grows for $\gamma < 0$. This suggests that it is preferable to work in a negative gain regime in which the noisy background is reduced – as long as the electronic noise is negligible. In practice, a small part of the reference beam scatters inside the crystal and is also amplified through TWM. This phenomenon is called beam fanning and increases the light background. Another interest of working in the negative gain regime is that this phenomenon is reduced.

APPENDIX B

The Radon transform

THE Radon transform is a mathematical tool used in order to recover an object from its projections along lower dimension spaces. Mathematical descriptions of the Radon transform can be found in many articles such as [193], books [194] or PhD theses [195], but this mathematical background rapidly becomes too heavy for the simple purpose we aim at here. In this appendix, I will quickly derive with a simple formalism the few properties used in this manuscript. A good review of historical background and practical considerations on computed tomography can be found in the paper of Brooks and Di Chiro [196] and a more recent point of view is given in the book of Gabor T. Herman [138]. In the following, capital letters will stand for the Radon transform, a tilde will denote the 1D Fourier transform whereas a hat stands for the 2D Fourier transform.

B.1 Radon transform and backprojection

Several definitions of the Radon transform can be found in literature. The definition used in this manuscript is the one given in [194] and is the one generally used for CT scanners. Let an object be described by a 2D function $g(x, y)$. The Radon transform of this object $G(r, \theta)$ is represented on figure B.1 and defined such as:

$$G(r, \theta) = \int_{-\infty}^{\infty} \int_{-\infty}^{\infty} g(x, y)\, \delta(r - x\cos\theta - y\sin\theta)\, \mathrm{d}x\mathrm{d}y \tag{B.1}$$

The first interesting property of this transform that is used in the manuscript is the straightforward consequence of the definition:

$$G(r, \theta) = G(-r, \theta + \pi) \tag{B.2}$$

This simply means that the projection along θ propagating toward $r > 0$ is the same as the one along $\theta + \pi$ propagating toward $r < 0$. Scanning angles over π is then enough to get all projections provided that $r \in [-\infty, +\infty]$.

The most immediate inversion of such a transform consists in attributing each value of one projection $G(r, \theta)$ to all points of the projected line that may have contributed to this value. The summation of the "backprojections" of all projections gives the final image as represented on figure B.2. This reconstruction method is called the backprojection algorithm. Though this

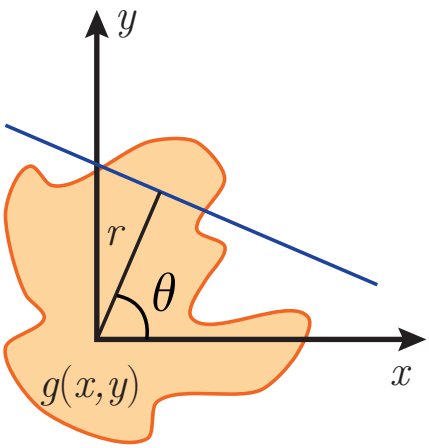

Figure B.1 – Schematic of the Radon transform. The radon transform $G(r,\theta)$ of an object is defined as the integral of the object along the blue line of polar parameters (r,θ).

inversion algorithm is quite immediate and easy to set up, it can be shown that such an approach gives a blurred version of the real image [194, Chapter 6].

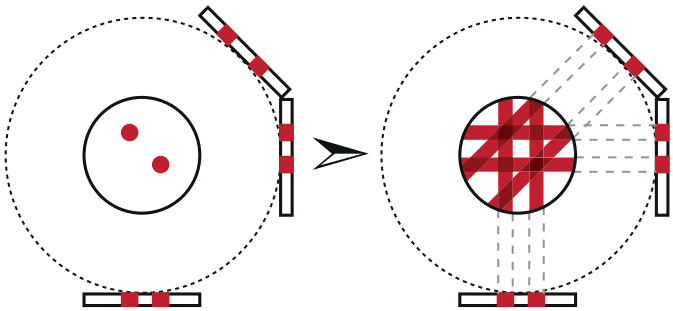

Figure B.2 – Backprojection consists in attributing each value of a projection to all points that contribute to this value. The shape of the final object is recovered by superposing all backprojected signals. It can be shown that the resulting image is a blurred version of the real object.

B.2 Analytical inversion of the Radon transform

In the previous section, I defined the Radon transform and showed a simple inversion approach: the backprojection algorithm. This technique was used in the first attempts to recover an image from its projections [197, 198]. However, this algorithm is not an exact inversion of the Radon transform and leads to blurred images. In order to overcome this difficulty, it is necessary to further study the Radon transform.

B.2.1 The projection-slice theorem

An interesting property of the Radon transform that allows demonstrating a lot of other ones lies in how the latter is related to the Fourier transform. This property is called the projection-slice theorem [199, 200] and states that the Fourier transform of a projection is equal to a slice of the Fourier transform of the final image along the direction of projection. Let us consider the Fourier transform of a projection along θ:

$$\widetilde{G}(\eta,\theta)=\int_{-\infty}^{\infty}G(r,\theta)\exp(-2i\pi\eta r)\,\mathrm{d}r \tag{B.3}$$

that can be developed completely:

$$\widetilde{G}(\eta,\theta)=\int_{-\infty}^{\infty}\left[\int_{-\infty}^{\infty}\int_{-\infty}^{\infty}g(x,y)\,\delta(r-x\cos\theta-y\sin\theta)\,\mathrm{d}x\mathrm{d}y\right]\exp(-2i\pi\eta r)\,\mathrm{d}r \tag{B.4}$$

By simply switching the integrals it comes:

$$\widetilde{G}(\eta,\theta)=\int_{-\infty}^{\infty}\int_{-\infty}^{\infty}g(x,y)\left[\int_{-\infty}^{\infty}\exp(-2i\pi\eta r)\,\delta(r-x\cos\theta-y\sin\theta)\,\mathrm{d}r\right]\mathrm{d}x\mathrm{d}y \tag{B.5}$$

which is just:

$$\widetilde{G}(\eta,\theta)=\int_{-\infty}^{\infty}\int_{-\infty}^{\infty}g(x,y)\exp\left[-2i\pi\left(x\eta\cos\theta-y\eta\sin\theta\right)\right]\mathrm{d}x\mathrm{d}y \tag{B.6}$$

One recovers here the spatial Fourier transform of the object along the direction $(\eta\cos\theta,\eta\sin\theta)$:

$$\widetilde{G}(\eta,\theta)=\widehat{g}(\eta\cos\theta,\eta\sin\theta) \tag{B.7}$$

The projection-slice theorem is represented on figure B.3 and gives another reconstruction method based on the reconstruction of the spatial Fourier space. This reconstruction technique was used in a lot of papers such as [200], particularly since the development of Fast Fourier Transform (FFT) algorithms. The major issue of such an approach is that the spatial Fourier space is naturally sampled on a polar grid so that measured data must often be interpolated over a Cartesian grid before inverse FFT is computed. This usually adds computation time and potential unwanted aliases.

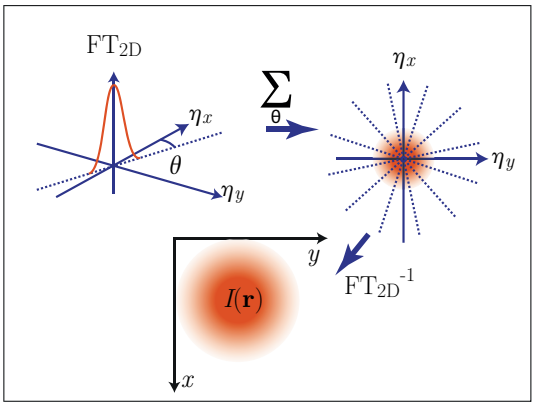

Figure B.3 – Illustration of the projection-slice theorem. The Fourier transform of a projection at θ is equal to a slice of the spatial Fourier transform of the final image along θ. The slice is placed back in its rightful place in the spatial Fourier space and summed over all angles. The inverse spatial Fourier transform of the reconstructed Fourier space gives the expected image.

B.2.2 The filtered backprojection

An good alternative to the use of Fourier transform is the filtered backprojection. This approach can be derived from the projection-slice theorem. This technique consists in a classical backprojection algorithm as described in section B.1 in which the blurring has been compensated. Let us start from the spatial Fourier transform of the final image expressed in polar coordinates:

$$g(x,y) = \int_0^{\pi} \int_{-\infty}^{\infty} \widehat{g}(\eta\cos\theta, \eta\sin\theta) \exp\left[2i\pi\left(x\eta\cos\theta - y\eta\sin\theta\right)\right] |\eta| \mathrm{d}\eta\mathrm{d}\theta \tag{B.8}$$

The projection-slice theorem allows us to replace the term $\widehat{g}(\eta\cos\theta, \eta\sin\theta)$ by the Radon transform:

$$g(x,y) = \int_0^{\pi} \int_{-\infty}^{\infty} \widetilde{G}(\eta,\theta) \exp\left[2i\pi\left(x\eta\cos\theta - y\eta\sin\theta\right)\right] |\eta| \mathrm{d}\eta\mathrm{d}\theta \tag{B.9}$$

If we express the term $\exp\left[2i\pi\left(x\eta\cos\theta - y\eta\sin\theta\right)\right]$ as:

$$\exp\left[2i\pi\left(x\eta\cos\theta - y\eta\sin\theta\right)\right] = \int_{-\infty}^{\infty} \exp\left(2i\pi\eta r\right) \delta\left(r - x\cos\theta - y\sin\theta\right) \mathrm{d}r \tag{B.10}$$

and switch the integrals a little bit, it is possible to express the final image as:

$$g(x,y) = \int_0^{\pi} \int_{-\infty}^{\infty} \left[\int_{-\infty}^{\infty} |\eta| \widetilde{G}(\eta,\theta) \exp\left(2i\pi\eta r\right) \mathrm{d}\eta\right] \delta\left(r - x\cos\theta - y\sin\theta\right) \mathrm{d}r\mathrm{d}\theta \tag{B.11}$$

Here the term between brackets is just a projection $G(r,\theta)$ filtered by a ramp filter $|\eta|$:

$$G_f(r,\theta) = \int_{-\infty}^{\infty} |\eta| \widetilde{G}(\eta,\theta) \exp\left(2i\pi\eta r\right) \mathrm{d}\eta \tag{B.12}$$

The final image is then the backprojection of the filtered projections:

$$\begin{aligned} g(x,y) &= \int_0^{\pi} \int_{-\infty}^{\infty} G_f(r,\theta) \delta\left(r - x\cos\theta - y\sin\theta\right) \mathrm{d}r\mathrm{d}\theta \\ &= \int_0^{\pi} G_f\left(x\cos\theta + y\sin\theta, \theta\right) \mathrm{d}\theta \end{aligned} \tag{B.13}$$

Here is then another possible way of reconstructing the final image: each projection is filtered by a ramp filter and backprojected as described in section B.1. This approach justifies *a posteriori* the blurring that appears on simply backprojected images. Indeed, the simply backprojected image can be expressed as:

$$\begin{aligned} \mathcal{B}[g](x,y) &= \int_0^{\pi} G\left(x\cos\theta + y\sin\theta, \theta\right) \mathrm{d}\theta \\ &= \int_0^{\pi} \int_{-\infty}^{\infty} \left[\int_{-\infty}^{\infty} \frac{1}{|\eta|} \widetilde{G_f}(\eta,\theta) \exp\left(2i\pi\eta r\right) \mathrm{d}\eta\right] \delta\left(r - x\cos\theta - y\sin\theta\right) \mathrm{d}r\mathrm{d}\theta \end{aligned} \tag{B.14}$$

where $\mathcal{B}[g]$ stands for the backprojection operator. If one defines $h(x,y)$ so that $\widehat{h}(\eta) = \frac{1}{|\eta|}$, the previous calculations can be done backward to recover the spatial Fourier transform of the simply backprojected object:

$$\begin{aligned} \mathcal{B}[g](x,y) &= \int_0^{\pi} \int_{-\infty}^{\infty} \widehat{h}(\eta) \widehat{g}(\eta\cos\theta, \eta\sin\theta) \exp\left[2i\pi\left(x\eta\cos\theta - y\eta\sin\theta\right)\right] |\eta| \mathrm{d}\eta\mathrm{d}\theta \\ &= g(x,y) * h(x,y) \end{aligned} \tag{B.15}$$

Tables of usual Fourier transforms gives the expression of $h(x,y)$ so that it comes [195]

$$\mathcal{B}[g](x,y) = g(x,y) * \frac{1}{\sqrt{x^2+y^2}} \tag{B.16}$$

which effect is to spread the PSF.

An interesting observation of the filtered backprojection is that the mean value corresponding to $\eta = 0$ is always multiplied by 0 so that it is lost during the process and must be corrected afterwards.

APPENDIX C

Of the inductive relationship of chapter 4

THIS appendix contains the details of the calculation of the inductive relationships given in chapter 4. Let us recall the formula for the PSF that was derived above in the manuscript.

$$\frac{PSF\left(r,\varphi\right)}{4\theta_m\eta_m^2} = \frac{J_1\left(2\pi\eta_m r\right)}{2\pi\eta_m r} + \sum_{p=1}^{+\infty} 2(-1)^p \mathrm{sinc}(2p\theta_m)\cos(2p\varphi)\int_0^1 J_{2p}\left(2\pi\eta_m r u\right) u\mathrm{d}u \tag{C.1}$$

This formula can be numerically computed in order to derive further properties of the PSF. Here the presence of the integral of J_{2p} still considerably slows the computation. It is interesting to develop this term and use the properties of the Bessel functions in order to find an inductive relationship between the different orders.

Thanks to the following property of the Bessel functions:

$$J_{n+1}\left(x\right) = \frac{nJ_n\left(x\right)}{x} - J_n'(x) \tag{C.2}$$

it is possible to write for all values of p:

$$\int_0^1 J_{2p}\left(2\pi\eta_m r u\right) u\mathrm{d}u = \frac{2p-1}{2\pi\eta_m r}\int_0^1 J_{2p-1}\left(2\pi\eta_m r u\right)\mathrm{d}u - \frac{1}{2\pi\eta_m r}\int_0^1 \frac{\mathrm{d}}{\mathrm{d}u}\left\{J_{2p-1}\left(2\pi\eta_m r u\right)\right\} u\mathrm{d}u \tag{C.3}$$

The second term of this expression can be calculated analytically through an integration by part:

$$\int_0^1 \frac{\mathrm{d}}{\mathrm{d}u}\left\{J_{2p-1}\left(2\pi\eta_m r u\right)\right\} u\mathrm{d}u = J_{2p-1}\left(2\pi\eta_m r\right) - \int_0^1 J_{2p-1}\left(2\pi\eta_m r u\right)\mathrm{d}u \tag{C.4}$$

so that it results

$$\int_0^1 J_{2p}\left(2\pi\eta_m r u\right) u\mathrm{d}u = \frac{2p}{2\pi\eta_m r}\int_0^1 J_{2p-1}\left(2\pi\eta_m r u\right)\mathrm{d}u - \frac{J_{2p-1}\left(2\pi\eta_m r\right)}{2\pi\eta_m r} \tag{C.5}$$

The second term of equation C.5 can be easily calculated through MATLAB and gives the term $\mathscr{B}_p$ in equation 4.18. Let us now focus on the remaining integral that will lead to the term $\mathscr{C}_p$ in equation 4.18. The Bessel functions obey the following inductive relationship:

$$J_{n-1}(x) = J_{n+1}(x) + 2J'_n(x) \tag{C.6}$$

By defining $c_p(r)$:

$$c_p(r) = \int_0^1 J_{2p-1}(2\pi\eta_m r u)\,\mathrm{d}u \tag{C.7}$$

we now have:

$$c_p(r) = \int_0^1 J_{2p+1}(2\pi\eta_m r u)\,\mathrm{d}u + \frac{1}{\pi\eta_m r}\int_0^1 \frac{\mathrm{d}}{\mathrm{d}u}\left\{J_{2p}(2\pi\eta_m r u)\right\}\mathrm{d}u \tag{C.8}$$

hence the inductive relationship of equation 4.19:

$$c_{p+1}(r) = c_p(r) - \frac{1}{\pi\eta_m r}\left(J_{2p}(2\pi\eta_m r) - J_{2p}(0)\right) \tag{C.9}$$

and the first term:

$$c_0(r) = \frac{J_0(2\pi\eta_m r) - 1}{2\pi\eta_m r} \tag{C.10}$$

Hence the expression of the PSF found in section 4.4.3 with the given expressions in equation 4.18 and equation 4.19.

APPENDIX D

Calculation of the delay in plane waves imaging

This appendix gives the details of the calculation of the time-of-flight in the filtered back-projection. The exact estimation of this delay is of prime interest in order to have a good reconstruction. Obviously, such a calculation strongly depends on the emitted delay line so that it must be adapted to the chosen law.

D.1 The emitted delay line

In our case, the emitted delay line is linear. The angle of propagation is defined by the angle between the vertical axis and the perpendicular to the wavefront as shown on figure D.1. For unclear hardware reasons, a delay must be added to the plane wave propagating vertically. The emitted delays are then defined as follows.

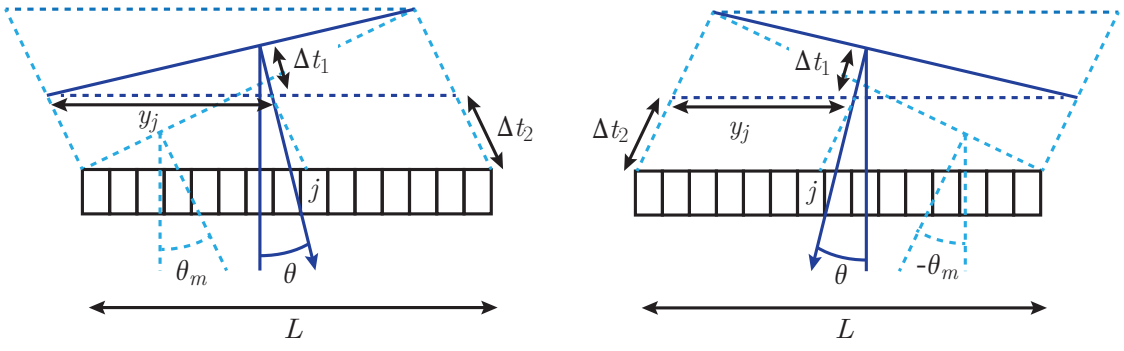

(a) Positive angles

(b) Negative angles

Figure D.1 – Schematic for the emitted delay line calculation.

For $\theta = \theta_m$, the delay line must be given by:

$$\Delta t_{\theta_m}(j) = \frac{y_j}{V_{\text{US}}} \sin(\theta_m) \tag{D.1}$$

all delays are calculated in relation to the upper point of this previous delay line $\Delta t_{\theta_m}(L) = \frac{L}{V_{\text{US}}} \sin(\theta_m)$:

$$\Delta t_0(j) = \frac{L}{V_{\text{US}}} \sin(\theta_m) \tag{D.2}$$

more generally, for a given positive angle, the delay line is the sum of two delays:

$$\Delta t_\theta(j) = \Delta t_1(j) + \Delta t_2(j) \tag{D.3}$$

where

$$\Delta t_1(j) = \frac{y_j}{V_{\text{US}}} \sin(|\theta|) \tag{D.4}$$

and

$$\Delta t_2(j) = \frac{L}{V_{\text{US}}} [\sin(\theta_m) - \sin(|\theta|)] \tag{D.5}$$

For positive angles, the delay is then given by:

$$\Delta t_\theta(j) = \frac{L}{V_{\text{US}}} \sin(\theta_m) - \frac{L - y_j}{V_{\text{US}}} \sin(|\theta|) \tag{D.6}$$

For negative angles, the delay line is:

$$\Delta t_\theta(j) = \frac{L}{V_{\text{US}}} \sin(\theta_m) - \frac{y_j}{V_{\text{US}}} \sin(|\theta|) \tag{D.7}$$

D.2 Time-of-flight calculation

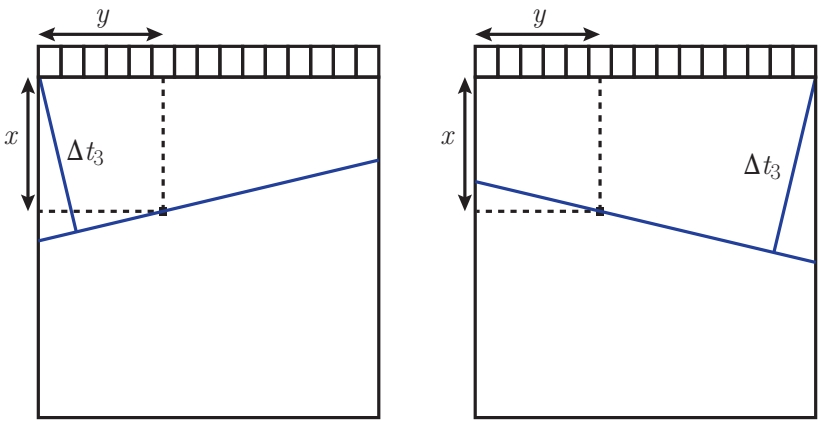

(a) Positive angles (b) Negative angles

Figure D.2 – Schematic for the time-of-flight calculation.

For positive angles, the time-of-flight of the plane wave is related to the distance from the wavefront to the point $(0, 0)$ given by:

$$\Delta t_3 = \frac{1}{V_{\text{US}}} (y \sin(\theta) + x \cos(\theta)) \tag{D.8}$$

For negative angles, the time-of-flight is related to the distance to the point $(0, L)$ given by:

$$\Delta t_3 = \frac{1}{V_{\text{US}}} ((y - L) \sin(\theta) + x \cos(\theta)) \tag{D.9}$$

The global delay for positive angles to voxel (x, y) is then:

$$\Delta t = \frac{1}{V_{\mathrm{US}}} \left[(y - L) \sin(\theta) + x \cos(\theta) \right] + \frac{L}{V_{\mathrm{US}}} \sin(\theta_m) \tag{D.10}$$

where the term $\frac{L}{V_{\mathrm{US}}} \left[\sin(\theta_m) - \sin(|\theta|) \right]$ comes from the emission delay line and is particular to our case.

For negative angles, the global delay is:

$$\Delta t = \frac{1}{V_{\mathrm{US}}} \left[y \sin(\theta) + x \cos(\theta) \right] + \frac{L}{V_{\mathrm{US}}} \sin(\theta_m) \tag{D.11}$$

A global expression working for all angles is then:

$$\Delta t = \frac{1}{V_{\mathrm{US}}} \left[\left(y - \frac{1}{2} \left\{ 1 + \mathrm{sign}(\theta) \right\} L \right) \sin(\theta) + x \cos(\theta) \right] + \frac{L}{V_{\mathrm{US}}} \sin(\theta_m) \tag{D.12}$$

where sign is the sign function that returns 1 if θ is positive and -1 if θ is negative.

APPENDIX E

Simple model for spectral holeburning

DETAILS of the calculations for the simple holeburning model presented in section 6.3.2 are presented here, the main results are recalled in the manuscript. Let us consider a system with three levels numbered {1}, {2} and {3}. The transition absorption cross section from {1} to {2} is noted σ. The spontaneous emission rate from {2} to {1} is noted w. The decay rate from {2} to {3} is noted β and the decay rate from {3} to {1} is noted γ. The schematic of the levels is presented on figure E.1. This model can also be found in french in [118] and a similar approach in [174, Chapter 30].

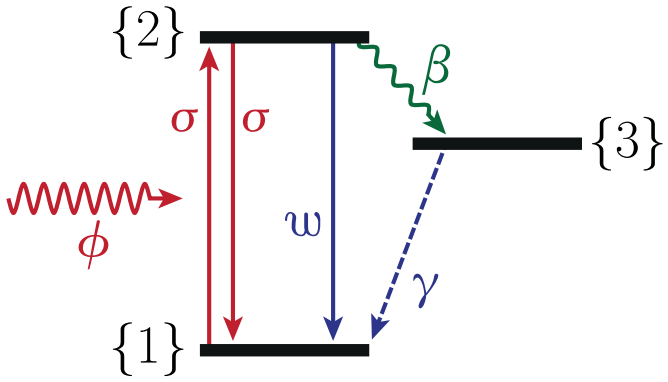

Figure E.1 – Levels involved in holeburning process. From the ground state {1}, atoms can be excited to the excited state {2} thanks to a number of photons per unit of time and surface ϕ. The absorption cross section of the transition is σ in cm^2. From the excited state, atoms can decay back to the ground state through spontaneous emission with a rate w (s^{-1}) or to the metastable state {3} through non radiative decay with a rate β (s^{-1}). From the metastable state, atoms can decay back to the ground state with a rate γ (s^{-1}). In the following it will be assumed that $\beta \gg w$ and $\beta \gg \gamma$.

E.1 About the different parameters

In order to make a connection with the quantities given before, the lifetime of {2} is given by $(w+\beta)^{-1}$ and is of the order of 400 µs around 8 K in the case of ${}^3H_4$ ($|e\rangle$). The lifetime of {3} is given by γ^{-1} and is of the order of 10 ms at low temperatures in the case of ${}^3F_4$ ($|m\rangle$).

The homogeneous transition cross section σ directly depends on the radiative decay rate w [174]. If the homogeneous linewidth is assumed to be a Lorentzian curve:

$$\sigma = \frac{g_2 \lambda^2 w}{4 g_1 \pi^2 \Gamma_h} \tag{E.1}$$

For the transition we consider $g_2 = 9$ and $g_1 = 13$, so that $\frac{g_1}{g_2} \sim 1$. This is why it will be considered in the following that the absorption and emission cross sections are the same. The spontaneous emission rate w is also the Einstein coefficient $A_{\{2\}\to\{1\}}$. This coefficient was computed at room temperature in [175] and is of the order of 110 s^{-1}. At room temperature, the transition cross-section is of the order of 10^{-20} cm^2 [176], however it increases at low temperatures as the homogeneous linewidth decreases. Using the value of $\Gamma_h = 44$ kHz measured in section 6.2.3, it comes that the transition cross section is of the order of 10^{-13} cm^2 at 3K[1].

E.2 Population equations and steady state

E.2.1 Population equations

Let N_1, N_2 and N_3 be the densities in cm^{-3} of population in respectively $\{1\}$, $\{2\}$ and $\{3\}$. Let N be the total ions concentration : $N = N_1 + N_2 + N_3$. Let ϕ be the number of photons per unit of time and surface. ϕ is related to the light irradiance on the crystal Φ_c ($W \cdot cm^{-2}$) through the relationship:

$$\phi = \frac{\Phi_c}{\hbar \nu} \tag{E.2}$$

Provided that the burning sequence is very long compared to T_2 so that all coherent processes such as Rabi oscillations are negligible, the equations driving the evolution of the populations can be expressed as:

$$\begin{cases} \dfrac{dN_1}{dt} = -\sigma\phi N_1 + (\sigma\phi + w) N_2 + \gamma N_3 \\ \dfrac{dN_2}{dt} = \sigma\phi N_1 - (\sigma\phi + w + \beta) N_2 \\ \dfrac{dN_3}{dt} = \beta N_2 - \gamma N_3 \end{cases} \tag{E.3}$$

In steady state when all time derivatives are zero, it is possible to derive the population of each state:

$$\begin{cases} N_1 = \dfrac{\gamma(\sigma\phi + w + \beta)}{(2\gamma + \beta)\sigma\phi + \gamma(w + \beta)} N \\ N_2 = \dfrac{\gamma\sigma\phi}{(2\gamma + \beta)\sigma\phi + \gamma(w + \beta)} N \\ N_3 = \dfrac{\beta\sigma\phi}{(2\gamma + \beta)\sigma\phi + \gamma(w + \beta)} N \end{cases} \tag{E.4}$$

[1]Here it is to be noted that the homogeneous cross section as defined above is the maximum value of the lorentzian homogeneous linewidth $\sigma(\nu)$.

In order to derive first simple properties, we will consider in first approximation that the optical irradiance is infinite so that it instantly pumps the transition: $\sigma\phi \gg w$, $\sigma\phi \gg \beta$ and $\sigma\phi \gg \gamma$. System E.4 can be written:

$$\begin{cases} N_1 = \dfrac{\gamma}{2\gamma+\beta}N \\ \\ N_2 = \dfrac{\gamma}{2\gamma+\beta}N \\ \\ N_3 = \dfrac{\beta}{2\gamma+\beta}N \end{cases} \tag{E.5}$$

Let us now assume that transfer from $\{2\}$ to $\{3\}$ is much faster than the other ones : $\beta \gg w$ and $\beta \gg \gamma$. Considering the values of the different rates given in section E.1, these hypotheses are rather natural. It comes that:

$$\begin{cases} N_1 = N_2 = \dfrac{\gamma}{\beta}N \\ \\ N_3 = \left(1 - 2\dfrac{\gamma}{\beta}\right)N \end{cases} \tag{E.6}$$

Here, it appears that the population of $\{1\}$ and $\{2\}$ are equal, meaning that the crystal is transparent at the wavelength corresponding to the transition. The condition of an infinite number of photons per unit of time and surface can be expressed in terms of optical irradiance which is a more natural parameter. $\sigma\phi \gg w$ can be rewritten:

$$\Phi_c \gg \frac{w\hbar\nu}{\sigma} \sim 300 \ \mu\mathrm{W}\cdot\mathrm{cm}^{-2} \tag{E.7}$$

Similarly, $\sigma\phi \gg \gamma$ is true if $\Phi_c \gg 300 \ \mu\mathrm{W}\cdot\mathrm{cm}^{-2}$. The third hypothesis $\sigma\phi \gg \beta$ implies that $\Phi_c \gg 6 \ \mathrm{mW}\cdot\mathrm{cm}^{-2}$. These values seem underestimated compared to experimental observations. However, it must be kept in mind that several parameters such as the laser linewidth or burning irradiance spatial inhomogeneity (Gaussian beams, burning beam absorption inside the crystal) are omitted in this simple approach.

E.2.2 Derivation of the absorption coefficient

Let us consider the transition from $\{1\}$ to $\{2\}$ without assuming anything about the photons number. When considering the variation $\mathrm{d}\phi$ of photons per unit of time and surface propagating through a small length $\mathrm{d}z$ of crystal, it comes:

$$\mathrm{d}\phi = -\sigma\left(N_1 - N_2\right)\phi\mathrm{d}z \tag{E.8}$$

which is the Beer-Lambert law related to transition $\{1\}$ to $\{2\}$. Estimating the absorption coefficient of the crystal then consists in deriving the expression of $N_1 - N_2$. Using equation E.4, the population difference can be expressed as:

$$N_1 - N_2 = \frac{1}{1 + \frac{2\gamma+\beta}{\gamma(w+\beta)}\sigma\phi}N \tag{E.9}$$

Let us define ζ:

$$\zeta = \frac{2\gamma + \beta}{\gamma\,(w + \beta)} \tag{E.10}$$

and the saturation number of photons per unit of time and surface:

$$\phi_s = \frac{1}{\sigma\zeta} \tag{E.11}$$

Therefore:

$$N_1 - N_2 = \frac{1}{1 + \frac{\phi}{\phi_s}} N \tag{E.12}$$

ϕ_s physically corresponds to the number of photons that creates a population difference of $\frac{N}{2}$. This intrinsic parameter quantifies the burning efficiency. Note that in case $\beta \gg \gamma$ and $\beta \gg w$, ζ only depends on the lifetime of the metastable state $\{3\}$ so that the longer it is, the easier transparency can be reached. It is interesting to notice at this point that the only criterion remaining in the end is the comparison between $\sigma\phi$ and γ. If ϕ is weak compared to ϕ_s, one retrieves the classical expression of Beer-Lambert law: $\phi\,(z) = \phi\,(0) \exp\,(-\sigma N z)$.

E.2.3 Effect of linewidth broadening

Up to now, I have considered a single infinitely narrow transition. However, it has to be taken into account that the transition is inhomogeneously broadened (Γ_{inh}) and each ion population has a homogeneous linewidth (Γ_h), see figure E.2. Both linewidths will be assumed Lorentzian-shaped. In the case of inhomogeneous linewidth, it was stated in section 6.2.2 that its shape was not straightforward. However, the Lorentzian-shape hypothesis is relevant as long as the considered homogeneous linewidth is located around the center of the linewidth, *i.e.* inside the FWHM. In the following, it will be assumed that $\Gamma_{inh} \gg \Gamma_h$, which typically occurs at low temperature. In order to recall the order of magnitude at 1.5 K, Γ_{inh} is of the order of several tens of GHz as Γ_h is of the order of few kHz. Let us now focus on a homogeneous transition at ν around the center of the inhomogeneous linewidth. As $\Gamma_{inh} \gg \Gamma_h$, it can be considered that the inhomogeneous spectral line is locally constant. The number of atoms $\mathrm{d}N_\nu$ at ν in a $\mathrm{d}\nu$ spectral region of the inhomogeneous linewidth is given by:

$$\mathrm{d}N_\nu = \frac{\frac{2N}{\pi\Gamma_{inh}}}{1 + \left(\frac{\nu - \nu_c}{\Gamma_{inh}/2}\right)^2} \mathrm{d}\nu \tag{E.13}$$

where ν_c is the central frequency of the inhomogeneous linewidth (793.3788 nm). In order to simplify further calculations, it will be considered that the central frequency of the homogeneous linewidth coincides with the central frequency of the inhomogeneous linewidth.

$$\mathrm{d}N_{\nu_c} = \frac{2N}{\pi\Gamma_{inh}} \mathrm{d}\nu \tag{E.14}$$

Similarly, the transition cross section of a homogeneous transition can be expressed as a Lorentzian function:

$$\sigma\,(\nu_c, \nu) = \frac{\sigma_h}{1 + \left(\frac{\nu - \nu_c}{\Gamma_h/2}\right)^2} \tag{E.15}$$

where σ_h is the homogeneous cross section calculated in section E.1, of the order of 10^{-13} cm^2.

Let us now return to equation E.12 that we will slightly adapt in order to study the variations of population inside a small spectral region $\mathrm{d}\nu$. Due to the inhomogeneous linewidth, the total population is not N anymore but $\mathrm{d}N_{\nu_c}$ and the transition cross section is now a Lorentzian function. In the spectral region $\mathrm{d}\nu$ centred around ν_c, the infinitesimal variation of population is given by:

$$\mathrm{d}(N_1 - N_2) = \frac{1}{1 + \zeta\sigma\left(\nu_c, \nu\right)\phi}\mathrm{d}N_{\nu_c} \tag{E.16}$$

or:

$$\mathrm{d}(N_1 - N_2) = \frac{\frac{2N}{\pi\Gamma_{inh}}}{1 + \zeta\phi\frac{\sigma_h}{1+\left(\frac{\nu-\nu_c}{\Gamma_h/2}\right)^2}}\mathrm{d}\nu \tag{E.17}$$

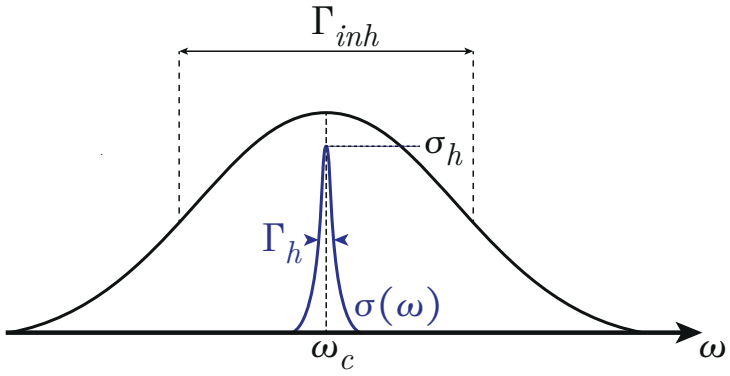

Figure E.2 – Schematic of the Lorentzian linewidths. The inhomogeneous linewidth Γ_{inh} is assumed much larger than the homogeneous linewidth Γ_h. In order to simplify the calculations, the homogeneous linewidth will be located at the center of the inhomogeneous linewidth.

E.3 Holeburning process in steady state

E.3.1 Reminder about holeburning process

Spectral holeburning process is based on two main steps: a burning and a probing sequence.

Burning sequence

The burning sequence consists in a narrowband light beam at ν_b within the inhomogeneous linewidth. In order to simplify equations, ν_b will be assumed equal to the centre frequency of the inhomogeneous linewidth ν_c. Refer to equation E.13 otherwise. The burning process is assumed very long compared to the coherence lifetime so that the populations close to ν_b are optically pumped as described above. Ions in $\{1\}$ are excited into $\{2\}$ and may non-radiatively decay into the metastable state $\{3\}$, according to the previously described model. In this section, the laser spectrum will be approximated to a Dirac distribution. I will only consider steady-state here because of coherent behaviour at short times and burning beam absorption that leads to a non-linear system of differential equations.

Probing sequence

After the burning sequence, a second weak light beam ($\phi_p \ll \phi_b$, and more important $\phi_p \ll \phi_s$) at ν_p is sent through the crystal. By weak beam, it is to be understood here that the probe should not move ions. Probe passes through the crystal and undergoes frequency-dependent absorption.

E.3.2 Absorption of the probing beam

Burning sequence

According to equation E.17, the burning pulse creates a frequency-dependent population inversion:

$$\mathrm{d}(N_1 - N_2)(\nu) = \frac{\frac{2N}{\pi\Gamma_{inh}}}{1 + \zeta\phi_b \frac{\sigma_h}{1+\left(\frac{\nu-\nu_b}{\Gamma_h/2}\right)^2}} \mathrm{d}\nu \tag{E.18}$$

Probing sequence

If we assume that $\phi_p \ll \phi_s$, the probing beam undergoes a classical Beer-Lambert absorption of coefficient $\alpha(\nu_p)$ given by:

$$\alpha(\nu_p) = \int_\nu \sigma(\nu, \nu_p)\, \mathrm{d}(N_1 - N_2)(\nu) \tag{E.19}$$

This equation basically states that the absorption is the sum of the contributions of all linewidths centred on ν at ν_p. Due to the homogeneous linewidth, all spectral lines can possibly absorb at ν_p. Equation E.19 can be expressed:

$$\alpha(\nu_p) = \int_\nu \frac{\sigma_h}{1 + \left(\frac{\nu_p-\nu}{\Gamma_h/2}\right)^2} \cdot \frac{\frac{2N}{\pi\Gamma_{inh}}}{1 + \zeta\phi_b \frac{\sigma_h}{1+\left(\frac{\nu-\nu_b}{\Gamma_h/2}\right)^2}} \mathrm{d}\nu \tag{E.20}$$

Let us develop equation E.20:

$$\alpha(\nu_p) = 2\frac{\sigma_h N}{\pi\Gamma_{inh}} \int_\nu \frac{1}{1 + \left(\frac{\nu_p-\nu}{\Gamma_h/2}\right)^2} \cdot \frac{1 + \left(\frac{\nu-\nu_b}{\Gamma_h/2}\right)^2}{1 + \left(\frac{\nu-\nu_b}{\Gamma_h/2}\right)^2 + \zeta\phi_b\sigma_h} \mathrm{d}\nu \tag{E.21}$$

that can be rewritten:

$$\alpha(\nu_p) = 2\frac{\sigma_h N}{\pi\Gamma_{inh}} \left[\int_\nu \frac{1}{1 + \left(\frac{\nu_p-\nu}{\Gamma_h/2}\right)^2} \mathrm{d}\nu - \int_\nu \frac{\zeta\phi_b\sigma_h}{\left[1 + \left(\frac{\nu_p-\nu}{\Gamma_h/2}\right)^2\right]\left[1 + \left(\frac{\nu-\nu_b}{\Gamma_h/2}\right)^2 + \zeta\phi_b\sigma_h\right]} \mathrm{d}\nu \right] \tag{E.22}$$

The first integral is easy to derive and is equal to $\frac{\pi\Gamma_h}{2}$. The other integral can be expressed as a convolution product between two Lorentzian functions. If $G^2 = \Gamma_h^2(1 + \zeta\phi_b\sigma_h)$, the second integral can be expressed as:

$$\begin{aligned} &\int_\nu \frac{\zeta\phi_b\sigma_h}{\left[1 + \left(\frac{\nu_p-\nu}{\Gamma_h/2}\right)^2\right]\left[1 + \left(\frac{\nu-\nu_b}{\Gamma_h/2}\right)^2 + \zeta\phi_b\sigma_h\right]} \mathrm{d}\nu = \\ &\pi^2 \left(\frac{\Gamma_h^3}{4G}\right) \zeta\phi_b\sigma_h \int_\nu \frac{\Gamma_h/2 \cdot G/2}{\pi\left[(\Gamma_h/2)^2 + (\nu_p - \nu)^2\right]\pi\left[(G/2)^2 + (\nu - \nu_b)^2\right]} \mathrm{d}\nu \end{aligned} \tag{E.23}$$

The convolution of two Lorentzians of FWHM respectively Γ_h and G is a Lorentzian of FWHM $\Gamma_{\mathrm{HB}} = \Gamma_h + G$. Absorption can then be expressed as:

$$\alpha(\nu_p) = \sigma_h N \frac{\Gamma_h}{\Gamma_{inh}} \left[1 - \frac{\Gamma_h^2}{2G} \zeta \phi_b \sigma_h \frac{\frac{2}{\Gamma_{\mathrm{HB}}}}{1 + \left(\frac{\nu_p - \nu_b}{\Gamma_{\mathrm{HB}}/2} \right)^2} \right] \tag{E.24}$$

When replacing G by its expression and re-introducing $\phi_s = \frac{1}{\zeta \sigma_h}$:

$$\alpha(\nu_p) = \sigma_h N \frac{\Gamma_h}{\Gamma_{inh}} \left[1 - \frac{\Gamma_h \frac{\phi_b}{\phi_s}}{2\sqrt{1 + \frac{\phi_b}{\phi_s}}} \frac{\frac{2}{\Gamma_{\mathrm{HB}}}}{1 + \left(\frac{\nu_p - \nu_b}{\Gamma_{\mathrm{HB}}/2} \right)^2} \right] \tag{E.25}$$

If noticing that:

$$\frac{\phi_b}{\phi_s} = 1 + \frac{\phi_b}{\phi_s} - 1 = \left(\sqrt{1 + \frac{\phi_b}{\phi_s}} - 1 \right) \left(\sqrt{1 + \frac{\phi_b}{\phi_s}} + 1 \right) \tag{E.26}$$

and replacing Γ_{HB} by its expression, we get:

$$\alpha(\nu_p) = \sigma_h N \frac{\Gamma_h}{\Gamma_{inh}} \left[1 - \frac{\sqrt{1 + \frac{\phi_b}{\phi_s}} - 1}{\sqrt{1 + \frac{\phi_b}{\phi_s}}} \frac{1}{1 + \left(\frac{\nu_p - \nu_b}{\Gamma_{\mathrm{HB}}/2} \right)^2} \right] \tag{E.27}$$

A schematic of the expected behaviour of the absorption is plotted in figure E.3. As expected, if $\phi_b \ll \phi_s$, the burning process is not efficient: absorption is constant and is equal to $\sigma_h N \frac{\Gamma_h}{\Gamma_{inh}}$. This is the same case as described in E.2.2 with an ion concentration that is not N anymore but $N \frac{\Gamma_h}{\Gamma_{inh}}$ due to linewidth broadening. In case $\phi_b \gg \phi_s$, absorption drops down to zero when $\nu_p = \nu_b$ and the crystal is fully transparent in first approximation. The FWHM of the hole starts at twice the homogeneous linewidth and increases as the square root of the burning power.

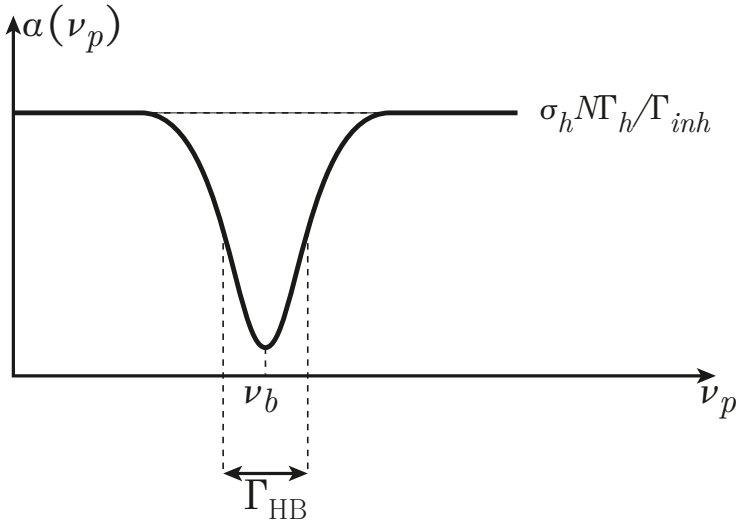

Figure E.3 – Schematic of absorption as a function of the probing frequency. The shape is a Lorentzian curve, the width of which is Γ_{HB}. The maximum transparency occurs at $\nu_p = \nu_b$.

It is interesting to evaluate the order of magnitude of the term $\sigma_h N \frac{\Gamma_h}{\Gamma_{inh}}$ which quantifies the absorption of the crystal. In the case of 2 at.% YAG, N is of the order of 10^{20} cm^{-3}:

$$\sigma_h N \frac{\Gamma_h}{\Gamma_{inh}} \sim 10^{-13} \cdot 10^{20} \cdot \frac{40 \cdot 10^3}{40 \cdot 10^9} \sim 10 \text{ cm}^{-1} \tag{E.28}$$

It is to be compared to the expected value of $\alpha_m L \sim 5$ of our crystal leading to an absorption of the order of 25 cm^{-1}, the difference being mostly due to the fact that the previous calculation was done with orders of magnitude only.

Influence of the laser linewidth

Here the absorption coefficient shape of the hole was calculated by approximating the laser linewidth to a Dirac distribution. In practice, the emission linewidth of the laser is rather a Lorentzian line. The hole shape can then be obtained by convolving the absorption calculated in E.27 to the laser linewidth once for the burning process and once for the probing sequence. The resulting hole is then given by:

$$\alpha\left(\nu_p - \nu_b\right) = \left[\alpha_\delta\left(\nu_p - \nu_b\right) * \mathcal{L}\left(\nu_b\right)\right] * \mathcal{L}\left(\nu_p\right) \tag{E.29}$$

where $*$ denotes the convolution product, α_δ is the absorption calculated in E.27 and $\mathcal{L}$ is the Lorentzian linewidth of the laser. The resulting hole is still Lorentzian-shaped but the FWHM is now

$$\Gamma_{\mathrm{HB}} = \Gamma_h\left(1 + \sqrt{1 + \frac{\phi_b}{\phi_s}}\right) + 2\Gamma_l \tag{E.30}$$

where Γ_l is the FWHM of the laser linewidth. Because of the conservation of excited ions, *i.e.* the area under the hole, the hole is expected not to be as deep as above. It is then more difficult to burn a hole.

Spatial variations of absorption

Here it was supposed that absorption was constant along the crystal thickness. However, the burning pulse is absorbed as it propagates through the crystal and this leads to a decrease of the saturation.

At a depth z inside the crystal, absorption is given by:

$$\alpha\left(\nu_p, z\right) = \sigma_h N \frac{\Gamma_h}{\Gamma_{inh}}\left[1 - \frac{\sqrt{1 + \frac{\phi_b(z)}{\phi_s}} - 1}{\sqrt{1 + \frac{\phi_b(z)}{\phi_s}}} \frac{1}{1 + \left(\frac{\nu_p - \nu_b}{\Gamma_{\mathrm{HB}}(z)/2}\right)^2}\right] \tag{E.31}$$

Here $\Gamma_{\mathrm{HB}}\left(z\right)$ also depends on the depth inside the crystal through the optical burning irradiance $\hbar\nu\phi_b\left(z\right)$. The optical irradiance obeys a Beer-Lambert law through:

$$\phi_b\left(z_0\right) = \phi_b\left(0\right)\exp\left(-\int_0^{z_0} \alpha\left(\nu_p, z\right) z\mathrm{d}z\right) \tag{E.32}$$

This problem is impossible to solve analytically but a discrete approach is very easy to implement numerically. Within a slice between z_0 and $z_0 + \Delta z$ it is possible to write:

$$\begin{cases} \phi_b\left(0\right) = \phi_b^0 \\ \\ \alpha\left(\nu_p, z_0\right) = \sigma_h N \frac{\Gamma_h}{\Gamma_{inh}}\left[1 - \frac{\sqrt{1 + \frac{\phi_b(z_0)}{\phi_s}} - 1}{\sqrt{1 + \frac{\phi_b(z_0)}{\phi_s}}} \frac{1}{1 + \left(\frac{\nu_p - \nu_b}{\Gamma_{\mathrm{HB}}(z_0)/2}\right)^2}\right] \\ \\ \phi_b\left(z_0 + \Delta z\right) = \phi_b\left(z_0\right)\exp\left(-\alpha\left(\nu_p, z_0\right)\Delta z\right) \end{cases} \tag{E.33}$$

The probed absorption is thus an integrated absorption over the thickness of the crystal. The lateral spatial variations of the burning irradiance over the probed surface, due to the use of Gaussian beams instead of plane waves for instance, can easily be added by discretizing the surface of the crystal.

E.3.3 Dynamics of hole erasure

The transient formation of a hole is not straightforward to study analytically due to the absorption of the burning beam while propagating inside the crystal and coherent effects that occur at short times. I will not theoretically study this point in this manuscript. However, it is interesting to study the dynamics of the hole erasure after the burning beam is switched off. Let us consider a thin section of the crystal in order to assume that the burning power is constant over the entire volume.

At $t = 0^-$, *i.e.* just before the burning beam is switched off, the inversion population in steady-state is:

$$\mathrm{d}(N_1 - N_2)(\nu, t = 0^-) = \frac{\frac{2N}{\pi\Gamma_{inh}}}{1 + \zeta\phi_b \frac{\sigma_h}{1+\left(\frac{\nu_b-\nu}{\Gamma_h/2}\right)^2}} \mathrm{d}\nu \tag{E.34}$$

and absorption is equal to:

$$\alpha\left(\nu_p, t = 0^-\right) = \sigma_h N \frac{\Gamma_h}{\Gamma_{inh}} \left[1 - \frac{\sqrt{1 + \frac{\phi_b}{\phi_s}} - 1}{\sqrt{1 + \frac{\phi_b}{\phi_s}}} \frac{1}{1 + \left(\frac{\nu_p - \nu_b}{\Gamma_{\mathrm{HB}}/2}\right)^2}\right] \tag{E.35}$$

From $t = 0$, populations obey the following equations:

$$\begin{cases} \dfrac{\mathrm{d}N_1}{\mathrm{d}t} = wN_2 + \gamma N_3 \\ \dfrac{\mathrm{d}N_2}{\mathrm{d}t} = -\left(w + \beta\right) N_2 \\ \dfrac{\mathrm{d}N_3}{\mathrm{d}t} = \beta N_2 - \gamma N_3 \end{cases} \tag{E.36}$$

This system is linear and gives the evolution of the populations after the burning sequence is shut off. Not surprisingly, atoms in $\{2\}$ obey an exponential decay as they return to $\{1\}$ and $\{3\}$.

$$N_2\left(t\right) = N_2\left(0\right) e^{-(w+\beta)t} \tag{E.37}$$

Thanks to equation E.37, it is possible to derive $N_3\left(t\right)$ then $N_1\left(t\right)$:

$$\begin{cases} N_2\left(t\right) = N_2\left(0\right) e^{-(w+\beta)t} \\ N_3\left(t\right) = \left(N_3\left(0\right) + \frac{\beta}{w+\beta-\gamma} N_2\left(0\right)\right) e^{-\gamma t} - \frac{\beta}{w+\beta-\gamma} N_2\left(0\right) e^{-(w+\beta)t} \\ N_1\left(t\right) = N - N_2\left(t\right) - N_3\left(t\right) \end{cases} \tag{E.38}$$

By replacing $N_2(0)$ and $N_3(0)$ by their expressions of E.4 in system E.38:

$$\begin{cases} N_2(t) = \frac{\sigma\phi_b}{(2\gamma+\beta)\sigma\phi_b+\gamma(w+\beta)} N\gamma e^{-(w+\beta)t} \\ N_3(t) = \frac{\sigma\phi_b}{(2\gamma+\beta)\sigma\phi_b+\gamma(w+\beta)} N\left[\frac{\beta(w+\beta)}{w+\beta-\gamma}e^{-\gamma t} - \frac{\beta\gamma}{w+\beta-\gamma}e^{-(w+\beta)t}\right] \\ N_1(t) = N - N\frac{\sigma\phi_b}{(2\gamma+\beta)\sigma\phi_b+\gamma(w+\beta)}\left[\frac{\beta(w+\beta)}{w+\beta-\gamma}e^{-\gamma t} + \frac{\gamma(w-\gamma)}{w+\beta-\gamma}e^{-(w+\beta)t}\right] \end{cases} \tag{E.39}$$

In order to simplify these expressions without altering the physics of the phenomenon, it will be considered in the following that the burning *flux* is very high, as in section E.2.1: $\sigma\phi_b \gg w$, $\sigma\phi_b \gg \beta$ and $\sigma\phi_b \gg \gamma$. Moreover, it will be assumed that $\beta \gg w$ and $\beta \gg \gamma$. The expressions of the populations decay are thus given by:

$$\begin{cases} N_1(t) = N\left[1 - \left(1 - \frac{\gamma}{\beta}\right)e^{-\gamma t} - \frac{\gamma(w-\gamma)}{\beta^2}e^{-\beta t}\right] \\ N_2(t) = \frac{\gamma}{\beta}Ne^{-\beta t} \\ N_3(t) = N\left[\left(1 - \frac{\gamma}{\beta}\right)e^{-\gamma t} - \frac{\gamma}{\beta}e^{-\beta t}\right] \end{cases} \tag{E.40}$$

$\frac{\gamma(w-\gamma)}{\beta^2}$ being of second order, it will be omitted in the following. The population difference between $\{1\}$ and $\{2\}$ is given by:

$$N_1 - N_2 = N\left[1 - \left(1 - \frac{\gamma}{\beta}\right)e^{-\gamma t} - \frac{\gamma}{\beta}e^{-\beta t}\right] \tag{E.41}$$

At $t = 0$ the crystal is transparent and it slowly recovers its absorption over time. It is noticeable that the increase of population difference occurs in two phases. A first fast decay over a time scale of the order of β^{-1} concerning a small amount of atoms ($N\frac{\gamma}{\beta}$) corresponding to the atoms decaying from $\{2\}$. It is followed by a slow one over γ^{-1} corresponding to the atoms returning to $\{1\}$.

Here β^{-1} is of the order of few hundreds of µs. After this characteristic time, $N\frac{\gamma}{\beta}$ atoms have returned back to the ground state. If the probing beam is switched on after this time – which is typically the case – the crystal has recovered $100 \times \frac{\gamma}{\beta}$ % of its original absorption.

APPENDIX F

Simple model for spectral holeburning under a magnetic field

THIS appendix contains a simple model for spectral holeburning under a magnetic field. A lot of points were already tackled in appendix E, the model developed here is just an adaptation for spectral holeburning under a magnetic field.

F.1 Model of the atomic levels

F.1.1 General model

The general model is represented on figure F.1. Let us consider six levels numbered $\{1\}$ to $\{6\}$ that respectively stand for the ground states $|g,+\rangle$ and $|g,-\rangle$, the excited states $|e,+\rangle$ and $|e,-\rangle$ and the metastable states $|m,+\rangle$ and $|m,-\rangle$. In the following, it will be assumed that due to the selection rules, optical transitions between $\{1\}$ and $\{4\}$ and between $\{2\}$ and $\{3\}$ are forbidden. The two transitions are then coupled only through the metastable states and very weak non radiative exchanges between $\{1\}$ and $\{2\}$. Let then σ_{ij}, w_{ij}, β_{ij} and γ_{ij} respectively stand for the transition cross section, the spontaneous decay rate, the non radiative decay rate to the metastable state and the decay rate from the metastable state, where the indices point to the concerned states number $\{i\}$ and $\{j\}$. κ_{ij} stands for the transition rate between the two ground states.

Due to symmetry considerations, the decay rates from $\{3\}$ to $\{5\}$ and from $\{4\}$ to $\{6\}$ are equal: $\beta_{35} = \beta_{46} = \beta$. Spontaneous emission rates are identical between the two Zeeman transitions: $w_{31} = w_{42} = w$. The decay rates γ_{51}, γ_{52}, γ_{61} and γ_{62} can be related to the inverse γ of the metastable lifetime thanks to a proportionality factor p between 0 and 1: $\gamma_{51} = \gamma_{62} = p\gamma$ and $\gamma_{52} = \gamma_{61} = (1-p)\,\gamma$.

F.1.2 Main assumptions

Let us consider again the levels represented on figure F.1. In the following, it will be considered that the transitions have the same cross sections so that $\sigma_{13} = \sigma_{31} = \sigma_{24} = \sigma_{42} = \sigma$. It will be assumed that the proportionality factor p introduced in the previous section is close to 0.5 so that $\gamma_{51} = \gamma_{52} = \gamma_{61} = \gamma_{62} = \frac{\gamma}{2}$. This assumption allows neglecting the Zeeman splitting of the metastable state. It will also be considered that, if the different values of decay rates

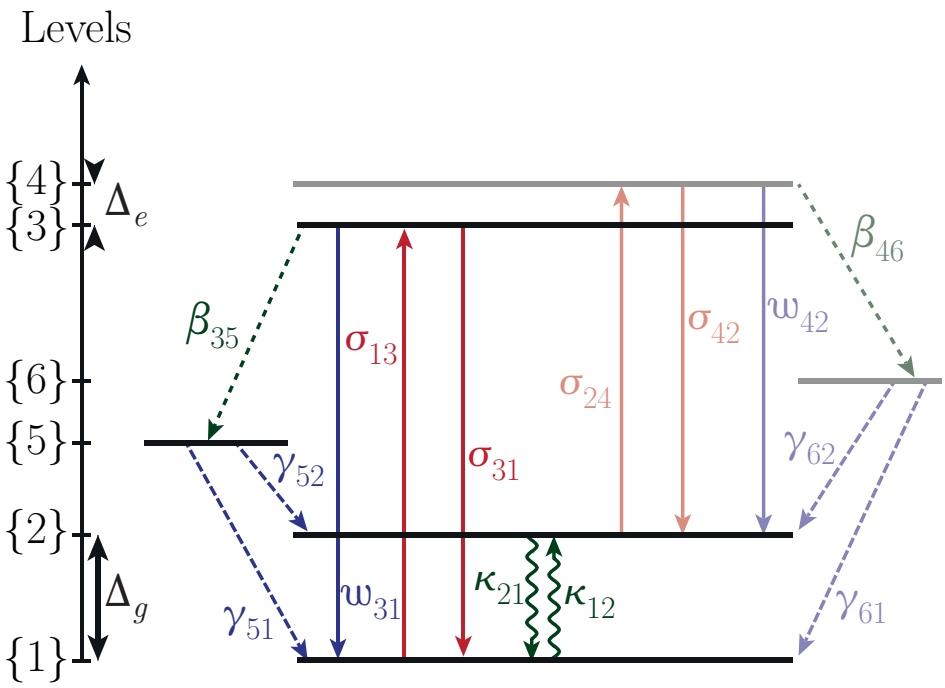

Figure F.1 – General model of the levels involved in holeburning process under a magnetic field.

changed after introducing a magnetic field, they remained of same order of magnitude than in the zero-magnetic-field case. Hypotheses that were made in appendix E still hold: $\beta \gg \gamma$ and $\beta \gg w$.

Moreover, it will also be assumed that the transition rate from $\{1\}$ to $\{2\}$ is the same as from $\{2\}$ to $\{1\}$ and will be noted κ. In our case, this transition rate is very weak so it will be assumed that $\kappa \ll \beta$, $\kappa \ll \gamma$ and $\kappa \ll w$.

The final assumption concerns the laser excitation. It will be considered in the following that the laser is narrowband enough and sufficiently weak so it can not excite both transitions from $\{1\}$ to $\{3\}$ and $\{2\}$ to $\{4\}$ at the same time. Depending on the transition the laser is tuned on, either level $\{4\}$ or $\{3\}$ will then be assumed empty at all time during the burning process. In the following, we will work on the simplified system presented on figure F.2 in which the level $\{6\}$ has been omitted.

F.2 Population equations and steady state

Let us consider that the laser is tuned on the transition from $\{1\}$ to $\{3\}$ so that $\{4\}$ is empty at all time. Equations driving the populations evolution are very similar to what was derived in appendix E and are the following with the same variables:

$$\begin{cases} \dfrac{\mathrm{d}N_1}{\mathrm{d}t} &= -\left(\sigma\phi + \kappa\right) N_1 + \kappa N_2 + \left(\sigma\phi + w\right) N_3 + \frac{\gamma}{2} N_5 \\ \dfrac{\mathrm{d}N_2}{\mathrm{d}t} &= \kappa N_1 - \kappa N_2 + \frac{\gamma}{2} N_5 \\ \dfrac{\mathrm{d}N_3}{\mathrm{d}t} &= \sigma\phi N_1 - \left(\sigma\phi + w + \beta\right) N_3 \\ N_4 &= 0 \\ \dfrac{\mathrm{d}N_5}{\mathrm{d}t} &= \beta N_3 - \gamma N_5 \end{cases} \tag{F.1}$$

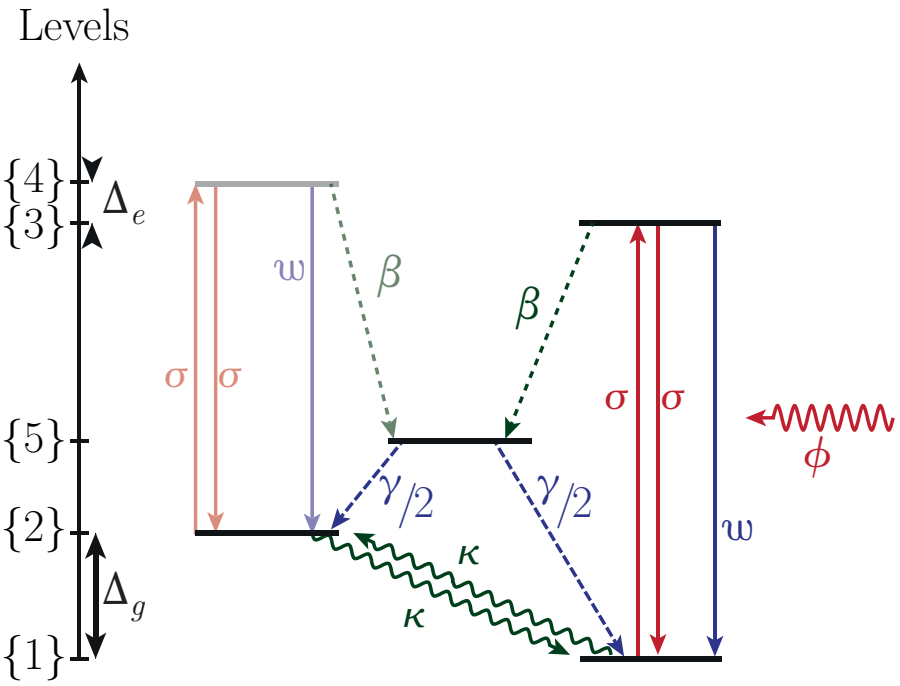

Figure F.2 – Simplified model of the levels involved in holeburning process under a magnetic field.

F.2.1 Steady-state solution

In steady-state the different populations are given by:

$$\begin{cases} N_1 &= \dfrac{2\kappa\gamma\left(\sigma\phi + w + \beta\right)}{\left(6\kappa\gamma + \beta\gamma + 2\kappa\beta\right)\sigma\phi + 4\kappa\gamma\left(w+\beta\right)}N \\ N_2 &= \dfrac{\gamma\left(2\kappa + \beta\right)\sigma\phi + 2\kappa\gamma\left(w+\beta\right)}{\left(6\kappa\gamma + \beta\gamma + 2\kappa\beta\right)\sigma\phi + 4\kappa\gamma\left(w+\beta\right)}N \\ N_3 &= \dfrac{2\kappa\gamma\sigma\phi}{\left(6\kappa\gamma + \beta\gamma + 2\kappa\beta\right)\sigma\phi + 4\kappa\gamma\left(w+\beta\right)}N \\ N_4 &= 0 \\ N_5 &= \dfrac{2\kappa\beta\sigma\phi}{\left(6\kappa\gamma + \beta\gamma + 2\kappa\beta\right)\sigma\phi + 4\kappa\gamma\left(w+\beta\right)}N \end{cases} \tag{F.2}$$

where $N = N_1 + N_2 + N_3 + N_4 + N_5$. A first reassuring point is that $N_1 = N_2 = N/2$ at equilibrium without light, as expected from thermal agitation. In the case of an infinite burning efficiency, the different populations are:

$$\begin{cases} N_1 &= \dfrac{2\kappa\gamma}{\left(6\kappa\gamma + \beta\gamma + 2\kappa\beta\right)}N \\ N_2 &= \dfrac{\gamma\left(2\kappa + \beta\right)}{\left(6\kappa\gamma + \beta\gamma + 2\kappa\beta\right)}N \\ N_3 &= \dfrac{2\kappa\gamma}{\left(6\kappa\gamma + \beta\gamma + 2\kappa\beta\right)}N \\ N_4 &= 0 \\ N_5 &= \dfrac{2\kappa\beta}{\left(6\kappa\gamma + \beta\gamma + 2\kappa\beta\right)}N \end{cases} \tag{F.3}$$

Under the assumptions $\beta \gg \gamma \gg \kappa$ and $\beta \gg w \gg \kappa$, we get at second order:

$$\begin{cases} N_1 &= \dfrac{2\kappa}{\beta} N \\ N_2 &= \left(1 - \dfrac{2\kappa}{\gamma} - \dfrac{4\kappa}{\beta}\right) N \\ N_3 &= \dfrac{2\kappa}{\beta} N \\ N_4 &= 0 \\ N_5 &= \dfrac{2\kappa}{\gamma} N \end{cases} \tag{F.4}$$

Here the crystal is also transparent at the burning frequency since populations in $\{1\}$ and $\{3\}$ are equal. The main difference is the proportion of atoms lying in the different levels. These values must be compared to the zero-magnetic-field case in which the proportion of atoms in the excited state is of the order of $\frac{\gamma}{\beta}N$ and the proportion of atoms in the metastable state is of the order of $\left(1 - \frac{2\gamma}{\beta}\right) N$. In the presence of an external magnetic field, the proportion of atoms staying the excited state is now of the order of $\frac{\gamma}{\kappa}$ times lower, which can be of several orders of magnitude. The problem of increasing absorption after atoms leave ${}^3H_4$ is thus expected to be drastically reduced. Similarly, after few tens of ms only $\frac{2\kappa}{\gamma}N$ atoms returned to the ground state as they were all back in the zero-magnetic-field case.

F.2.2 Population difference

Similarly to what was derived in appendix E, it is possible to extract the absorption coefficient from the population difference between $\{1\}$ and $\{3\}$:

$$N_1 - N_3 = \frac{1}{2} \frac{1}{1 + \frac{6\kappa\gamma + \beta\gamma + 2\kappa\beta}{4\kappa\gamma(w+\beta)} \sigma\phi} N \tag{F.5}$$

By defining the same coefficient ζ that was defined in appendix E:

$$\zeta = \frac{2\gamma + \beta}{\gamma\,(w + \beta)} \tag{F.6}$$

and set ζ_B as:

$$\zeta_B = \frac{2\kappa + \beta}{4\kappa\,(w + \beta)} \tag{F.7}$$

it comes that:

$$\frac{6\kappa\gamma + \beta\gamma + 2\kappa\beta}{4\kappa\gamma\,(w + \beta)} = \zeta_B + \frac{\zeta}{2} \tag{F.8}$$

It is thus possible to define a new saturation photon number ϕ_s as follows:

$$\phi_s = \frac{1}{\sigma\left(\zeta_B + \frac{\zeta}{2}\right)} \tag{F.9}$$

so that it comes out the same result as for the zero-magnetic-field case:

$$N_1 - N_3 = \frac{1}{2}\frac{1}{1+\frac{\phi}{\phi_s}}N \tag{F.10}$$

According to this model, the behaviour of the main hole will be the same as described in appendix E. A first difference is that if $\kappa \ll \gamma$, $\beta \gg \gamma$ and $\beta \gg w$, the coefficient ζ_B is much larger than in the no-field situation: $\zeta_B \sim \frac{1}{4\kappa}$ as $\zeta \sim \frac{1}{\gamma}$. The saturation photon number will be much smaller and the hole will thus be burnt much more easily in the presence of an external magnetic field. A second difference concerns the transition from $\{2\}$ to $\{4\}$ for which the population difference is now:

$$N_2 - N_4 = N_2 = \frac{\frac{1}{2} + \frac{2\kappa+\beta}{4\kappa(w+\beta)}\sigma\phi}{1+\frac{6\kappa\gamma+\beta\gamma+2\kappa\beta}{4\kappa\gamma(w+\beta)}\sigma\phi}N \tag{F.11}$$

By replacing the previously introduced variables ζ and ζ_B:

$$N_2 - N_4 = \frac{N}{2} + \frac{\left(\zeta_B - \frac{\zeta}{2}\right)\sigma\phi}{1+\left(\zeta_B + \frac{\zeta}{2}\right)\sigma\phi}\frac{N}{2} \tag{F.12}$$

In the absence of light, the difference of population is given by the $\frac{N}{2}$ ions in $\{2\}$ – remember that the model assumes $N_4 = 0$ at all time. As the light power increases, this difference of population tends toward:

$$N_2 - N_4 = \frac{N}{2} + \frac{\zeta_B - \frac{\zeta}{2}}{\zeta_B + \frac{\zeta}{2}}\frac{N}{2} \sim \left(1 - \frac{\zeta}{\zeta_B}\right)N \tag{F.13}$$

In order to simplify future calculations, due to ζ being very small compared to ζ_B, it will be assumed that $\zeta_B - \frac{\zeta}{2} \sim \zeta_B + \frac{\zeta}{2} \sim \zeta_B$. In this case, the previous equations can be rewritten:

$$\begin{cases} \phi_s &= \dfrac{1}{\sigma\zeta_B} \\ N_1 - N_3 &= \dfrac{1}{2}\dfrac{1}{1+\frac{\phi}{\phi_s}}N \\ N_2 - N_4 &= \dfrac{N}{2} + \dfrac{\frac{\phi}{\phi_s}}{1+\frac{\phi}{\phi_s}}\dfrac{N}{2} \end{cases} \tag{F.14}$$

The third and final difference concerns the factor $\frac{1}{2}$ in all equations. It comes from the fact that the population N of the considered class of ions was split into the two Zeeman levels. However, this does not mean that crystal absorption was divided by two. Both classes of ions for which either $|g,+\rangle$ to $|e,+\rangle$ or $|g,-\rangle$ to $|e,-\rangle$ match a given frequency contribute to the crystal absorption. All previous equations must also be written for the population class at $\nu_b + \Delta_g - \Delta_e$, where ν_b is the burning frequency and the same must be done for every other levels. The corresponding schematic is presented on figure F.3. Here we characterized a population class through the frequency of its corresponding transition $|g,+\rangle$ to $|e,+\rangle$.

In light of this remark, the population difference generated by a burning pulse can be written

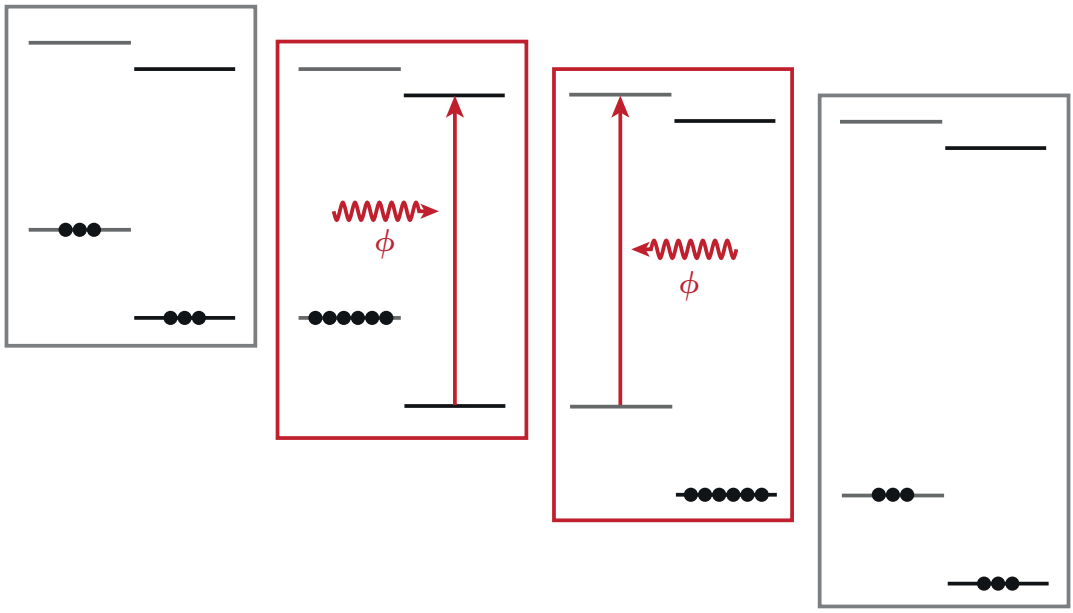

Figure F.3 – Two classes of atoms (framed in red) can participate to the transitions at one given frequency. During the holeburning process, two other classes (framed in gray) take part to the anti-hole absorption. These classes did not interact with the burning beam.

as a function of the burning pulsation ν_b:

$$\begin{cases} \Delta N\left(\nu_b\right) & = N - \dfrac{\frac{\phi}{\phi_s}}{1+\frac{\phi}{\phi_s}} N \\ \Delta N\left(\nu_b + \Delta_g - \Delta_e\right) & = N + \dfrac{\frac{\phi}{\phi_s}}{1+\frac{\phi}{\phi_s}} \dfrac{N}{2} \\ \Delta N\left(\nu_b - \Delta_g + \Delta_e\right) & = N + \dfrac{\frac{\phi}{\phi_s}}{1+\frac{\phi}{\phi_s}} \dfrac{N}{2} \end{cases} \tag{F.15}$$

F.2.3 The homogeneous linewidth

Here, it will be assumed that the splitting is large compared to the homogeneous linewidth but small compared to the inhomogeneous linewidth so that the total ions concentration is constant over the probed spectral domain. Similarly to the approach of appendix E, it will be considered that the probed transitions are located around the top of the inhomogeneous linewidth:

$$\mathrm{d}N_{\nu_c} = \frac{2N}{\pi\Gamma_{inh}}\mathrm{d}\nu \tag{F.16}$$

For a given transition centred on ν_0, the cross section is given by:

$$\sigma\left(\nu_0, \nu\right) = \frac{\sigma_h}{1+\left(\frac{\nu-\nu_0}{\Gamma_h/2}\right)^2} \tag{F.17}$$

In the presence of a burning beam, the population difference as a function of ν is given by:

$$\mathrm{d}\left[\Delta N\left(\nu\right)\right] = \frac{2N}{\pi\Gamma_{inh}} + \frac{2N}{\pi\Gamma_{inh}}\left[\frac{-\zeta_B\sigma\left(\nu_0,\nu\right)\phi}{1+\zeta_B\sigma\left(\nu_0,\nu\right)\phi} * \delta\left(\nu_0-\nu_b\right) + \frac{\zeta_B\sigma\left(\nu_0,\nu\right)\phi}{2\left(1+\zeta_B\sigma\left(\nu_0,\nu\right)\phi\right)} * \left(\delta\left(\nu_0-\nu_b-\Delta_g+\Delta_e\right)+\delta\left(\nu_0-\nu_b+\Delta_g-\Delta_e\right)\right)\right]\mathrm{d}\nu \tag{F.18}$$

where "$*$" denotes the convolution product and δ stands for the Dirac distribution. Here the burning beam is assumed sufficiently weak and narrowband compared to the Zeeman splitting so it does not excites the two Zeeman transitions at once. Under the same assumptions as in E, the absorption coefficient is given by:

$$\alpha\left(\nu_p\right) = \int_\nu \sigma\left(\nu_p,\nu\right)\mathrm{d}\left[\Delta N\left(\nu\right)\right] \tag{F.19}$$

Let us now derive each term separately.

Hole behaviour

The hole corresponding to the first term centred on ν_b behaves exactly as if there was no magnetic field. Absorption around ν_b is:

$$\alpha\left(\nu_p\sim\nu_b\right) = \sigma_h N\frac{\Gamma_h}{\Gamma_{inh}}\left[1-\frac{\sqrt{1+\frac{\phi_b}{\phi_s}}-1}{\sqrt{1+\frac{\phi_b}{\phi_s}}}\frac{1}{1+\left(\frac{\nu_p-\nu_b}{\Gamma_{\mathrm{HB}}/2}\right)^2}\right] \tag{F.20}$$

where ϕ_s and Γ_{HB} are:

$$\phi_s = \frac{1}{\zeta_B\sigma_h} \tag{F.21}$$

$$\Gamma_{\mathrm{HB}} = \Gamma_h\left(1+\sqrt{1+\frac{\phi_b}{\phi_s}}\right) \tag{F.22}$$

Anti-holes behaviour

The two anti-holes behave identically. Let us focus on one of them.

$$\alpha\left(\nu_p\sim\nu_b-\Delta_g+\Delta_e\right) = \frac{2N}{\pi\Gamma_{inh}}\int_\nu \frac{\sigma_h}{1+\left(\frac{\nu_p-\nu}{\Gamma_h/2}\right)^2}\cdot\left(1+\frac{\zeta_B\frac{\sigma_h}{1+\left(\frac{\nu-\nu_b+\Delta_g-\Delta_e}{\Gamma_h/2}\right)^2}\phi_b}{2\left(1+\zeta_B\frac{\sigma_h}{1+\left(\frac{\nu-\nu_b+\Delta_g-\Delta_e}{\Gamma_h/2}\right)^2}\phi_b\right)}\right)\mathrm{d}\nu \tag{F.23}$$

Equation F.23 can be rewritten:

$$\alpha\left(\nu_p\sim\nu_b-\Delta_g+\Delta_e\right) = \sigma_h N\frac{\Gamma_h}{\Gamma_{inh}} + \frac{\sigma_h N}{\pi\Gamma_{inh}}\int_\nu \frac{1}{1+\left(\frac{\nu_p-\nu}{\Gamma_h/2}\right)^2}\cdot\frac{\zeta_B\sigma_h\phi_b}{1+\zeta_B\sigma_h\phi_b+\left(\frac{\nu-\nu_b+\Delta_g-\Delta_e}{\Gamma_h/2}\right)^2}\mathrm{d}\nu \tag{F.24}$$

The integral was already calculated in appendix E and is equal to:

$$\int_\nu \frac{1}{1+\left(\frac{\nu_p-\nu}{\Gamma_h/2}\right)^2}\cdot\frac{\zeta_B\sigma_h\phi_b}{1+\zeta_B\sigma_h\phi_b+\left(\frac{\nu-\nu_b+\Delta_g-\Delta_e}{\Gamma_h/2}\right)^2}\mathrm{d}\nu=\frac{\pi\Gamma_h}{2}\cdot\frac{\sqrt{1+\frac{\phi_b}{\phi_s}}-1}{\sqrt{1+\frac{\phi_b}{\phi_s}}}\cdot\frac{1}{1+\left(\frac{\nu_p-\nu_b+\Delta_g-\Delta_e}{\Gamma_{\mathrm{HB}}/2}\right)^2} \quad \text{(F.25)}$$

So that it comes for the anti-holes:

$$\alpha\left(\nu_p\sim\nu_b\pm\Delta_g\mp\Delta_e\right)=\sigma_h N\frac{\Gamma_h}{\Gamma_{inh}}\left[1+\frac{\sqrt{1+\frac{\phi_b}{\phi_s}}-1}{2\sqrt{1+\frac{\phi_b}{\phi_s}}}\frac{1}{1+\left(\frac{\nu_p-\nu_b\mp\Delta_g\pm\Delta_e}{\Gamma_{\mathrm{HB}}/2}\right)^2}\right] \quad \text{(F.26)}$$

Absorption profile

The hole is twice as high as the anti-holes and the respective behaviours are the same as expected due to conservation of the number of atoms. The main difference from the no-magnetic-field case is that the saturation number of photons per unit of time and surface is now much smaller – at least one order of magnitude. The total absorption profile is given as follows:

$$\begin{aligned}\alpha\left(\nu_p\right)=\sigma_h N\frac{\Gamma_h}{\Gamma_{inh}}\Bigg[1+\\ \frac{\sqrt{1+\frac{\phi_b}{\phi_s}}-1}{\sqrt{1+\frac{\phi_b}{\phi_s}}}\left(\frac{1}{2}\frac{1}{1+\left(\frac{\nu_p-\nu_b+\Delta_g-\Delta_e}{\Gamma_{\mathrm{HB}}/2}\right)^2}-\frac{1}{1+\left(\frac{\nu_p-\nu_b}{\Gamma_{\mathrm{HB}}/2}\right)^2}+\frac{1}{2}\frac{1}{1+\left(\frac{\nu_p-\nu_b-\Delta_g+\Delta_e}{\Gamma_{\mathrm{HB}}/2}\right)^2}\right)\Bigg]\end{aligned} \quad \text{(F.27)}$$

To derive this expression, it was assumed that both the laser and homogeneous linewidths were small compared to the Zeeman splitting. This assumption can be specified a little bit further here. The underlying hypothesis is that the burning beam should not move populations in both Zeeman ground states at the same time. Due to the homogeneous linewidth however, this may not be true, depending not only on the splitting as first assumed but also on the burning power. Indeed, when tuned on a transition, the burning beam also interacts with the others with a transition cross-section:

$$\sigma\left(\nu_b\pm\Delta_g\mp\Delta_e,\nu_b\right)=\frac{\sigma_h}{1+\left(\frac{\Delta_g-\Delta_e}{\Gamma_h/2}\right)^2} \quad \text{(F.28)}$$

This defines another characteristic number of photons and gives a condition on the burning power. The absorption profile expression derived here stands for ϕ_b that verifies:

$$\phi_b\ll\frac{1+\left(\frac{\Delta_g-\Delta_e}{\Gamma_h/2}\right)^2}{\sigma_h\zeta_B}=\left[1+\left(\frac{\Delta_g-\Delta_e}{\Gamma_h/2}\right)^2\right]\phi_s \quad \text{(F.29)}$$

This can be also interpreted as a condition on the hole width that must remain small enough so that there are no significant overlap between the hole and anti-holes. For high burning powers (resp. low splitting) the model must be rewritten while considering the optical pumping of the two optical transitions at the same time.

F.2.4 Comparison with the no-magnetic-field case

In order to compare the two behaviours, the absorption profile derived here was computed at 793 nm. In order to have parameters similar to the experimental ones, the magnetic field was taken equal to 84 G. The splitting $\delta_g - \delta_e$ was taken equal to 23 kHz.G^{-1}. The decay rate κ was taken equal to 1 s^{-1}, the decay rate γ equal to 100 s^{-1} and the decay rate β equal to 2500 s^{-1}. The homogeneous cross section was taken equal to 10^{-13} cm^2 and the homogeneous linewidth equal to 44 kHz. Given these different values, it comes that the interaction between the burning beam and the other Zeeman level can be neglected if the burning irradiance verifies $\Phi_b \ll 80$ mW $\cdot$ cm^{-2}. In order to ensure that this condition was verified, absorption profiles were plotted with and without magnetic field for a burning irradiance of 800 µW $\cdot$ cm^{-2}. The inhomogeneous linewidth was taken equal to 36 GHz and the ions density of the order of 10^{-20} cm^{-3}. The computed absorption profiles are plotted on figure F.4(a) and the corresponding transmission for a crystal thickness of 0.2 cm is plotted on figure F.4(b). Here the effect of the laser linewidth was not taken into account.

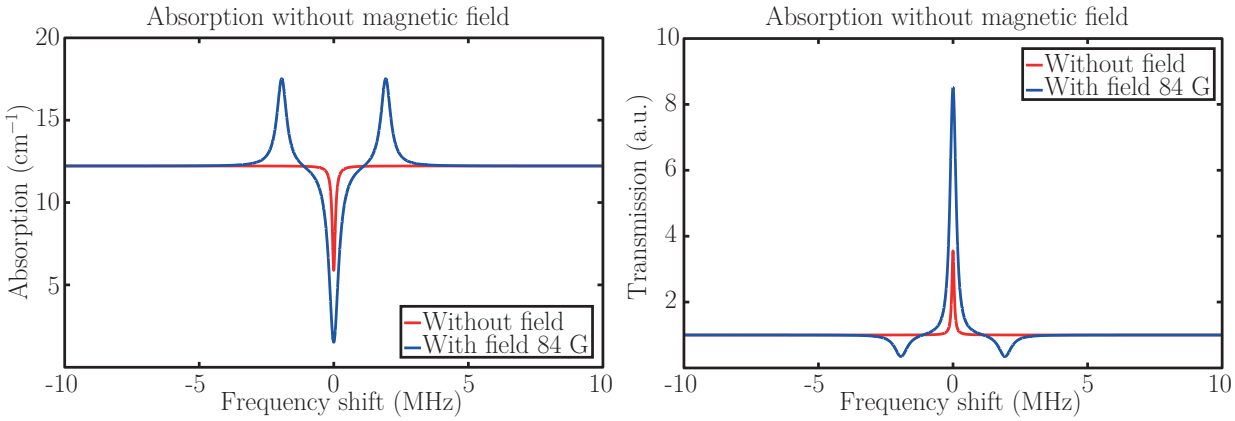

(a) Absorption profiles (b) Crystal transmission

Figure F.4 – (a) Absorption profile with and without magnetic field at 800 µW $\cdot$ cm^{-2} burning irradiance. (b) Crystal transmission at 800 µW $\cdot$ cm^{-2} burning irradiance. The crystal thickness was taken equal to 0.2 cm.

The behaviour of the main hole depth (in terms of absorption coefficient) and width were compared for burning irradiance ranging from 0 to 8 mW $\cdot$ cm^{-2} in order to remain in the model hypotheses. Results are plotted on figure F.5. As expected, holes are easier to burn in the presence of an external magnetic field. It can be noticed that holes are also expected to be broader in this case.

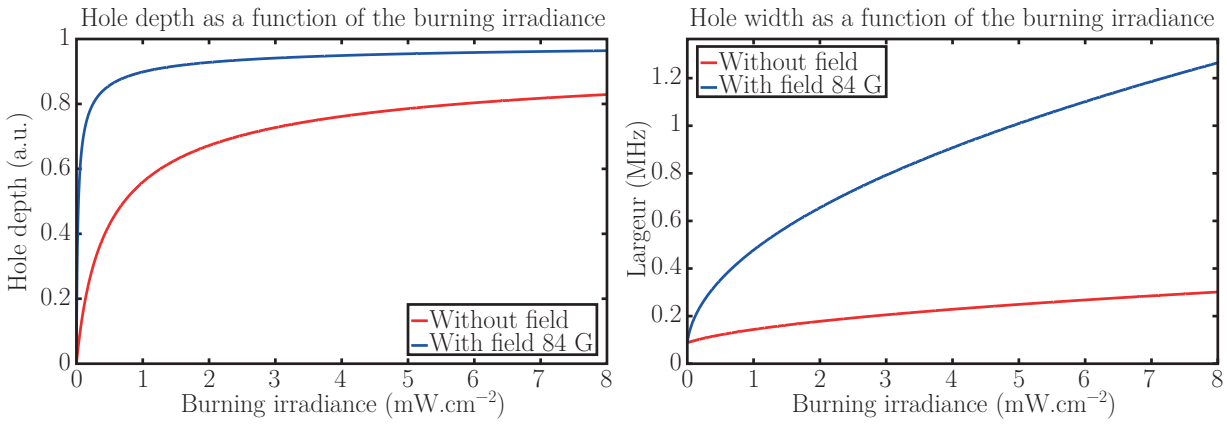

(a) Hole depth (b) Hole width

Figure F.5 – (a) Hole depth (in terms of absorption coefficient) as a function of the burning irradiance with and without magnetic field. (b) Hole width (in terms of absorption coefficient) as a function of the burning irradiance with and without magnetic field.

F.2.5 Dynamics of hole erasure

Beside deeper holes, the main advantage of introducing an external magnetic field is the much slower hole erasure. Let us consider the system after the burning beam has been shut off.

$$\begin{cases} \dfrac{\mathrm{d}N_1}{\mathrm{d}t} &= -\kappa N_1 + \kappa N_2 + wN_3 + \frac{\gamma}{2}N_5 \\ \dfrac{\mathrm{d}N_2}{\mathrm{d}t} &= \kappa N_1 - \kappa N_2 + \frac{\gamma}{2}N_5 \\ \dfrac{\mathrm{d}N_3}{\mathrm{d}t} &= -\left(w+\beta\right)N_3 \\ N_4 &= 0 \\ \dfrac{\mathrm{d}N_5}{\mathrm{d}t} &= \beta N_3 - \gamma N_5 \end{cases} \tag{F.30}$$

The evolution of N_3 and N_5 can be derived the same way as in appendix E.

$$\begin{cases} N_3\left(t\right) &= N_3\left(0\right)e^{-(w+\beta)t} \\ N_5\left(t\right) &= \left(N_5\left(0\right) + \frac{\beta}{w+\beta-\gamma}N_3\left(0\right)\right)e^{-\gamma t} - \frac{\beta}{w+\beta-\gamma}N_3\left(0\right)e^{-(w+\beta)t} \end{cases} \tag{F.31}$$

The population difference $N_1 - N_3$ thus obeys the following equation:

$$\frac{\mathrm{d}\left(N_1-N_3\right)}{\mathrm{d}t} = -2\kappa\left(N_1-N_3\right) + \kappa N + \left(2w+\beta-3\kappa\right)N_3 + \left(\frac{\gamma}{2}-\kappa\right)N_5 \tag{F.32}$$

that can be rewritten:

$$\frac{\mathrm{d}\left(N_1-N_3\right)}{\mathrm{d}t} + 2\kappa\left(N_1-N_3\right) = \kappa N + C_1 e^{-(w+\beta)t} + C_2 e^{-\gamma t} \tag{F.33}$$

where:

$$\begin{cases} C_1 &= \left[2w+\beta-3\kappa-\frac{\left(\frac{\gamma}{2}-\kappa\right)\beta}{w+\beta-\gamma}\right] N_3\left(0\right) \\ C_2 &= \left(\frac{\gamma}{2}-\kappa\right)\left(N_5\left(0\right)+\frac{\beta}{w+\beta-\gamma}N_3\left(0\right)\right) \end{cases} \tag{F.34}$$

The solution can then be expressed as:

$$\left(N_1-N_3\right)\left(t\right)=\frac{N}{2}+C_0e^{-2\kappa t}-\frac{C_1}{w+\beta-2\kappa}e^{-(w+\beta)t}-\frac{C_2}{\gamma-2\kappa}e^{-\gamma t} \tag{F.35}$$

where

$$\begin{aligned} C_0 &= N_1\left(0\right)-N_3\left(0\right)-\frac{N}{2}+\frac{C_1}{w+\beta-2\kappa}+\frac{C_2}{\gamma-2\kappa} \\ &= \frac{N_1\left(0\right)}{2}-\frac{N_2\left(0\right)}{2}+\frac{w}{w+\beta-2\kappa}\frac{N_3\left(0\right)}{2} \end{aligned} \tag{F.36}$$

Given the expressions of the different populations derived in section F.2.1 under the assumption of an infinitely efficient burning, with $\beta \gg \gamma \gg \kappa$ and $\beta \gg w \gg \kappa$, it comes the following expression for the evolution of the difference of population of the transition:

$$\left(N_1-N_3\right)\left(t\right)=\frac{N}{2}\left[1-\left(1-\frac{2\kappa}{\gamma}-\frac{6\kappa}{\beta}\right)e^{-2\kappa t}-\left(\frac{2\kappa}{\gamma}+\frac{2\kappa}{\beta}\right)e^{-\gamma t}-\frac{4\kappa}{\beta}e^{-\beta t}\right] \tag{F.37}$$

The same approach can be used to derive the temporal evolution of the difference of population for the other class of ions contributing to the hole. The model being symmetrical, the difference of population at ν_b is:

$$\Delta N\left(\nu_b,t\right)=N\left[1-\left(1-\frac{2\kappa}{\gamma}-\frac{6\kappa}{\beta}\right)e^{-2\kappa t}-\left(\frac{2\kappa}{\gamma}+\frac{2\kappa}{\beta}\right)e^{-\gamma t}-\frac{4\kappa}{\beta}e^{-\beta t}\right] \tag{F.38}$$

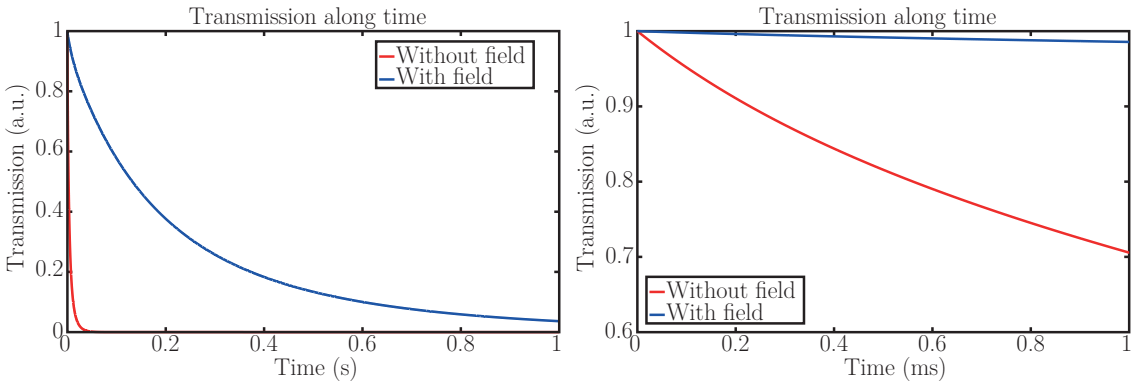

(a) Hole decay over 1 s

(b) Hole decay: zoom over 1 ms

Figure F.6 – (a) Decay of the hole maximum over 1 s. (b) Zoom over 1 ms. Without magnetic field, the crystal recovered about 30% of its original absorption and this amount is bigger as $\alpha_m L$ is increased.

As it was qualitatively guessed in section 7.2.1, the hole erasure now occurs in three stages. The first decay occurs over a time β^{-1} and corresponds to ions leaving the excited states $|e,+\rangle$ and $|e,-\rangle$. Unlike the zero-magnetic-field case, only $\frac{4\kappa}{\beta}N$ atoms left – instead of $\frac{\gamma}{\beta}N$. The second decay occurs over a characteristic time γ^{-1} corresponding to atoms leaving the metastable state. Here again, only $\left(\frac{2\kappa}{\gamma}+\frac{2\kappa}{\beta}\right)N$ returned back to the ground states where they were almost all re-

turned back in the absence of an external magnetic field. The rest of the ions returns back to $|g,+\rangle$ – respectively $|g,-\rangle$ – over a characteristic time $(2\kappa)^{-1}$ as they leave $|g,-\rangle$ – respectively $|g,+\rangle$. Using the same parameters as in F.2.4, the crystal transmission at hole maximum was computed for the two cases. Here the transmission was given by the hole depth:

$$\frac{\exp\left(-\sigma_h\left(\Delta N\left(\nu_b,t\right)-N\right)\frac{\Gamma_h}{\Gamma_{inh}}L\right)-1}{\exp\left(\sigma_h N\frac{\Gamma_h}{\Gamma_{inh}}L\right)-1} \tag{F.39}$$

so that it is equal to 1 when crystal is fully transparent and 0 when its absorption went back to normal. The decay of the hole maximum is plotted on figure F.6.

APPENDIX G

Scientific contributions

Papers

J.-B. Laudereau, E. Benoit à La Guillaume, V. Servois, P. Mariani, A. A. Grabar, M. Tanter, J.-L. Gennisson and F. Ramaz, "Multi-modal acousto-optic/ultrasound imaging of *ex vivo*liver tumors at 790 nm using a $Sn_2P_2S_6$ wavefront adaptive holographic setup", J. Biophoton. (2014)

K. Barjean, K. Contreras, **J.-B. Laudereau**, E. Tinet, D. Ettori, F. Ramaz, and J.-M. Tualle, "Fourier transform acousto-optic imaging with a custom-designed CMOS smart-pixels array", Opt. Lett., Vol. 40(5) pp. 705-708 (2015)

J.-B. Laudereau, A. A. Grabar, M. Tanter, J.-L. Gennisson and F. Ramaz, "Ultrafast acousto-optic imaging with ultrasonic plane waves", Opt. Express, Vol. 24(4) pp. 3774-3789 (2016)

Patent request

J.-B. Laudereau, M. Tanter, J.-L. Gennisson and F. Ramaz, "Imagerie acousto-optique ultra-rapide", Patent request PCT/FR 2015/051448 (2015)

Oral presentations

Underlined name stands for the speaker.

J.-B. Laudereau, E. Benoit à La Guillaume, V. Servois, P. Mariani, A. A. Grabar, M. Tanter, J.-L. Gennisson and F. Ramaz, "Multi-modal acousto-optic/echography imaging of *ex vivo* liver tumors at 800 nm by wavefront adaptive holography", Paper 8943-23, SPIE Photonics West 2014, San Francisco

J.-B. Laudereau, P. Goldner, A. Ferrier, A. Chauvet, T. Chanelière and F. Ramaz, "Imagerie acousto-optique par hole-burning spectral dans des cristaux de Tm^{3+}:YAG", SFO JIONC 2015, Paris

J.-B. Laudereau, "Imagerie acousto-optique : son et lumières pour voir à travers les tissus biologiques", SFP Rencontres des Jeunes Physicie(n)n(e)s 2015, Paris

C. Dupuy, **J.-B. Laudereau**, A. A. Grabar, M. Tanter, J.-L. Gennisson, F. Ramaz, "Imagerie acousto-optique ultrarapide par ondes planes ultrasonores", SFO JIONC 2016, Paris

J.-B. Laudereau, A. A. Grabar, M. Tanter, J.-L. Gennisson, F. Ramaz, "Imagerie acousto-optique ultrarapide par ondes planes ultrasonores", SFO Opt'Diag 2016, Paris

J.-B. Laudereau, A. Chauvet, A. Ferrier, Ph. Goldner, T. Chanelière, F. Ramaz, "Acousto-optic imaging using spectral holeburning in Tm^{3+}:YAG crystals", 19^{th} International Conference on Dynamical Processes in Excited States of Solids (DPC'16), Paris

Poster presentations

Underlined name stands for the speaker.

J.-B. Laudereau, E. Benoit à La Guillaume, V. Servois, P. Mariani, A. A. Grabar, M. Tanter, J.-L. Gennisson, F. Ramaz, "Multi-modal acousto-optic/ultrasound imaging of *ex vivo* liver tumors at 790 nm by wavefront adaptive holography", 2014 IEEE International Ultrasonics Symposium, Chicago

J.-B. Laudereau, E. Benoit à La Guillaume, V. Servois, P. Mariani, A. A. Grabar, M. Tanter, J.-L. Gennisson and F. Ramaz, "Couplage échographie/imagerie acousto-optique pour l'imagerie de tumeurs du foie *ex vivo*", SFO Opt'Diag 2014, Paris

J.-B. Laudereau, E. Benoit à La Guillaume, F. Devaux, U. Bortolozzo, A. A. Grabar, J.-P. Huignard, S. Residori and F. Ramaz, "Dynamic ultrasound modulated optical tomography by self-referenced photorefractive holography", Poster 9323-175, SPIE Photonics West 2015, San Francisco

APPENDIX H

Résumé (FR)

Les progrès récents dans le domaine de l'imagerie médicale ont permis d'améliorer fortement la qualité des images obtenues. En conséquence directe, les procédures cliniques deviennent de moins en moins invasives grâce à une meilleure compréhension des pathologies, un diagnostic toujours plus précoce et un ciblage plus précis des interventions. Il est apparu durant la dernière décennie que, si les techniques actuelles ont acquis une très bonne sensibilité (*i.e.* la capacité à détecter ou non la présence d'une pathologie), certaines d'entre elles parmi les plus utilisées, comme l'échographie ou les scanners, manquent cruellement de spécificité (*i.e.* la capacité à différencier une pathologie d'une autre). Dans cette dynamique, les développements récents s'attachent à pallier ce manque de deux manières. La première est l'imagerie dite moléculaire qui consiste à ajouter aux procédures d'imagerie conventionnelles des traceurs qui interagissent spécifiquement avec les pathologies ciblées afin d'en accroître le contraste. La deuxième est l'imagerie dite multi-modale qui consiste à associer plusieurs modalités d'imagerie, en général une technique très spécifique mais peu résolue avec une technique très bien résolue mais peu spécifique, de manière à extraire le meilleur de chacune. L'échographie est l'une des techniques d'imagerie les plus répandues dans les hôpitaux car elle est moins chère, plus compacte, mobile et permet de traiter un plus grand nombre de patients que la plupart des autres modalités. Il est donc naturel de constater qu'une des tendances de ces dernières années consiste à créer des plateformes d'imagerie qui couplent l'échographie à différentes modalités afin d'en augmenter la spécificité. Parmi les différentes possibilités, l'imagerie optique semble être une solution prometteuse car elle permet d'obtenir à la fois une information de nature chimique et une information structurelle sur les tissus biologiques. C'est dans cette dynamique que s'inscrit l'imagerie acousto-optique.

H.1 À la recherche du contraste optique dans les milieux biologiques

Avant de pousser plus loin l'étude de l'imagerie acousto-optique, il est important de s'intéresser aux difficultés de l'optique en tant que technique d'imagerie médicale. Il faut garder à l'esprit que de telles techniques doivent être non-invasives autant que faire se peut et imager sur des profondeurs de l'ordre de la taille d'un organe (plusieurs centimètres) avec une résolution compatible avec les objets à voir (en général quelques millimètres).

H.1.1 Imagerie optique des tissus biologiques

À l'heure actuelle, il y a principalement deux techniques optiques utilisées de manière routinière lors de procédures cliniques. La première est la microscopie qui consiste à imager la réflectivité ou l'absorption de tranches de tissus très fines avec une résolution donnée par la limite de diffraction (à savoir quelques micromètres). Parmi les applications de la microscopie, l'une des plus importantes est l'anatomopathologie, discipline dans laquelle le médecin détermine la nature des tissus et les limites d'objets à réséquer à l'aide de coupes histologiques. La deuxième technique est la spectroscopie qui consiste à déterminer la nature chimique ou la concentration d'une espèce via la manière dont elle absorbe la lumière. La technique la plus classique de spectroscopie utilisée en clinique est sans doute l'oxymétrie de pouls [12] qui mesure la saturation en oxygène dans un doigt ou une oreille. Il faut noter cependant qu'aucune de ces deux approches n'est compatible avec les exigences de l'imagerie médicale. Dans un cas, si la microscopie fournit des images à haute résolution, elle est malheureusement limitée à des profondeurs de l'ordre de quelques micromètres. Dans l'autre, si les techniques spectroscopiques fonctionnent sur des volumes bien plus importants, elles se contentent en général de fournir simplement la valeur d'un paramètre intégré sur tout ce volume.

Les premières techniques optiques d'imagerie médicale ont été suggérées au début des années 30 [9] et utilisées cliniquement dans les années 80 [8] principalement dans le but d'éviter le recours à des techniques plus invasives ou ionisantes comme les rayons X. Ces techniques fonctionnaient de la manière la plus simple et immédiate pour imager un objet : l'organe (le sein en l'occurrence) était éclairé par derrière à l'aide d'une puissante source de lumière blanche ou dans le proche infrarouge et la lumière transmise était enregistrée sur une plaque photosensible. Si une telle technique présentait l'avantage évident d'être très facile à mettre en place, il a été montré rapidement que les images qu'elle fournissait n'étaient pas significatives [10] et les médecins sont retournés à l'utilisation de la mammographie, pourtant ionisante.

La principale difficulté que rencontrent toutes ces techniques optiques trouve son origine dans le phénomène de diffusion de la lumière. Lorsqu'elle se propage dans un milieu, la lumière interagit avec les différentes espèces qu'elle rencontre. À cette occasion, elle peut être soit absorbée – ce qui renseigne sur la nature chimique de l'espèce – soit diffusée – ce qui renseigne en général sur la structure locale. Dans le cas des tissus biologiques, il s'avère que les coefficients de diffusion typiques dans le proche infrarouge sont environ un ordre de grandeur supérieurs aux coefficients d'absorption [20, Chapitre 2]. Il en découle qu'au delà d'une distance caractéristique de quelques millimètres qu'on appelle le libre parcours moyen de transport, la lumière est multiplement diffusée et l'information qu'elle contient est complètement aléatoire et impossible à interpréter au sens de l'optique géométrique. La conséquence directe est que la résolution des techniques travaillant sur la lumière fortement diffusée est limitée au cinquième de l'épaisseur de tissus traversée [11]. C'est ce qui explique que la microscopie qui a une résolution optique soit limitée à des échantillons très fins et que les techniques spectroscopiques qui sondent des volumes plus importants ne soient pas résolues. Dans le cas de l'imagerie du sein, l'inefficacité des techniques optiques vient du fait que les tumeurs précoces de quelques millimètres de diamètre ne sont pas détectées.

Par ailleurs, il s'avère que la lumière infrarouge est fortement absorbée par l'eau tandis que la lumière visible est absorbée par les différents autres chromophores comme le sang [14]. Lorsque la contribution de toutes ces espèces est prise en compte, il apparaît une fenêtre spectrale étroite dans le proche infrarouge entre 650 et 1300 nm dans laquelle les tissus biologiques sont peu absorbants (quelques cm^{-1} [20, Chapter 2]). Cette fenêtre s'appelle la fenêtre thérapeutique optique et c'est dans cette région qu'il est préférable de se placer afin de pénétrer en profondeur dans les tissus.

H.1.2 Des milieux fortement diffusants à l'imagerie acousto-optique

Les régimes de propagation

Comme expliqué ci-dessus, le principal obstacle à l'imagerie optique en profondeur dans les tissus biologiques est la diffusion de la lumière qui brouille l'information après seulement quelques millimètres. Dans un milieu diffusant, il existe plusieurs distances caractéristiques qui définissent autant de régimes de propagation. Dans le cas idéal d'un milieu homogène et non-diffusant, l'atténuation d'un faisceau lumineux est seulement due à l'absorption par le milieu et obéit à une simple loi de Beer-Lambert. L'absorption est alors définie par le libre parcours moyen d'absorption l_a qui est la distance moyenne que parcourt un photon avant de subir un événement d'absorption. Le libre parcours moyen d'absorption est relié au plus classique coefficient d'absorption μ_a qu'il est plus habituel de manipuler via $\mu_\mathrm{a} = 1/l_a$.

Lorsque le milieu devient diffusant, l'atténuation d'un faisceau obéit à une équation de Beer-Lambert généralisée qui prend en compte le fait que l'énergie ne se propage plus nécessairement dans la direction du faisceau incident. La diffusion est alors caractérisée par le libre parcours moyen de diffusion l_s qui est la distance moyenne qu'un photon parcourt avant de subir un événement de diffusion. Lorsque la diffusion est isotrope, c'est-à-dire que la probabilité que le photon diffusé soit ré-émis dans une direction donnée est indépendante de cette direction, un seul événement de diffusion suffit à brouiller l'information et la lumière perd la mémoire de son histoire passée après une distance de l'ordre de l_s. Dans la pratique, la diffusion n'est pas isotrope et les photons diffusés sont majoritairement ré-émis vers l'avant. L'information se conserve alors sur plusieurs événements de diffusion et on définit le libre parcours moyen de transport l^* qui quantifie la distance moyenne qu'un photon peut parcourir avant que l'information qu'il contient soit aléatoire.

Ces distances caractéristiques définissent ainsi différents régimes de propagation selon la profondeur que l'on va sonder. Pour des profondeurs inférieures au libre parcours moyen de diffusion, la lumière se propage de manière dite balistique. Les photons n'ont pas encore eu le temps de subir un événement de diffusion et se propagent en ligne droite. Lorsque la profondeur sondée devient de l'ordre du libre parcours moyen de diffusion, la lumière est en régime de diffusion simple. Il y a alors coexistence entre photons balistiques – qui n'ont subi aucun événement de diffusion – et photons simplement diffusés – qui n'ont subi qu'un seul événement de diffusion. C'est dans ces deux régimes que travaillent les techniques d'imagerie basées sur l'optique géométrique.

A delà du libre parcours moyen de diffusion, il n'est plus possible de négliger les événements de diffusion multiples – c'est-à-dire que les photons subissent en moyenne plusieurs événements de diffusion. C'est le régime de diffusion multiple. À partir de ce point, les photons balistiques et simplement diffusés – qui contiennent de l'information interprétable – s'atténuent exponentiellement au profit des photons multiplement diffusés dont l'information est de plus en plus aléatoire. Jusqu'à des profondeurs de l'ordre du libre parcours moyen de transport, il y a coexistence entre les trois types de photons. Lorsque les profondeurs sondées sont grandes devant le libre parcours moyen de transport, il n'y a plus que des photons multiplement diffusés dont l'information est aléatoire. L'intensité lumineuse obéit alors, en première approximation, à une équation de diffusion et peut être considérée comme isotrope.

Face à des milieux diffusant, il y a donc deux manières de faire de l'imagerie. La première consiste à travailler avec les photons balistiques et simplement diffusés. La résolution est alors théoriquement définie par la diffraction et la principale limitation vient du ratio entre le nombre de ces photons et de ceux multiplement diffusés. De nombreuses approches ont été explorées dans ce régime, comme l'OCT [34,35], et le principal enjeu est alors de rejeter le maximum de photons issus de la diffusion multiple. La profondeur d'imagerie de ces techniques est donnée par le ratio

entre diffusion simple et diffusion multiple et peut atteindre dans les meilleurs des cas un ou deux libres parcours moyens de transport.

Parce qu'ils sont beaucoup plus abondants, il peut être commode de travailler avec les photons issus de la diffusion multiple. Dans ce cas, les profondeurs atteignables peuvent être supérieures d'un ordre de grandeur environ mais la résolution est alors limitée par la profondeur. L'enjeu de telles techniques est de conserver une résolution compatible avec les objets à imager et le problème devient alors un problème de super-résolution. Parmi ces techniques, la plus étudiée est la DOT [41] qui consiste à résoudre numériquement un problème de diffusion inverse. La difficulté réside alors dans le fait que le problème soit intrinsèquement mal posé de telle sorte que la reconstruction d'images est complexe et demande du temps et des ressources informatiques importantes.

L'imagerie acousto-optique

Afin de contourner la difficulté posée par le problème inverse rencontré en DOT, des approches multi-ondes ont été envisagées. Les plus remarquables sont les techniques, au nombre de deux, couplant lumière et ultrasons. Ces deux techniques sont la photoacoustique, qui ne sera pas décrite ici, et l'imagerie acousto-optique. Le principe général de ces techniques est d'utiliser les ultrasons, qui se propagent de manière balistique sur des profondeurs de l'ordre de la dizaine de centimètres, afin de localiser la provenance de l'information optique qui a été perdue suite à la diffusion multiple.

Lorsque les ultrasons se propagent dans une zone illuminée, ces derniers modulent la position des diffuseurs et l'indice de réfraction des tissus. Par effet acousto-optique, cette modulation génère des bandes latérales dans le spectre de la lumière diffuse. Les photons contenus dans ces bandes latérales, appelés *photons marqués*, ont deux propriétés fondamentales mais essentielles pour l'imagerie acousto-optique.

- Les photons marqués ne peuvent provenir que d'une région où il y a à la fois lumière et ultrasons. Le volume occupé par les ultrasons fait donc office de source virtuelle de photons marqués dont la position dans le milieu diffusant est parfaitement connue.

- L'intensité des photons marqués est proportionnelle à l'intensité lumineuse locale intégrée sur le volume occupé par les ultrasons.

En exprimant la modulation de la position des diffuseurs [61, 77] et celle de l'indice de réfraction [78], il est possible de montrer que la modulation acoustique peut s'interpréter comme une modulation globale des chemins optiques empruntés par la lumière dans le milieu diffusant. Une approche de type marche aléatoire fait alors facilement apparaître la présence de bandes latérales dans le champ électrique qui s'écrit :

$$\mathcal{E}_S\left(\mathbf{r}', t\right) = E_0 e^{i\omega_0 t} \sum_m \mathcal{S}_m\left(\mathbf{r}'\right) \exp\left(im\omega_{US} t\right) \tag{H.1}$$

où $\mathcal{S}_m\left(\mathbf{r}'\right)$ représente une figure de tavelure, c'est-à-dire une figure d'interférence aléatoire – dans la suite j'utiliserai son nom anglophone *speckle*, plus usuel. ω_0 et ω_{US} sont respectivement les pulsations de la lumière et des ultrasons. Il est possible de montrer que l'énergie associée aux termes $\mathcal{S}_m\left(\mathbf{r}'\right)$ décroît vite avec m de telle sorte qu'on ne conserve en général que les termes $m = 0$ correspondant aux *photons non-marqués* et $m = \pm 1$ qui contiennent les photons marqués à $\pm\omega_{US}$. Une propriété importante du champ est que la figure de speckle des photons non-marqués et celle des photons marqués sont *a priori* spatialement décorrélées.

Dans ce cas, la puissance des photons marqués en sortie de milieu diffusant peut s'écrire approximativement dans le cas d'un faible taux de modulation et d'une onde plane propagative [77] :

$$\Psi_T(\mathbf{r}') = \beta\Psi_0 \int \Omega(\mathbf{r},\mathbf{r}')\,\Phi(\mathbf{r})\,P_0(\mathbf{r})^2\,\mathrm{d}\mathbf{r} \tag{H.2}$$

où β est un coefficient de proportionnalité qui assure l'homogénéité, Ψ_0 est la puissance lumineuse en entrée de milieu diffusant, $\Omega(\mathbf{r},\mathbf{r}')$ est la probabilité qu'un photon marqué en $\mathbf{r}$ atteigne le détecteur en $\mathbf{r}'$, $\Phi(\mathbf{r})$ est l'intensité lumineuse dans le milieu diffusant et $P_0(\mathbf{r})$ est l'amplitude de l'onde de pression. Ici, l'intégration traduit simplement le fait que le détecteur compte indifféremment les photons marqués quelle que soit leur origine au sein du volume occupé par les ultrasons. Il vient alors naturellement que la puissance de la lumière marquée est proportionnelle à l'intensité lumineuse locale dans le milieu diffusant intégrée sur le volume occupé par l'onde ultrasonore. Cette expression fait apparaître par ailleurs un terme supplémentaire $\Omega(\mathbf{r},\mathbf{r}')$ qui dépend de la position de la source et du détecteur. En pratique, l'imagerie acousto-optique n'est pas sensible à la répartition de l'intensité lumineuse brute $\Phi(\mathbf{r})$, mais à la quantité de photons qui atteignent le détecteur $\Omega(\mathbf{r},\mathbf{r}')\,\Phi(\mathbf{r})$. Dans la suite, je considérerai que la source et le détecteur sont à des positions fixées et définissent ainsi la forme de la tache de lumière. Dans ce cas, j'abandonnerai la dépendance en $\mathbf{r}'$ et le problème se résumera à retrouver l'image acousto-optique $I(\mathbf{r}) = \Omega(\mathbf{r})\,\Phi(\mathbf{r})$.

H.2 Vers l'imagerie acousto-optique clinique ?

A la suite du modèle développé dans la partie précédente, il apparaît assez naturellement qu'il est possible de reconstruire la répartition de la lumière diffuse dans l'échantillon à l'aide d'une méthode capable de filtrer et compter les photons marqués ou, ce qui est équivalent, de mesurer le taux de modulation de la lumière diffuse – je passerai indifféremment d'une interprétation à l'autre dans la suite.

Il s'avère que la mesure de cette modulation est complexe pour plusieurs raisons :

- la quantité de photons marqués est très faible – moins de 1 pour 1000 – de telle sorte que les techniques de filtrages doivent être très efficaces.

- le décalage en fréquence est petit – quelques MHz – comparé à la fréquence de la lumière – 10^{14} ou 10^{15} Hz. En termes de longueur d'ondes, cela correspond à un décalage de $\sim 10^{-6}$ nm à 800 nm, bien trop étroit pour la plupart des techniques de filtrage classiques.

- compte-tenu des deux précédents points, les techniques les plus immédiates sont des techniques interférométriques avec une référence plane. Cependant, à cause du caractère aléatoire de la lumière diffuse, la modulation acousto-optique s'additionne de manière incohérente dès que l'on somme plusieurs grains de speckle et le rapport signal-à-bruit de ces approches est limité à celui d'un seul d'entre eux, quelle que soit la surface du détecteur – ce qui n'est pas avantageux compte-tenu de la très faible étendue optique d'un seul grain.

- dans le cas de l'imagerie *in vivo*, il apparaît que le speckle se décorrèle avec les mouvements du milieu sur des temps caractéristiques inférieurs à la milliseconde [29]. Il convient donc de s'assurer que la bande passante du phénomène responsable du filtrage soit suffisamment large pour suivre ces changements.

H.2.1 Détection des photons marqués et résolution

Les techniques de détection des photons marqués peuvent être divisées en trois catégories. Les deux premières constituent les techniques dites *cohérentes* car elles travaillent avec le champ diffusé et sont donc sensibles à la décorrélation du speckle *in vivo*. La première catégorie se base sur des matrices de pixels capables de traiter en parallèle chaque grain de speckle indépendamment des autres. Comparées à des techniques interférométriques classiques, ces approches augmentent en général le rapport signal-à-bruit proportionnellement à la racine carrée du nombre de pixels utilisés – soit en général 10^6 pixels. On compte notamment parmi elles des techniques caméras comme l'holographie numérique [92] ou le contraste de speckle [86, 87] ainsi que des approches basées sur des capteurs CMOS intelligents associés à une détection synchrone capable de démoduler directement la lumière diffuse pixel par pixel [83–85].

La deuxième catégorie de techniques, toujours parmi les techniques cohérentes, est basée sur l'interférométrie adaptative – ou holographie temps réel. Puisque le rapport signal-à-bruit des techniques interférométriques classiques avec une référence plane est limité par le front d'onde aléatoire de la lumière diffuse, le principe de ces techniques consiste à déformer en temps réel le front d'onde de la référence afin de l'adapter à celui de la lumière diffuse. Ce faisant, la modulation acousto-optique peut se sommer de manière spatialement cohérente en tout point d'un mono-détecteur de grande surface et le rapport signal-à-bruit croît comme la racine carrée du nombre de grains de speckle qui ont été adaptés – en général 10^8 grains de speckle pour une surface active de 1 cm^2. Les approches holographiques utilisées classiquement pour ce genre de détection sont le mélange à deux ondes dans les milieux photoréfractifs [97, 98], les milieux à gain [103] ou les valves optiques [101]. Il est aussi possible de trouver certaines approches basées sur le mélange à quatre ondes – ou conjugaison de phase – qui permet de corriger les aberrations apportées par le milieu diffusant en générant le champ conjugué se propageant en sens inverse. Les milieux qui ont été utilisés dans ce cas sont plutôt des milieux à gain [104] ou photoréfractifs [74, 105].

Dans le cas des techniques de détection cohérentes, il est important de garder à l'esprit qu'elles sont gouvernées par deux temps caractéristiques qui doivent être distingués clairement. Le premier temps caractéristique ici est le temps de réponse de la détection, c'est-à-dire le temps d'établissement du phénomène physique responsable du filtrage – ou de la mesure de modulation. Ce temps caractéristique va quantifier la capacité qu'a cette technique à suivre des changements qui s'opèrent dans le speckle et à mesurer un signal acousto-optique correct en milieu vivant. Une technique de détection cohérente robuste doit donc avoir un temps de réponse inférieur au temps de décorrélation du speckle *in vivo*. L'autre temps caractéristique à prendre en compte est le temps d'imagerie de la technique, intrinsèquement limité par la durée et le nombre des tirs ultrasonores nécessaires à la formation d'une image. Ce temps caractéristique quantifie plutôt la capacité de la méthode de détection à obtenir des images en temps réel.

Par exemple, les techniques multiplexées de la première catégorie sont potentiellement robustes face à la décorrélation du speckle car le temps d'exposition du détecteur peut être inférieur au temps de décorrélation. Il est ainsi possible d'acquérir du signal acousto-optique malgré les mouvements. En revanche, la plupart des caméras actuelles facilement accessibles ont des cadences vidéo qui ne permettent pas de suivre la propagation des ultrasons. Il est donc nécessaire d'utiliser des approches stroboscopiques dans lesquelles il convient d'associer un tir ultrasonore à chaque pixel de l'image finale, ce qui conduit à des cadences d'imagerie trop faibles pour être compatibles avec le temps réel. A l'inverse, les approches holographiques peuvent être utilisées avec des mono-détecteurs de grande surface dont la bande passante est souvent suffisante pour suivre la propagation des ultrasons avec une résolution inférieure au millimètre. Ces techniques peuvent

donc être facilement couplées à des impulsions et les cadences d'imagerie théoriques sont, dans ce cas, celles de l'échographie standard. Cependant, les phénomènes physiques responsables de l'adaptation de front d'onde sont des processus qui s'établissent avec un certain temps caractéristique, supérieur à plusieurs millisecondes pour les cristaux photoréfractifs par exemple. Dans les cas où le milieu se décorrèle trop rapidement, l'adaptation de front d'onde se fait mal et il est difficile d'acquérir du signal acousto-optique.

La troisième et dernière catégorie de techniques est constituée de filtres spectraux ultrafins et regroupe les techniques de détection dites *incohérentes*. Ces approches ont été suggérées afin d'obtenir des détecteurs disposant à la fois de la robustesse à la décorrélation du speckle et de la bande passante des mono-détecteurs. Ces méthodes consistent à générer des filtres spectraux dont la largeur est suffisamment fine pour distinguer les photons non-marqués des photons marqués. Ces techniques permettent ainsi de mesurer directement la puissance des photons marqués et sont par essence insensibles à la décorrélation du champ mais demandent souvent une instrumentation plus lourde que les techniques cohérentes. On trouve deux approches dans cette catégorie : le filtrage à l'aide de cavités Fabry-Perot confocales stabilisées [107,156] et le filtrage par creusement spectral dans des cristaux dopés avec des terres rares [108].

De la méthode de détection choisie et de sa sensibilité dépend souvent le choix de la séquence ultrasonore. Comme expliqué plus haut, la résolution de l'imagerie acousto-optique est donnée par le volume occupé par les ultrasons. Il y a donc de nombreuses manières de jouer sur les séquences afin de reconstruire une image acousto-optique. Les premières méthodes de détections, assez peu sensibles, nécessitaient l'utilisation de transducteurs mono-élément et d'ultrasons continus afin de marquer une grande quantité de photons [64, 82]. Dans ce cas, la résolution dans la direction des ultrasons est égale à la taille de l'échantillon et il fallait faire tourner le transducteur autour de l'échantillon afin de reconstruire les images par tomographie [109]. Avec l'utilisation des cristaux photoréfractifs et l'amélioration de la sensibilité, il a été possible de changer les ultrasons continus pour des impulsions de quelques cycles dont le déplacement à travers l'échantillon peut être suivi en temps réel. Ces approches ont permis une augmentation de la cadence d'imagerie : il suffisait alors d'un tir seulement pour obtenir une ligne de l'image et d'un balayage horizontal du transducteur pour reconstruire l'image [110]. Dans ce cas, la résolution dans la direction des ultrasons est donnée par le nombre de cycles mais s'obtient au détriment de la quantité de signal. D'autres approches plus astucieuses ont été mises au point afin d'augmenter la quantité de photons marqués en augmentant le temps d'exposition du détecteur ou la longueur des impulsions ultrasonores tout en conservant la résolution longitudinale. Les deux plus remarquables sont la tomographie acousto-optique cohérente par bascules de phase aléatoires [111] et l'imagerie acousto-optique par transformée de Fourier [83].

H.2.2 Imagerie bi-modale couplant acousto-optique et échographie

Parce qu'elles nécessitent peu d'instrumentation et utilisent des mono-détecteurs capables de suivre la propagation d'une impulsion ultrasonore, les techniques de détection par holographie photoréfractive ont naturellement été envisagées afin de coupler l'imagerie acousto-optique à l'échographie standard. La première plateforme de ce genre a été rapportée par E. Bossy *et al.* [116]. Le principal inconvénient de cette plateforme réside dans le choix du cristal photoréfractif (BSO) fonctionnant autour de 532 nm, en dehors de la fenêtre thérapeutique optique. Au cours de sa thèse à l'Institut Langevin, S. Farahi [118] a étudié plusieurs cristaux fonctionnant autour de 800 nm afin de se placer dans une région spectrale dans laquelle les tissus sont moins absorbants. A l'issue de ces travaux, E. Benoit et S. Farahi ont mis au point une plateforme d'imagerie bimodale basée sur

des cristaux de SPS dopés avec des ions tellure, bien plus appropriés. Dans cette partie, je vais décrire plus en détail le fonctionnement de cette plateforme et montrer les premiers résultats *ex vivo* obtenus au début de ma thèse.

Principe de la détection photoréfractive

Avant de décrire un peu plus en détails le principe de la plateforme d'imagerie, il est intéressant de comprendre comment fonctionne l'effet photoréfractif et comment il peut servir à détecter des photons marqués.

Un cristal photoréfractif est un cristal qui est à la fois photoconducteur et électro-optique. En présence d'une illumination inhomogène, par exemple une figure d'interférence entre deux faisceaux, des porteurs de charge sont excités dans les régions de forte intensité, vers la bande de conduction pour les électrons, ou la bande de valence pour les lacunes. Une fois dans une de ces bandes, les porteurs peuvent diffuser dans le volume et se recombiner ailleurs dans le cristal [188]. Au bout d'un temps caractéristique qu'on appelle le temps de réponse photoréfractif et qu'on note τ_{PR}, un régime stationnaire s'établit dans lequel il y a accumulation de porteurs dans les régions de faible intensité lumineuse. Cette répartition inhomogène de charges induite par la lumière crée des champs électriques locaux qui modulent spatialement l'indice de réfraction du cristal par effet Pockels. Les deux faisceaux qui ont servi à créer le réseau d'indice peuvent diffracter dessus et donner lieu à un phénomène appelé le mélange à deux ondes. Il s'opère alors une adaptation des fronts d'onde des deux faisceaux de telle sorte qu'ils interfèrent de manière cohérente sur toute la surface adaptée. Selon l'orientation du cristal, il est possible de contrôler si les interférences dans une direction sont constructives ou destructives, de telle sorte que le phénomène de mélange à deux ondes s'accompagne aussi d'un transfert d'énergie d'un des faisceaux vers l'autre. Ce transfert d'énergie est quantifié par un gain qu'on appelle le gain photoréfractif défini par :

$$\Phi_S(L) = \Phi_S(0) \exp\left[(\gamma_{\mathrm{PR}} - \alpha) L\right] \tag{H.3}$$

où $\Phi_S(L)$ est la puissance lumineuse dans la direction du faisceau signal après le cristal d'épaisseur L, $\Phi_S(0)$ est la puissance avant le cristal, γ_{PR} est le gain photoréfractif et α est le coefficient d'absorption du cristal [187].

Dans le cas de l'imagerie acousto-optique, la lumière diffuse interfère avec une référence plane dont la fréquence est celle des photons *non-marqués* sur un cristal de SPS :Te. En quelques millisecondes, l'hologramme des photons non-marqués est inscrit dans le cristal et après le cristal, la référence et les photons non-marqués sont adaptés. Dans notre cas, le cristal que nous utilisons est dans une configuration dite de gain négatif, ce qui signifie que l'interférence entre la référence et les photons non-marqués est destructive après le cristal – ce qui se traduit par un gain négatif. En l'absence d'ultrasons, le mélange à deux ondes atténue le fond des photons non-marqués et est responsable d'un signal DC sur la photodiode. Lorsque les ultrasons se propagent dans l'échantillon, ils génèrent des photons marqués qui ne subissent plus le mélange à deux ondes et ne sont pas adaptés avec la référence. Les photons marqués n'interfèrent pas et ne sont pas atténués de telle sorte que le signal sur la photodiode augmente. En récupérant la partie AC du signal, il est donc possible de mesurer le signal des photons marqués. Dans le cas d'une détection photoréfractive, le bruit de la mesure est limité au bruit de grenaille des photons non-marqués, dans le cas idéal. En pratique, une partie de la référence diffuse sur les impuretés du cristal et subit le mélange à deux ondes avec la référence non diffusée. Ce phénomène de mélange à deux ondes entre la référence et elle-même est appelé *coma photoréfractive* et crée un fond de lumière diffuse qui domine très largement le bruit de la mesure.

La plateforme d'imagerie

Grâce à l'utilisation de mono-détecteurs, la détection photoréfractive permet de résoudre temporellement la propagation d'une impulsion ultrasonore à travers le milieu biologique. Cette propriété en fait une technique idéale pour coupler l'imagerie acousto-optique avec de l'échographie standard basée sur un balayage linéaire d'impulsions focalisées.

Ce montage d'imagerie acousto-optique a donc été couplé à un échographe commercial (Aixplorer, Supersonic Imagine, Aix-en-Provence) selon le schéma de la figure H.1. L'échographe pilote une sonde de fréquence centrale 8 MHz (SL15-4, Supersonic Imagine, 256 éléments, 0.2 mm de pitch) permettant d'obtenir à la fois des images échographiques standard et des images acousto-optiques. La partie lumineuse est apportée par une diode laser amplifiée par une amplificateur 2 W selon un principe MOPA (Sacher Laser Technik GmbH). Le faisceau est séparé en deux bras, un bras signal guidé jusqu'à l'échantillon et un bras référence guidé jusqu'au cristal. En sortie d'échantillon, le faisceau signal est collecté par des lentilles de forte ouverture numérique et guidé jusqu'au cristal photoréfractif pour filtrage. La lumière est ensuite mesurée sur une photodiode de grande surface et la composante AC est filtrée et amplifiée électroniquement.

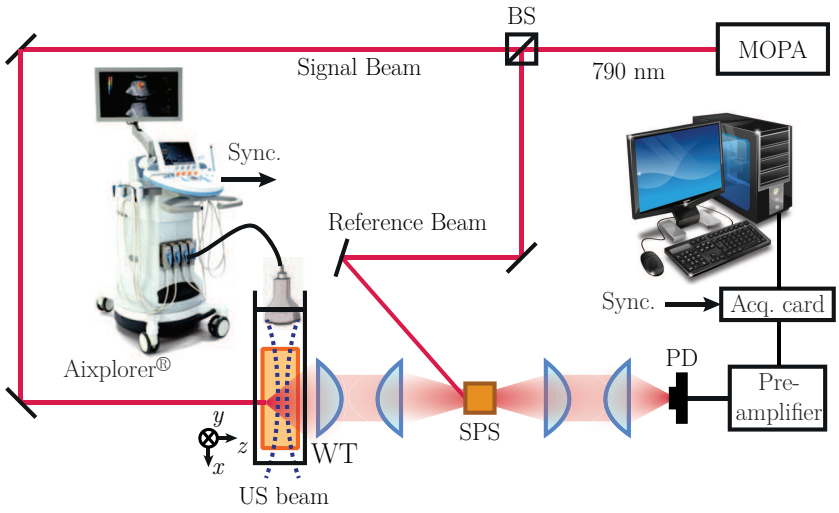

Figure H.1 – La plateforme multi-modale. WT : cuve remplie d'eau, MOPA : Master Oscillator Power Amplifier, BS : cube séparateur, PD : photodiode.

H.2.3 Preuve de concept

Afin d'établir une preuve de concept d'un tel procédé, la plateforme a été testée sur des biopsies de foie contenant des métastases de mélanome uvéal. Je donne un des exemples fournis dans le manuscrit ici.

Le mélanome uvéal

Le mélanome uvéal est un mélanome qui se développe dans l'uvée, c'est-à-dire la partie pigmentée de l'œil se trouvant entre la rétine et la scléra comptant l'iris entre autres. C'est le cancer de l'œil le plus répandu dans la population caucasienne. Si la tumeur principale est souvent assez simple à traiter, il y a développement de métastases dans le foie dans 50% des cas après un intervalle moyen de 3 ans. En cas d'apparition de métastases, l'espérance de vie est réduite à six mois en

l'absence de traitement. Quand elle est possible, la résection chirurgicale de toutes les tumeurs est le seul moyen efficace d'augmenter la survie des patients [128].

Il est donc, dans un premier temps, fondamental d'estimer précisément le nombre de métastases en préopératoire afin d'adapter le traitement au cas du patient – les patients avec trop de métastases seront d'abord traités par chimio- ou radiothérapie tandis que la chirurgie sera privilégiée pour les autres. Une fois en chirurgie, il est ensuite primordial de pouvoir se reposer sur des techniques d'imagerie fiables afin de localiser précisément les tumeurs à retirer. Dans le cas du mélanome uvéal, ces deux points posent problème. En préopératoire, les tumeurs localisées sur la surface du foie sont invisibles à l'IRM et aux rayons X car localisées dans une région particulièrement bruitée, ce qui conduit à des sous-estimations importantes de la profusion de métastases [129]. En peropératoire, les métastases localisées en profondeur ont un faible contraste acoustique les rendant souvent invisibles à l'échographie, ce qui conduit à la résection de portions de foie anormalement volumineuses.

Il s'avère par ailleurs que ces tumeurs, lorsqu'elles sont accessibles pour l'œil, sont facilement détectables à cause de dépôts mélaniques les rendant souvent très sombres. L'imagerie acousto-optique pourrait donc servir d'alternative aux techniques existantes, autant en préopératoire pour détecter les tumeurs sur la surface, localisées à quelques centimètres de profondeur dans le corps humain, qu'en peropératoire en temps que technique complémentaire à l'échographie.

Résultats *ex vivo*

Un des résultats présentés dans le manuscrit est reporté ici. Le morceau est une biopsie de foie de $2 \times 1 \times 1$ cm^3 enfermée dans un hydrogel multiplement diffusant d'agar mélangé à de l'intralipide 10% de dimensions $4 \times 4 \times 4$ cm^3 et de coefficient de diffusion réduit 10 cm^{-1}.

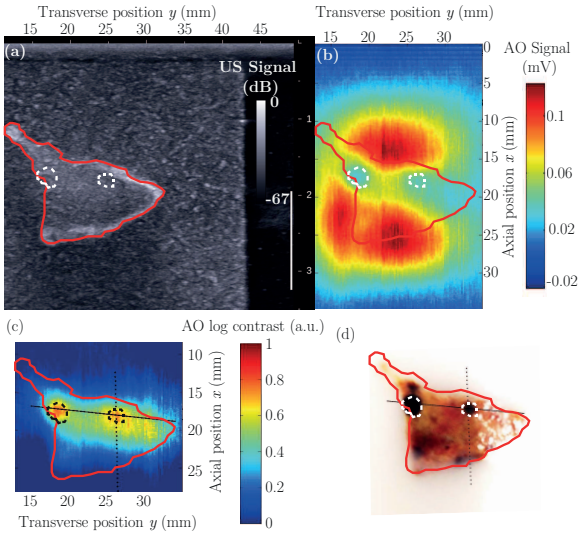

Figure H.2 – Résultats *ex vivo*. Les tumeurs sont entourées en blanc sur les différentes images. (a) échographie standard ; le contraste n'est pas significatif. Les contours du morceau de foie sont reportés en rouge. (b) image acousto-optique ; plusieurs régions apparaissent mais la tache diffuse rend l'interprétation difficile. (c) contraste optique ; la tache diffuse est retirée à l'aide d'un ajustement gaussien et les tumeurs apparaissent. (d) une photo de la biopsie de foie sur laquelle les tumeurs noires sont visibles.

Les résultats sont présentés sur la figure H.2. L'image échographique standard de l'échantillon est représentée sur la figure H.2(a) sur laquelle les métastases (région délimitée par les tirets blancs) sont invisibles car le contraste acoustique n'est pas significatif. La figure H.2(b) montre l'image

acousto-optique correspondante. Différentes régions se dessinent ici, preuve que la technique détecte quelque chose. Cependant, il apparaît assez clairement que l'image d'intensité lumineuse est difficile à interpréter telle quelle, notamment à cause de la tache diffuse qui introduit une ligne de base courbe. Afin de pouvoir interpréter les images, il est important de revenir à une information de propriétés optiques, indépendante de la répartition de l'intensité lumineuse. Pour ce faire, un ajustement de la tache diffuse par une Gaussienne de révolution (ce qui correspond à la tache diffuse théorique dans un milieu homogène) permet de s'en affranchir en fournissant une information optique directement proportionnelle au coefficient de diffusion effectif. La figure correspondante se trouve sur la figure H.2(c) sur laquelle les deux métastases sont facilement visible. La figure H.2(d) présente la photo de la biopsie de foie prise avant fermeture du gel diffusant à titre de comparaison.

Les limitations de la plateforme

Les premiers tests de faisabilité de la technique présentés dans ce manuscrit ont tous montré que l'imagerie acousto-optique pouvait être couplée à l'échographie commerciale en tant que technique complémentaire permettant de pallier le manque de spécificité des ultrasons. Ces résultats jouent le rôle d'un tout premier pas en direction de l'imagerie clinique.

Cependant, ces résultats ont aussi mis en évidence quelques obstacles qui se dressent entre la technique telle qu'elle est à l'heure actuelle et les exigences de l'imagerie clinique.

- Jusqu'à présent, tous les tests réalisés sont dans une configuration en transmission, ce qui n'est pas envisageable pour la plupart des applications auxquelles on peut penser. Il est donc important de commencer à s'intéresser à d'autres configurations en rétro-diffusion plus favorables à l'imagerie clinique. Dans cette optique, il convient de mener un travail d'optimisation sur le nombre et la position des sources et détecteurs optiques afin de contrôler le mieux possible la répartition de la lumière dans le milieu diffusant.

- Il est apparu clairement dans les différents tests que les images acousto-optiques sont difficiles à interpréter car elles renseignent sur la répartition de l'intensité lumineuse là où il serait préférable d'avoir une information de propriétés optiques indépendante des conditions d'éclairage. Pour ce faire, de nombreuses approches alternatives peuvent être envisagées comme des approches à plusieurs longueurs d'onde apportant une information purement spectrale [133], des approches à plusieurs pressions ultrasonores [134] ou des approches quantitatives basées sur la résolution du problème inverse posé par l'imagerie acousto-optique [132].

- La cadence de tir des échographes commerciaux est en général limitée à 1 tir toutes les 100 µs pour différentes raisons. Il faut à peu près 100 lignes pour reconstruire une image ce qui conduit à une cadence d'imagerie théorique pour l'imagerie acousto-optique d'à peu près 100 Hz. Dans la pratique, le niveau de signal acousto-optique est très faible et il faut moyenner chaque ligne quelques milliers de fois. Une image acousto-optique prend donc plusieurs dizaines de secondes, ce qui est incompatible avec l'imagerie temps réel. Il est donc primordial de réduire ce temps d'imagerie avant de penser à des applications cliniques.

- Le temps de réponse du cristal de SPS est de plusieurs millisecondes, un peu trop long pour suivre la décorrélation du speckle *in vivo*. Par conséquent, la technique est nécessairement limitée en rapport signal-à-bruit – car l'hologramme n'est pas gravé correctement – et en profondeur – car plus les photons se propagent en profondeur, plus le speckle se décorrèle vite. Il faut donc trouver une technique de détection robuste vis-à-vis de la décorrélation du

speckle, soit parce que son temps de réponse est suffisamment court, soit parce qu'elle en est intrinsèquement indépendante.

Les deux parties suivantes seront consacrées à la proposition d'approches alternatives afin de contourner les difficultés imposées par les deux derniers points, les deux premiers faisant partie d'un autre sujet de thèse.

H.3 Imagerie ultra-rapide par ondes planes ultrasonores

J'ai montré dans la partie précédente que la cadence d'imagerie acousto-optique par ultrasons focalisés est trop basse pour permettre de l'imagerie temps réel. Je vais consacrer cette partie au développement d'une nouvelle approche utilisant des ondes planes ultrasonores et une reconstruction tomographique afin d'augmenter la cadence d'imagerie d'au moins un ordre de grandeur.

H.3.1 Principe de l'imagerie acousto-optique en ondes planes

Reprenons l'approche développée dans la partie H.1.2 en utilisant cette fois des impulsions planes de quelques cycles se propageant dans le milieu avec un angle θ. Le principe de la technique est schématisé sur la figure H.3. Si l'onde de pression s'écrit :

$$P_{US}\left(\mathbf{r},t\right)=P_0\left(t-\frac{\mathbf{K}_{US}\cdot\mathbf{r}}{\omega_{US}}\right)\sin(\omega_{US}t) \tag{H.4}$$

avec le potentiel retardé, il est possible de montrer en utilisant l'approche de Kempe *et al.* [77] que le signal mesuré sur la photodiode $s_{\mathrm{PD}}\left(t,\theta\right)$ après la détection photoréfractive s'exprime :

$$s_{\mathrm{PD}}\left(t,\theta\right)\propto\iint I\left(x,y\right)\left[P_0^2\left(t\right)*\delta\left(t-\frac{x\cos\theta+y\sin\theta}{V_{\mathrm{US}}}\right)\right]\mathrm{d}x\mathrm{d}y \tag{H.5}$$

où $I\left(x,y\right)$ est l'image acousto-optique à reconstruire et δ est la distribution de Dirac.

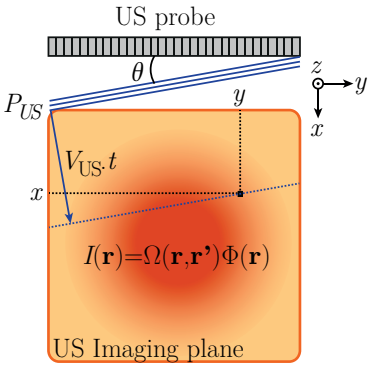

Figure H.3 – Schéma d'une onde plane se propageant dans un plan d'un échantillon éclairé avec un angle θ. Les lignes bleues représentent l'onde plane se propageant à V_{US}. Au temps t, l'onde est à la position de la ligne en pointillés. Un voxel (le carré noir) est repéré par ses coordonnées (x,y). Les photons sont marqués le long de tout le front d'onde et leur origine est perdue par diffusion de telle sorte que le signal enregistré sur le détecteur est proportionnel à l'intensité lumineuse locale intégrée le long de la ligne pointillée bleue.

La double intégrale de la formule précédente traduit simplement le fait que les photons sont marqués tout le long du front d'onde acoustique et comptés de manière indiscernable sur le détec-

teur : il mesure donc la projection de la répartition spatiale de la lumière le long de la direction définie par le front d'onde (perpendiculaire à la direction de propagation). Il apparaît ici que le problème de l'imagerie acousto-optique en ondes planes ultrasonores est très similaire au problème de tomographie à rayons X des scanners. En conséquence, il sera possible de bénéficier de tous les développements qui sont intervenus dans ce domaine. Selon une approche semblable aux rayons X, l'idée est d'envoyer une série d'ondes planes se propageant selon différentes directions θ pour faire un balayage angulaire de l'objet et récolter un ensemble de projections appelé sinogramme. L'image finale est reconstruite à l'aide de techniques déjà utilisées pour les scanners, en particulier la méthode d'inversion dite de la rétroprojection qui constitue l'approche la plus simple et la plus répandue. Cette technique consiste à attribuer chaque valeur d'une projection donnée à tous les points du volume ayant contribué à cette valeur. En sommant sur le domaine angulaire exploré (idéalement 180°), l'image finale peut être reconstruite. Il est possible de montrer qu'une telle approche donne une version floue de l'image réelle et on lui préfère en général une version dans laquelle ce flou est corrigé en filtrant au préalable chacune des projections par une rampe en fréquence. Cette méthode corrigée s'appelle la rétroprojection filtrée [153] et donne un résultat plus proche de l'inversion analytique.

H.3.2 Simulation de la fonction d'étalement du point (PSF)

Dans le cas de l'imagerie acousto-optique, nous disposons d'une sonde linéaire standard dont la directivité des éléments est de l'ordre de ±20° – autrement dit il n'est pas possible d'émettre des ondes planes se propageant avec des angles plus importants que $\theta_m = 20°$. Dans un souci de cadence d'imagerie, il n'est pas intéressant de déplacer mécaniquement la sonde afin d'augmenter l'exploration angulaire et un balayage purement électronique sera privilégié. Avec une seule sonde linéaire, il est donc attendu que l'image finale sera dégradée. Dans le but de quantifier un peu plus en détails cette dégradation, la fonction d'étalement du point (PSF, acronyme de l'appellation anglo-saxonne "point-spread function") peut être simulée numériquement pour différentes valeurs de domaine angulaire et une bande passante temporelle de type fonction porte de largeur 4 MHz. La PSF pour une exploration angulaire limitée à 40° (±20°) est présentée sur la figure H.4. Il apparaît ici que l'exploration limitée a pour effet d'étaler la PSF dans la direction latérale d'un facteur environ égal à 3.

Cet étalement peut s'interpréter facilement en repositionnant le problème dans l'espace de Fourier. A partir de la transformée de Fourier temporelle de la formule H.5, il est possible de montrer que le problème d'une exploration angulaire limitée se traduit dans l'espace de Fourier par l'absence d'information en dehors d'un cone défini par le domaine angulaire accessible et la bande passante électronique du système, comme représenté sur la figure H.5. En première approximation, dans la direction longitudinale (axe x), la fréquence maximale accessible est *a priori* limitée par la bande passante du système η_m. En revanche, dans la direction latérale (axe y), la fréquence spatiale maximale est limitée aussi par l'exploration angulaire et vaut dans ces conditions $\eta_m \sin\theta_m = 0.34\eta_m$ dans le cas d'une exploration maximale de 20°, soit une résolution dégradée d'un facteur d'environ 3.

Ici, à cause du découpage en forme de cône, la fréquence maximale accessible dans la direction latérale dépend directement du contenu spectral de l'objet à retrouver de telle sorte qu'on s'attend plutôt à un étirement horizontal général de l'image et non à un simple flou anisotrope.

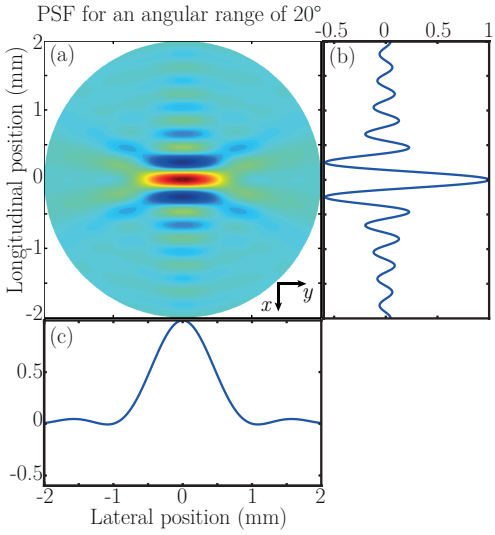

Figure H.4 – (a) PSF pour un domaine angulaire de $\pm 20°$, domaine typique pour une sonde linéaire en PZT. La PSF est étalée dans la direction latérale par rapport au cas idéal limité par la diffraction où on attend une tache d'Airy isotrope. (b) Profil le long de la direction $\varphi = 0°$ (axe x). (c) Profil le long de la direction $\varphi = 90°$ (axe y).

H.3.3 Preuve de concept expérimentale

En guise de preuve de concept, ce type de séquences a été testé sur un échantillon constitué d'une inclusion cylindrique noire de diamètre 2.5 mm et de coefficient d'absorption de l'ordre de 5 cm^{-1} enfermée dans une matrice de gel diffusant de dimensions $4 \times 4 \times 3$ cm^3 et de coefficient de diffusion réduit 10 cm^{-1}. L'image obtenue en impulsions focalisées se trouve sur la figure H.6 et servira de référence pour les comparaisons suivantes. A titre indicatif, il a fallu 188 lignes, chacune moyennée 2000 fois pour obtenir l'image, ce qui conduit à une séquence ultrasonore d'environ 40 s en tirant toutes les 100 µs. Un profil vertical (figure H.6(b)) et un profil horizontal (figure H.6(c)) permettent d'ajuster l'enveloppe lumineuse et l'inclusion par des Gaussiennes, bonne approximation pour des signaux acousto-optique en milieux homogènes [114]. Le diamètre de l'inclusion est déterminé par la largeur à mi-hauteur de la Gaussienne correspondante et vaut 2.5 mm comme attendu. En définissant ensuite le rapport contraste-à-bruit (CNR, acronyme de l'appellation anglo-saxonne "contrast-to-noise ratio") comme étant le rapport entre la profondeur de l'inclusion et le bruit de l'image, il vient un CNR de 9.

La même image est ensuite obtenue en utilisant une séquence en ondes planes balayant de $-20°$ à $20°$ par pas de $1°$ et reconstruite par rétroprojection filtrée. L'image correspondante est représentée sur la figure H.7(a) avec un profil vertical sur la figure H.7(b) et horizontal sur la figure H.7(c). La largeur de l'inclusion vaut ici environ 9 mm dans la direction horizontale, de l'ordre de ce qui était attendu ($> 3 \times 2.5$ mm), et environ 2 mm dans la direction verticale, un peu plus petit qu'attendu et signe d'une légère déformation de l'image dans cette direction aussi (qui peut se prédire par simulation). Le point important de cette image réside dans le CNR qui est à première vue plus important qu'en impulsions focalisées. Plus précisément, il vaut environ 24, selon la même méthode que précédemment, suggérant que le nombre de tirs de moyenne peut être réduit d'environ un facteur 10. Pour ce faire, plusieurs images en ondes planes ont été reconstruites en diminuant progressivement le nombre de moyennes. La figure H.8 représente l'évolution du CNR en fonction du nombre de moyennes par ligne. Comme attendu, à CNR équivalent il suffit d'environ 200 tirs de moyenne, ce qui correspond à une séquence qui dure 0.82 s à 1 tir par 100 µs, soit presque 50 fois plus rapide.

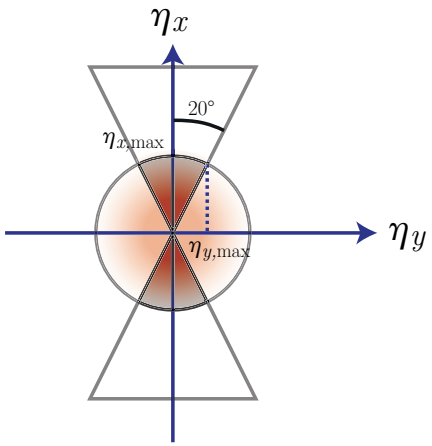

Figure H.5 – La bande passante des ultrasons et de la détection limitent la fréquence maximale accessible tandis que la sonde linéaire limite le domaine angulaire de telle sorte que la portion accessible de l'espace de Fourier est limitée à la partie en gris foncé.

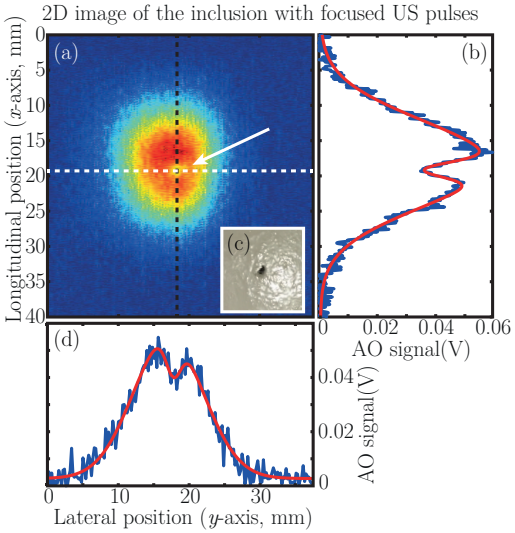

Figure H.6 – (a) Image acousto-optique en impulsions focalisées. La flèche blanche pointe vers l'inclusion. (b) Profil vertical le long de la ligne en pointillés noirs. (c) Photo de l'inclusion avant d'être recouverte de gel diffusant. (d) Profil horizontal le long de la ligne blanche.

La justification physique de cette augmentation de CNR tient au fait qu'à cause de la directivité des éléments des sondes linéaires, seulement quelques dizaines d'entre eux peuvent participer à la focalisation d'une impulsion là où toute la sonde est utilisée en ondes planes. La quantité d'énergie ultrasonore déposée dans le milieu est donc plus importante que pour une impulsion focalisée, ce qui conduit à un meilleur marquage. Un effet secondaire intéressant de l'utilisation d'ondes planes est que cette énergie est mieux répartie dans le milieu là où, pour des impulsions focalisées, elle se concentre au point focal et peut y entraîner de la cavitation. Pour quantifier le risque de créer de la cavitation dans les tissus biologiques, on définit l'indice mécanique comme le rapport de la valeur du pic de pression négative (en MPa) par la racine de la fréquence ultrasonore (en MHz). Ce dernier est limité par la FDA (organisme de régulation des normes médicales américain) à des valeurs inférieures à 1.9. Dans notre cas, l'indice mécanique de notre séquence ultrasonore focalisée a été mesuré à 1.14 contre 0.43 pour les ondes planes. La pression pourrait donc être augmentée dans le cas des ondes planes jusqu'à atteindre au moins la valeur en ultrasons focalisés, permettant ainsi une augmentation supplémentaire du signal acousto-optique.

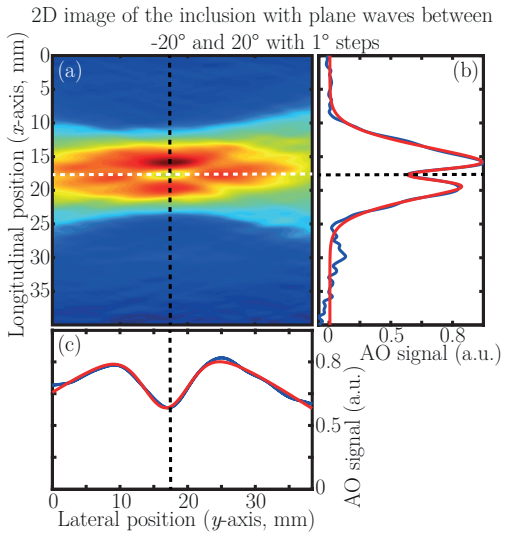

Figure H.7 – (a) Image acousto-optique obtenue en balayant les ondes planes de $-20°$ to $+20°$ avec un pas de $1°$. (b) Profil vertical le long de la ligne noire. (c) Profil horizontal le long de la ligne blanche.

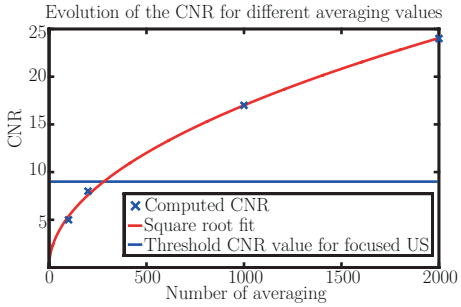

Figure H.8 – Évolution du CNR en fonction du nombre de moyennes par ligne. La ligne bleue indique la valeur seuil du CNR en impulsions focalisées à titre de comparaison.

H.3.4 Perspectives pour les ondes planes

Dans cette partie, j'ai montré qu'une séquence basée sur des ondes planes ultrasonores et une approche tomographique permettaient d'augmenter la cadence d'imagerie d'au moins un ordre de grandeur au prix d'une déformation de l'image dans la direction latérale. En revanche, une telle approche s'accompagne d'une augmentation du signal acousto-optique et d'une diminution de l'indice mécanique. Pour des applications n'autorisant pas un accès à 360° autour de l'objet à imager, la déformation induite par une approche à une seule sonde rend difficile l'interprétation des images dès que l'objet devient plus complexe. Elle pourrait cependant servir pour une localisation rapide et préliminaire des zones suspectes à inspecter plus en détails avec des méthodes plus lentes et précises. Dans tous les cas, plusieurs approches peuvent être explorées afin de retrouver la résolution latérale dégradée par la déformation comme l'utilisation d'éléments plus directifs ou des sondes légèrement courbées capables d'atteindre des angles au-delà de 20° éventuellement couplées à des ondes divergentes pour augmenter le champ de vue. Des approches de reconstruction avec des connaissances *a priori* de la forme des objets recherchés peuvent aussi être envisagées. Dans ce cas, ces informations pourraient être extraites des échographies standard.

Cependant, un bon moyen de retrouver la résolution latérale est de venir explorer aussi l'échantillon depuis la direction latérale, en mettant par exemple une deuxième sonde à 90° de la première comme montré sur la figure H.9. Ici, l'échantillon est constitué de deux inclusions placées côte à

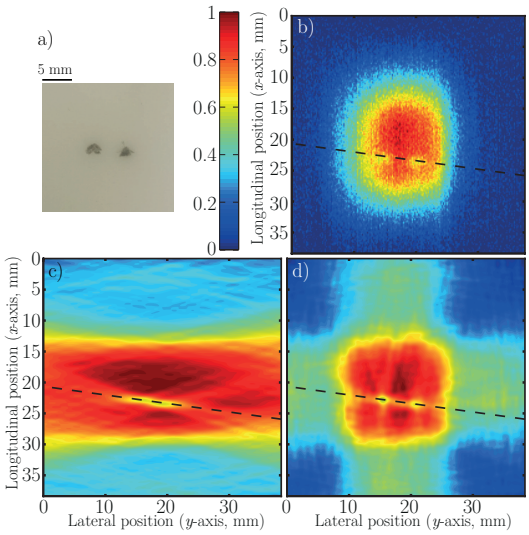

Figure H.9 – Images dans une configuration à deux sondes orthogonales. L'echelle de couleur est la même sur toutes les images. (a) Photo du gel contenant deux inclusions côte à côte. (b) En ultrasons focalisés. (c) En ondes planes depuis une seule sonde. (d) En ajoutant l'information fournie par la deuxième sonde.

côte et suffisamment proches pour ne pas être distinguées sur l'image en ondes planes avec une seule sonde. En ajoutant une séquence en ondes planes provenant d'une sonde placée orthogonalement, il est possible de distinguer les deux inclusions. Ces résultats pourraient remettre au goût du jour des approches tomographiques pour l'imagerie acousto-optique pour des applications qui le permettent comme l'imagerie du sein ou du petit animal. Dans ce cas, cela pourrait conduire au développement de sondes en anneau comme utilisées pour la tomographie photoacoustique.

H.4 Imagerie acousto-optique par creusement spectral

Dans la partie précédente, j'ai proposé une approche pour résoudre le problème des séquences ultrasonores trop longues qui conduisent à des cadences d'imagerie trop lentes pour envisager un passage en clinique. Dans cette partie, je vais m'intéresser au problème de la décorrélation du speckle *in vivo*. Je vais proposer une méthode de détection par creusement de trous spectraux – j'utiliserai dans la suite l'appellation holeburning spectral, plus usuelle – dans des cristaux dopés avec des terres rares. Cette approche, initialement proposée par Li *et al.* en 2008 [108], a été abandonnée assez rapidement pour des questions d'instrumentation lourde mais présente l'avantage d'être robuste face à la décorrélation du speckle.

H.4.1 Réalisations de filtres ultrafins par holeburning spectral dans des cristaux de Tm^{3+} :YAG

Propriétés du cristal

Nous cherchons ici une technique dite incohérente capable de mesurer directement la puissance des photons marqués – autrement dit un filtre spectral ultrafin d'une largeur d'à peine quelques MHz capable de discriminer les photons marqués des photons non marqués. Nous cherchons ainsi dans le holeburning spectral une technique capable d'absorber les photons non marqués tout en transmettant les photons marqués.

Les ions terres rares sont particulièrement intéressants dans notre cas car les transitions optiquement actives sont écrantées par des couches atomiques plus externes. En conséquence, ces transitions sont particulièrement fines et peu influencées par l'environnement. Parmi ces différents éléments, les ions Tm^{3+} en matrice cristalline de YAG (noté Tm^{3+} :YAG) possèdent une transition autour de 793 nm ($^3H_6$ vers $^3H_4$ que je noterai dans la suite $|g\rangle$ – $|e\rangle$), en plein cœur de la fenêtre thérapeutique optique, qui en fait de bons candidats pour l'imagerie biologique.

Nous cherchons par ailleurs à absorber fortement les photons marqués, bien plus nombreux que les photons non marqués, il faut donc des cristaux épais fortement dopés afin d'avoir le coefficient d'absorption le plus haut possible et maximiser l'atténuation. Dans notre cas, le cristal est dopé à 2% at. de dimensions $1 \times 1 \times 0.2$ cm^3.

Dans ce matériau, il faut ensuite s'arranger pour créer une bande spectrale transparente très fine afin de laisser passer les photons marqués. C'est le phénomène de holeburning spectral. Lorsqu'on considère une classe d'atomes dans un environnement identique pour tous, la raie d'absorption correspondante est appelée raie *homogène* et possède une largeur définie, entre autres, par les couplages avec la matrice cristalline et entre les ions eux-mêmes. Dans une matrice cristalline réelle, l'environnement d'un ion à l'autre est toujours différent à cause de contraintes, dislocations ou impuretés par exemple, de telle sorte que la raie d'absorption qui en résulte n'est pas une unique raie homogène mais une superposition de plusieurs raies homogènes légèrement décalées les unes par rapport aux autres selon la distribution statistique des défauts. L'élargissement qui en résulte est appelé élargissement *inhomogène* – c'est cette raie dite inhomogène qu'on mesure avec un spectromètre. À température ambiante, la largeur homogène est très grande devant l'élargissement inhomogène. Ce n'est plus le cas en revanche pour des températures inférieures à 4 K, pour lesquelles la largeur homogène fait moins de quelques centaines de kHz et la largeur inhomogène autour de 20 GHz. Pour le cristal à disposition, la largeur homogène à 3 K a été mesurée autour de 40 kHz et la largeur inhomogène à environ 35 GHz.

Le principe du holeburning spectral consiste à exciter sélectivement une classe d'ions afin de vider le niveau fondamental de la transition optique correspondante. Dans ce cas, lorsqu'un faisceau sonde dont la fréquence est celle de la transition excitée traverse le cristal, ce dernier rencontre une transition homogène vide et le cristal est transparent. En revanche, les transitions voisines qui n'ont pas été excitées sont toujours aussi absorbantes et cela se traduit par une fenêtre de transparence de quelques largeurs homogènes dans la raie inhomogène du cristal.

Principe du holeburning spectral

Considérons la transition $|g\rangle$ – $|e\rangle$ à 793 nm décrite plus haut. Dans une version simplifiée du système, il existe un autre niveau intermédiaire entre $|g\rangle$ et $|e\rangle$ ($^3F_4$ qu'on notera $|m\rangle$ dans la suite) comme représenté sur la figure H.10.

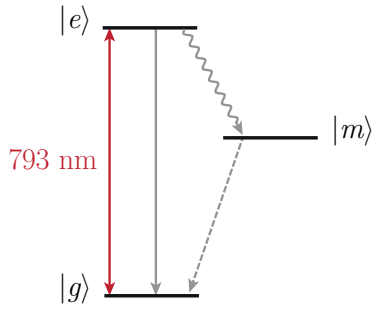

Figure H.10 – Le système que nous considérons est un système à trois niveaux composé de $|g\rangle$, $|e\rangle$ et $|m\rangle$.

Les temps de vie des niveaux $|e\rangle$ et $|m\rangle$ sont respectivement de l'ordre de quelques centaines de microsecondes et 10 ms – c'est à cause de ce long temps de vie que le niveau $|m\rangle$ est appelé *métastable*. Le holeburning spectral se déroule en deux étapes. La première, appelée gravure, consiste à pomper optiquement la transition afin de placer les atomes dans le niveau métastable. La seconde, appelée sonde, consiste à sonder l'absorption du cristal avec un faisceau de faible intensité. Un modèle simple d'équations de populations permet d'exprimer l'absorption du cristal α en fonction de la fréquence du faisceau sonde ν_p :

$$\alpha\left(\nu_p\right) = \sigma_h N \frac{\Gamma_h}{\Gamma_{inh}} \left[1 - \frac{\sqrt{1+\frac{\phi_b}{\phi_s}} - 1}{\sqrt{1+\frac{\phi_b}{\phi_s}}} \frac{1}{1+\left(\frac{\nu_p-\nu_b}{\Gamma_{\mathrm{HB}}/2}\right)^2}\right] \tag{H.6}$$

où σ_h est la section efficace d'absorption homogène, N la population totale en ions Tm^{3+}, Γ_h et Γ_{inh} sont les largeurs homogène et inhomogène, ϕ_b le nombre de photons par unités de temps et surface, ν_b est la fréquence de gravure et Γ_{HB} est la largeur du trou donnée par l'expression :

$$\Gamma_{\mathrm{HB}} = \Gamma_h \left(1 + \sqrt{1 + \frac{\phi_b}{\phi_s}}\right) \tag{H.7}$$

Le paramètre ϕ_s est appelé le *flux* de photons de saturation et correspond au nombre de photons par unités de temps et de surface nécessaire pour placer la moitié des atomes dans le niveau métastable. Ce paramètre est intrinsèque à la transition et est ici inversement proportionnel au temps de vie du niveau métastable. Il quantifie l'efficacité de la gravure : plus le *flux* de photons de saturation est faible, plus il est facile de graver des trous profonds et larges. Ces expressions sont vraies dans le cas où le laser est infiniment fin et stable et le système est considéré en régime stationnaire à la fin de la gravure.

Il va de soi qu'au delà de quelques millisecondes, les atomes quittent le niveau métastable pour retourner dans le niveau fondamental et le trou s'efface. C'est ce qui est illustré sur la figure H.11 où le trou disparaît exponentiellement au cours du temps avec un temps caractéristique de l'ordre du temps de vie du niveau métastable.

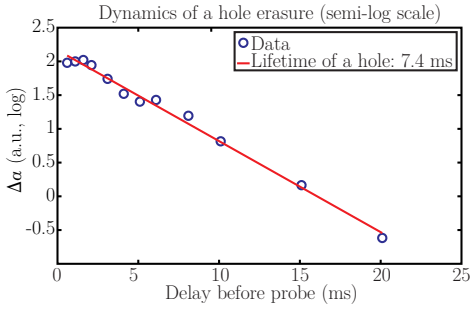

Figure H.11 – Le nombre d'atomes dans le niveau métastable (l'aire du trou) diminue exponentiellement au cours du temps avec un temps caractéristique d'environ 10 ms.

Pour l'imagerie acousto-optique, c'est la transmission du cristal $\exp\left(-\alpha L\right)$ qui va affecter les photons marqués et non marqués. Dans la suite, il est important de la distinguer du trou qui est une diminution du coefficient d'absorption.

Limites du holeburning spectral

D'autres caractérisations faites sur les trous à l'Institut de Chimie de Paris dans l'équipe de Philippe Goldner ont montré que le modèle précédent marche relativement bien, même dans des conditions expérimentales non-idéales, à condition de définir une intensité de saturation effective, correspondant à l'intensité lumineuse nécessaire pour placer la moitié des atomes dans le niveau métastable, qui intègre les conditions expérimentales.

Dans ces conditions, plusieurs paramètres influencent l'efficacité de gravure comme la stabilité du laser, l'homogénéité spatiale du faisceau de gravure à l'échelle de la surface de la sonde ou l'absorption de la gravure dans l'épaisseur du cristal. Cependant, en l'état, la principale limite réside dans le temps de vie du niveau métastable qui est trop court pour être compatible avec de l'imagerie clinique. Puisque le temps de vie est court, il faut répéter la séquence de gravure régulièrement pour entretenir un trou profond : lors de la preuve de concept de Li *et al.* en 2008, près de la moitié de la séquence d'imagerie est utilisée par la répétition de la gravure. Autre conséquence du temps de vie trop court, il faut des puissances de gravures très élevées pour pomper efficacement la transition. Parmi les effets indésirables, de fortes puissances de gravure peuvent entraîner des soucis de stabilité ou une augmentation locale de la température dans le cristal. Cependant, le principal inconvénient reste purement expérimental : des réflexions parasites de la gravure dans le cryostat peuvent éblouir le détecteur. Afin de se prémunir contre ce problème, Li *et al.* utilisent un obturateur mécanique devant leur détecteur qui s'ouvre en environ 1.5 ms. Le temps que l'obturateur s'ouvre complètement, le cristal a perdu 50% de sa transmission.

H.4.2 Holeburning spectral sous champ magnétique

La principale limite du holeburning spectral en tant que technique de détection pour l'imagerie acousto-optique réside ainsi dans le temps de vie du niveau métastable, trop court pour être utilisable en clinique. Il est donc naturel de s'interroger sur la possibilité d'augmenter cette durée de vie. En 2003, Ohlsson *et al.* [181] ont rapporté l'observation d'une augmentation sensible du temps de stockage de propriétés spectrales lorsque le cristal est placé dans un champ magnétique externe. Dans cette optique, le montage a été déplacé au Laboratoire Aimé Cotton dans l'équipe d'Anne Chauvet et Thierry Chanelière afin d'étudier l'utilisation du holeburning spectral sous champ magnétique pour l'imagerie acousto-optique.

Principe du holeburning spectral sous champ

Lorsque le cristal est placé dans un champ magnétique, la dégénérescence des états de spin magnétique des ions Tm^{3+} est levée de telle sorte que chaque niveau est divisé en sous-niveaux Zeeman comme représenté sur la figure H.12. Dans la suite, nous supposerons que l'éclatement Zeeman du niveau métastable n'influence pas le processus de holeburning spectral en considérant qu'une fois dans un des sous-niveaux métastables, la désexcitation dans l'un ou l'autre des sous-niveaux fondamentaux est équiprobable. Je négligerai donc l'effet Zeeman sur le niveau métastable.

Le phénomène de holeburning spectral reste très similaire sous champ magnétique. La différence principale tient maintenant au fait que si le spin magnétique change à cause de processus non-radiatifs lors de la désexcitation vers le niveau fondamental, il est possible d'accumuler les atomes dans le niveau dit Zeeman ($|g,+\rangle$ si la transition excitée est $|g,-\rangle - |e,-\rangle$, $|g,-\rangle$ si la transition excitée est $|g,+\rangle - |e,+\rangle$). Une fois dans le niveau Zeeman, les processus responsables du retour des atomes dans l'autre niveau sont des processus impliquant un retournement de spin via l'échange de phonons, négligeables en dessous de 3 K, ou des processus de type *flip-flop* à énergie constante

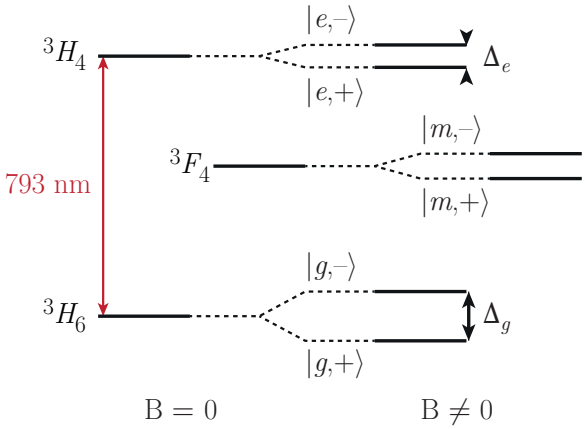

Figure H.12 – Niveaux d'énergie de la transition à 793 nm sous champ magnétique. Les niveaux $^3H_6$ ($|g\rangle$), $^3H_4$ ($|e\rangle$) et $^3F_4$ ($|m\rangle$) sont séparés respectivement en sous-niveaux Zeeman $|g,+\rangle$ et $|g,-\rangle$, $|e,+\rangle$ et $|e,-\rangle$, $|m,+\rangle$ et $|m,-\rangle$. L'éclatement du niveau fondamental est Δ_g ($= \delta_g \times B_0$) et celui du niveau excité Δ_e ($= \delta_e \times B_0$). Dans la suite l'éclatement du niveau métastable sera négligé.

entre ions différents. En conséquence, le temps de vie du niveau Zeeman peut être extrêmement long (plusieurs secondes). Le trou a donc une durée de vie au moins deux ordres de grandeur supérieure à ce qu'elle était en l'absence de champ magnétique comme illustré sur la figure H.13.

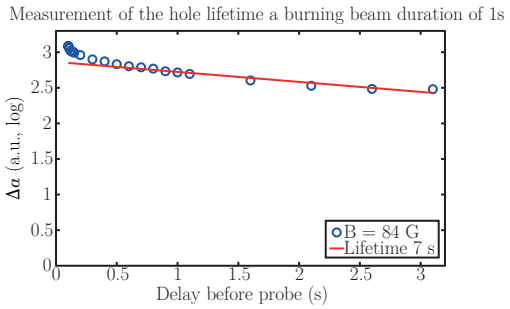

Figure H.13 – Disparition du trou au cours du temps. Un première décroissance rapide est visible aux temps courts et correspond au niveau métastable qui se vide vers le niveau fondamental. Elle est suivie d'une décroissance exponentielle lente avec un temps caractéristique de l'ordre de 7 s correspondant au niveau Zeeman se vidant dans le niveau fondamental.

Un effet secondaire intéressant du champ magnétique externe est une augmentation de l'absorption du cristal lorsque la fréquence de la sonde est calée sur la transition depuis le niveau Zeeman : la gravure y a stocké les atomes de la transition de telle sorte que le nombre d'atomes à exciter est maintenant plus important. Ce phénomène s'appelle des *anti-trous* et est associé à une augmentation de l'absorption du cristal qui peut atteindre une fois et demie l'absorption maximale du cristal. Un profil d'absorption typique peut être simulé à l'aide d'un modèle d'équations aux populations très similaire à celui utilisé précédemment dans lequel le couplage entre la gravure et le niveau de stockage est négligé. Le résultat est présenté sur la figure H.14 et comparé au trou sans champ magnétique dans les mêmes conditions. Ici les anti-trous sont bien visibles. En conséquence de l'augmentation de la durée de vie du trou, il est plus facile de graver des trous profonds avec des puissances moindres.

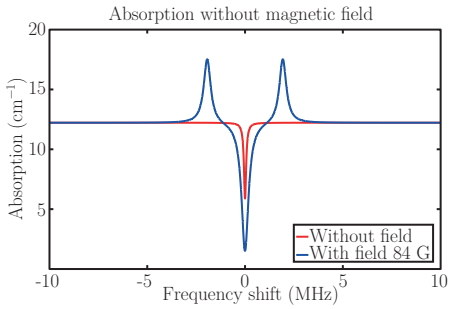

Figure H.14 – Profil de l'absorption du cristal avec et sans champ magnétique avec une intensité de gravure de 800 $\mu W \cdot cm^{-2}$.

Imagerie acousto-optique

La présence d'un champ magnétique externe a deux avantages majeurs pour l'imagerie acousto-optique. L'augmentation significative du temps de vie du trou permet de graver plus profond avec des puissances moindres et de réduire le taux de répétition de l'étape de gravure. La présence d'anti-trous permettrait d'augmenter la dynamique d'absorption du cristal en jouant sur le champ magnétique pour les faire coïncider avec les photons non-marqués. Pour la preuve de concept d'imagerie acousto-optique que je vais montrer ici, l'influence des anti-trous n'a pas été étudiée. La séquence optique d'imagerie a été optimisée pour donner le maximum de signal acousto-optique sans champ magnétique. Les résultats ci-dessous ont été obtenus en ajoutant simplement le champ externe obtenu à l'aide de deux bobines de Helmoltz parcourues par un courant. Elles génèrent un champ magnétique de 7 $G \cdot A^{-1}$.

Le montage expérimental est représenté sur la figure H.15. La lumière est émise par une diode laser stabilisée sur une cavité Fabry-Perot confocale externe selon une méthode Pound-Drever-Hall [179, 180] et amplifiée par une succession de laser esclaves. Les ultrasons sont générés à l'aide d'un transducteur mono-élément Olympus Panametrics NDT A307S (diamètre 1", focale 2") émettant 10 cycles à sa fréquence centrale de 5 MHz. Il est à noter ici que la gravure se fait par le côté du cristal (poli sur ses six faces) car les fenêtres en face sont obstruées par des lentilles épaisses servant à collecter le speckle. Afin de ne pas éblouir le détecteur à cause de réflexions parasites de la gravure dans le cryostat, un obturateur mécanique Uniblitz VS14S1T1 (non représenté sur la figure H.15) est positionné devant la photodiode à avalanche et ne s'ouvre qu'à la fin de la gravure. L'obturateur met environ 1,5 ms à s'ouvrir.

Une première étude du signal acousto-optique sur de la lumière balistique montre que, parce que la durée de vie du trou est bien plus longue, la quantité de signal acousto-optique est bien plus élevée à faibles puissances de gravure comme montré sur la figure H.16(a). Une preuve de concept en milieu diffusant (1.5 cm d'épaisseur, $\mu_s' = 12$ cm^{-1}) se trouve sur la figure H.16(b) pour une puissance de sonde de 200 mW et une gravure à 110 mW pendant 10 ms, le signal est moyenné 300 fois.

Il est à noter sur ce dernier exemple que le signal acousto-optique est à peu près deux fois plus important sous champ magnétique que sans. La justification physique est probablement une conjonction de deux phénomènes. Le premier vient du fait que la gravure se fait par le côté, dimension pour laquelle le cristal est très épais (1 cm). La gravure étant absorbée au cours de sa propagation dans le cristal, il est tout à fait possible que la région transparente soit plus importante sous champ magnétique que sans. Le second tient au fait que pendant l'ouverture de l'obturateur mécanique, le trou s'efface moins vite sous champ magnétique et la transparence est encore bonne.

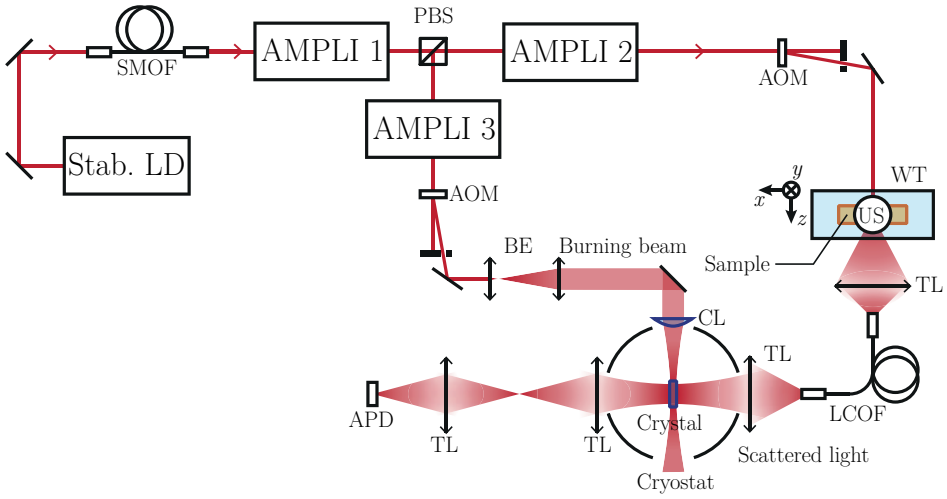

Figure H.15 – Montage d'imagerie acousto-optique. La lumière émise par la diode laser stabilisée est amplifiée par différents étages d'amplifications. WT : cuve remplie d'eau ; LCOF : fibre optique à cœur liquide ; TL : lentille épaisse de diamètre 3 pouces. US : ultrasons. La gravure est en configuration orthogonale et focalisée par une lentille cylindrique (CL). APD : photodiode à avalanche. PBS : cube séparateur de polarisation ; BE : agrandisseur de faisceau, SMOF : fibre optique mono-mode, AOM : modulateur acousto-optique.

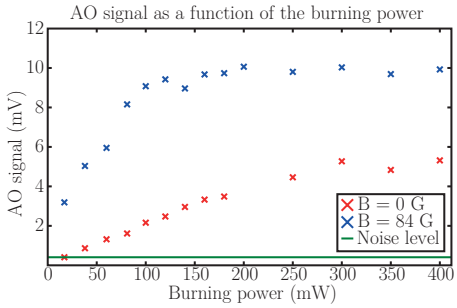

(a) Signal acousto-optique en fonction de la puissance de gravure

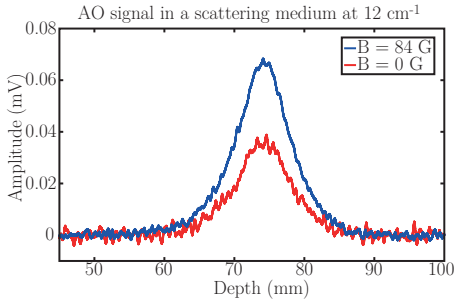

(b) Signal acousto-optique en milieu diffusant

Figure H.16 – Signal acousto-optique dans différentes conditions. (a) Signal acousto-optique en fonction de la puissance de gravure sur de la lumière balistique. (b) Signal acousto-optique en milieu diffusant, 1.5 cm d'épaisseur, $\mu_s' = 12\ \mathrm{cm}^{-1}$.

Perspectives pour le holeburning spectral

Le holeburning spectral sous champ magnétique permet donc un allongement du temps de vie du trou d'au moins deux ordres de grandeur. Les différentes caractérisations qui ont été faites au cours de cette thèse ont montré que, outre des difficultés d'ordre instrumental et d'encombrement, cette amélioration s'accompagne de certains inconvénients.

La durée de vie du trou étant très longue, le processus est beaucoup plus sensible aux instabilités du laser. Une dérive lente de la fréquence du laser sur plusieurs dizaines de secondes risquerait par exemple de réexciter les atomes placés dans les anti-trous et d'effacer le trou principal.

La raie d'émission du laser présentant un profil Lorentzien plutôt qu'une distribution de Dirac, il y a en général un petit recouvrement avec les anti-trous. Il y a donc un risque d'en exciter les atomes et d'effacer le trou lorsqu'on grave avec de fortes puissances. Ce phénomène est d'autant plus important que le temps de vie est long et qu'une faible puissance suffit à graver des trous profonds.

La transparence du cristal utilisé pour filtrer découle en fait d'un trou moyenné sur tout le front d'onde de la gravure. En général les faisceaux utilisés sont Gaussiens, de telle sorte que les trous sont profonds au centre du front d'onde et superficiels sur les bords. En augmentant la puissance de gravure, les trous sur les bords deviennent plus profonds, mais les trous au centre finissent par être effacés selon le point précédent. Il y a donc fort à parier qu'il existe un optimum de puissance de gravure pour lequel le trou moyenné soit le plus profond. Dans tous les cas cependant, il y a de fortes chances que le cristal ne soit pas aussi transparent qu'espéré.

Néanmoins, l'augmentation du temps de vie du trou permet de graver avec des puissances bien moindres, d'atteindre une meilleure transparence en profondeur dans le cristal et de réduire la cadence de répétition de la gravure. Il reste à court terme à optimiser la séquence de gravure sous champ et à explorer l'influence des anti-trous sur la dynamique de filtrage du cristal.

Afin de résoudre à plus long terme les différents problèmes liés à la présence du champ magnétique, il peut être envisagé d'asservir le laser sur un trou directement plutôt que sur une cavité externe, ce qui permettrait d'atteindre des stabilités plus importantes en réduisant l'influence des dérives thermiques et des vibrations entre le laser et le cryostat. Puisqu'il est possible de graver avec des puissances moindres, il peut être intéressant d'élargir très fortement la gravure ou de la filtrer spatialement afin d'obtenir un front d'onde le plus plan possible quitte à perdre de la lumière.

H.5 Conclusion et perspectives

Dans ce manuscrit, j'ai montré que l'imagerie acousto-optique couplée à une détection photoréfractive permettait de retrouver du contraste optique en profondeur dans les tissus biologiques. Les premiers tests de faisabilité *ex vivo* ont montré des premières pistes d'exploration. Dans l'optique de passer sur de l'imagerie clinique, il convient de résoudre plusieurs difficultés qui rendent difficile le passage vers l'imagerie *in vivo*.

Les deux premiers points, qui n'ont pas été traités dans cette thèse, consistent à passer sur une configuration en rétrodiffusion pour laquelle l'illumination, la collection et les ultrasons sont du même côté, et à fournir une information de propriétés optiques directement, plutôt qu'une information d'intensité lumineuse. D'un point de vue imagerie *in vivo*, cette thèse a été consacrée à la résolution de deux problèmes majeurs : la cadence d'imagerie acousto-optique, bien trop basse pour être compatible avec l'imagerie dynamique, et la décorrélation du speckle *in vivo* qui s'opère sur des temps trop courts pour que la détection photoréfractive puisse pleinement fonctionner.

En termes de cadence d'imagerie, j'ai montré qu'il était possible d'utiliser une approche en ondes planes ultrasonores couplée à une reconstruction tomographique qui permet d'augmenter la quantité de signal acousto-optique. En réduisant le nombre de moyennes, il devient alors possible d'augmenter la cadence d'imagerie d'au moins un ordre de grandeur au prix d'une déformation latérale de l'image. L'utilisation d'ondes planes s'accompagne de deux effets secondaires intéressants pour l'imagerie acousto-optique. En premier lieu, une approche en ondes planes est plus robuste face à des absorbeurs ou réflecteurs acoustiques. Parce qu'elle "insonifie" le milieu depuis plusieurs directions, une approche en ondes planes permet d'explorer dans tous les cas des régions situées sous un obstacle acoustique. Le deuxième point intéressant est une réduction de l'indice mécanique qui quantifie le risque de cavitation dans les tissus. Ce paramètre est régulé par des normes médicales strictes et, dans le cas des ondes planes, il est plus de deux fois plus faible. Il peut donc être envisagé d'augmenter la pression acoustique pour se ramener au niveau des ondes focalisées et ainsi d'accroître le niveau de signal acousto-optique.

La déformation de l'image rendant difficile l'interprétation de formes complexes, la technique pourrait être utilisée telle qu'elle pour une localisation préliminaire et rapide de zones suspectes, avant de recourir à des techniques plus précises, plus lentes et plus invasives. Dans ce cas, quelques possibilités peuvent tout de même être envisagées afin d'améliorer la résolution latérale comme l'utilisation d'éléments plus directifs ou de sondes légèrement courbées couplées à des ondes divergentes. Pour les applications qui s'y prêtent, une approche tomographique à 360° permettrait de retrouver sans difficulté la résolution latérale tout en bénéficiant de l'augmentation du signal acousto-optique associée aux ondes planes. L'imagerie du petit animal pour les études pré-cliniques ou l'imagerie du sein par exemple seraient des applications possibles. Toutes ces pistes peuvent bénéficier des avancées en termes de reconstruction d'image du domaine des scanners comme l'intégration de connaissances *a priori* pour améliorer la reconstruction.

En termes d'imagerie *in vivo*, il avait été montré en 2008 que l'utilisation du holeburning spectral en tant que filtre ultrafin permettait d'avoir une technique de détection insensible à la décorrélation du speckle. Outre une instrumentation lourde, la plupart des difficultés de la technique viennent de la durée de vie des trous spectraux, trop courte pour que l'utilisation du phénomène soit confortable. J'ai montré qu'il était possible de placer le cristal dans un champ magnétique afin d'augmenter cette durée de vie d'au moins deux ordres de grandeur. Cette augmentation permet de graver des trous plus profonds avec des puissances moindres, d'obtenir une transparence plus importante dans l'épaisseur du cristal et de diminuer la répétition de la séquence de gravure. Outre l'augmentation de la durée de vie du trou, la présence du champ magnétique induit l'apparition d'anti-trous associés à une augmentation de l'absorption du cristal, de telle sorte qu'un choix judicieux de la valeur du champ permettrait d'augmenter la dynamique de filtrage du cristal. J'ai montré que cette approche permettait d'augmenter le niveau de signal acousto-optique par rapport à une approche optimisée sans champ magnétique.

Il reste à court terme à optimiser la séquence de gravure sous champ et étudier l'influence des anti-trous. A plus long terme, il est intéressant d'envisager un asservissement du laser sur un trou plutôt que sur une cavité externe. Un tel asservissement permettrait théoriquement d'être moins sensible aux vibrations du montage ou aux dérives thermiques. Dans le but d'alléger le montage, des crysotats en circuit fermé permettraient de s'affranchir du remplissage régulier d'hélium et de rendre le système plus portatif. Il peut être intéressant d'étudier la possibilité de faire de l'imagerie multi-spectrale en utilisant deux cristaux différents ou des cristaux co-dopés. Il convient de garder à l'esprit que, si l'utilisation d'un cryostat peut sembler un lourd handicap, l'IRM est aussi une technique fonctionnant à températures cryogéniques et demande une instrumentation bien plus coûteuse.

Parce qu'elle est simple à mettre en place, la détection photoréfractive a encore de beaux jours devant elle. Dans le but de mettre en place une plateforme plus compacte, il est nécessaire de converger vers un système tout fibré utilisant des sondes acousto-optiques intégrant à la fois la partie optique et la partie acoustique. Afin de résoudre le problème du temps de réponse du cristal, il peut être intéressant de travailler avec des matériaux plus rapides ou d'augmenter la puissance de la référence, bien que ce dernier point soit limité par le bruit supplémentaire apporté par la référence. Dans tous les cas, il est important de continuer à explorer des pistes d'applications avec l'holographie photoréfractive. Parmi elles, l'imagerie multi-spectrale est une application prometteuse qui permettrait de faire de l'imagerie fonctionnelle ou de remonter directement aux propriétés optiques des tissus. Ce dernier point est un point important car les images d'intensité lumineuse sont difficiles à interpréter. Un gros travail sur le modèle direct et la résolution du problème inverse posé par l'imagerie acousto-optique est actuellement en cours afin de pouvoir passer de l'image d'intensité lumineuse aux propriétés optiques.

References

[1] W.-F. Cheong, S. A. Prahl, and A. J. Welch. A Review of the Optical Properties of Biological Tissues. *IEEE Journal of Quantum Electronics*, 26(12):2166–2185, 1990.

[2] G. Muehllehner and J. S. Karp. Positron emission tomography. *Phys. Med. Biol.*, 51(13):R117, 2006.

[3] M. Analoui, J. D. Bronzino, and D. R. Peterson, editors. *Medical imaging: principles and practices*. Taylor & Francis/CRC Press, 2013.

[4] Paul C. Lauterbur. Image Formation by Induced Local Interactions: Examples Employing Nuclear Magnetic Resonance. *Nature*, 242(5394):190–191, 1973.

[5] P. R. Luyten, A. J. Marien, W. Heindel, P. H. van Gerwen, K. Herholz, J. A. den Hollander, G. Friedmann, and W. D. Heiss. Metabolic imaging of patients with intracranial tumors: H-1 MR spectroscopic imaging and PET. *Radiology*, 176(3):791–799, 1990.

[6] J. Bercoff, G. Montaldo, T. Loupas, D. Savery, F. Meziere, M. Fink, and M. Tanter. Ultrafast compound doppler imaging: providing full blood flow characterization. *IEEE Transactions on Ultrasonics, Ferroelectrics, and Frequency Control*, 58(1):134–147, 2011.

[7] E. Macé, G. Montaldo, I. Cohen, M. Baulac, M. Fink, and M. Tanter. Functional ultrasound imaging of the brain. *Nature Methods*, 8(8):662–664, 2011.

[8] V. Marshall, D. C. Williams, and K. D. Smith. Diaphanography as a means of detecting breast cancer. *Radiology*, 150, 1984.

[9] Max Cutler. Transillumination Of The Breast. *Ann. Surg.*, 93(1):223–234, 1931.

[10] Barabra Monsees. Light scan evaluation of nonpalpable breast lesions. *Radiology*, 163, 1987.

[11] J. A. Moon, R. Mahon, M. D. Duncan, and J. Reintjes. Resolution limits for imaging through turbid media with diffuse light. *Opt. Lett.*, 18(19):1591–1593, 1993.

[12] James E. Sinex. Pulse oximetry: Principles and limitations. *The American Journal of Emergency Medicine*, 17(1):59–66, 1999.

[13] Elizabeth M. C. Hillman. Optical brain imaging *in vivo*: techniques and applications from animal to man. *J. Biomed. Opt.*, 12(5):051402, 2007.

[14] Valery V. Tuchin. Tissue Optics and Photonics: Light-Tissue Interaction. *Journal of Biomedical Photonics & Engineering*, 1(2):98–134, 2015.

[15] G. Hong, S. Diao, J. Chang, A. L. Antaris, C. Chen, B. Zhang, S. Zhao, D. N. Atochin, P. L. Huang, K. I. Andreasson, C. J. Kuo, and H. Dai. Through-skull fluorescence imaging of the brain in a new near-infrared window. *Nat. Photon.*, 8(9):723–730, 2014.

[16] J. G. Elmore, M. B. Barton, V. M. Moceri, S. Polk, P. J. Arena, and S. W. Fletcher. Ten-Year Risk of False Positive Screening Mammograms and Clinical Breast Examinations. *New Eng. J. Med.*, 338(16):1089–1096, 1998.

[17] P. T. Huynh, A. M. Jarolimek, and S. Daye. The false-negative mammogram. *RadioGraphics*, 18(5):1137–1154, 1998.

[18] B. W. Pogue, S. P. Poplack, T. O. McBride, W. A. Wells, K. S. Osterman, U. L. Osterberg, and K. D. Paulsen. Quantitative Hemoglobin Tomography with Diffuse Near-Infrared Spectroscopy: Pilot Results in the Breast. *Radiology*, 218(1):261–266, 2001.

[19] A. Koenig, L. Hervé, A. Da Silva, J.-M. Dinten, J. Boutet, M. Berger, I. Texier, P. Peltié, P. Rizo, V. Josserand, and J.-L. Coll. Whole body small animal examination with a diffuse optical tomography instrument. *Nucl. Instrum. Met. A*, 571(1-2):56–59, 2007.

[20] Tuan Vo-Dinh. *Biomedical Photonics Handbook*. CRC Press, 2003.

[21] Akira Ishimaru. *Wave propagation and scattering in random media: Volume 1*. Academic Press, New York, 1978.

[22] Akira Ishimaru. *Wave propagation and scattering in random media: Volume 2*. Academic Press, 1978.

[23] C. F. Bohren and D. R. Huffman. *Absorption and scattering of light by small particles*. Wiley-VCH, 1983.

[24] Steven L. Jacques. Optical properties of biological tissues: a review. *Phys. Med. Biol.*, 58(11):R37, 2013.

[25] H. J. van Staveren, C. J. M. Moes, J. van Marie, S. A. Prahl, and M. J. C. van Gemert. Light scattering in Intralipid-10% in the wavelength range of 400-1100 nm. *Appl. Opt.*, 30(31):4507–4514, 1991.

[26] J. Bertolotti, E. G. van Putten, C. Blum, A. Lagendijk, W. L. Vos, and A. P. Mosk. Non-invasive imaging through opaque scattering layers. *Nature*, 491(7423):232–234, 2012.

[27] Joseph W. Goodman. *Speckle phenomena in optics: theory and applications*. Roberts & Co, 2007.

[28] Joseph W. Goodman. Some fundamental properties of speckle. *J. Opt. Soc. Am.*, 66(11):1145–1150, 1976.

[29] M. Gross, P. Goy, B. C. Forget, M. Atlan, F. Ramaz, A. C. Boccara, and A. K. Dunn. Heterodyne detection of multiply scattered monochromatic light with a multipixel detector. *Opt. Lett.*, 30(11):1357–1359, 2005.

[30] Vasilis Ntziachristos. Going deeper than microscopy: the optical imaging frontier in biology. *Nat. Methods*, 7(8):603–614, 2010.

[31] Shinya Inoue. Foundations of Confocal Scanned Imaging in Light Microscopy. In James B. Pawley, editor, *Handbook Of Biological Confocal Microscopy*, pages 1–19. Springer US, 2006.

[32] W. Denk, . H. Strickler, and W. W. Webb. Two-Photon Laser Scanning Fluorescence Microscopy. *Science*, 248(4951):73–76, 1990.

[33] M. D. Cahalan, I. Parker, S. H. Wei, and M. J. Miller. Two-photon tissue imaging: seeing the immune system in a fresh light. *Nat. Rev. Immunol.*, 2(11):872–880, 2002.

[34] D. Huang, E. A. Swanson, C. P. Lin, J. S. Schuman, W. G. Stinson, W. Chang, M. R. Hee, T. Flotte, K. Gregory, C. A. Puliafito, and J. G. Fujimoto. Optical Coherence Tomography. *Science*, 254(5035):1178–1181, 1991.

[35] A. Dubois, K. Grieve, G. Moneron, R. Lecaque, L. Vabre, and C. Boccara. Ultrahigh-resolution full-field optical coherence tomography. *Appl. Opt.*, 43(14):2874–2883, 2004.

[36] J. L. Martin, Y. Lecarpentier, A. Antonetti, and G. Grillon. Picosecond laser stereometry light scattering measurements on biological material. *Med. Biol. Eng. Comput.*, 18(2):250–252, 2004.

[37] S. Kang, S. Jeong, W. Choi, H. Ko, T. D. Yang, J. H. Joo, J.-S. Lee, Y.-S. Lim, Q.-H. Park, and W. Choi. Imaging deep within a scattering medium using collective accumulation of single-scattered waves. *Nat. Photon.*, 9:253–258, 2015.

[38] A. Badon, D. Li, G. Lerosey, A. C. Boccara, M. Fink, and A. Aubry. Smart optical coherence tomography for ultra-deep imaging through highly scattering media. *arXiv:1510.08613 [physics]*, 2015.

[39] C. Prada and M. Fink. Eigenmodes of the time reversal operator: A solution to selective focusing in multiple-target media. *Wave Motion*, 20(2):151–163, 1994.

[40] J. C. Hebden, D. J. Hall, and D. T. Delpy. The spatial resolution performance of a time-resolved optical imaging system using temporal extrapolation. *Med. Phys.*, 22(2):201–208, 1995.

[41] D. A. Boas, D. H. Brooks, E. L. Miller, C. A. DiMarzio, M. Kilmer, R. J. Gaudette, and Quan Zhang. Imaging the body with diffuse optical tomography. *IEEE Signal Proc. Mag.*, 18(6):57–75, 2001.

[42] Simon R. Arridge. Optical tomography in medical imaging. *Inverse Probl.*, 15(2):R41, 1999.

[43] D. A. Boas and A. K. Dunn. Laser speckle contrast imaging in biomedical optics. *J. Biomed. Opt*, 15(1):011109–011109–12, 2010.

[44] J. David Briers. Laser Doppler, speckle and related techniques for blood perfusion mapping and imaging. *Physiol. Meas.*, 22(4):R35, 2001.

[45] O. Katz, P. Heidmann, M. Fink, and S. Gigan. Non-invasive single-shot imaging through scattering layers and around corners via speckle correlations. *Nat. Photon.*, 8(10):784–790, 2014.

[46] M. Fink and M. Tanter. Multiwave imaging and super resolution. *Phys. Today*, 63(2):28–33, 2010.

[47] C. M. Sehgal and J. F. Greenleaf. Scattering of Ultrasound by Tissues. *Ultrasonic Imaging*, 6(1):60–80, 1984.

[48] Paul Beard. Biomedical photoacoustic imaging. *Interface Focus*, 1(4):602–631, 2011.

[49] S. A. Akhmanov, V. E. Gusev, and A. A. Karabutov. Pulsed laser optoacoustics: Achievements and perspective. *Infrared Physics*, 29(2):815–838, 1989.

[50] K. Daoudi, P.J. van den Berg, O. Rabot, A. Kohl, S. Tisserand, P. Brands, and W. Steenbergen. Handheld probe integrating laser diode and ultrasound transducer array for ultrasound/photoacoustic dual modality imaging. *Opt. Express*, 22(21):26365, 2014.

[51] A. P. Jathoul, J. Laufer, O. Ogunlade, B. Treeby, B. Cox, E. Zhang, P. Johnson, A. R. Pizzey, B. Philip, T. Marafioti, M. F. Lythgoe, R. B. Pedley, M. A. Pule, and P. Beard. Deep in vivo photoacoustic imaging of mammalian tissues using a tyrosinase-based genetic reporter. *Nat. Photon.*, 9:239–246, 2015.

[52] Baptiste Jayet. *Acousto-optic and photoacoustic imaging of scattering media using wavefront adaptive holography techniques in $NdYO_4$*. phdthesis, Université Pierre et Marie Curie - Paris VI, 2015.

[53] A. Hochreiner, T. Berer, H. Grün, M. Leitner, and P. Burgholzer. Photoacoustic imaging using an adaptive interferometer with a photorefractive crystal. *J. Biophoton.*, 5(7):508–517, 2012.

[54] C. Kim, T. N. Erpelding, L. Jankovic, M. D. Pashley, and L. V. Wang. Deeply penetrating in vivo photoacoustic imaging using a clinical ultrasound array system. *Biomed. Opt. Express*, 1(1):278–284, 2010.

[55] Y. Zhou, G. Li, L. Zhu, C.e Li, L. A. Cornelius, and L. V. Wang. Handheld photoacoustic probe to detect both melanoma depth and volume at high speed *in vivo*. *J. Biophoton.*, 8(11-12):961–967, 2015.

[56] C. Li, A. Aguirre, J. Gamelin, A. Maurudis, Q. Zhu, and L. V. Wang. Real-time photoacoustic tomography of cortical hemodynamics in small animals. *J. Biomed. Opt*, 15(1):010509–010509–3, 2010.

[57] L. Xiang, B. Wang, L. Ji, and H. Jiang. 4-D Photoacoustic Tomography. *Sci. Rep.*, 3:1113, 2013.

[58] J. Yao, L. Wang, J.-M. Yang, K. I. Maslov, T. T. W. Wong, L. Li, C.-H. Huang, J. Zou, and L. V. Wang. High-speed label-free functional photoacoustic microscopy of mouse brain in action. *Nat. Methods*, 2015.

[59] M. Heijblom, W. Steenbergen, and S. Manohar. Clinical Photoacoustic Breast Imaging: The Twente experience. *IEEE Pulse*, 6(3):42–46, 2015.

[60] S. Mallidi, G. P. Luke, and S. Emelianov. Photoacoustic imaging in cancer detection, diagnosis, and treatment guidance. *Trends in Biotechnology*, 29(5):213–221, 2011.

[61] W. Leutz and G. Maret. Ultrasonic modulation of multiply scattered light. *Physica B*, 204(1–4):14–19, 1995.

[62] P. Debye and F. W. Sears. On the Scattering of Light by Supersonic Waves. *PNAS*, 18(6):409–414, 1932.

[63] R. Lucas and P. Biquard. Propriétés optiques des milieux solides et liquides soumis aux vibrations élastiques ultra sonores. *J. Phys. Radium*, 3(10):464–477, 1932.

[64] L. V. Wang, S. L. Jacques, and X. Zhao. Continuous-wave ultrasonic modulation of scattered laser light to image objects in turbid media. *Opt. Lett.*, 20(6):629–631, 1995.

[65] J.-B. Laudereau, E. Benoit à La Guillaume, V. Servois, P. Mariani, A. A. Grabar, M. Tanter, J.-L. Gennisson, and F. Ramaz. Multi-modal acousto-optic/ultrasound imaging of *ex vivo* liver tumors at 790 nm using a $Sn_2P_2S_6$ wavefront adaptive holographic setup. *J. Biophoton.*, 8:429–436, 2014.

[66] Emilie Benoit À La Guillaume. *Imagerie acousto-optique dans les milieux diffusants épais : de l'amélioration technique à l'application pré-clinique ex vivo*. phdthesis, Université Pierre et Marie Curie - Paris VI, 2013.

[67] P. Lai, J. R. McLaughlan, A. B. Draudt, T. W. Murray, R. O. Cleveland, and R. A. Roy. Real-Time Monitoring of High-Intensity Focused Ultrasound Lesion Formation Using Acousto-Optic Sensing. *Ultrasound Med. Biol.*, 37(2):239–252, 2011.

[68] Gail ter Haar. Ultrasound focal beam surgery. *Ultrasound Med. Biol.*, 21(9):1089–1100, 1995.

[69] J. E. P. Honeysett, E. Stride, J. Deng, and T. S. Leung. An algorithm for sensing venous oxygenation using ultrasound-modulated light enhanced by microbubbles. pages 82232Z–9. International Society for Optics and Photonics, 2012.

[70] M. Kobayashi, T. Mizumoto, Y. Shibuya, M. Enomoto, and M. Takeda. Fluorescence tomography in turbid media based on acousto-optic modulation imaging. *Appl. Phys. Lett.*, 89(18):181102, 2006.

[71] M. Kobayashi, N. Kikuchi, and A. Sato. Optical tomography of fluorophores in dense scattering media based on ultrasound-enhanced chemiluminescence. *Appl. Phys. Lett.*, 106(2):021103, 2015.

[72] K. Daoudi, A. Hussain, E. Hondebrink, and W. Steenbergen. Correcting photoacoustic signals for fluence variations using acousto-optic modulation. *Opt. Express*, 20(13):14117–14129, 2012.

[73] A. Lev and B. Sfez. Acousto-optical detection of hidden objects via speckle based imaging. *Opt. Express*, 23(20):26460–26471, 2015.

[74] X. Xu, H. Liu, and L. V. Wang. Time-reversed ultrasonically encoded optical focusing into scattering media. *Nat. Photon.*, 5(3):154–157, 2011.

[75] H. Ruan, M. Jang, B. Judkewitz, and C. Yang. Iterative Time-Reversed Ultrasonically Encoded Light Focusing in Backscattering Mode. *Sci. Rep.*, 4(7156):1–4, 2014.

[76] G. D. Mahan, W. E. Engler, J. J. Tiemann, and E. Uzgiris. Ultrasonic tagging of light: Theory. *PNAS*, 95(24):14015–14019, 1998.

[77] M. Kempe, M. Larionov, D. Zaslavsky, and A. Z. Genack. Acousto-optic tomography with multiply scattered light. *J. Opt. Soc. Am. A*, 14(5):1151–1158, 1997.

[78] Lihong V. Wang. Mechanisms of Ultrasonic Modulation of Multiply Scattered Coherent Light: An Analytic Model. *Phys. Rev. Lett.*, 87(4):043903, 2001.

[79] M. Gross, F. Ramaz, B. Forget, M. Atlan, A. Boccara, P. Delaye, and G. Roosen. Theoretical description of the photorefractive detection of the ultrasound modulated photons in scattering media. *Opt. Express*, 13(18):7097–7112, 2005.

[80] Sava Sakadžić and Lihong V. Wang. Modulation of multiply scattered coherent light by ultrasonic pulses: An analytical model. *Phys. Rev. E*, 72(3):036620, 2005.

[81] S. Lévêque, A. C. Boccara, M. Lebec, and H. Saint-Jalmes. Ultrasonic tagging of photon paths in scattering media: parallel speckle modulation processing. *Opt. Lett.*, 24(3):181–183, 1999.

[82] G. Yao and L. V. Wang. Theoretical and experimental studies of ultrasound-modulated optical tomography in biological tissue. *Appl. Opt.*, 39(4):659–664, 2000.

[83] K. Barjean, K. Contreras, J.-B. Laudereau, E. Tinet, D. Ettori, F. Ramaz, and J.-M. Tualle. Fourier transform acousto-optic imaging with a custom-designed CMOS smart-pixels array. *Opt. Lett.*, 40(5):705–708, 2015.

[84] S. P. Morgan, C. Li, B. R. Hayes-Gill, N. B. E. Sawyer, and C. Kongsavatsak. CMOS detection methods in ultrasound modulated optical tomography. volume 6086, pages 608615–8, 2006.

[85] Y. Liu, Y. Shen, C. Ma, J. Shi, and L. V. Wang. Lock-in camera based heterodyne holography for ultrasound-modulated optical tomography inside dynamic scattering media. *Appl. Phys. Lett.*, 108(23):231106, 2016.

[86] J. Li, G. Ku, and L. V. Wang. Ultrasound-modulated optical tomography of biological tissue by use of contrast of laser speckles. *Appl. Opt.*, 41(28):6030–6035, 2002.

[87] R. Zemp, S. Sakadžić, and L. V. Wang. Stochastic explanation of speckle contrast detection in ultrasound-modulated optical tomography. *Phys. Rev. E*, 73(6):061920, 2006.

[88] S.G. Resink, E. Hondebrink, and W. Steenbergen. Towards acousto-optic tissue imaging with nanosecond laser pulses. *Opt. Express*, 22(3):3564, 2014.

[89] S. Resink, E. Hondebrink, and W. Steenbergen. Solving the speckle decorrelation challenge in acousto-optic sensing using tandem nanosecond pulses within the ultrasound period. *Opt. Lett.*, 39(22):6486–6489, 2014.

[90] S. G. Resink and W. Steenbergen. Tandem-pulsed acousto-optics: an analytical framework of modulated high-contrast speckle patterns. *Phys. Med. Biol.*, 60(11):4371, 2015.

[91] S. G. Resink and W. Steenbergen. Tandem pulsed acousto-optics: obtaining the tagged light fraction from modulated non-ideal speckle patterns. *Phys. Med. Biol.*, 61(2):504, 2016.

[92] M. Gross, P. Goy, and M. Al-Koussa. Shot-noise detection of ultrasound-tagged photons in ultrasound-modulated optical imaging. *Opt. Lett.*, 28(24):2482–2484, 2003.

[93] M. Gross and M. Atlan. Digital holography with ultimate sensitivity. *Opt. Lett.*, 32(8):909–911, 2007.

[94] F. Verpillat, F. Joud, M. Atlan, and M. Gross. Digital Holography at Shot Noise Level. *J. Display Technol.*, 6(10):455–464, 2010.

[95] P. Delaye, S. de Rossi, and G. Roosen. High-amplitude vibrations detection on rough surfaces using a photorefractive velocimeter. *Opt. Laser Eng.*, 33(5):335–347, 2000.

[96] B. Campagne, A. Blouin, L. Pujol, and J.-P. Monchalin. Compact and fast response ultrasonic detection device based on two-wave mixing in a gallium arsenide photorefractive crystal. *Rev. Sci. Instrum.*, 72(5):2478, 2001.

[97] T. W. Murray, L. Sui, G. Maguluri, R. A. Roy, A. Nieva, F. Blonigen, and C. A. DiMarzio. Detection of ultrasound-modulated photons in diffuse media using the photorefractive effect. *Opt. Lett.*, 29(21):2509–2511, 2004.

[98] F. Ramaz, B. Forget, M. Atlan, A. C. Boccara, M. Gross, P. Delaye, and G. Roosen. Photorefractive detection of tagged photons in ultrasound modulated optical tomography of thick biological tissues. *Opt. Express*, 12(22):5469–5474, 2004.

[99] Y. Suzuki, P. Lai, X. Xu, and L. V. Wang. High-sensitivity ultrasound-modulated optical tomography with a photorefractive polymer. *Opt. Lett.*, 38(6):899–901, 2013.

[100] U. Bortolozzo, S. Residori, A. Petrosyan, and J.-P. Huignard. Pattern formation and direct measurement of the spatial resolution in a photorefractive liquid crystal light valve. *Opt. Comm.*, 263(2):317–321, 2006.

[101] U. Bortolozzo, S. Residori, and J.-P. Huignard. Picometer detection by adaptive holographic interferometry in a liquid-crystal light valve. *Opt. Lett.*, 34(13):2006–2008, 2009.

[102] U. Bortolozzo, D. Dolfi, J.-P. Huignard, S. Molin, A. Peigné, and S. Residori. Self-adaptive vibrometry with CMOS-LCOS digital holography. *Opt. Lett.*, 40(7):1302, 2015.

[103] B. Jayet, J-P. Huignard, and F. Ramaz. Fast wavefront adaptive holography in Nd:YVO_4 for ultrasound optical tomography imaging. *Opt. Express*, 22(17):20622, 2014.

[104] B. Jayet, J.-P. Huignard, and F. Ramaz. Optical phase conjugation in Nd:YVO_4 for acousto-optic detection in scattering media. *Opt. Lett.*, 38(8):1256–1258, 2013.

[105] P. Lai, X. Xu, H. Liu, and L. V. Wang. Time-reversed ultrasonically encoded optical focusing in biological tissue. *J. Biomed. Opt.*, 17(3):0305061–0305063, 2012.

[106] Jean-Pierre Monchalin. Optical detection of ultrasound at a distance using a confocal Fabry–Perot interferometer. *Appl. Phys. Lett.*, 47(1):14–16, 1985.

[107] S. Sakadžić and L. V. Wang. High-resolution ultrasound-modulated optical tomography in biological tissues. *Opt. Lett.*, 29(23):2770, 2004.

[108] Y. Li, H. Zhang, C. Kim, K. H. Wagner, Ph. Hemmer, and L. V. Wang. Pulsed ultrasound-modulated optical tomography using spectral-hole burning as a narrowband spectral filter. *Appl. Phys. Lett.*, 93(1):011111, 2008.

[109] J. Li and L. V. Wang. Ultrasound-modulated optical computed tomography of biological tissues. *Appl. Phys. Lett.*, 84(9):1597, 2004.

[110] L. Sui, R. A. Roy, C. A. DiMarzio, and T. W. Murray. Imaging in diffuse media with pulsed-ultrasound-modulated light and the photorefractive effect. *Appl. Opt.*, 44(19):4041–4048, 2005.

[111] Max Lesaffre. *Imagerie acousto-optique de milieux diffusants épais par détection photoréfractive*. phdthesis, Université Pierre et Marie Curie - Paris VI, 2009.

[112] M. Lesaffre, S. Farahi, M. Gross, P. Delaye, A. C. Boccara, and F. Ramaz. Acousto-optical coherence tomography using random phase jumps on ultrasound and light. *Opt. Express*, 17(20):18211–18218, 2009.

[113] M. Lesaffre, S. Farahi, A. C. Boccara, F. Ramaz, and M. Gross. Theoretical study of acousto-optical coherence tomography using random phase jumps on ultrasound and light. *J. Opt. Soc. Am. A*, 28(7):1436–1444, 2011.

[114] M. Lesaffre, S. Farahi, F. Ramaz, and M. Gross. Experimental study of z resolution in acousto-optical coherence tomography using random phase jumps on ultrasound and light. *Appl. Opt.*, 52(15):949–957, 2013.

[115] K. Barjean, F. Ramaz, and J.-M. Tualle. Theoretical study of Fourier-transform acousto-optic imaging. *J. Opt. Soc. Am. A*, 33(5):854–862, 2016.

[116] E. Bossy, L. Sui, T. W. Murray, and R. A. Roy. Fusion of conventional ultrasound imaging and acousto-optic sensing by use of a standard pulsed-ultrasound scanner. *Opt. Lett.*, 30(17):744–746, 2005.

[117] S. Farahi, E. Benoit à La Guillaume, A. A. Grabar, J.-P. Huignard, and F. Ramaz. Time resolved three-dimensional acousto-optic imaging of thick scattering media. *Opt. Lett.*, 37(13):2754–2756, 2012.

[118] Salma Farahi. *Spectroscopic and holographic filtering applied to acousto-optic imaging of thick scattering media*. Theses, Universié Pierre et Marie Curie - Paris VI, 2011.

[119] P. Delaye, A. Blouin, D. Drolet, L.-A. De Montmorillon, G. Roosen, and J.-P. Monchalin. Detection of ultrasonic motion of a scattering surface by photorefractive InP:Fe under an applied dc field. *J. Opt. Soc. Am. B*, 14(7):1723–1734, 1997.

[120] Herwig Kogelnik. Coupled Wave Theory for Thick Hologram Gratings. *Bell System Technical Journal*, 48(9):2909–2947, 1969.

[121] Pochi Yeh. *Introduction to photorefractive nonlinear optics*. Wiley Interscience, 1993.

[122] L.-A. De Montmorillon, P. Delaye, J.-C. Launay, and G. Roosen. Novel theoretical aspects on photorefractive ultrasonic detection and implementation of a sensor with an optimum sensitivity. *J. Appl. Phys.*, 82(12):5913–5922, 1997.

[123] A. A. Grabar, M. Jazbinšek, A. N. Shumelyuk, Y. M. Vysochanskii, G. Montemezzani, and P. Günter. Photorefractive effects in $Sn_2P_2S_6$. In P. Günter and J.-P. Huignard, editors, *Photorefractive Materials and their Applications*, pages 327–362. Springer US, 2007.

[124] X. Xu, H. Zhang, P. Hemmer, D. Qing, C. Kim, and L. V. Wang. Photorefractive detection of tissue optical and mechanical properties by ultrasound modulated optical tomography. *Opt. Lett.*, 32(6):656–658, 2007.

[125] M. Lesaffre, F. Jean, F. Ramaz, A. C. Boccara, M. Gross, P. Delaye, and G. Roosen. In situ monitoring of the photorefractive response time in a self-adaptive wavefront holography setup developed for acousto-optic imaging. *Opt. Express*, 15(3):1030, 2007.

[126] D. Haertle, G. Caimi, A. Haldi, G. Montemezzani, P. Günter, A. A. Grabar, I. M. Stoika, and Y. M. Vysochanskii. Electro-optical properties of $Sn_2P_2S_6$. *Opt. Comm.*, 215(4):333–343, 2003.

[127] T. Bach, M. Jazbinšek, G. Montemezzani, P. Günter, A. A. Grabar, and Y. M. Vysochanskii. Tailoring of infrared photorefractive properties of $Sn_2P_2S_6$ crystals by Te and Sb doping. *J. Opt. Soc. Am. B*, 24(7):1535–1541, 2007.

[128] P. Mariani, S. Piperno-Neumann, V. Servois, M. G. Berry, T. Dorval, C. Plancher, J. Couturier, C. Levy-Gabriel, L. Lumbroso-Le Rouic, L. Desjardins, and R. J. Salmon. Surgical management of liver metastases from uveal melanoma: 16 years' experience at the Institut Curie. *Eur. J. Surg. Oncol.*, 35(11):1192–1197, 2009.

[129] V. Servois, P. Mariani, C. Malhaire, S. Petras, S. Piperno-Neumann, C. Plancher, C. Levy-Gabriel, L. Lumbroso-Le Rouic, L. Desjardins, and R. J. Salmon. Preoperative staging of liver metastases from uveal melanoma by magnetic resonance imaging (MRI) and fluorodeoxyglucose-positron emission tomography (FDG-PET). *Eur. J. Surg. Oncol.*, 36(2):189–194, 2010.

[130] J. R. van der Vorst, B. E. Schaafsma, M. Hutteman, F. P. R. Verbeek, G.-J. Liefers, H. H. Hartgrink, V. T. H. B. M. Smit, C. W. G. M. Löwik, C. J. H. van de Velde, J. V. Frangioni, and A. L. Vahrmeijer. Near-infrared fluorescence-guided resection of colorectal liver metastases. *Cancer*, 119(18):3411–3418, 2013.

[131] S. T. Flock, M. S. Patterson, B. C. Wilson, and D. R. Wyman. Monte Carlo modeling of light propagation in highly scattering tissues. I. Model predictions and comparison with diffusion theory. *Biomedical Engineering, IEEE Transactions on*, 36(12):1162–1168, 1989.

[132] S. Powell, S. Arridge, and T. S. Leung. Gradient-based quantitative image reconstruction in ultrasound-modulated optical tomography: first harmonic measurement type in a linearised diffusion formulation. *IEEE T. Med. Imaging*, pages 1–12, 2015.

[133] C. Kim and L. V. Wang. Multi-optical-wavelength ultrasound-modulated optical tomography: a phantom study. *Opt. Lett.*, 32(16):2285–2287, 2007.

[134] P. Lai, R. A. Roy, and T. W. Murray. Quantitative characterization of turbid media using pressure contrast acousto-optic imaging. *Opt. Lett.*, 34(18):2850–2852, 2009.

[135] Puxiang Lai. *Photorefractive crystal-based acousto-optic imaging in the near-infrared and its applications*. PhD thesis, Boston University, 2011.

[136] S. Gunadi, S. Powell, C. E. Elwell, and T. S. Leung. Optimization of the acousto-optic signal detection in cylindrical geometry. pages 756431–6, 2010.

[137] P. Lai, X. Xu, and L. V. Wang. Ultrasound-modulated optical tomography at new depth. *J. Biomed. Opt.*, 17(6):066006, 2012.

[138] Gabor T. Herman. *Fundamentals of computerized tomography: image reconstruction from projections*. Advances in pattern recognition. Springer, 2009.

[139] M. Dahlbom, E. J. Hoffman, C. K. Hoh, C. Schiepers, G. Rosenqvist, R. A. Hawkins, and M. E. Phelps. Whole-Body Positron Emission Tomography: Part I. Methods and Performance Characteristics. *J. Nucl. Med.*, 33(6):1191–1199, 1992.

[140] J. Sharpe, U. Ahlgren, P. Perry, B. Hill, A. Ross, J. Hecksher-Sørensen, R. Baldock, and D. Davidson. Optical projection tomography as a tool for 3D microscopy and gene expression studies. *Science*, 296(5567):541–545, 2002.

[141] J. Huisken, J. Swoger, F. Del Bene, J. Wittbrodt, and E. H. K. Stelzer. Optical sectioning deep inside live embryos by Selective Plane Illumination Microscopy. *Science*, 305(5686):1007–1009, 2004.

[142] G. Ku and L. V. Wang. Deeply penetrating photoacoustic tomography in biological tissues enhanced with an optical contrast agent. *Opt. Lett.*, 30(5):507–509, 2005.

[143] J. Xia, M. R. Chatni, K. Maslov, Z. Guo, K. Wang, M. Anastasio, and L. V. Wang. Whole-body ring-shaped confocal photoacoustic computed tomography of small animals *in vivo*. *J. Biomed. Opt.*, 17(5), 2012.

[144] P. van Es, S. K. Biswas, H. J. Bernelot Moens, W. Steenbergen, and S. Manohar. Initial results of finger imaging using photoacoustic computed tomography. *J. Biomed. Opt.*, 19(6):060501–060501, 2014.

[145] P. Kuchment and L. Kunyansky. Synthetic focusing in ultrasound modulated tomography. *Inverse Probl. Imaging*, 4(14):665–673, 2010.

[146] J. Provost, W. Kwiecinski, M. Fink, M. Tanter, and M. Pernot. Ultrafast acoustoelectric imaging. In 2014 IEEE, editor, *Proceedings of IEEE 11th International Symposium on Biomedical Imaging*, pages 702–705, 2014.

[147] L. Sandrin, S. Catheline, M. Tanter, X. Hennequin, and M. Fink. Time-resolved pulsed elastography with ultrafast ultrasonic imaging. *Ultrasonic Imaging*, 21(4):259–272, 1999.

[148] G. Montaldo, M. Tanter, J. Bercoff, N. Benech, and M. Fink. Coherent plane-wave compounding for very high frame rate ultrasonography and transient elastography. *IEEE Trans. Ultrason. Ferr.*, 56(13):489–506, 2009.

[149] G. S. Alberti, H. Ammari, F. Romero, and T. Wintz. Mathematical Analysis of Ultrafast Ultrasound Imaging. *arXiv:1604.04604 [math]*, 2016. arXiv: 1604.04604.

[150] Ronald N. Bracewell. Strip Integration in Radio Astronomy. *Aust. J. Phys.*, 9(2):198–217, 1956.

[151] D. J. De Rosier and A. Klug. Reconstruction of Three Dimensional Structures from Electron Micrographs. *Nature*, 217(5124):130–134, 1968.

[152] S. Cha and C. M. Vest. Interferometry and reconstruction of strongly refracting asymmetric-refractive-index fields. *Opt. Lett.*, 4(10):311, 1979.

[153] N. G. Ramachandran and V. A. Lakshminarayanan. Three-dimensional reconstruction from radiographs and electron micrographs: application of convolutions instead of fourier transforms. *PNAS*, 68(19):2236–2240, 1971.

[154] R. Rangayyan, A. P. Dhawan, and R. Gordon. Algorithms for limited-view computed tomography: an annotated bibliography and a challenge. *Appl. Opt.*, 24(23):4000–4012, 1985.

[155] T. Sato, S. J. Norton, M. Linzer, O. Ikeda, and M. Hirama. Tomographic image reconstruction from limited projections using iterative revisions in image and transform spaces. *Appl. Opt.*, 20(3):395–399, 1981.

[156] G. Rousseau, A. Blouin, and J.-P. Monchalin. Ultrasound-modulated optical imaging using a high-power pulsed laser and a double-pass confocal Fabry-Perot interferometer. *Opt. Lett.*, 34(21):3445–3447, 2009.

[157] G. F. Imbusch and R. Kopelman. Optical spectroscopy of electronic centers in solids. In Professor William M. Yen and Peter M. Selzer M.D, editors, *Laser Spectroscopy of Solids*, number 49 in Topics in Applied Physics, pages 1–37. Springer Berlin Heidelberg, 1981.

[158] Anne Louchet. *Manipulation optique d'une cohérence de spin nucléaire dans l'ion thulium en matrice cristalline*. PhD thesis, Université Paris XI, 2008.

[159] B. Henderson and G. F. Imbusch. *Optical Spectroscopy of Inorganic Solids*. Monographs on the physics and chemistry of materials. Oxford University Press, 1989.

[160] Roger M Macfarlane. High-resolution laser spectroscopy of rare-earth doped insulators: a personal perspective. *Journal of Luminescence*, 100(1–4):1–20, 2002.

[161] M. G. Shelyapina, V. S. Kasperovich, and P. Wolfers. Electronic structure and electric-field-gradients distribution in $Y_3Al_5O_{12}$: An *ab initio* study. *Journal of Physics and Chemistry of Solids*, 67(4):720–724, 2006.

[162] Ł. Dobrzycki, E. Bulska, D. A. Pawlak, Z. Frukacz, and K. Woźniak. Structure of YAG Crystals Doped/Substituted with Erbium and Ytterbium. *Inorg. Chem.*, 43(24):7656–7664, 2004.

[163] Francis S. Galasso. *Structure and Properties of Inorganic Solids*. Pergamon Press, 1970.

[164] C. Greiner, B. Boggs, T. Loftus, T. Wang, and T. W. Mossberg. Polarization-dependent Rabi frequency beats in the coherent response of Tm^{3+} in YAG. *Phys. Rev. A*, 60(4):R2657–R2660, 1999.

[165] J. B. Gruber, M. E. Hills, R. M. Macfarlane, C. A. Morrison, G. A. Turner, G. J. Quarles, G. J. Kintz, and L. Esterowitz. Spectra and energy levels of $Tm^{3+} : Y_3Al_5O_{12}$. *Phys. Rev. B*, 40(14):9464–9478, November 1989.

[166] G. Gorju, A. Louchet, D. Paboeuf, F. Bretenaker, F. Goldfarb, T. Chanelière, I. Lorgeré, J. L. Le Gouët, O. Guillot-Noël, and Ph Goldner. Stimulated optical pumping in a Tm3+: YAG crystal. *Journal of Physics: Condensed Matter*, 19(38):386226, 2007.

[167] Robert C. Hilborn. Einstein coefficients, cross sections, f values, dipole moments, and all that. *American Journal of Physics*, 50(11):982–986, 1982.

[168] L. Allen and J. H. Eberly. *Optical Resonance and Two-Level Atoms*. Wiley Interscience, 1975.

[169] Arthur M. Stoneham. Shapes of inhomogeneously broadened resonance lines in solids. *Rev. Mod. Phys.*, 41(1):82–108, 1969.

[170] G. Gorju, V. Crozatier, I. Lorgeré, J. L. Le Gouët, and F. Bretenaker. 10-GHz bandwidth RF spectral analyzer with MHz resolution based on spectral hole burning in Tm^{3+} :YAG. *IEEE Photonics Technology Letters*, 17(11):2385–2387, November 2005.

[171] Roger M. Macfarlane. Photon-echo measurements on the trivalent thulium ion. *Opt. Lett.*, 18:1958–1960, 1993.

[172] Roger M. Macfarlane. Direct process thermal line broadening in Tm:YAG. *Journal of luminescence*, 85(4):181–186, 2000.

[173] G. Armagan, A. M. Buoncristiani, and B. Di Bartolo. Excited state dynamics of thulium ions in Yttrium Aluminum Garnets. *Optical Materials*, 1(1):11–20, 1992.

[174] Anthony E. Siegman. *Lasers*. University Science Books, Mill Valley, Calif., 1986.

[175] J. Caird, L. DeShazer, and J. Nella. Characteristics of room-temperature 2.3-μm laser emission from Tm^{3+} in YAG and $YAlO_3$. *IEEE Journal of Quantum Electronics*, 11(11), 1975.

[176] S. A. Payne, L. L. Chase, L. K. Smith, W. L. Kway, and W. F. Krupke. Infrared cross-section measurements for crystals doped with Er^{3+}, Tm^{3+}, and Ho^{3+}. *IEEE Journal of Quantum Electronics*, 28(11):2619–2630, 1992.

[177] Y. Li, Ph. Hemmer, C. Kim, H. Zhang, and L. V. Wang. Detection of ultrasound-modulated diffuse photons using spectral-hole burning. *Optics express*, 16(19):14862–14874, 2008.

[178] Matthieu Bonarota. *Optimisation de la programmation d'un cristal dopé aux ions de terres rares, opérant comme processeur analogique d'analyse spectrale RF, ou de stockage d'information quantique*. PhD thesis, Paris 11, 2012.

[179] R. W. P. Drever, J. L. Hall, F. V. Kowalski, J. Hough, G. M. Ford, A. J. Munley, and H. Ward. Laser phase and frequency stabilization using an optical resonator. *Appl. Phys. B*, 31(2):97–105, 1983.

[180] Eric D. Black. An introduction to Pound–Drever–Hall laser frequency stabilization. *American Journal of Physics*, 69(1):79–87, 2001.

[181] N. Ohlsson, M. Nilsson, S. Kröll, and R. K. Mohan. Long-time-storage mechanism for Tm:YAG in a magnetic field. *Opt. Lett.*, 28(6):450–452, 2003.

[182] O. Guillot-Noël, Ph. Goldner, E. Antic-Fidancev, and J. L. Le Gouët. Analysis of magnetic interactions in rare-earth-doped crystals for quantum manipulation. *Phys. Rev. B*, 71(17):174409, 2005.

[183] F. de Seze, A. Louchet, V. Crozatier, I. Lorgeré, F. Bretenaker, J.-L. Le Gouët, O. Guillot-Noël, and Ph. Goldner. Experimental tailoring of a three-level λ system in tm^{3+} : yag. *Phys. Rev. B*, 73(8):085112, 2006.

[184] A. Louchet, J. S. Habib, V. Crozatier, I. Lorgeré, F. Goldfarb, F. Bretenaker, J.-L. Le Gouët, O. Guillot-Noël, and Ph. Goldner. Branching ratio measurement of a λ system in Tm^{3+} : YAG under a magnetic field. *Phys. Rev. B*, 75(3):035131, 2007.

[185] Ph. Goldner, O. Guillot-Noël, A. Louchet, F. de Sèze, V. Crozatier, I. Lorgeré, F. Bretenaker, and J. L. Le Gouët. Hyperfine structure of Tm^{3+} in YAG for quantum storage applications. *Optical Materials*, 28(6–7):649–654, 2006.

[186] R. L. Ahlefeldt, M. F. Pascual-Winter, A. Louchet-Chauvet, T. Chanelière, and J.-L. Le Gouët. Optical measurement of heteronuclear cross-relaxation interactions in Tm:YAG. *Phys. Rev. B*, 92(9):094305, 2015.

[187] Louis-Anne De Montmorillon. *Capteur photorefractif d'ultrasons : choix et optimisation d'un matériau holographique ; étude et réalisation d'un prototype*. phdthesis, Université Paris Sud - Paris XI, 1997.

[188] N. V. Kukhtarev, V. B. Markov, S. G. Odulov, M. S. Soskin, and V. L. Vinetskii. Holographic storage in electrooptic crystals. I. steady state. *Ferroelectrics*, 22(1):949–960, 1978.

[189] M. C. Bashaw, M. Jeganathan, and L. Hesselink. Theory of two-center transport in photorefractive media for low-intensity, continuous-wave illumination in the quasi-steady-state limit. *J. Opt. Soc. Am. B, JOSAB*, 11(9):1743–1757, 1994.

[190] F. P. Strohkendl, J. M. C. Jonathan, and R. W. Hellwarth. Hole–electron competition in photorefractive gratings. *Opt. Lett.*, 11(5):312–314, 1986.

[191] G. Montemezzani and M. Zgonik. Light diffraction at mixed phase and absorption gratings in anisotropic media for arbitrary geometries. *Phys. Rev. E*, 55(1):1035–1047, 1997.

[192] P. Delaye, L.-A. de Montmorillon, and G. Roosen. Transmission of time modulated optical signals through an absorbing photorefractive crystal. *Opt. Comm.*, 118(1–2):154–164, 1995.

[193] Donald C. Solmon. The X-ray transform. *J. Math. Anal. Appl.*, 56(11):61–83, 1976.

[194] Stanley R. Deans. *The Radon Transform and Some of Its Applications*. Wiley, 1983.

[195] Peter A. Toft. *The Radon Transform – Theory and Implementation*. PhD thesis, Technical University of Denmark, Department of Mathematical Modelling, 1996.

[196] R. A. Brooks and G. Di Chiro. Principles of computer assisted tomography (CAT) in radiographic and radioisotopic imaging. *Phys. Med. Biol.*, 21(5):689, 1976.

[197] William H. Oldendorf. Isolated Flying Spot Detection of Radiodensity Dis-Continuities-Displaying the Internal Structural Pattern of a Complex Object. *IRE Transactions on Bio-Medical Electronics*, 8(1):68–72, 1961.

[198] D. E. Kuhl and R. Q. Edwards. Image Separation Radioisotope Scanning. *Radiology*, 80(4):653–662, 1963.

[199] R. M. Mersereau and A. V. Oppenheim. Digital reconstruction of multidimensional signals from their projections. *Proceedings of the IEEE*, 62(10):1319–1338, 1974.

[200] S. Dunne, S. Napel, and B. Rutt. Fast reprojection of volume data. In 1990 IEEE, editor, *Proceedings of the First Conference on Visualization in Biomedical Computing*, pages 11–18, 1990.